The impact of interior insulation on the hygrothermal performance of rammed earth walls

Margaux Indekeu

UNIVERSITÉ SAVOIE MONT BLANC

THÈSE

Pour obtenir le grade de

DOCTEUR DE L'UNIVERSITÉ SAVOIE MONT BLANC

Spécialité : **Sciences pour l'ingénieur**

Arrêté ministériel : 25 Mai 2016

Présentée par

Margaux L. INDEKEU

Thèse dirigée par **Monika WOLOSZYN**

préparée au sein du **Laboratoire LOCIE**
dans **l'École Doctorale Sciences Ingénierie Environnement**

L'impact de l'isolation intérieure sur les performances hygro-thermiques des murs en pisé

Thèse soutenue publiquement le **16 Novembre 2023**,
devant le jury composé de :
Mme, Monika, WOLOSZYN
Professeure Université Savoie Mont-Blanc, Directrice de thèse
M, Rafik, BELARBI
Professeur Université de La Rochelle, Rapporteur
M, Sofiane, AMZIANE
Professeur Université Clermont Auvergne, Rapporteur
Mme, Stéphanie, GIROUX-JULIEN
Professeure Université de Lyon, Examinateur
M, André, REVIL
Directeur de recherche Université Savoie Mont-Blanc, Président

Preface

First of all, I would like to thank Monika Woloszyn for entrusting me with this project, and Christophe Menezo and Christian Ruyer-Quil for (co-)supervision. Furthermore, I thank Hans Janssen for a fruitful collaboration.

For the material support, I thank Antonin Fabbri, Eric Maire, and Bruno Pinjon. Further, I would like to thank Chi Feng for the valuable sharing of his expertise in hygric characterisation and Evy Vereecken for providing me with some essential tools here and there. Moreover, I would like to thank the men of the X-ray and the people of Fablab. Furthermore, I express thanks to the technical staff involved for the necessary support.

Finally, I would like to thank my family for their support.

Margaux L. Indekeu

Abstract

The thermal renovation of rammed earth constructions presents a challenge in the current evolution towards energy efficient buildings. To preserve the character of the building, interior insulation is appropriate. The hygrothermal risks involved, however, need to be minimised to avoid damage. To this end, the present work investigates the impact of different interior insulation systems on the hygrothermal performance of rammed earth walls (unplastered, above the stem wall, and while rising damp is excluded). To enable this research, it is first studied how the hygric properties of rammed earth materials can be determined reliably and how the mechanical response of rammed earth walls can be elaborated.

The methodology consists of literature study, experimental material characterisation, theoretical performance indicator development, and hygrothermal numerical component simulation. The state of the art reveals that there is a lack of determined hygric properties. Hence, rammed earth materials are extracted from existing constructions for a complete hygric characterisation in the lab. The results of this are used as an input into the hygrothermal numerical simulation analysis of the behaviour of rammed earth walls under realistic climate conditions. Moreover, studying the state of the art reveals a lack of elaborated performance criteria adapted for rammed earth applications, specifically including the mechanical aspects. These mechanical aspects are redeveloped and implemented in the performance analysis with respect to the insulatability.

It is found that wood decay, interstitial mould growth, dripping moisture, and possibly fracture failure and buckling failure are the main risks to be minimised for the interior insulation of rammed earth walls. A capillary active calcium silicate insulation system providing an optimal inward drying of the absorbed wind-driven rain, serves best for minimising the risks. Besides, the observation that overhygroscopic responses play a considerable role in the hygrothermal performance of rammed earth walls, demonstrates the importance of the complete hygric material characterisation.

List of publications

Journal articles

Indekeu M. L., Janssen H., & Woloszyn M. (2022). Determination of the moisture diffusivity of rammed earth from transient capillary absorption moisture content profiles. *Construction and Building Materials*, *318*, 125978. https://doi.org/10.1016/j.conbuildmat.2021.125978.

Indekeu M. L., Feng C., Janssen H., & Woloszyn M. (2021). Experimental study on the capillary absorption characteristics of rammed earth. *Construction and Building Materials*, *283*, 122689. https://doi.org/10.1016/j.conbuildmat.2021.122689.

Conference proceedings

Indekeu, M. L., Feng, C., Janssen, H., & Woloszyn, M. (2019). Rammed earth hygric properties and evolution. In *MATEC Web of Conferences*, *282*, 02100. 4th Central European Symposium on Building Physics. https://doi.org/10.1051/matecconf /201928202100.

Indekeu, M., Woloszyn, M., Grillet, A., Soudani, L., & Fabbri, A. (2017). Towards hygrothermal characterisation of rammed earth with small-scale dynamic methods. *Energy Procedia*, *132*, 297–302. 11th Nordic Symposium on Building Physics. https://doi.org/10.1016/j.egypro.2017.09.731.

Langmans, J., Indekeu, M., & Roels, S. (2017). The impact of workmanship on the thermal performance of cavity walls with rigid insulation boards: Where are we today? *Energy Procedia*, *132*, 255–260. 11th Nordic Symposium on Building Physics. https://doi.org/10.1016/j.egypro.2017.09.711.

Contents

1 Introduction

1.1 Context and problem statement

Historical rammed earth buildings are widely present in several countries (Schroeder, 2012), including European countries such as France and Spain (HYGROBA, 2013b); (Dorothée, 2018). These building walls typically have 'boots', i.e. the stem wall, and a 'hat', i.e. the roof. The rammed earth wall itself is made of earth from the site. This earth is moistened poured between a wall-wide temporary formwork to be rammed in successive layers of ca. 10 cm height. The clay particles in the earth form the natural binder. Fig. 1.1 shows three traditional rammed earth buildings in France. These buildings are often more than 100 years old.

(a)

(b) (c)

Fig. 1.1: Typical cases of the target building stock of patrimonial rammed earth houses. (a) Farm, right on a rainy winter day (Scarato, 2014); (b) mill (Gutiérrez, 2016); (Bui, 2008); (c) dwelling (Scarato, 2014).

In the past decades, a growing awareness and recognition of the need of significant energy savings has settled. Among other sectors, the building sector (construction industry and households) is a significant user of energy (Hens, 2011), hence, harbouring large potentials for energy savings. The heat losses through the building envelope are responsible for a large share of the total energy use in buildings and form the most essential factor that can be influenced by the construction sector by providing thermal insulation (Deconinck, 2017).

For the thermal insulation of rammed earth building envelopes, interior insulation is appropriate to preserve the exterior façade looks (Calabrese, 2012). Interior insulation can however bring about problems due to the consequential modified hygrothermal state of the wall (the exterior construction becomes wetter and colder). These are problems such as an increased risk on wood decay, mould growth, and frost damage. Fig. 1.2 shows that for rammed earth constructions moreover the risk on severe structural damage increases. These risks involved hence need to be analysed beforehand in order to guide the retrofit decisions (Vereecken, 2013).

(a) (b) (c)

Fig. 1.2: Examples of collapse consequent to inappropriate thermal renovation of rammed earth walls with interior insulation. (a) (Scarato, 2014); (Fabbri et al., 2019); (Gallipoli et al., 2022); (b) (Galmiche, 2019); (c) (Scarato, 2014).

1.2 Objectives and research question

In response to the burning questions in renovation practice, the present work aims at evaluating the interior insulatability of rammed earth walls via numerical simulation. The associated research question is: 'What is the impact of interior insulation on the hygrothermal performance of rammed earth walls?'. Two subobjectives need to be tackled for this: 'How to perform a complete hygric material characterisation for rammed earth?' and 'How to provide a complete set of performance indicators for rammed earth?'.

Objective 1: Hygric material characterisation

In order to be able to simulate the hygrothermal behaviour of rammed earth walls that are exposed to driving rain, the complete hygric material characterisation is needed, including the properties in the overhygroscopic range. These hygric properties in the overhygroscopic range are systematically missing for rammed earth materials in the literature. This fundamental lack of knowledge is attributed to the material unstability of rammed earth samples at high moisture contents. The available tests for this overhygroscopic hygric material characterisation, such as the capillary absorption test, will hence need to be redeveloped for rammed earth materials to eliminate this material evolution.

Objective 2: Performance indicator development

To enable assessing the hygrothermal performance of rammed earth walls as seen in practice, mechanical performance indicators need to be added to the usual set of hygrothermal performance indicators for the analysis. This usual set of performance indicators for the insulatability of stable building walls consists of the thermal insulation quality, the thermal and hygric transient response, the interior and interstitial mould growth, the dripping moisture, the wood decay, and the frost damage. For rammed earth building walls, additionally the overall strength and stiffness and the differential hygrothermal stresses and strains, as well as the erosion by wind-driven rain, need to be developed into performance indicators.

Objective 3: Interior insulatability evaluation

Using the complete hygrothermal material characterisation and the mechanically completed set of performance indicators, the ultimate objective is addressed: the evaluation of the interior insulatability of rammed earth walls. More specifically, the objective is to first gain insight into the hygrothermal performance of non-insulated rammed earth walls, and next quantify the impact of different interior insulation systems.

1.3 Methodology and structure

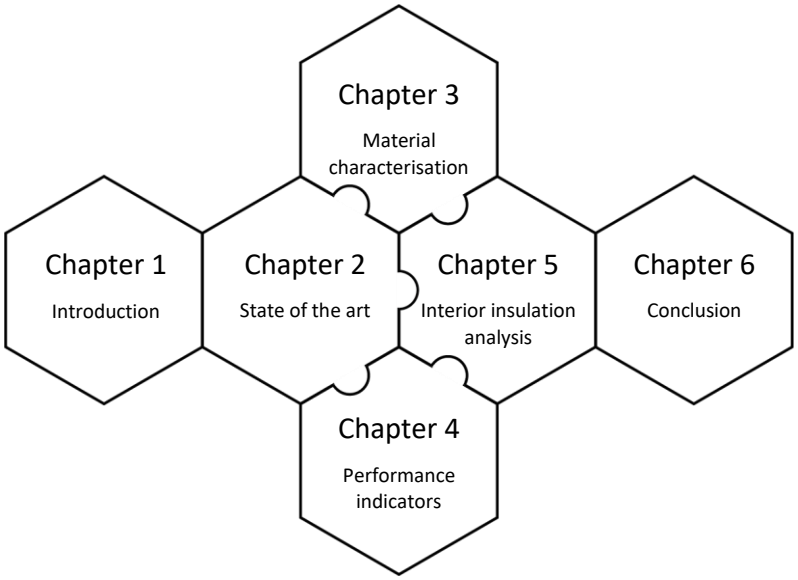

Fig. 1.3: Thesis outline with puzzle connections that represent links from one chapter to another. Idea: (Protopapadaki, 2018).

In Section 2, the **state of the art** of the interior insulatability of rammed earth walls is reviewed. This concerns three main topics to be addressed: hygrothermal performance analysis, hygrothermal component simulation modelling, and hygrothermal material characterisation. The hygrothermal performance analysis deals with works that are similar to the ultimate objective of the present work: the evaluation of the insulatability. The performance indicators are herein discussed: thermal insulation quality, thermal transient response, biological deterioration or dripping moisture, hygric transient response, mechanical response, frost damage, erosion, and rising damp. The hygrothermal component simulation modelling provides the physical equations behind the numerical simulation program to be used. And the hygrothermal material characterisation treats the needed hygric and thermal properties of rammed earth materials.

In Section 3, the full-range hygric **material characterisation** of two different traditional rammed earth building materials is elaborated in the lab. This hygric characterisation comprises the moisture retention curve and the moisture permeability curve, which are both needed as input in component simulations. The moisture retention curve is determined by means of traditional measurement techniques that avoid material evolution due to wetting in the high range (desiccator testing and mercury intrusion porosimetry). The moisture permeability curve is determined through capillary absorption testing with X-ray radiography (besides cup testing). For this, the standard capillary absorption test is to be adapted to be applicable for rammed earth.

In Section 4, the new mechanical **performance indicators** relevant for the interior insulation of rammed earth walls are developed. First, the overall strength and stiffness of rammed earth walls is overhauled. Two performance indicators follow from this: fracture failure and buckling failure. Next, differential hygrothermal stresses and strains including clay swelling damage are explained. The hygric clay swelling damage by repeated shearing of a surface layer of the rammed earth wall is developed further into a third performance indicator. Finally, an erosion criterion is designed as the fourth new performance indicator.

In Section 5, the **interior insulation analysis** of rammed earth walls is performed by means of hygrothermal numerical component simulation. The hygric properties of the rammed earth materials determined in Section 3 are used as an input. Realistic atmospheric boundary conditions including wind-driven rain are imposed. The hygrothermal performance is quantified by means of risk indicators for thermal insulation quality, hygro-thermal insulation quality, thermal transient response, interior mould growth, interstitial mould growth, dripping moisture, wood decay, hygric transient response, fracture failure, buckling failure, clay swelling damage, frost damage, and erosion. First, the hygrothermal performance of the non-insulated reference rammed earth wall is evaluated. Next, the impact of different interior insulation systems on the hygrothermal performance is analysed. The preferred retrofit system would yield the lowest damage risks and at the same time the highest improved thermal insulation quality. The field of results is expanded by studying the influence of the insulation thickness, the rammed earth material, the rammed earth wall thickness, and the wall orientation, to enable drawing more substantiated and comprehensive conclusions regarding the insulatability of rammed earth walls. Finally, the influence of the mechanical performance indicators of fracture failure, buckling failure and clay swelling damage is evaluated, including the impact of the mechanical properties on the risk assessment.

2 State of the art

2.1 Introduction

The term state of the art expresses the current state of affairs, technology, or knowledge. It is thus the highest level of development reached at this time. About the interior insulatability of rammed earth walls, there are especially a lot of questions in practice and there is a lack of adequate scientific research.

The goal of this literature study is to identify specific gaps in the field of knowledge that need to be resolved to assess the interior insulatability of rammed earth walls. In this way, the refined goals and research questions of the present work are determined.

The hygrothermal performance investigation of building walls by means of numerical simulation can be structured into three hatches: the hygrothermal analysis, modelling, and material characterisation. The present state of the art study follows this same three-part subdivision.

In Section 2.2, information on hygrothermal performance analysis is introduced. From the four main performance criteria and the heat and moisture balance equations at the building level, over the performance requirements at the envelope level and their function in the (deterministic or probabilistic) hygrothermal performance analysis, to a review of hygrothermal performance analyses applied to rammed earth constructions and the divided opinions on the interior insulatability of rammed earth walls. Furthermore, the hygrothermal performance criteria at the envelope level are reviewed in more detail: the thermal insulation quality, thermal transient response, interior mould growth, interstitial mould growth, dripping moisture, wood decay, hygric transient response, mechanical response, frost damage, erosion, and rising damp.

In Section 2.3, theoretical background on hygrothermal component simulation modelling is given. This comprises the heat and moisture balance equations at the component level that are implemented in the numerical simulation software and the surface balances that are used to apply the atmospheric boundary conditions.

In Section 2.4, hygrothermal material characterisation is reviewed for the hygric and the thermal properties that are needed simulation input. The usual determination methods for stable building materials are summarised and the available data for rammed earth materials are collected.

2.2 Hygrothermal performance analysis

The four main performance criteria of comfort, durability, health, and sustainability according to which the physical quality of a building is assessed are determined by the hygrothermal response of the building (Hens, 2011). The target buildings in the present work are dwellings. The hygrothermal response concerns the heat, air, and moisture interaction in and between a construction and its environment. The key tool to gain insight into and control the heat, air, and moisture flows and states in building zones and component materials is the formulation of balances. These balances embody conservation equations, which state that an increase of stored quantity (of energy or mass e.g.) in a system equals the amount of the quantity which flows in minus the amount which flows out of the system over time.

For the evaluation of building enclosure parts on hygrothermal response, a combination of heat, air, and moisture balances formulated separately at the building level (Fig. 2.1 and Eqs. (2.1) and (2.2)) and at the component level (Section 2.3) may be necessary (Hens et al., 2006) or the simulation of one of both levels may suffice depending on the purpose of the study (Janssen & Roels, 2009); (Tijskens et al., 2017). In the present work, the analysis is simply performed at the component level because the more holistic perspective falls out of the scope since (a lack of) more fundamental research gains priority (as will be shown). Nevertheless, the balance equations at the building level are still presented below, to demonstrate which phenomena and factors determine the interior environment climate conditions.

Fig. 2.1 shows a rammed earth house that is used as the application example for the hygrothermal analysis in the present study. Eqs. (2.1) and (2.2) are the zone heat and moisture balance, respectively, written for the interior air volume assuming that ideal convective mixing, no buoyancy effects, no surface condensation, and steady state air exchange by the ventilation only occur, and with heating-period-consistent transport directions. Eq. (2.1) shows that the interior temperature is governed by solar heat gains, interior heat production, ventilation heat losses, and transmission heat losses. Eq. (2.2) shows that the interior humidity is governed by interior moisture sources, moisture transport by ventilation air, and moisture exchange with the enclosure. The interior gains of heat and vapour production by human occupants and their activities are mainly from heating, living, cooking, cleaning, showering, and laundering. The links with the transfers in the enveloping wall component are elaborated in Section 2.3.2; for a given surface temperature and vapour pressure, the only hygrothermal coupling at the building level is the temperature input for the vapour density (ideal gas law), as well as the advective transports. The other transport terms in the equations are formulated using the principal laws of physics for conduction (Fourier), convection (Newton), and radiation (Stefan-Boltzmann) mechanisms.

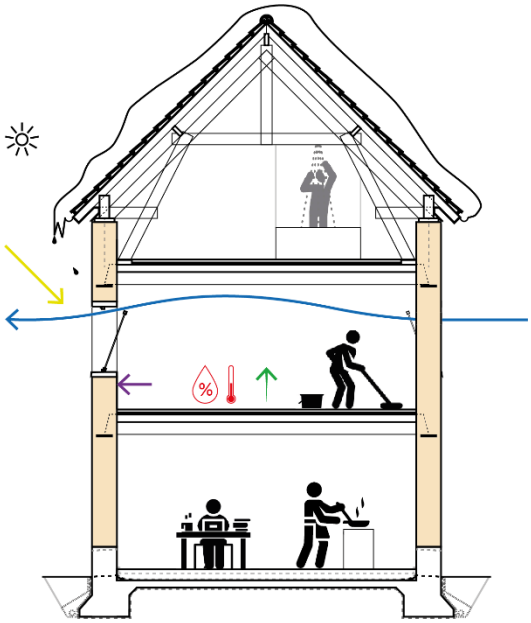

Fig. 2.1: Heat and moisture transfer mechanisms at building level.

$$\rho_a c_a V \frac{\partial T_i}{\partial t} = A_g g_g q_{S,se} + Q_{prod} - \frac{nV}{3600}\rho_a c_a (T_i - T_e) - A h_i (T_i - T_{si}) \tag{2.1}$$

$$\frac{V}{R_v T_i}\frac{\partial p_{v,i}}{\partial t} = G_{v,prod} - \frac{nV}{3600 R_v T_i}\left(p_{v,i} - p_{v,e}\right) - A\beta\left(p_{v,i} - p_{v,si}\right) \tag{2.2}$$

ρ_a	density of air	1.225	kg/m³
c_a	specific heat capacity of air	1000	J/(kg K)
V	air volume		m³
T	temperature		K
t	time		s
A	surface area		m²
g	solar heat gain coefficient		-
$q_{S,se}$	incident short-wave radiation heat flux from sun		W/m²
Q	heat flow		W
n	air change rate		h^{-1}
h	surface heat transfer coefficient		W/(m² K)
R_v	gas constant for water vapour	462	J/(kg K)
p_v	vapour pressure		Pa
G_v	vapour flow		kg/s
β	convective surface moisture transfer coefficient		s/m
$e/i/g/s/prod$	exterior / interior / glass / surface / production		

From the four performance criteria at the building level, several performances required at the envelope level follow: thermal insulation quality, thermal transient response, biological deterioration or dripping moisture, hygric transient response, overall strength and stiffness, differential hygrothermal stresses and strains and clay swelling damage, frost damage, erosion, rising damp, air tightness, thermal bridging, salt damage, chemical degradation, and material evolution. Only the first eight to nine performances are considered in the present work, Fig. 2.2. Of these, the usual set investigated in hygrothermal analyses is limited to nos. 1, 3, 4, and 7 (Vereecken et al., 2015). The three (to four) most hygromechanically tinted performance requirements, i.e. nos. 5, 6, 8 (, and 9), are additionally developed for rammed earth applications in the present work. This is because rammed earth constructions are typically moisture-vulnerable, whence these nos. appear indispensable, supported by field observations, cf. Fig. 1.2.

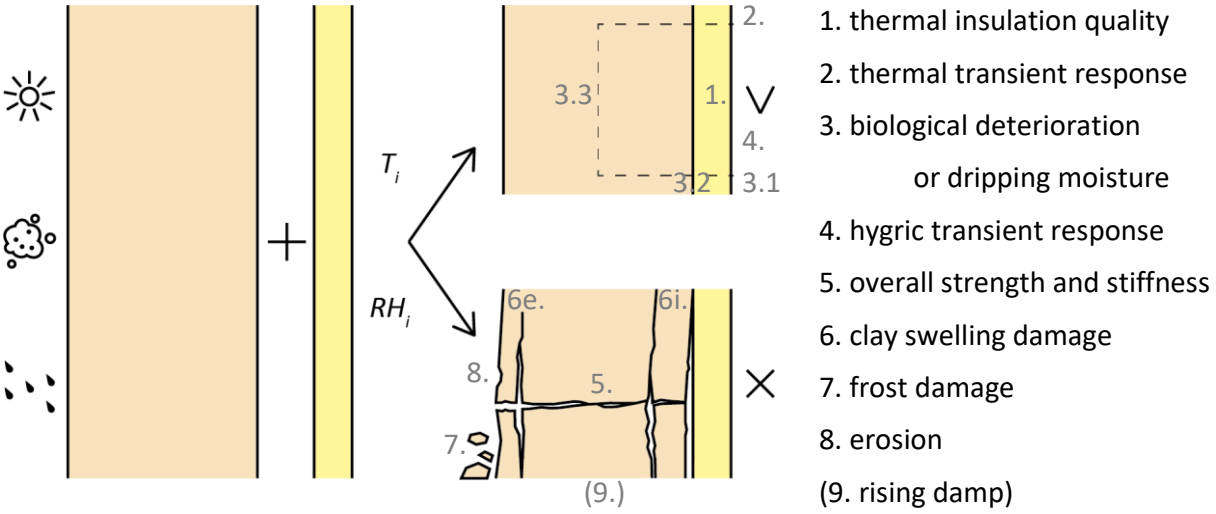

Fig. 2.2: Overview hygrothermal performances for interior insulation of rammed earth walls.

Per performance, a quantifiable indicator is defined (to which a threshold value can be coupled and moreover a minimum required reliability level in a probabilistic approach). The hygrothermal analysis basically consists of a comparison of these indicator values before and after the retrofit for each insulation option. Life threatening failure events such as the collapse of rammed earth structures induced by dangerous rising damp (or other ways of moisture accumulation) or the collapse of wooden floor beams by rot are clearly less acceptable than e.g. the reduced quality of thermal insulation materials by moisture or the reduced thermal inertia comfort during the day in summer. The interior insulation system solution resulting in the best balance between the benefits and the risks needs to be selected. The total risk for this is in a probabilistic context defined as the sum over the failure events of the product of the probability of the failure event and the summed severity of the consequences of that event expressed in costs (Hens et al., 2006). The probability

points to the stochastic nature of all elements dealt with in buildings (the exterior climate, interior climate, material quality, workmanship quality) that is taken into account in the simulations by varying these input parameters and sampling. To limit the chances of damage hence, it is appropriate to build in redundancies where possible in the detail solutions. A probabilistic study falls out of the scope of the present work and a deterministic approach is used instead to study the most crucial variants.

Comprehensive hygrothermal analyses applied to rammed earth constructions are rare (HYGROBA, 2013a;b). The studies that are available typically show limitations. These limitations are both concerning the input parameters and the outputs. As for the inputs, the material properties are often only measured in the hygroscopic range, and wind-driven rain is often omitted as a boundary condition (François et al., 2017); (Bui et al., 2020). As for the outputs, they often only comprise thermal (Hall & Allinson, 2008) and hygric (Allinson & Hall, 2010) performance criteria. The mechanical performances (Kianfar & Toufigh, 2016); (Fabbri et al., 2018) remain unaddressed. These limitations are also the case in (HYGROBA, 2013a;b), in which furthermore only externally plastered wall assemblies are studied. In the present work, it is presumed that in such cases, exterior insulation would be used instead of interior insulation.

In the past decade, several interior insulation systems have been promoted for the retrofit action of rammed earth walls. At first, vapour tight systems were considered a possible solution (avoiding interstitial condensation) (HYGROBA, 2013a;b); (Heitz et al., 2015). However, a consensus has grown that these should actually be avoided, being the most risky with regard to rising damp as well as driving rain accumulation (Galmiche, 2019); (Atelier Chevillotte, 2020). People besides often speak of “allowing the rammed earth walls to breathe” (Buzo et al., 2014), which could imply using a vapour open insulation system. However, several sources are against vapour open insulation systems, see Table 2.1, because these lead also to moisture accumulation in the wall and moreover degradation of the insulation material. Capillary active insulation systems are finally advocated (buffering interstitial condensation) (Livradois-Forez, 2011); (Atelier Chevillotte, 2020).

Table 2.1: Opinions on how to interior-insulate rammed earth walls.

	Pro	Contra
Vapour tight	(HYGROBA, 2013b); (Heitz et al., 2015)	(Galmiche, 2019); (Heitz et al., 2015); (Atelier Chevillotte, 2020)
Vapour open	-	(Galmiche, 2019); (Atelier Chevillotte, 2020)
Capillary active	(Heitz et al., 2015); (Livradois-Forez, 2011)	-

2.2.1 Thermal insulation quality

The thermal transmittance or U-value (U, W/(m² K)) of a building envelope wall is required to be (within a range from 0.15 W/(m² K) to) about 0.3 W/(m² K) maximum in European countries with a temperate oceanic climate (Hens, 2011), mainly for energy efficiency. This stationary U-value is defined on the basis of conservation of energy (surface heat balance without heat source or sink) and using Fourier's law, as the conductive heat flux through the wall per degree temperature difference from environment to environment, Eq. (2.3). It indicates how easily heat is transported through the wall. Its inverse is the total thermal resistance (R, (m² K)/W) of the wall including the exterior and interior surface heat transfer resistances (Section 2.3.2), Eq. (2.4).

$$q_{trans} = U\left(T_{i,equ} - T_{e,equ}\right) \tag{2.3}$$

$$U = \frac{1}{R} = \frac{1}{R_{si} + \sum_{i-e} R + R_{se}} = \frac{1}{1/h_i + \sum_{i-e} d/\lambda + 1/h_e} \tag{2.4}$$

q	heat flux		W/m²
U	thermal transmittance		W/(m² K)
T	temperature		K
R	thermal resistance		m² K/W
d	thickness		m
λ	thermal conductivity		W/(m K)
h	surface heat transfer coefficient	8 (h_i) or 25 (h_e)	W/(m² K)
$trans/i/e/equ/s$	transmission / interior / exterior / equivalent / surface		
$min/req/v/sat$	minimum / required / vapour / saturation (cf. below)		

With a dry thermal conductivity of 0.6 W/(m K) for rammed earth material (Section 2.4.2) and an average wall thickness of 0.5 m, Fig. 2.3 (a), the U-value of a rammed earth wall amounts to 1 W/(m² K). This excessive U-value is reflected in the great energy consumption for space heating, Fig. 2.3 (b). The massive building walls need to be insulated to increase their thermal resistance (Soebarto, n.d.). Thermal insulation materials with a small to a less small thermal conductivity lead to a needed insulation thickness of 6 cm (e.g. XPS) to 15 cm (e.g. wood fibre, calcium silicate), Eq. (2.5).

$$d_{insulation,min} = \lambda_{insulation}\left(\frac{1}{U_{req}} - R_{si} - \frac{d_{rammed\ earth}}{\lambda_{rammed\ earth}} - R_{se}\right) = 2.34\ \frac{m^2K}{W} \times \lambda_{insulation} \tag{2.5}$$

(a) (b)

Fig. 2.3: Typical rammed earth wall thickness and energy consumption for space heating.

The thermal renovation of massive walls is commonly performed by means of interior insulation because this method is cheap and practically easy to apply relative to exterior insulation with typically demanding assemblies. It is moreover especially suitable if one aims to preserve the original looks of the building from the outside, which is often the case for heritage building façades, such as those of quality rammed earth. The rammed earth buildings in the present work are presumed not to be plastered exteriorly. For the application of interior insulation, while leaving the outside untouched, it is required that the building does not show existing deficits such as structural issues (Livradois-Forez, 2011); (Scarato, 2014); (Avons-Bariot, 2017); (Calabrese, 2012) or rising damp in particular, which would make interior insulation dangerous and is further presumed to be excluded in this work. The addition of an interior thermal insulation layer modifies the hygrothermal performance of the wall which on average becomes colder and wetter, Fig. 2.4. Phenomena like moisture accumulation by interstitial condensation, reduced drying ability, and increased damage can start to play and need to be analysed before the retrofit to find insulation solutions that keep the chances of moisture problems to a minimum, cf. Fig. 2.2. Herein, the hygric properties of both the wall material and the insulation material are of interest (Vereecken et al., 2015); (Zhou et al., 2018), which is also why insulation systems are classified according to their hygric rather than thermal properties.

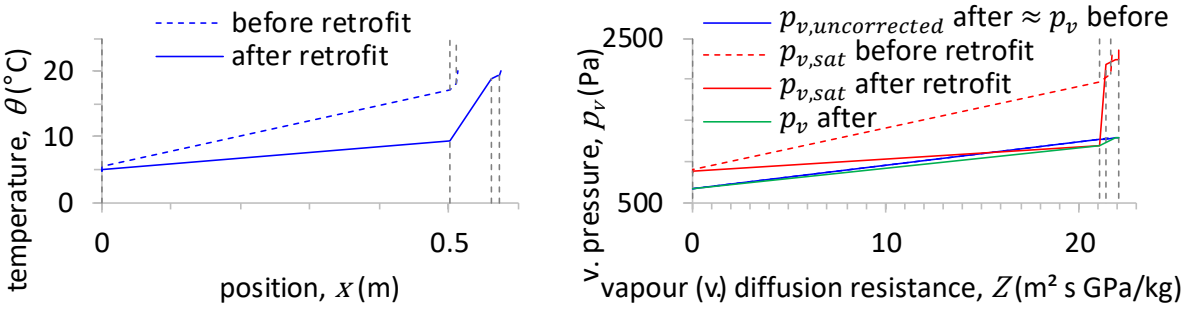

(a) (b)

Fig. 2.4: Winter temperature profile and interstitial condensation with vapour open insulation.

Three systems are distinguished, Fig. 2.5, depending on their strategy on how to deal with the two main moisture sources for building walls: wind-driven rain (Janssen et al., 2007b) (for at least one orientation (Abuku et al., 2009a)) and interstitial condensation (if any, especially pronounced in winter, Fig. 2.4 (b)). The first option would be to apply a vapour tight system (e.g. XPS). In this way, however, the wall becomes besides thermally also hygrically isolated from the interior whereby all inward drying ability of the absorbed wind-driven rain is eliminated. In spite of interstitial condensation being avoided, biological deterioration can hence still become a problem. Furthermore, the moisture accumulation can lead to reduced strength and stiffness, wooden beam ends decay, frost damage, etc. The second option is a vapour open system (e.g. mineral wool). While the inward drying is enabled by evaporation, free rein is given to interstitial condensation and/or moisture accumulation, depending on the absorption by the wall material. The third option is a capillary system (e.g. hydrophilic mineral wool, cellulose, wood wool, wood fibre, or calcium silicate). The difference with the second option is that the insulation absorbs moisture as well. Consequently, the inward drying and redistribution can be optimised. Moreover, the interstitial condensation can be manipulated in several ways (Vereecken, 2013). This option should yield the lowest moisture contents in the wall (close to the original state). However, the thermal insulation quality reduces as the insulation moistens.

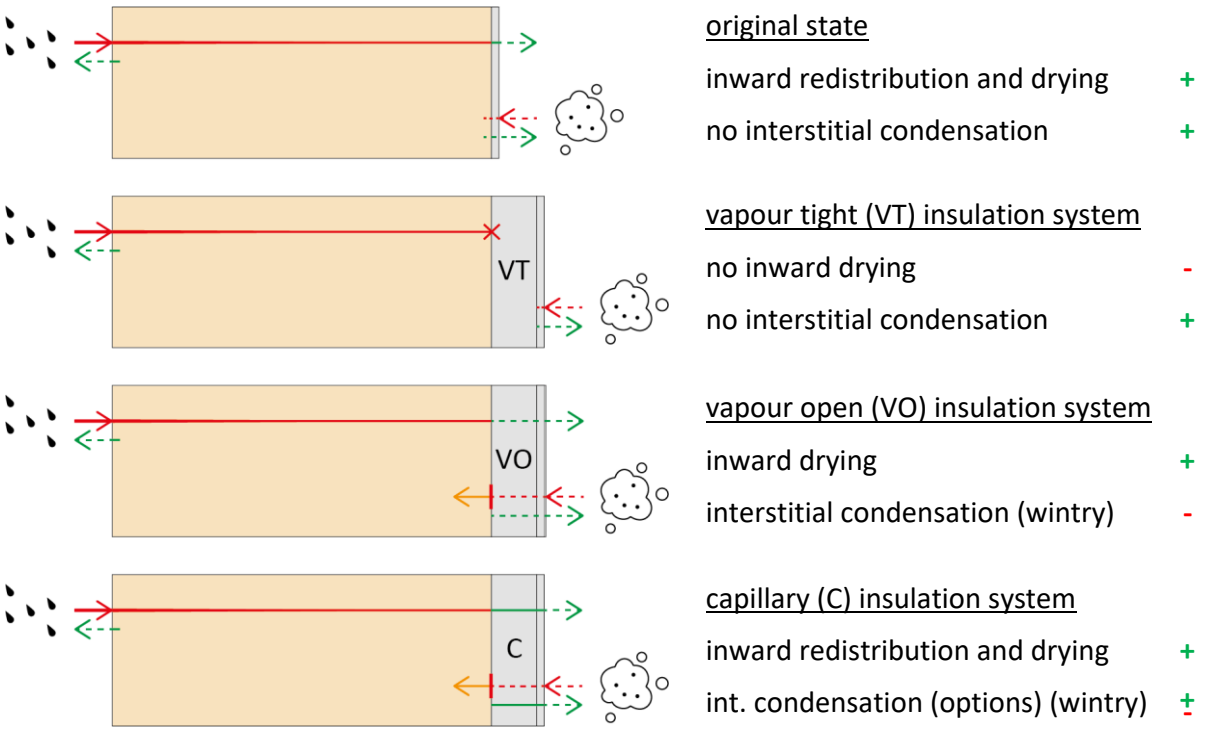

Fig. 2.5: Three main types of interior insulation systems.

The interior plaster layer that is typically present in traditional residential rammed earth buildings (cf. Fig. 2.8) is (necessarily) chopped off prior to the retrofit, Fig. 2.6. It is assumed that a 4 mm glue mortar layer (besides insulation plugs) is used to adhere the insulation systems to the rammed earth wall; except for insulation systems comprising of mineral wool, that are mounted between stainless steel studs against the wall. It is assumed that a 10 mm thick gypsum plaster layer is applied as interior finishing for the (sufficiently dense/hard) insulation systems; again except for the mineral wool systems, where a 12 mm thick gypsum board is applied.

(a) (b)

Fig. 2.6: Interior finishing plaster layer of traditional rammed earth buildings chopped off before retrofit.

The effect of the moisture content dependent thermal conductivity on the total thermal resistance of the wall can be estimated using Eq. (2.4) (Vereecken & Roels, 2015). This is only correct if no heat sources or sinks from water phase changes occur within the wall though. Otherwise, the heat flow is not constant throughout the wall and Eq. (2.3) should be used wherein the conductive heat flux of interest through the wall is determined by that from the interior to the interior surface, Eq. (2.6) (b). This heat flux is obtained as a result of numerical simulation, on an hourly time step basis. Besides the U-value itself, a requirement exists that the increase in U-value by moisture should not exceed 10% (Hens, 2011).

$$U \overset{Eq.\ (2.3)}{\underset{(a)}{=}} \frac{q_{trans}}{\left(T_{i,equ} - T_{e,equ}\right)} \underset{(b)}{=} \frac{q_{si}}{\left(T_{i,equ} - T_{e,equ}\right)} \tag{2.6}$$

2.2.2 Thermal transient response

The thermal transient response of a building wall is determined by three harmonic characteristics (for each of which quantitative requirements exist (Hens, 2011); their relative importance can depend on the climate (Hens, 2010)). By the addition of a thermal insulation layer to a massive wall, the dynamic thermal resistance and the temperature damping increase, but the admittance strongly decreases if interior insulation is applied, which is mainly because the thermal mass is eliminated. An in-depth analysis of the thermal transient performance (Hall & Allinson, 2008) falls out of the scope of the present work (because the need to thermally insulate a building against the cold during winter is considered more important than summer comfort, besides the reasons mentioned below); the main definition is yet to be given. The admittance (W/(m² K)) is the ratio of the complex heat flux and the complex temperature at the interior surface. It is related to the thermal effusivity (J/(m² $s^{-1/2}$ K)), which is the square root of the product of the volumetric heat capacity and the thermal conductivity. It is a measure for the extent to which a wall can absorb heat at its interior surface with a fluctuating temperature. It should be greater than the interior surface heat transfer coefficient divided by two. A wall with a great admittance can temper interior temperature fluctuations (thermal inertia), which can contribute to the thermal comfort; especially when no appropriate exterior shading system for east over south (in the northern hemisphere) to west-oriented large glass areas (or eventually a cooling system) is provided to prevent overheating during summer.

For the thermal comfort, it is required that the weighted average of the interior air- and radiation temperature remains within certain bands (Hens, 2011); (Olesen & Parsons, 2002); (Olesen, 2005), e.g. 26.5 °C max in summer. If only the building component is simulated and not the building zone or architecture, the interior temperature is commonly imposed in accordance with the standard (EN 15026) and the interior surrounding surfaces are assumed to be at this same temperature (like in the present work). Consequently, an evaluation of the risk on thermal discomfort or overheating falls out of the scope of work. To roughly assess any significant changes in the thermal transient response, specifically the admittance, still, the heat flux from the interior in and out of the interior surface can be used.

2.2.3 Biological deterioration or dripping moisture

2.2.3.1 Interior mould growth

Moulds develop when their spores that are present in the air find the suitable conditions to germinate on surfaces. They prefer humid and warm conditions plus they need some time. Visible as well as non-visible mould growth on the interior surface of a wall should be avoided for reasons of comfort, health, and durability. The empirical updated VTT model (Vereecken & Roels, 2012) is commonly used for the evaluation of the mould growth risk, see Appendix A. Alternatively, a less precise but simpler criterion can be used that is based on a single critical surface relative humidity value (Vereecken et al., 2015).

Any biological deterioration of the exterior surface of the wall (e.g. by plants, moss growth, or algae) (Chatel, 2012); (Galmiche, 2019); (Fazio et al., 2015) is not considered in the present work.

2.2.3.2 Interstitial mould growth or dripping moisture

Moulds can develop as well on surfaces and at interfaces in the construction (if no perfect contact is presumed or in case of air open materials such as mineral wool). This can occur as a result of persistent accumulating interstitial (or summer) condensation and/or accumulated wind-driven rain. It could (like in the present work) e.g. be assumed that a mould index (Appendix A) smaller than 5 here remains acceptable, which means that moderate mould growth at microscopic level or visually detectable is allowed. This requirement is less strict than for the interior surface because the aerial (and visual) contact with the inhabitants is absent or less direct.

Besides, moisture dripping from interfaces owing to interstitial (or internal surface, or summer) condensation where two non-capillary materials are involved should be avoided.

2.2.3.3 Structural wood decay

Structural wood decay or wood rot is caused by giant moulds (fungi) that eat the cellulose or the lignin whereby the strength, stiffness, and cohesion of the wood is lost, proportional to its mass loss. The mass loss of wooden elements is unrecoverable and becomes problematic when structural failure occurs. The empirical VTT wood decay model (Viitanen et al., 2010) is commonly used to evaluate the risk on this decay development. In this way, it can be assessed whether wood treatments are required prior to the retrofit. Rammed earth constructions typically have wooden floor beams embedded, for ca. 2/3 of their height, Fig. 2.7 (a,b). They also typically have wooden

lintels, Fig. 2.7 (c,d), and they may have other integrated wooden elements such as distribution boards (Livradois-Forez, 2011) or corner reinforcements (TERA, 2018).

Suppose that all wooden elements except the floor beams are already treated against decay. The mass loss ML (%) of the wooden floor beam ends is calculated by the model based on the temperature and the ambient relative humidity, Eqs. (2.7)-(2.9). To give an idea, the critical relative humidity of 95% corresponds to a moisture content of ca. 20%, kg/kg, i.e. 100 kg/m³ with a bulk density of 500 kg/m³, translated using a typical moisture retention curve for construction wood (Hens, 2011).

Activation process:

$$\alpha_{t+\Delta t} = \alpha_t + \underbrace{\Delta t}_{1\text{h}} \times \begin{cases} \dfrac{1}{24 \times 30 \times t_{cri}}(\theta, RH) & when\ \theta > 0\ °C\ and\ RH > 95\% \\ -\dfrac{1}{17520h} & otherwise \end{cases} \tag{2.7}$$

$$t_{cri} = \frac{2.3\theta + 0.035RH - 0.024\theta \times RH}{-42.9 + 0.14\theta + 0.45RH} \tag{2.8}$$

Mass loss process:

$$ML_{t+\Delta t} = ML_t + \underbrace{\Delta t}_{1\text{h}} \times \begin{cases} (-0.0596 + 0.000196\theta + 0.000625RH)\ when\ \alpha \geq 1\ and\ \theta > 0\ °C\ and\ RH > 95\% \\ 0 \quad otherwise \end{cases} \tag{2.9}$$

α	relative measure of the state of the fungi with respect to its state at the initiation of the mass loss process	-
t_{cri}	critical time required to reach α=1 (start growth)	months
θ	temperature	°C
RH	relative humidity	%
ML	mass loss	%

(a) (b) (c) (d)

Fig. 2.7: (a,b) Wooden floor beams embedded in rammed earth construction, (b) with presumed integrated distribution board. (c,d) Wooden lintels in rammed earth construction.

2.2.4 Hygric transient response

The hygric transient response concerns the ability of a wall to temper interior humidity fluctuations, whence it is also called the hygric inertia or moisture buffering. This response can contribute to the indoor air quality comfort where humid air is typically perceived as less fresh (Hens, 2011) and dry air can lead to sensory irritation in the eyes and airways (Wolkoff, 2018). Residential buildings in European countries with a temperate oceanic climate (that are heated when necessary for a minimum interior temperature of 20 °C), whether their interior finishing is optimal for moisture buffering or not, typically do not require a system to control the interior humidity. This reflects that this performance is less important than the thermal quality. Some appropriate natural ventilation suffices against wetness, while a small moisture load suffices against dryness. Besides, the interior walls, floors, ceilings, and objects contribute to the moisture buffering (which can also be the case for the thermal transient response).

The risk on interior humidity discomfort can be quantified as the number of hours that the interior relative humidity exceeds 70% throughout a considered period, or falls below 30%. Like for heat, the interior humidity evolution can be assessed by simulating both the building component and the building zone, and by imposing boundary conditions to the zone rather than directly to the wall (Janssen & Roels, 2009). This requires the simultaneous solution of an additional system of equations for the zone air which is not standardly implemented in component simulation tools (Abuku et al., 2009a); (Vereecken et al., 2015); (Tijskens et al., 2017). To circumvent this, the interior humidity is commonly imposed in accordance with the standard (EN 15026). An in-depth study of the moisture penetration depth (Wan et al., 2017) from the interior surface of the

humidity fluctuations in the building zone falls out of the present work scope. Since the moisture penetration depth for 24 h amounts to ca. 3 cm for gypsum plaster (Rode et al., 2005), while this layer is only 1 cm thick, Fig. 2.8, the material beneath the plaster can still play a role. Any significant interior moisture buffering effects by the component can therefore be assessed qualitatively through the vapour flux in and out of the interior surface.

(a) (b)

Fig. 2.8: Interior finishing plaster layer of traditional rammed earth buildings.

2.2.5 Mechanical response

In case of rammed earth, potential hygrothermal consequences of interior insulation do not only include thermal and hygric but also mechanical performances and risks (Augarde, 2012); (Gallipoli et al., 2022); (Calabrese, 2012). Although frequently observed in practice, cf. Fig. 1.2, these mechanical risks have (almost: (Berger et al., 2015)) never been translated into performance criteria for hygrothermal analyses before (HYGROBA, 2013a); (Brinkmann & Wiehle, 2023). Mainly three mechanical performance indicators are hence to be newly developed in the present work (Section 4): fracture failure, buckling failure, and clay swelling damage. Besides, an erosion risk indicator is provided. Rising damp is discussed below.

2.2.6 Frost damage

The chances of frost damage (Gallipoli et al., 2022) increase upon interior insulation (Minke, 2006); (Hens, 2011); (Vereecken, 2013). The risk on frost damage, as the number of frost-thaw cycles, can be evaluated by means of a fixed minimum saturation degree and maximum temperature combination (Vereecken et al., 2015). Besides, frost performance evaluation functions exist that take into account the mechanical material characteristics in a more advanced way (Feng et al., 2019). In case there is a lack of measurement data for this (as in the present work, for rammed earth), an elaborated temperature – moisture content relationship (Koči et al., 2017); (Zhou et al.,

2017) can be used, that, however, does not take into account mechanical material characteristics, see Appendix B.

2.2.7 Erosion

A destructive natural action most specific to rammed earth walls is wind-driven rain erosion (Calabrese, 2012); (Morris, 2012); (Gallipoli et al., 2022). In spite of various architectural measures to counter this erosion, such as a protruding roof construction, it can still occur in practice. As the moisture contents in the wall typically tend to increase upon interior insulation, the risk on erosion damage at the exterior surface could increase, and the erosion risk needs to be monitored.

2.2.8 Rising damp

Rising damp is a criterion that is usually never explored in the analysis of interior insulation. This is because, if rising damp is present, interior insulation is not applied unless the rising damp problem is fixed first. This in turn is because rising damp can only invigorate upon interior insulation and it results in high moisture contents, with all its consequences. When it comes to rammed earth constructions, any rising damp problems need to be fixed at the height of the stony stem wall (to avoid rising damp-induced collapse) (TERA, 2018); (Heitz, 2014); (Livradois-Forez, 2011); (Hens, 2011); (Scarato, 2014); (Morris, 2012); (Gallipoli et al., 2022); (Calabrese, 2012). Rising damp therefore falls out of the present work scope.

2.3 Hygrothermal component simulation modelling

2.3.1 Transfer equations

The numerical simulation tool that is used to simulate the hygrothermal behaviour of building components is based on a theoretical model (Carmeliet, 2006); (Hagentoft et al., 2004); (Nicolai & Grunewald, 2006). The hygrothermal transfer in the construction envelope under imposed exterior and interior boundary conditions is modelled, Fig. 2.9 (a). Hygrothermal transfer means storage and transport of heat, air, and moisture. In the present work, it is assumed that no air transfer occurs. The conservation equations apply to representative elementary material volumes, Fig. 2.9 (b). A major assumption is that the porous building material remains stable. As no material evolution occurs, material properties such as the open porosity are constant. The material properties link the transfers to their driving potentials.

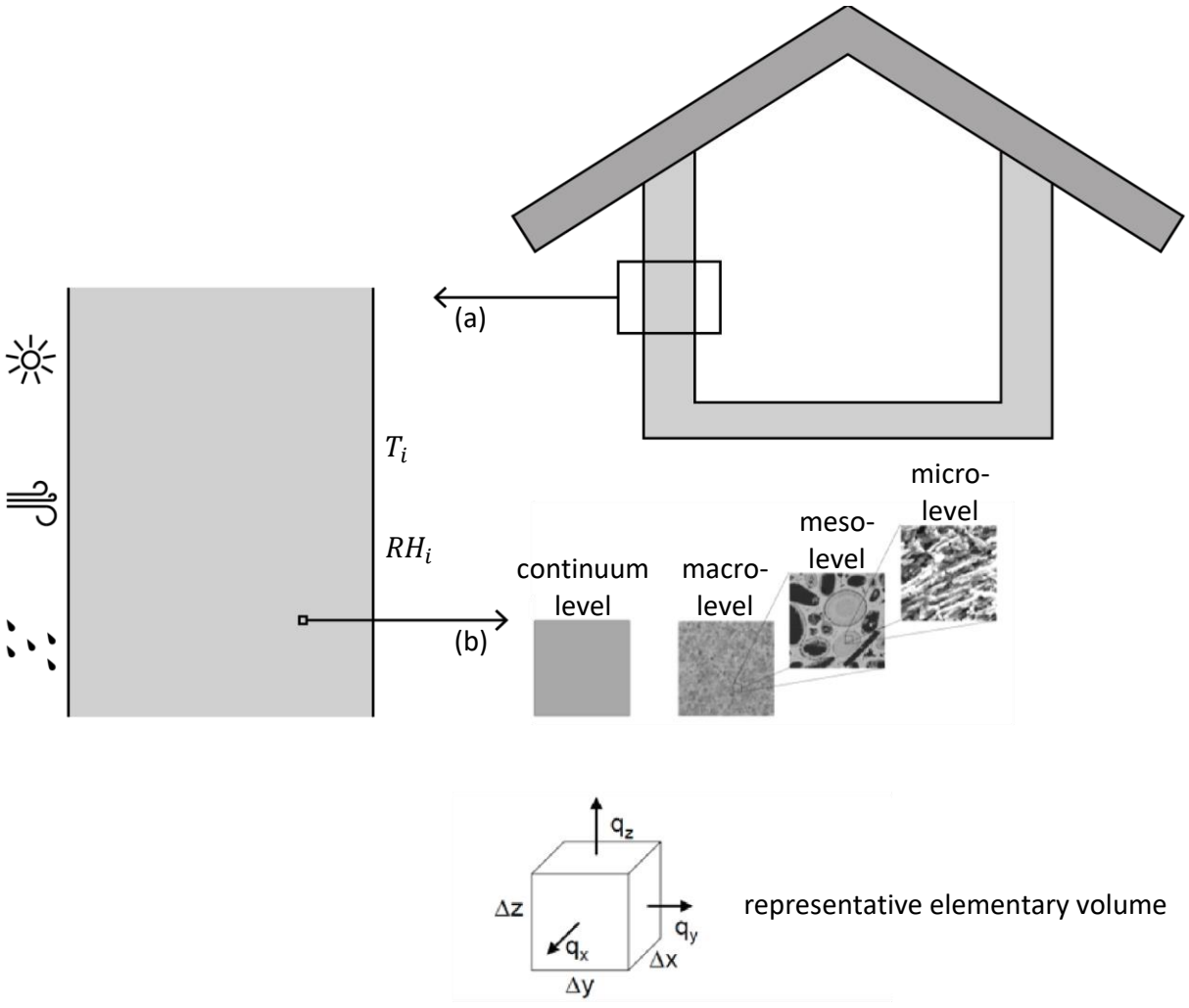

Fig. 2.9: Description of an unsaturated porous medium at different levels of observation and the representative elementary volume at the continuum level (Carmeliet, 2006).

The moisture mass balance is given by:

$$\frac{\partial w}{\partial t} = -\boldsymbol{\nabla} \cdot \boldsymbol{g}_m \tag{2.10}$$

$$\frac{\partial w_l}{\partial p_c}\frac{\partial p_c}{\partial t} = -\boldsymbol{\nabla} \cdot (\boldsymbol{g}_l + \boldsymbol{g}_v) = -\boldsymbol{\nabla} \cdot (-k_l \boldsymbol{\nabla} p_c - \delta \boldsymbol{\nabla} p_v) \tag{2.11}$$

w	volumetric moisture content	kg/m³
t	time	s
$\boldsymbol{g}$	mass flux	kg/(m² s)
p	pressure	Pa
k	permeability	s
δ	vapour permeability	s
$_{m/l/c/v}$	moisture / liquid water / capillary / water vapour	

For the storage term, the following definitions and assumptions are relevant. The open pore space (in contrast to the inaccessible matrix) is assumed to be partially filled by liquid water, which may transform into water vapour forming a gaseous mixture with dry air. The assumption that the water cannot transform into ice significantly simplifies the modelling in which the constant open porosity is shared by the liquid and the gaseous phase: $\Psi_o = \theta_l + \theta_g$. The mass of the liquid water phase per unit volume of the material, the volumetric liquid water content, is given by the following relation: Eq. (2.12). Liquid water is assumed to be incompressible and the liquid water density is taken as constant at ρ_l = 1000 kg/m³. No hysteresis is assumed, so the degree of liquid water saturation is a unique function of the capillary pressure. It is assumed that the gaseous phase does not contribute markedly to the moisture storage: Eq. (2.13).

$$w_l(p_c) = \rho_l \Psi_o S_l(p_c) = \rho_l \theta_l(p_c) \tag{2.12}$$

$$w = w_l + w_v \approx w_l \tag{2.13}$$

ρ	density	kg/m³
Ψ_o	open porosity	m³/m³
S_l	degree of liquid water saturation	m³/m³
θ_l	liquid water content	m³/m³

The physical meaning of the capillary pressure is the energy state of the pore water. The capillary pressure exists where capillary condensation has occurred inside the material pores. The definition of the capillary pressure, Eq. (2.14), which is also called the Young-Laplace equation, can be derived from a force equilibrium for a circular pore. Any pore has been replaced by an equivalent circular pore with the same section and consequently an equivalent diameter or radius. The capillary pressure is the pressure difference between the inside and the outside of a curved surface that forms the boundary between a gas region and a liquid region. The pressure difference is caused by the surface tension of the interface between liquid and gas. The surface tension is assumed to be independent of the temperature and taken as a constant at 72.5 x 10^{-3} N/m.

$$p_c = P_l - P_g = (-2\sigma \cos\vartheta)/r \tag{2.14}$$

P	total pressure	Pa
σ	surface tension, for water-air 72.5 x 10^{-3} N/m at 20 °C	N/m
ϑ	contact angle, zero radian for water-material contact	-
r	equivalent pore radius	m
$_g$	gas	

For the transport terms, Darcy's law is used for the advective liquid water transport. It is herein assumed that the total gas pressure gradient is negligible since the variations are negligible as compared to the total pressure. Moreover, it is assumed that the gravitational force can be neglected as compared to the capillary suction, which is especially valid for fine pores in contrast to macro-pores or cracks. Furthermore, it is assumed that the material is isotropic.

For the water vapour transport, pure diffusion remains (no advective vapour transport) if the total pressure gradient is neglected and gravity is neglected. Fick's law is used for the diffusive water vapour transport. It is herein assumed that the total gas density is constant. The ideal gas law is used. And it is assumed that no moisture transport due to thermal gradients occurs.

Kelvin equation, Eq. (2.15), describes the change in vapour pressure due to a curved liquid-vapour interface for a circular pore. It expresses the isothermal thermodynamic equilibrium at the meniscus. The vapour pressure is hence determined by the temperature and the pore radius. In combination with the Young-Laplace equation, it gives a relationship between the relative humidity and the capillary pressure.

$$\varphi^{(*)} = \frac{p_{v(,sat)}^{(*)}}{p_{v,sat}(T)} = exp\left(\frac{-2\sigma \cos\vartheta}{r\rho_l R_v T}\right) = exp\left(\frac{p_c^{(*)}}{\rho_l R_v T}\right) \tag{2.15}$$

φ	relative humidity		-
R_v	specific gas constant of water vapour	461.52	J/(kg K)
$^{(*)}/\ _{sat}$	(for one pore) / saturation		

The heat balance is given by:

$$\frac{\partial \epsilon}{\partial t} = -\boldsymbol{\nabla} \cdot \boldsymbol{q} \tag{2.16}$$

=

$$\begin{aligned}\frac{\partial}{\partial t}(\rho_d c_d T + w_l c_l T + w_v(c_v T + L_v) + w_a c_a T) &= -\boldsymbol{\nabla} \cdot (\boldsymbol{q}_{cond} + \boldsymbol{q}_l + \boldsymbol{q}_v) \\ &= -\boldsymbol{\nabla} \cdot \left(-\lambda \boldsymbol{\nabla} T + \boldsymbol{g}_l c_l T + \boldsymbol{g}_v(c_v T + L_v)\right)\end{aligned} \tag{2.17}$$

ϵ	volumetric energy content		J/m³
$\boldsymbol{q}$	heat flux		W/m²
c	specific heat capacity		J/(kg K)
T	temperature		K
L_v	latent heat of vapourisation	2.5 x 10^6	J/kg
λ	thermal conductivity		W/(m K)
$_{d/a}$	for dry material / for air		

It is assumed that there is a local thermal equilibrium between the phases, so $T = T_d = T_l = T_v = T_a$. Fourier's law is used for the heat conduction.

2.3.2 Surface balances

To each representative material volume at the boundary of a building component, atmospheric boundary conditions are imposed (Janssen et al., 2007a); (Nicolai & Grunewald, 2006). The boundary conditions are a statement of balance for the heat, air, and moisture flows meeting at the interface, where the interface is treated as a surface (zero thickness). The fluxes at the surface are always considered to be normal (perpendicular to the wall). In this way, the boundary conditions due to atmospheric excitation form the driving forces for the heat, air, and moisture transfer in a building component. It is still assumed that no air transfer occurs in the present work. Fig. 2.10 gives an overview of the heat and moisture fluxes due to atmospheric excitation at the exterior surface and at the interior surface. In Appendix C, more detailed information on the calculation of the fluxes is given.

Fig. 2.10: Atmospheric boundary fluxes.

The moisture mass balance at the exterior wall surface is given by:

$$g_{m,se} = -g_{l,e} + g_{v,e} \tag{2.18}$$

$$= -\alpha U_{10} {R_h}^{0.88} \cos(\theta - \varphi)\,(1/3600 s/h) + \beta_e \left(p_{v,se} - p_{v,e}\right)$$

g	mass flux	kg/(m² s)
α	wind-driven rain coefficient	s/m
U_{10}	reference wind speed	m/s
R_h	unobstructed horizontal rainfall intensity	kg/(m² h)
θ	wind direction (degrees from north)	°
φ	surface normal (degrees from north)	°
β	convective surface moisture transfer coefficient	s/m
p_v	vapour pressure	Pa

$_{m/s/e/l/v}$ moisture / surface / exterior / liquid / vapour

The heat balance at the exterior wall surface is given by:

$$q_{se} = q_{conv,e} + q_{rad,e} - q_{solar} - q_{l,e} + q_{v,e} \tag{2.19}$$

$$= h_{conv,e}\left(T_{se} - T_{e,g}\right) + h_{rad,e}\left(T_{se} - T_{e,rad}\right) - \alpha_{S,se} q_{S,se} - c_l T_{e,g} g_{l,e} + \left(c_v T_{se/e,g} + L_v\right) g_{v,e}$$

$$= h_e\left(T_{se} - T_{e,equ}\right) - c_l T_{e,g} g_{l,e} + \left(c_v T_{se/e,g} + L_v\right) g_{v,e}$$

q	heat flux	W/m²
h	surface heat transfer coefficient	W/(m² K)
T	temperature	K
α_S	short-wave absorptivity	-
c	specific heat capacity	J/(kg K)
L_v	latent heat of vapourisation	J/kg
$_{conv/rad/g/S/equ}$	convective / radiative / gas / short-wave / equivalent	

wherein

$$h_e = h_{conv,e} + h_{rad,e} \tag{2.20}$$

and

$$T_{e,equ} = \frac{h_{conv,e} T_{e,g} + h_{rad,e} T_{rad,e} + q_{solar}}{h_e} \tag{2.21}$$

The moisture mass balance at the interior wall surface is given by:

$$g_{m,si} = g_{v,i} = \beta_i\left(p_{v,i} - p_{v,si}\right) \tag{2.22}$$

$_i$ interior

The heat balance at the interior wall surface is given by:

$$q_{si} = q_{conv,i} + q_{rad,i} + q_{v,i} = q_i + q_{v,i} \tag{2.23}$$

$$= h_i\left(T_{i,g} - T_{si}\right) + \left(c_v T_{i,g/si} + L_v\right) g_{v,i}$$

2.4 Hygrothermal material characterisation

The material properties that are needed as an input in the hygrothermal component simulations come forth from the transfer equations (Section 2.3.1). Table 2.2 gives an overview of these hygric and thermal material properties. They need to be determined through research (Fabbri et al., 2021).

Table 2.2: Overview of hygrothermal material properties.

	Capacity	Permeability
Moisture	$\partial w/\partial p_c$	$\delta; k_l$
Heat	ρc	λ

2.4.1 Hygric properties

2.4.1.1 Moisture storage

The moisture retention curve $w(p_c)$ is typically obtained from a series of experimental tests such as sorption isotherm measurements and pressure plate measurements (EN 15026); (Feng & Janssen, 2019) and/or mercury intrusion analysis. When the pressure plate technique is applied to a specimen initially at capillary moisture content, the main wetting curve can be approximated (Carmeliet & Roels, 2002); (Carmeliet & Roels, 2001); or the technique can be used in absorption (Feng & Janssen, 2020); (Feng & Janssen, 2021). Fig. 2.11 shows the hysteresis definitions.

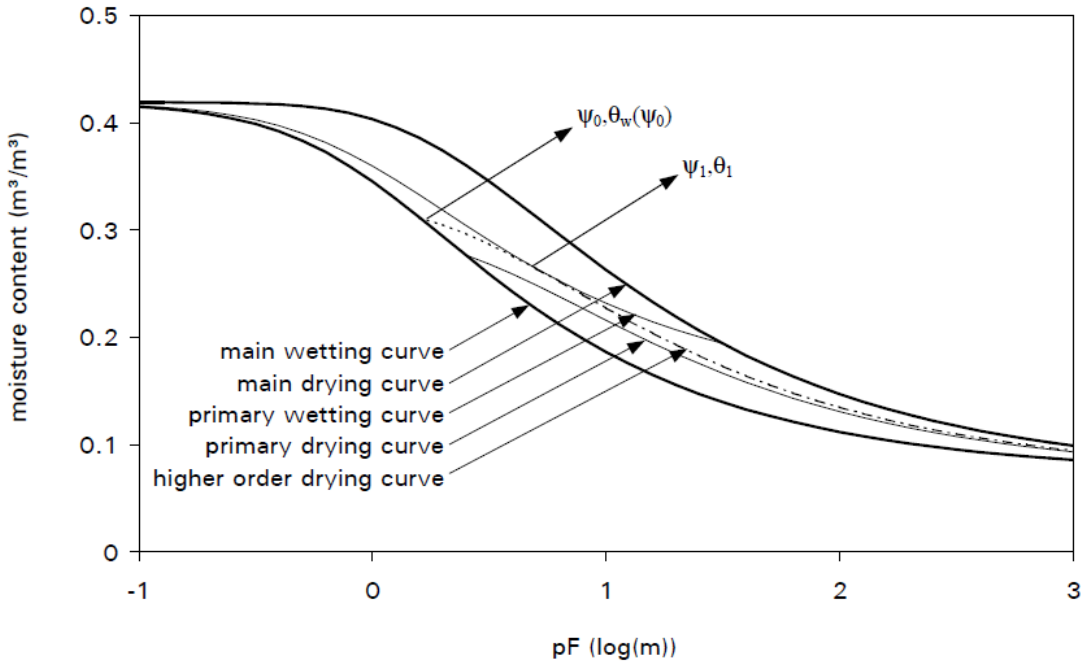

Fig. 2.11: Main, primary and higher order wetting and drying moisture retention curves for a loam soil (Janssen, 2002).

Fig. 2.12 shows a review of the moisture retention curve of different rammed earth materials. It is observed that rammed earth materials are typically hygroscopic: they have a high moisture storage capacity in the hygroscopic range.

Three measurement tactics for the moisture retention curve are distinguished. The first tactic uses a combination of mercury intrusion porosimetry in the overhygroscopic range and desiccator testing in the hygroscopic range (Arrigoni et al., 2017); (Hall et al., 2013).

The second tactic measures the moisture retention curve in desorption starting from the manufacturing moisture content of ca. 0.08 kg/kg to 0.125 kg/kg (Bui et al., 2014); (Gerard et al., 2015); (Jaquin et al., 2009). The manufacturing moisture content should be equal to or slightly smaller than the optimum water content, which depends on the compaction pressure and the soil, Fig. 2.13. Most often, filter papers are used to measure the capillary pressure. The filter papers should be calibrated in the lab and this both in the hygroscopic and in the overhygroscopic range.

The third tactic works with samples manufactured at different moisture contents (Abhilash, 2016a); (Soudani, 2017); (Nowamooz & Chazallon, 2011). The manufacturing moisture content should preferably stay below the optimum water content to minimise changes in pore structure (Delage et al., 1996); (Cuisinier et al., 2011); (Beckett & Ciancio, 2014).

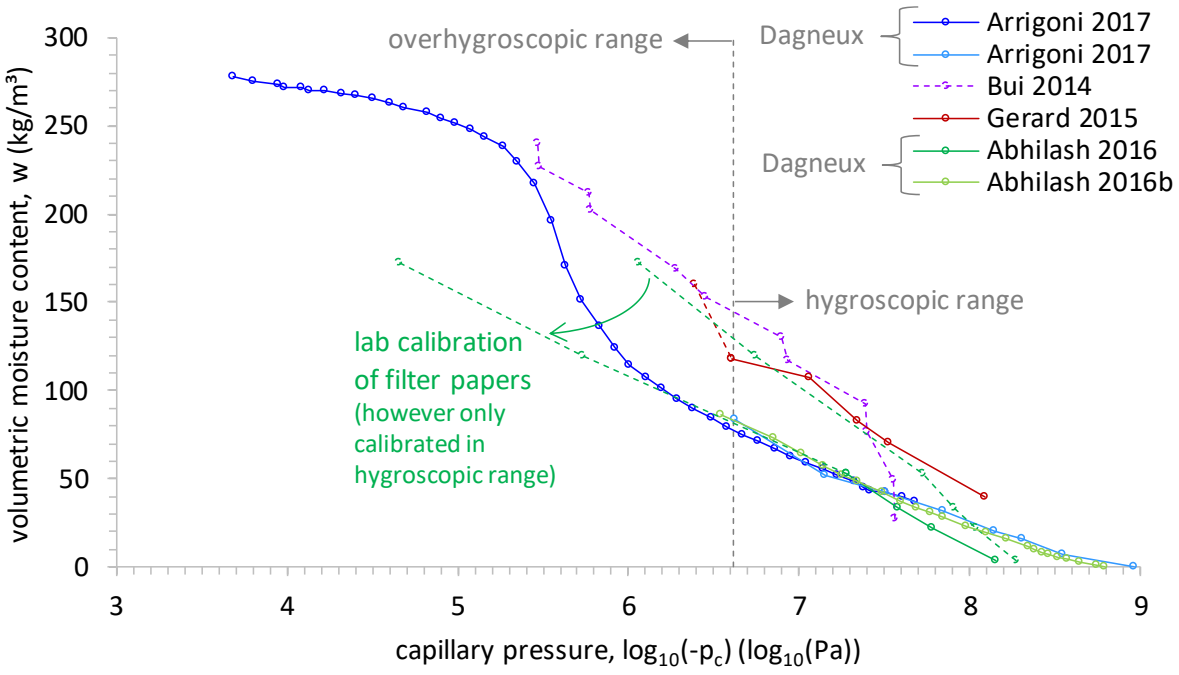

Fig. 2.12: Moisture retention curve of different rammed earth materials.

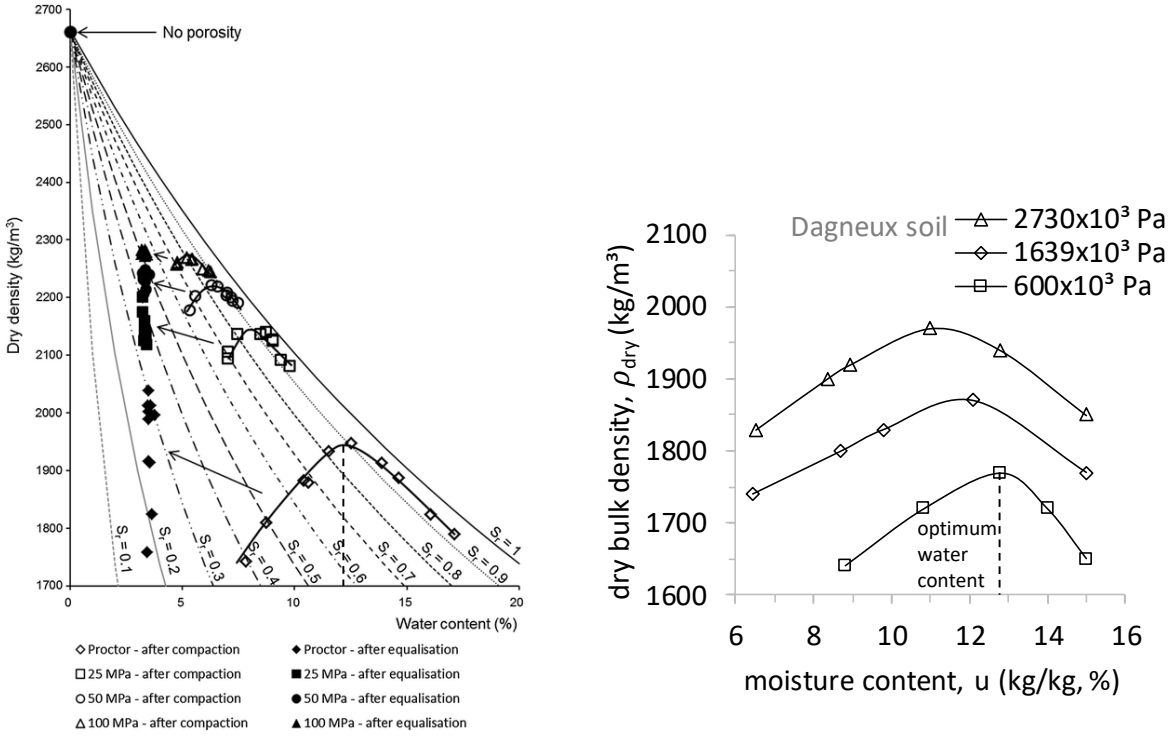

(a) (b)

Fig. 2.13: Compaction curves for two different soils: (a) (Bruno et al., 2017); (b) (Abhilash, 2016a).

2.4.1.2 Moisture transport

The vapour permeability curve is usually determined based on the dry cup vapour permeability, the moisture retention curve, and the vacuum saturation moisture content, using a bundle-of-tubes approach: Eq. (2.24) (Scheffler & Plagge, 2010). The vacuum saturation moisture content is standardly determined by means of the vacuum saturation test, plus underwater weighing for the bulk density. The vapour permeability using the capillary pressure as potential rather than the vapour pressure is given by Eq. (3.27), which is obtained using Kelvin equation, Eq. (2.15).

$$\delta = \frac{\delta_{air}}{\mu}\left(1 - \frac{w}{w_{sat}}\right) \tag{2.24}$$

δ	vapour permeability, with vapour pressure as driving potential	s
δ_{air}	vapour permeability of air, 1.9 x 10^{-10} s at 20 °C and sea level pressure	s
μ	vapour resistance factor (from dry cup test)	-
w	moisture content	kg/m³
$_{sat}$	saturation	

The liquid permeability curve is commonly determined as the product of the moisture diffusivity function and the moisture capacity function, the derivative of the moisture retention curve, Eq. (2.25) (Carmeliet et al., 2004). The moisture diffusivity can be determined in various ways based on a capillary absorption test (Ren et al., 2019). In particular the capillary absorption test with X-ray radiography is a well-established method for determining the moisture diffusivity and hence permeability in the high range (Carmeliet et al., 2004). If supplemented by an isothermal drying test calibration with eventual adjustment of the permeability in the intermediate range (Zhao & Plagge, 2015), the complete moisture permeability curve can be determined.

$$k_m = D_m \frac{\partial w}{\partial p_c} \tag{2.25}$$

k_m	moisture permeability	s
D_m	moisture diffusivity	m²/s
p_c	capillary pressure	Pa

An attempt to review of the moisture permeability curve of different rammed earth materials leads to the observation that mostly only the (equivalent) vapour permeability is measured (Hall & Allinson, 2009a). The dry cup vapour resistance factor of rammed earth materials typically ranges from 9 to 11 (Chabriac, 2014). The open porosity can be determined by means of helium pycnometry (Liuzzi et al., 2013); (Bruno, 2016); (Cuccurullo et al., 2020). It can also be estimated through Eq. (2.26) (Hall et al., 2013) based on the bulk density and using a typical matrix density of 2650 kg/m³. Or it can be estimated by means of the combination of mercury intrusion porosimetry and desiccator testing. The capillary absorption coefficient of rammed earth materials typically ranges from about 0.2 kg/(m² $s^{0.5}$) to 0.4 kg/(m² $s^{0.5}$) (for an open porosity from ca. 0.3 m³/m³ to 0.4 m³/m³), and is generally proportional to the open porosity (Hall & Djerbib, 2004); (Hall & Allinson, 2009b); (Fabbri et al., 2019). The capillary absorption pattern is typically ideal. Usually, only the capillary absorption coefficient is assessed, or even only the initial rate of suction. The capillary moisture content remains undiscussed in the literature.

$$\Psi_o \approx \Psi = 1 - \rho_{bul}/\rho_{matrix} \tag{2.26}$$

Ψ_o	open porosity	m³/m³
ρ_{bul}	bulk density	kg/m³

2.4.2 Thermal properties

The volumetric heat capacity indicates the amount of thermal energy that needs to be added to a unit volume of material to increase its temperature by one degree. It mainly determines the transient response. The literature review in (Chabriac, 2014) shows that the specific heat capacity of rammed earth materials typically ranges from 650 J/(kg K) to 1100 J/(kg K). The heat capacity of moisture and air in the pores is taken into account separately (Section 2.3.1) and the material heat capacity is taken constant in the important temperature range for building physics (Hens, 2010).

The thermal conductivity is the main thermal property indicating the ability of a material to conduct thermal energy (transmission of atomic kinetic energy, resulting in sensible heat transport). It is directly related to the material density. In (Chabriac, 2014), it is shown based on a literature review that for rammed earth materials with a bulk density ranging from ca. 1550 kg/m³ to 1850 kg/m³, the dry thermal conductivity typically ranges from ca. 0.25 W/(m K) to 1.0 W/(m K). Eq. (2.27) shows that the thermal conductivity increases linearly with the moisture content of a material, which follows from water being a better conductor than air in the material pores. The moisture content factor of rammed earth materials typically ranges from 0.002 W m²/(kg K) to 0.0056 W m²/(kg K) (Hall & Allinson, 2009a); (Chabriac, 2014). Further, temperature has a directly proportional effect on the thermal conductivity of a material: increasing temperature increases the ease of atomic vibration transmission. This effect is usually disregarded though, which is defensible under standard temperature conditions.

$$\lambda = \lambda_{dry} + a\,w + b\,T \tag{2.27}$$

λ	thermal conductivity	W/(m K)
λ_{dry}	dry thermal conductivity at standard temperatures	W/(m K)
a	moisture content factor	(W/(m K))/(kg/m³)
w	moisture content	kg/m³
b	temperature factor	W/(m K²)
T	temperature	K

2.5 Conclusion

In Section 2.2, numerical simulation research on the interior insulatability of building walls is reviewed. It is hence observed that there is no such research available for (exteriorly unplastered) rammed earth walls that are exposed to driving rain, despite the burning questions in practice. In response to this lack of research, the insulatability of rammed earth walls will be analysed in the present work (Section 5). Moreover, the hygrothermal performance criteria for the insulatability analysis of building walls are reviewed. It is hence observed that mechanical performance indicators are missing for rammed earth. For this, new performance indicators concerning the mechanical behaviour appropriate for rammed earth will be developed in the present work (Section 4).

In Section 2.3, the theoretical background of the hygrothermal simulation model is presented. As such, the transfer equations, in which the material properties are defined, are formulated. And the surface balances with the atmospheric boundary conditions are formulated. This led to the respective observations that if the material is assumed to remain stable and if the wind-driven rain load is assumed to be similar as for other buildings, rammed earth can be modelled regularly.

In Section 2.4, the hygric and thermal material properties that are needed as input in the hygrothermal simulation model are reviewed. This led to the observation that in particular knowledge on the moisture transport properties in the overhygroscopic range is missing for rammed earth materials. As rammed earth building walls in practice are also exposed to driving rain, these overhygroscopic transport properties need to be determined. For this, the capillary absorption test will be redeveloped for rammed earth materials in the present work (Section 3).

Besides the moisture permeability, the mechanical performance indicators, and the interior insulation analysis of rammed earth walls, a few gaps were identified that will not be treated in the present work. First, rising damp and the insulatability of the stem wall. Second, the possible impact of material evolution in practice. Third, the precise wind-driven rain load on rammed earth building walls. And fourth, the isothermal drying test and the moisture permeability in the intermediate range for rammed earth materials.

3 Material characterisation

3.1 Introduction

The hygric properties of rammed earth materials are needed to investigate the insulatability of rammed earth walls via simulation. These hygric material properties are standardly incomplete in the literature, which can be explained by the material unstability at high moisture contents. Particularly the determination of the moisture permeability curve in the overhygroscopic range is problematic. This determination is typically based on the capillary absorption test. Rammed earth materials however liquefy and expand upon contact with water. Nevertheless, these overhygroscopic moisture transfer properties need to be determined, as rammed earth building walls in practice are also exposed to driving rain, e.g.

The objective is to perform a complete hygric characterisation of a few rammed earth target materials. The main asset is to redevelop the capillary absorption test, including the Boltzmann transformation method, to enable its proper application to rammed earth materials.

In Section 3.2, the collection of candidate rammed earth materials for the characterisation is presented. The few target materials to be characterised are selected based on their differences in pore volume distribution as well as for their homogeneity. In Section 3.3, the moisture retention curve of the materials is determined. And in Section 3.4, the moisture permeability curve of the materials is determined.

3.2 Material information

3.2.1 Collection

The investigated rammed earth materials are extracted from existing constructions at six different locations in the Auvergne-Rhône-Alpes region, France, Fig. 3.1 (a). In this way, a set of rammed earth materials which is considered to be fairly representative for the main target building stock is obtained. The earth of house 1 (H1) is crushed (El Nabouch, 2017), to then be reproduced in the lab via pressing or ramming (P/R). The material of houses 2 to 6 on the other hand is used directly, extracted by means of core drilling. For the H1 rammed earth, the particle size distribution is known (Abhilash, 2016a), Fig. 3.1 (b): 20% clay, 65% silt, 14.5% sand, and 0.5% gravel fraction. Moreover, it is known that its clay fraction comprises illite and vermiculite (Arrigoni et al., 2017).

(a) (b)

Fig. 3.1: (a) Situation of the collected rammed earth materials; (b) Particle size distribution of H1 rammed earth.

3.2.2 Bulk density

3.2.2.1 Introduction

The bulk density is defined as the mass of a (per) unit volume of dry material, and it is thus inversely related to the porosity of the same material. While the reliable determination of the dry mass is the basis for characterising the hygrothermomechanical properties of porous building materials, the bulk density is subsequently useful to convert the intensive properties to volumetric quantities. Moreover, the bulk density is an important quantity in construction, indicating the building part loads and thermal conductivity and often, in particular in the case of rammed earth, also strength (Gerard et al., 2015); (Kianfar & Toufigh, 2016) and durability (Bui et al., 2009).

The primary goal is to gain knowledge of the reference bulk density for the materials collected. For this, the bulk density is determined for multiple samples per material and the bulk density obtained via different methods is compared. It is explicitly chosen not to aim for an investigation of the spatial variability in this material property, nor of the influence of the sample size, here, but rather to tackle the material (in)homogeneity through the pore structure analysis in Section 3.2.3.

3.2.2.2 Materials and methods

The bulk density from two volume determination methods will be compared: the mercury intrusion porosimetry bulk density and the caliper bulk density. Two to nine samples per material of approximately 1x1x2 cm^3 are used for the mercury intrusion porosimetry bulk density (cf. Section 3.2.3). Larger samples are used for the caliper bulk density: for the pressed material of house 1, twelve cylindrical samples of 7 cm diameter and 3 cm height; for its rammed material, a block of

40x20x30 cm³; for house 2, six samples of 7 cm diameter and 10 cm height; for house 3, eight samples of about 3x2x2 cm³; for house 4, one sample of 4x3x3 cm³ and two of 3x2x1 cm³; for house 5, three samples of 3x2x1 cm³; for house 6, one sample of 7 cm diameter and 3 cm height.

For the dry mass determination, the samples are dried at an elevated temperature of 70 °C in a ventilated oven. This drying method choice is supported by the concerns on the 105 °C suitability for rammed earth (Ciancio et al., 2013) and by a literature-based estimation of a corresponding difference of ca. 0.3% in dry mass (or 5 kg/m³ in moisture content) which is considered insignificant relative to the moisture storage function. It is furthermore the derivative that is important (Section 2.4). For comparison, moreover, four small samples of the pressed material of house 1 are dried at 105 °C. The mass is measured by an analytical balance with 0.001 g readability up to 1010 g, otherwise 1 g. The dry mass is taken as the average of three weighing results at ≥ 48 hour intervals showing < 0.1% non-monotonous evolution.

Next, the volume of the dry samples is determined by means of dimension measurement with a caliper for the larger samples and by means of immersion for the 1x1x2 cm³ samples. Obviously, the standard method of the vacuum saturated underwater weighing is not an option for rammed earth because the material liquefies when immersed in water (cf. Section 3.2.4). Instead, mercury is used as the displacement medium, and the mercury intrusion porosimetry penetrometer as a container which is each time filled up to the same constant volume. Being a non-wetting liquid, the mercury does not enter the material pores spontaneously. Assuming an ideal contact between the sample and the surrounding mercury though, the volume of the sample is derived. Hence, the bulk density of the sample determined by mercury intrusion porosimetry is given by Eq. (3.1). Herein, V_{pen} is the volume inside the penetrometer, $M_{pen+mer}$ is the mass of the penetrometer completely filled with mercury only, M_{pen} is the mass of the empty penetrometer, $M_{pen+sam+mer}$ is the mass of the penetrometer with the sample and the surrounding mercury inside, $M_{pen+sam}$ is the mass of the penetrometer with the sample inside before the filling with mercury, and $\rho_{mer} = 13549$ kg/m³.

$$\rho_{bul} = \frac{M_{dry}}{V_{pen} - \left(V_{pen} - V_{sam}\right)} = \frac{M_{dry}}{\frac{M_{pen+mer} - M_{pen} - \left(M_{pen+sam+mer} - M_{pen+sam}\right)}{\rho_{mer}}} \tag{3.1}$$

ρ	density	kg/m³
M	mass	kg
V	volume	m³

$_{bul/pen/sam/mer}$ bulk / penetrometer / sample / mercury

3.2.2.3 Results and discussion

Table 3.1 and Fig. 3.2 present the results. It is observed that the caliper bulk density is usually smaller than the mercury intrusion porosimetry (MIP) bulk density, which is explained by sample surface roughness and the consequent errors involved in the measurement of the dimensions. The following trend furthermore applies: the smaller the caliper samples or the more irregular their shape, the larger the difference between the caliper and the mercury intrusion porosimetry bulk density. In (Feng et al., 2013), it is shown that caliper and underwater weighing results differ similarly (for autoclaved aerated concrete).

Hence, considering the obtained mercury intrusion porosimetry bulk density reliable, and discarding the caliper bulk density, the average bulk density of the authentic rammed earth materials is 1734 kg/m³, ranging from 1540 kg/m³ (for house 4) to 1860 kg/m³ (for house 2). The bulk density of the rammed material of house 1, 1757 kg/m³, falls within this range. The bulk density of ca. 1900 kg/m³ chosen to produce the pressed samples at on the other hand, is relatively high. For this material only, the caliper bulk density is retained because for this twelve different samples are used whereas almost all the porosimetry samples come from one single sample.

For the 70 °C versus 105 °C drying method, a difference of 4 kg/m³ in moisture content (or 0.2% in dry mass) is found for the pressed material of house 1. This is fairly negligible (cf. Section 3.3), motivating the further 70 °C use (even though this choice deviates from most of the past studies).

Table 3.1: Average bulk density for the collected materials via drying at 70 °C for two volume determination methods (MIP, caliper).

ρ_{bul} (kg/m³)	H1P	H1R	H2	H3	H4	H5	H6
MIP	1890 ±0.5% [a]	1757 ±1.9%	1860 ±0.8%[b]	1773 ±0.6%[b]	1540 ±22.5%	1790 ±3.1%	1708 ±2.7%
caliper	1901 ±1.2%	1735 -	1762 ±1.7%	1422 ±7.5%	1421 ±18.8%	1563 ±12.3%	1675 -

[a] At 105 °C: 1886 kg/m³. [b] Deviation instead of standard deviation because of only two samples.

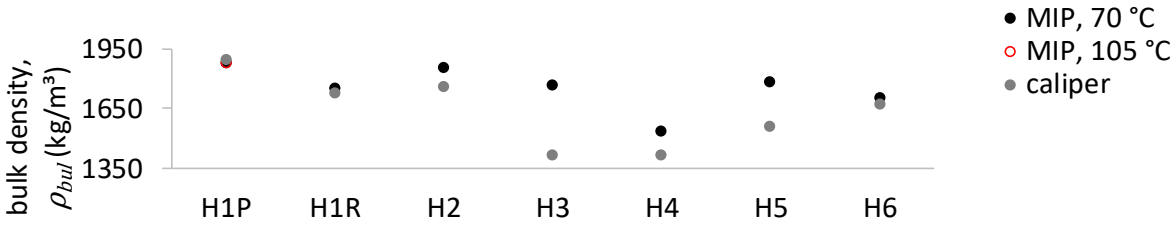

Fig. 3.2: Average bulk density comparison per material for two volume determination methods

(MIP, caliper).

3.2.2.4 Conclusion

The bulk density of rammed earth cannot be determined by means of the standard vacuum saturated underwater weighing, and hence it is instead determined by means of immersion in a non-wetting liquid (mercury), as a part of the mercury intrusion porosimetry test procedure. Relative to the caliper volume determination method, the mercury gives more reliable results for the in general relatively rough rammed earth samples. Hence, the mercury intrusion porosimetry bulk density is retained. Resultantly, the bulk density of the rammed earth materials studied ranges from 1540 kg/m³ to 1860 kg/m³ with an average of 1738 kg/m³. The pressed samples' bulk density is relatively high, and based hereon, this material is discarded. Further, the bulk density obtained from two drying methods is compared. The 70 °C oven drying used in this work deviates from the 105 °C used in most of the past rammed earth research. The corresponding dry mass difference is limited, though (to 0.2% (or 4 kg/m³ moisture content) for the most fine-porous pressed material of house 1).

3.2.3 Pore structure

3.2.3.1 Introduction

The pore structure of a building material impacts its hygric properties. While the open porosity and the pore volume distribution indicate the moisture storage capacity, they also enable a qualitative assessment of the moisture transport properties. In the case of a rammed earth material, several parameters influence the pore structure, such as the particle size distribution of the used soil, the manufacturing moisture content, and the compaction pressure. Hence, besides the site-related variations, inhomogeneity could occur within a single rammed earth component.

The goal is to gain insight into the pore structure of the collected rammed earth materials. For this, the pore volume distribution of the different materials is determined by means of mercury intrusion porosimetry. Although this measurement technique does not necessarily give a correct weight to the pore subsystems, it does allow to inspect the main part of the pore structure in a fast way in terms of homogeneity, moisture storage and transport parameters, and peak pore radii. Further, the comparison of the mercury intrusion porosimetry result with the actual moisture retention curve can provide more insight (Section 3.3).

3.2.3.2 Test setup and method

The mercury intrusion porosimetry is performed on at least two samples per material, of about 1x1x2 cm³. This sample size is mainly determined by the dimensions of the penetrometer sample cup (1.5 cm diameter, 2.5 cm height). Besides, based on an estimated value of the open porosity for rammed earth (30%), the combination sample size and penetrometer stem volume (1.131 ml) is chosen in order to use 25% to 90% of the stem volume for accurate results. For each material, the samples tested come as much as possible from different positions within the wall. The use of samples with the same size facilitates the comparison of the homogeneity in material properties.

A Micromeritics AutoPore IV 9500 porosimeter, Fig. 3.3 (a), is used for the mercury intrusion porosimetry (Micromeritics, 2001). The porosimetry involves the forced intrusion of mercury into a dry and vacuum porous sample, Fig. 3.3 (b). The procedure is mainly full-automatic: the pressure is increased stepwise in a range corresponding to $\log_{10}(-p_c) = 2.9$ $\log_{10}$(Pa) to 7.7 $\log_{10}$(Pa), Eq. (3.2), with an equilibrium time of 250 s per step, chosen based on some trial and error experience and an estimation of the main peak pore radius. The increased intrusion pressure yields an increased volume intruded; the data are collected automatically.

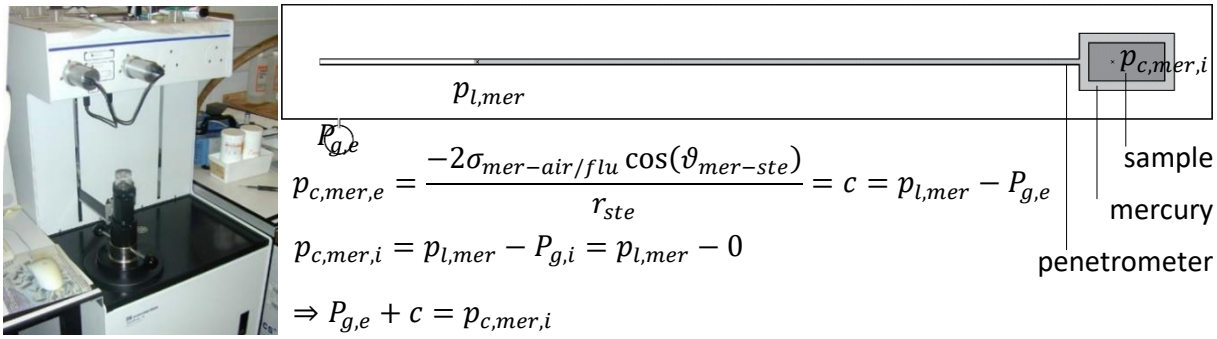

(a) (b)

Fig. 3.3: (a) Mercury intrusion porosimetry test apparatus; (b) Measurement principle sketch.

The mercury intrusion porosimetry gives the mercury retention curve indicating how much mercury is intruded in the material at a certain mercury (-vacuum) capillary pressure: $V_{mer,int}/M_{dry}$ versus $p_{c,mer}$. Assuming cylindrical pores and using the Young-Laplace equation, Eq. (2.14), with $\sigma_{mer-vac} = 0.485$ N/m and $\vartheta_{mer-mat} = 130° \pi / 180°$, the corresponding pore (entry) radius is found. Hence, the mercury retention curve is converted into a moisture retention curve, calculating the corresponding (water) capillary pressure as following (Roels et al., 2001):

$$p_c = \frac{-2\sigma_{wat-air}\cos(\vartheta_{wat-mat})}{r} = \frac{\sigma_{wat-air}\cos(\vartheta_{wat-mat})}{\sigma_{mer-vac}\cos(\vartheta_{mer-mat})} p_{c,mer} \approx -\frac{1}{4.276} p_{c,mer} \quad (3.2)$$

p_c	capillary pressure	Pa
σ	surface tension; for water-air 72.5x10^{-3} N/m at 20 °C	N/m
ϑ	contact angle; zero radian for water-material contact	-
r	equivalent pore radius	m
$_{wat/mat/mer/vac}$	water / material / mercury / vacuum	

Given that the large pores are filled first by the mercury (since smaller overpressures are necessary), the mercury intrusion porosimetry result corresponds to the main drainage moisture retention curve. Hence, at each capillary pressure, the corresponding moisture content is calculated as following:

$$w = w_{sat} - \frac{V_{mer,int}}{M_{dry}} \rho_l \rho_{bul} \quad (3.3)$$

w	moisture content	kg/m³
V	volume	m³
M	mass	kg
ρ	density	kg/m³
$_{sat/int/l/bul}$	saturation / intruded / liquid water / bulk	

The moisture content is expressed in kg/m³, in contrast to kg/kg, because this is considered to be more comprehensive and interesting for relatively heavy and massive building materials like rammed earth. For this, the bulk density of the individual sample, Eq. (3.1), is used here Eq. (3.3) in order to obtain an as-correct-as-possible representation of the variations between samples.

The upper limit of the mercury intrusion apparatus pressure range, using Kelvin equation, Eq. (2.15), corresponds to about 70% relative humidity, which means that not the full porosity is filled. Hence, the obtained curve is shifted upwards by the use of the saturation moisture content in Eq. (3.3), which is usually determined by means of another experimental method. Instead of the commonly applied vacuum saturation test for this, helium pycnometry could be used for rammed earth. In this work, alternatively, the total open porosity is estimated by the sum of the intruded mercury volume at the pressure corresponding to 75% relative humidity and the pore volume

filled by moisture during isothermal absorption up to 75% relative humidity (Section 3.3.1). The saturation moisture content of the sample as determined by this mix of methods is given by:

$$w_{sat} = \frac{V_{mer,int,75\%}}{M_{dry}} \rho_l \rho_{bul} + u_{75\%,mat} \rho_{bul,mat} = \Psi_o \rho_l \tag{3.4}$$

u	moisture content	kg/kg
Ψ_o	open porosity	m³/m³
$_{75\%}$	at 75% relative humidity	

In this way, it is assumed that hysteresis is negligible at this point of 75% relative humidity (Hall & Allinson, 2009a); (Allinson & Hall, 2010); (Chabriac, 2014); (Abhilash, 2016a). In terms of ink-bottle effects (Roels et al., 2001), this would mean that all the pores with a radius larger than that corresponding to 75% relative humidity are filled by the mercury intrusion porosimetry, be it by direct accessibility or via other larger pores. In Eq. (3.4), an average value for the considered material of the absorption moisture content at 75% relative humidity is used, since it is measured with other samples than those used for the porosimetry. For the same reason, the material bulk density is used for its conversion into a volumetric moisture content.

The derivative of the moisture retention curve is the pore volume distribution, Eq. (3.6). In order to provide continuous derivatives, the moisture retention curve obtained as described above is approximated by fitting an analytical function onto it. This function is multi-modal (Durner, 1994) and formed by the superposition of unimodal subcurves (van Genuchten, 1980):

$$w = w_{sat} S \underset{(Durner)}{=} w_{sat} \sum_{i=1}^{k} (f_i S_i) \underset{(van\ Genuchten)}{=} w_{sat} \sum_{i=1}^{k} \left(f_i \left(1 + \left(\alpha_i \frac{|p_c|}{\rho_{wat} g} \right)^{n_i} \right)^{\left(\frac{1}{n_i} - 1\right)} \right) \tag{3.5}$$

S	degree of moisture saturation	kg/kg
k	modality	-
f_i	weighing factor for subcurve i, $0 < f_i < 1, \sum f_i = 1$	-
S_i	subcurve i	-
α_i	scaling parameter, $\alpha_i > 0$	m^{-1}
g	gravitational acceleration	m/s²
n_i	shape parameter, $n_i > 1$	-

Depending on the desired accuracy of the representation, the open porosity can be divided into a number of pore systems (qua size), i.e. the modality. The weighing factor for each moisture retention subcurve indicates the percentage of the total pore volume that the pores of the corresponding system occupy. Further, the scaling parameter determines the position of the pore volume maximum, and the shape parameter the shape of the subcurve, respectively. Finally, the corresponding (apparent) pore volume distribution is determined by (Carmeliet & Roels, 2002):

$$f_v = \frac{\partial w}{\partial log_{10}(r)} = -\frac{\partial w}{\partial log_{10}(|p_c|)} = -\frac{\partial w}{\partial |p_c|}\ln(10)\,|p_c| \tag{3.6}$$

f_v pore volume distribution kg/(m³ $\log_{10}$(Pa))

3.2.3.3 Results and discussion

Fig. 3.4 (a-g) indicate that the materials collected can be considered fairly homogeneous, except for the material of house 4. This is also reflected by the material errors given in Table 3.1 and Table 3.2, which are of similar magnitude as for other building materials (Feng et al., 2015). This is important information that could determine the way to experiment and model (Roels, 2000). The desiccator test results cf. Section 3.3 are already indicated in Fig. 3.4.

Table 3.2 summarises the average values of the obtained open porosity for the different materials. It is found that the open porosity ranges from 0.293 m³/m³ (for house 2) to 0.406 m³/m³ (for house 4), with an average of 0.338 m³/m³ (excluding the pressed material of house 1). The correctness of this property estimation, assuming hysteresis negligible, is assessed in three ways. Firstly, Table 3.1 and Table 3.2 show the in general inverse relation between the bulk density and the open porosity, which is as it should be. Secondly, the saturation should exceed the capillary moisture content (Table 3.8), and the main drainage the main wetting curve (Section 3.3.2). Thirdly, assuming the total porosity open to the exterior, it is verified that the matrix density determined via Eq. (2.26) is acceptable as compared to typical particle densities of soil constituents, ranging from about 2600 kg/m³ to 2750 kg/m³.

Table 3.2: Average open porosity for the materials collected.

	H1P	H1R	H2	H3	H4	H5	H6
Ψ_o (m³/m³)	0.301 ±1.1%	0.352 ±5.6%	0.293 ±1.9%[a]	0.324 ±0.4%[a]	0.406 ±30.0%	0.317 ±2.4%	0.338 ±2.4%

[a] Deviation instead of standard deviation because only two samples are involved.

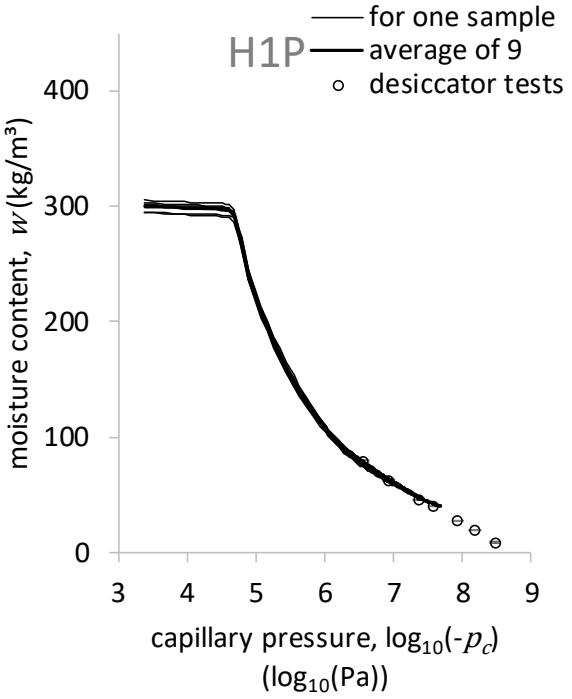
H1P
for one sample
average of 9
desiccator tests
moisture content, w (kg/m³)
capillary pressure, $\log_{10}(-p_c)$ ($\log_{10}$(Pa))

(a)

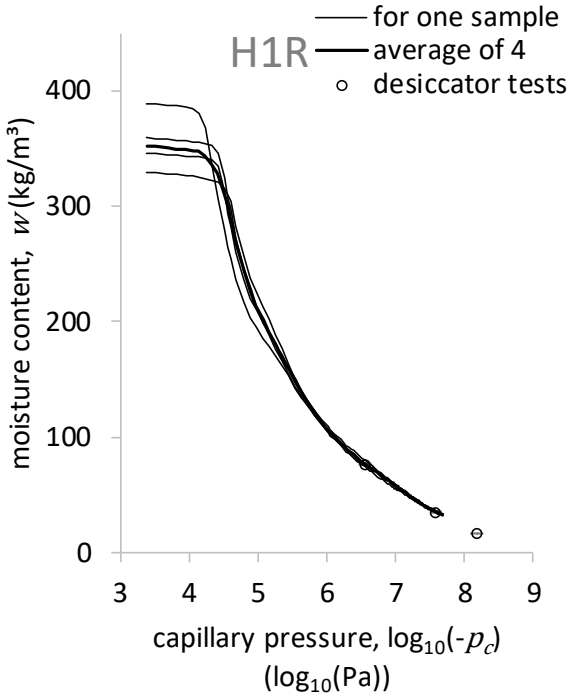
H1R
for one sample
average of 4
desiccator tests
moisture content, w (kg/m³)
capillary pressure, $\log_{10}(-p_c)$ ($\log_{10}$(Pa))

(b)

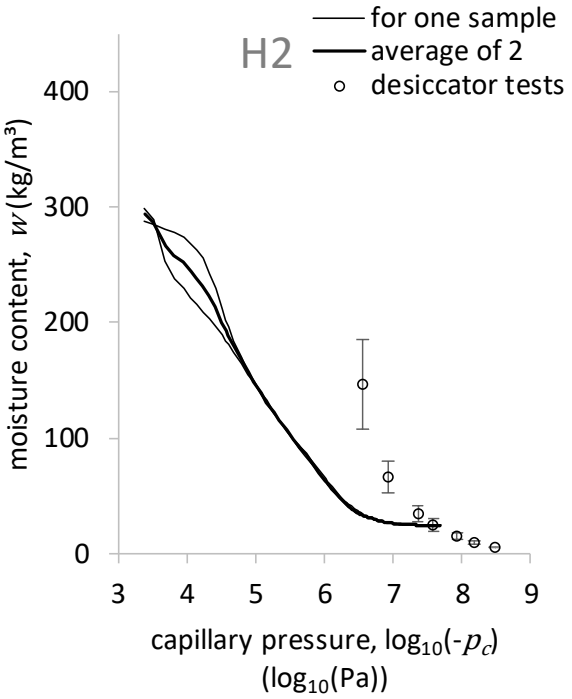
H2
for one sample
average of 2
desiccator tests
moisture content, w (kg/m³)
capillary pressure, $\log_{10}(-p_c)$ ($\log_{10}$(Pa))

(c)

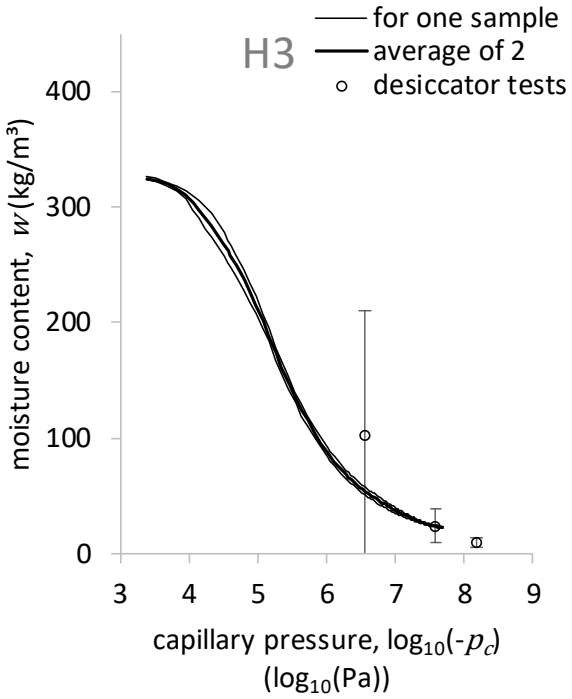
H3
for one sample
average of 2
desiccator tests
moisture content, w (kg/m³)
capillary pressure, $\log_{10}(-p_c)$ ($\log_{10}$(Pa))

(d)

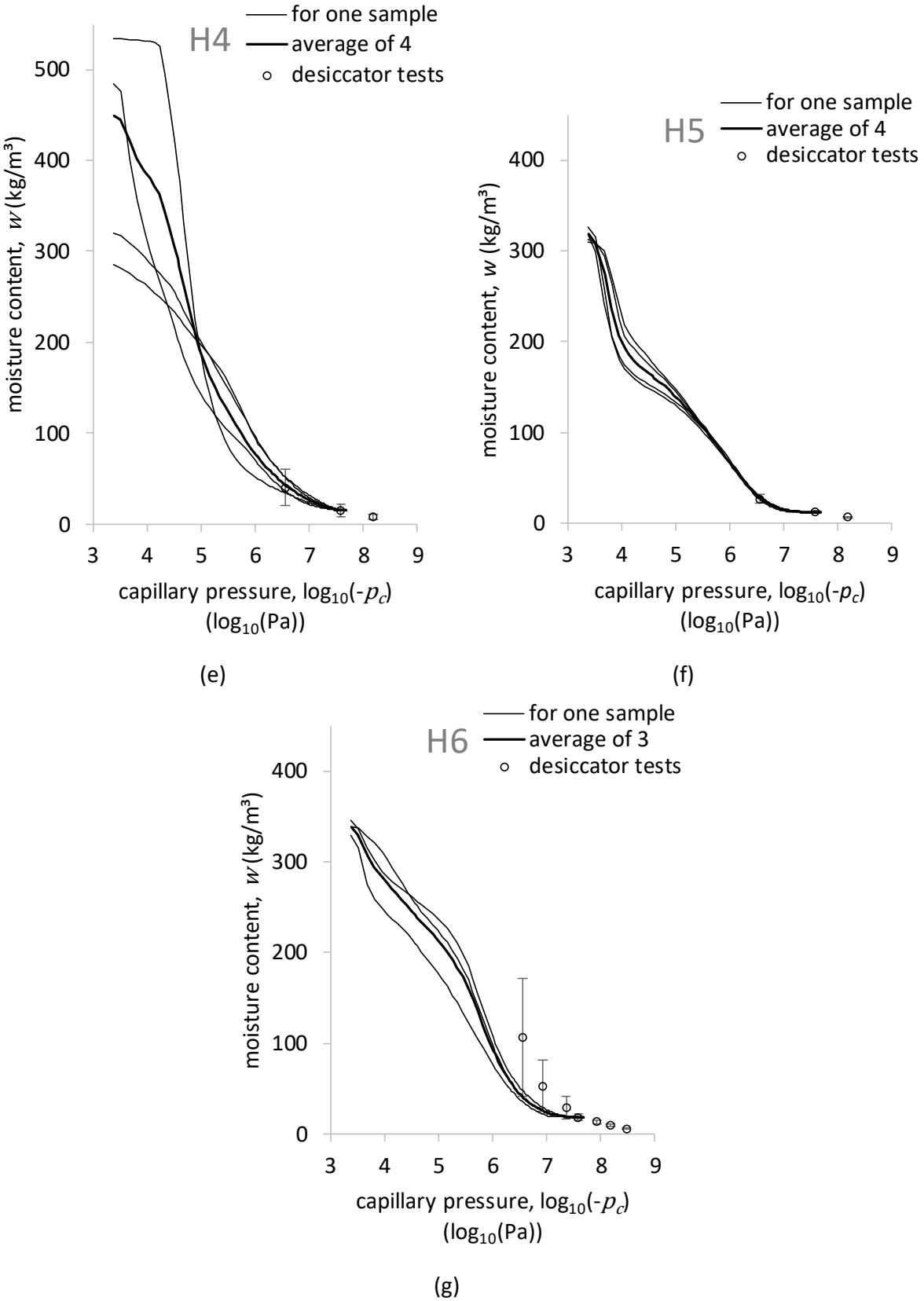

Fig. 3.4: Moisture retention curve by mercury intrusion porosimetry for samples of (a) house 1 pressed, (b) house 1 rammed, (c) house 2, (d) house 3, (e) house 4, (f) house 5, and (g) house 6.

Fig. 3.5 and Fig. 3.6 collect the average obtained moisture retention curve and the corresponding apparent pore volume distribution, respectively, for the different materials. It is observed that the materials are clearly distinguishable. Based on their differences (and excluding the H4 material for its heterogeneity), a selection of three materials is made that will be characterised further: the H1 rammed earth, the H2 rammed earth with a small open porosity, and the H6 rammed earth with an important mid-size pore system. The pore structure of the pressed samples shows a reasonable agreement with the rammed material of house 1, except for the smaller open porosity (reflecting the bulk density trend).

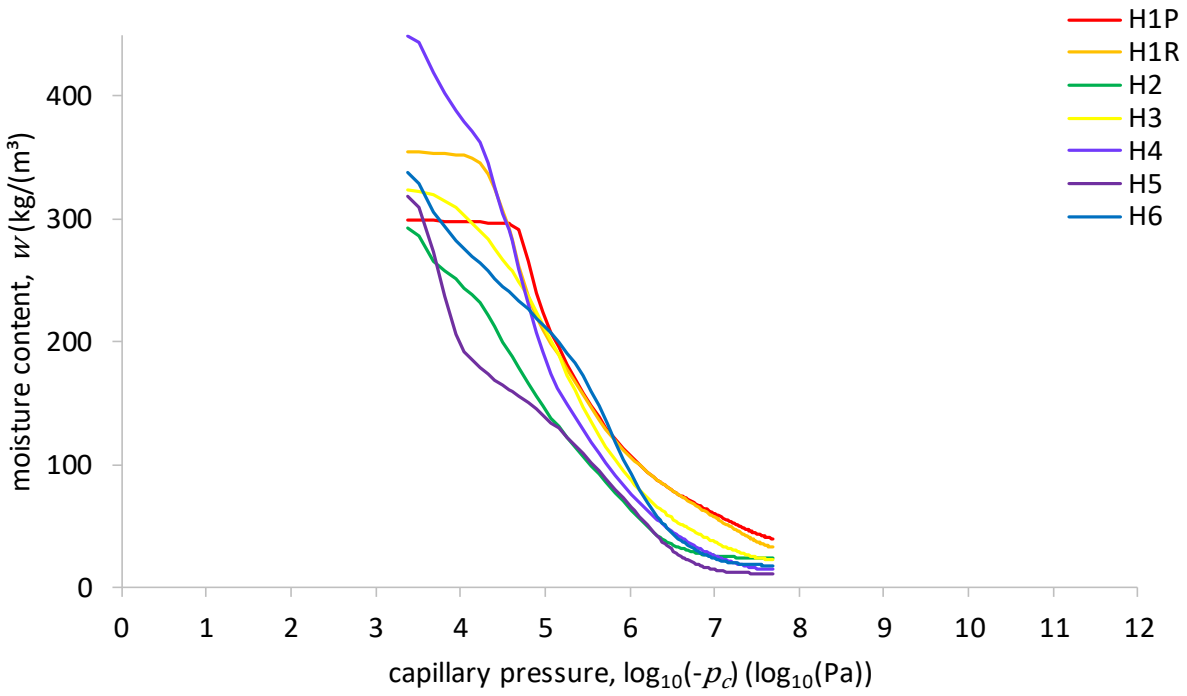

Fig. 3.5: Average moisture retention curve by mercury intrusion porosimetry per material.

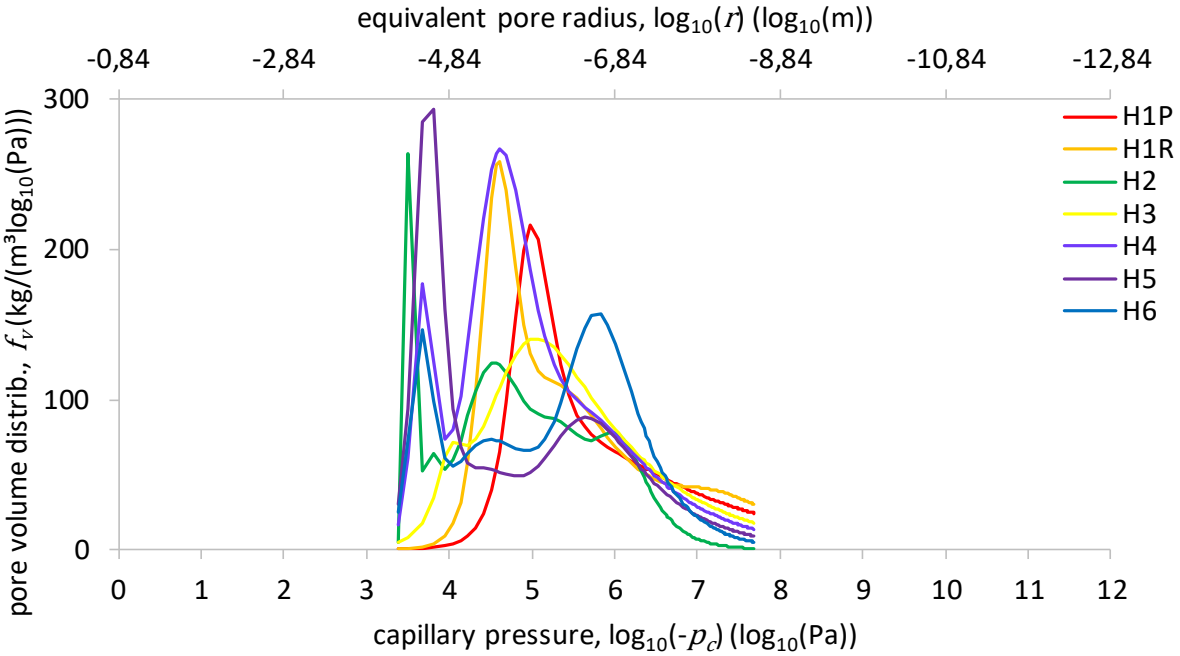

Fig. 3.6: Average apparent volume distribution per material.

3.2.3.4 Conclusion

The pore structure of the rammed earth materials as determined by means of mercury intrusion porosimetry is found to be regularly homogeneous in general. Based on their differences in pore structure, a maximally representative selection is made of the materials to be characterised further: the rammed material of house 1, the material of house 2, and that of house 6.

The open porosity is estimated by the sum of the intruded mercury volume at the pressure corresponding to 75% relative humidity and the pore volume filled by moisture at the 75% relative humidity equilibrium moisture content (in absorption). Resultantly, the open porosity of the rammed earth materials collected ranges from 0.293 m^3/m^3 to 0.406 m^3/m^3, with an average of 0.338 m^3/m^3.

3.2.4 Water stability

3.2.4.1 Introduction

Unstabilised rammed earth materials typically expand and liquefy upon significant contact with moisture. This material evolution could impact the hygric properties, in particular in view of the material characterisation study focussing on the overhygroscopic range. Hence, the goal is to determine to which extent the selected materials are unstable upon contact with water and in which way this influences the pore structure.

3.2.4.2 Test setup and method

A small prior test shows that each of the rammed earth materials liquefies upon contact with water, Fig. 3.7 (a). Further, an adapted small water uptake test is performed for evaluating the expansiveness of at least one initially dry 3x2x2 cm^3 sample per material, Fig. 3.7 (b). Herein, a 'wick' (Hall & Djerbib, 2004) is introduced to avoid the liquefaction. A filter paper enhances the hydraulic contact at the sample-wick interface. The strain is quantified (graphically) after the moisture front has reached the top and the swelling has stopped.

After redrying of the samples in the oven, small samples are sawn from them for a mercury intrusion porosimetry test for determining the impact on the pore structure cf. Section 3.2.3. Besides, a confined small water stability test variant in which the expansion is impeded, Fig. 3.7 (c), is performed for a virgin sample of the most expansive material in order to check the resulting pore structure.

Fig. 3.7: (a) Liquefaction; (b) Unconfined small water stability test; (c) Confined test.

3.2.4.3 Results and discussion

Table 3.3 collects the observed one-dimensional strain at capillary saturation in the horizontal direction, in the vertical direction, and taken overall - derived from the volumetric strain. It is found that the horizontal and the overall strain range from 1% (for house 6) to 10% (for the pressed material of house 1). The strain in the vertical direction is generally less pronounced. Taking into account such dimensional changes in the data processing of the forthcoming material characterisation tests is considered inconvenient. Moreover, the modified pore structure could significantly influence the hygric material properties.

Table 3.3: Capillary strain comparison for different rammed earth materials.

	H1P	H1R	H2	H6
horizontal strain at capillary saturation (m/m, %)	10	7	4	1
vertical strain at capillary saturation (m/m, %)	9	5	1	0
overall strain at capillary saturation (m/m, %)	10	6	3	1

Table 3.4 and Fig. 3.8 (for H1P) give the mercury intrusion porosimetry results for the dry material of house 1 before (original) and after (modified) the unconfined small water stability test. It is found that the bulk density reduces by 9%/5%, the open porosity increases by 19%/9%, and the pores widen, in particular in the capillary range, for the pressed/rammed material consequent to the unconfined absorption. It is herein used that the moisture content at 75% relative humidity is not affected by the material evolution. The material evolution impact is thus more important than the material errors (Table 3.1, Table 3.2). Besides, it is noted that the material becomes considerably more crumbly.

When a confining sealing is applied during the water uptake and drying, on the other hand, the material remains unaffected, Fig. 3.8 'post confined'. From this, it follows that the confined way of testing is chosen to be used for the hygric characterisation based on capillary absorption.

Table 3.4: Bulk density, open porosity, and median pore-throat radius - corresponding to the 50% mercury saturation - for the original and the modified ([a]) materials of house 1 (P/R).

	bulk density (kg/m^3)	open porosity (m^3/m^3)	median pore-throat radius (m, $x10^{-6}$)
H1P	1901 | 1737 [a]	0.301 | 0.358 [a]	0.64 | 1.50 [a]
H1R	1757 | 1670 [a]	0.352 | 0.384 [a]	1.04 | 1.72 [a]

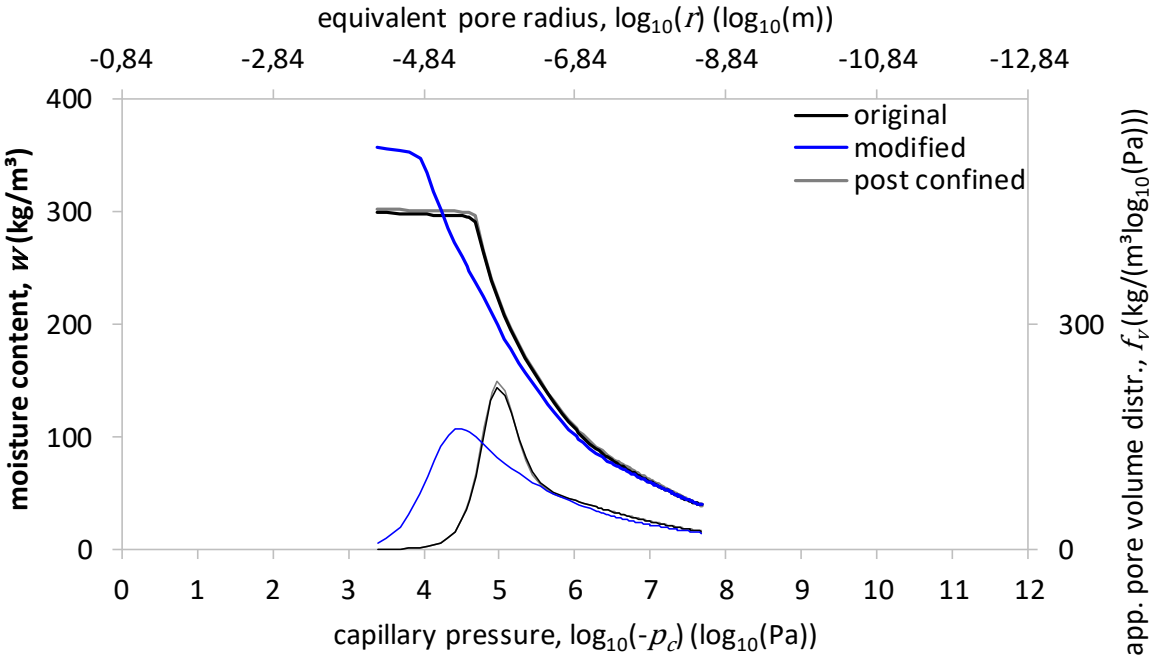

Fig. 3.8: Original versus modified/preserved pore structure after the unconfined/confined water uptake test, respectively, by mercury intrusion porosimetry for house 1 pressed.

3.2.4.4 Conclusion

The exploratory unconfined small water stability test with wick is found to yield one-dimensional strains at capillary saturation possibly up to 10%, resulting in a partly irreversible expansion of the pore space. On the other hand, the material evolution is eliminated when a confining sealing is additionally applied during the capillary absorption and redrying. In what follows, it is hence chosen to use this confined way of testing in order to obtain a consistent (reference) characterisation per material.

3.3 Moisture storage

3.3.1 Sorption isotherm

3.3.1.1 Introduction

A hygroscopic building material stores already a significant amount of moisture at a low relative humidity, which is of importance in the moisture response of a building element (e.g. regarding moisture buffering, mould growth). As the hygroscopic moisture content increases with the available pore surface area, fine-porous materials are more hygroscopic. The purpose is to determine for the selected rammed earth materials the moisture retention curve in the hygroscopic range, which is formed by the absorption isotherm.

3.3.1.2 Test setup and method

The absorption isotherm is measured for three samples per material per condition, of 3x2x1 cm^3 or $\pi x1.6^2 x0.5$ cm^3, for 11%, 33%, 53%, 75%, 85%, 94%, and 97% relative humidity, at 23.4 °C. For this, the initially dry samples, provided with a glass or metal holder to avoid crumble loss and touching impact, are put inside a ventilated desiccator where a saturated salt solution regulates the relative humidity according to (ISO 12571), Fig. 3.9 (a). After ≥ 9 days, the samples are weighed at ≥ 72 hour intervals, Fig. 3.9 (b). The average of three < 0.1% non-monotonous fluctuation readings is used for the equilibrium moisture content.

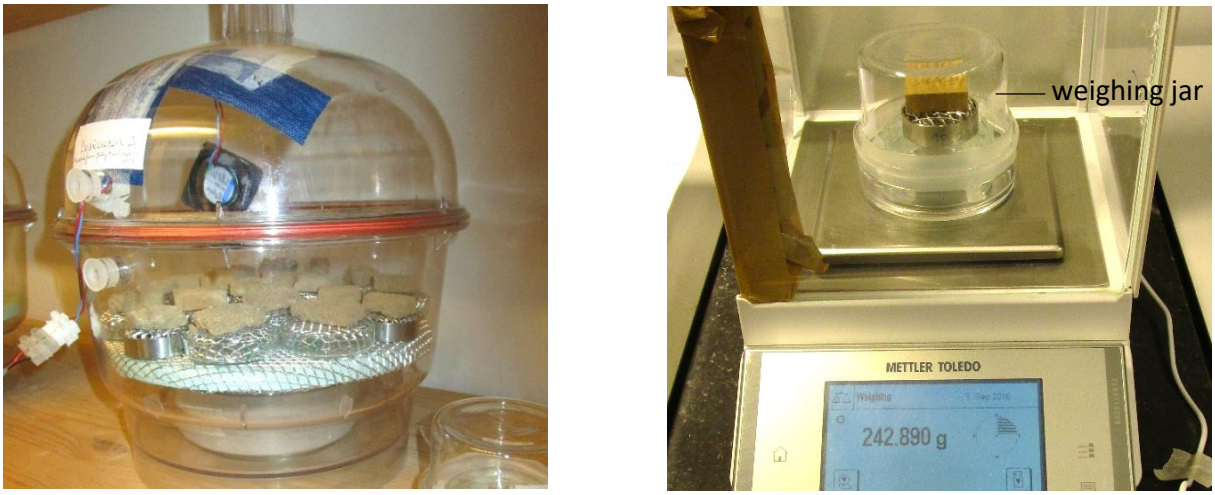

(a) (b)

Fig. 3.9: Sorption isotherm test (a) set-up, (b) weighing with weighing jar.

3.3.1.3 Results and discussion

Fig. 3.10 shows the determined absorption isotherm for the selected materials. The error bars represent the standard deviations for the three samples. Due to practical limitations, for the rammed material of house 1 only the 33%, 75%, and 97% relative humidity data are gathered. In order to give an idea of the missing data for the rammed material of house 1, the curve for the pressed material of house 1 - which is expected and found to be similar - is included. Moreover, Fig. 3.11 shows the absorption isotherm for the H1 rammed earth from two literature sources (Arrigoni et al., 2017); (Abhilash, 2016b) besides the data from the present work. The results are similar.

In Fig. 3.10, two distinct types of hygroscopic behaviour are observed. Firstly, the material of house 1 is strongly fine-porous - having a larger pore surface area, whereby larger amounts of moisture are stored as adsorbate (films on the pore walls). This can be related to its soil constituents, Fig. 3.1 (b), and/or manufacturing method (the material is crushed, homogenised (mixed), and sieved for 2 mm, to then be reconstructed in the lab).

Secondly, the material of house 2 and house 6 is less hygroscopic in the lower range (up to 75% relative humidity), but the moisture content strongly increases at higher relative humidity. For stable materials, this would indicate capillary condensation - films convert to liquid islands - filling the pores; for rammed earth materials, this could also indicate material evolution (see also Section 3.3.2). E.g. the expansion of clays between the grains tends to open (micro)cracks along grain boundaries, leading to an increase in porosity, and deformation could also lead to becoming available and swelling of clay inclusions (Scherer, 2006). The differences between samples in equilibrium moisture content above 75% relative humidity are significantly more pronounced for these authentic materials.

According to the classification of (Sing et al., 1985), the H1 rammed earth, as well as the H2 and H6 rammed earth materials, would fall under a type II isotherm, which is the normal form that is first concave and then convex to the relative humidity axis. The point at the beginning of the almost linear middle section of the sorption isotherm is often taken to indicate the stage at which monolayer adsorption is complete and multilayer adsorption is about to begin (Carmeliet, 2006); (Hall & Allinson, 2009a). The inset in Fig. 3.10 shows for the H1 and the H6 rammed earth the specific moisture content, which is the derivative of the sorption isotherm (Hens, 2010) and is determined using the fitting from Section 3.3.2.

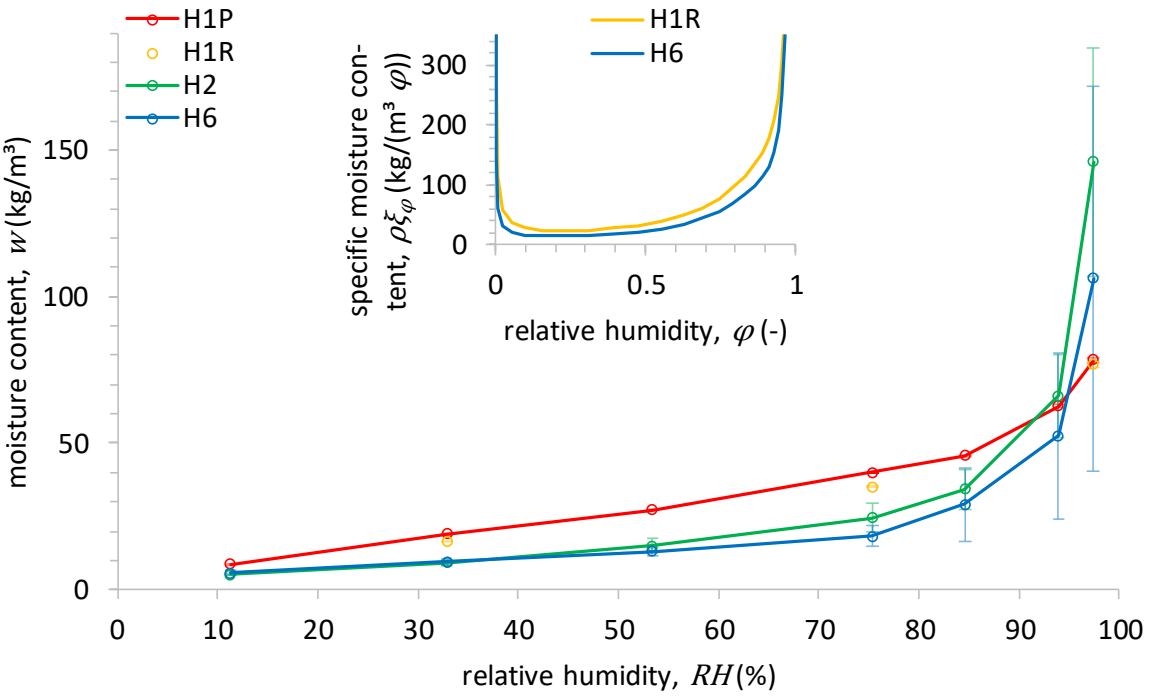

Fig. 3.10: Absorption isotherm for the material of house 1, house 2, and house 6.

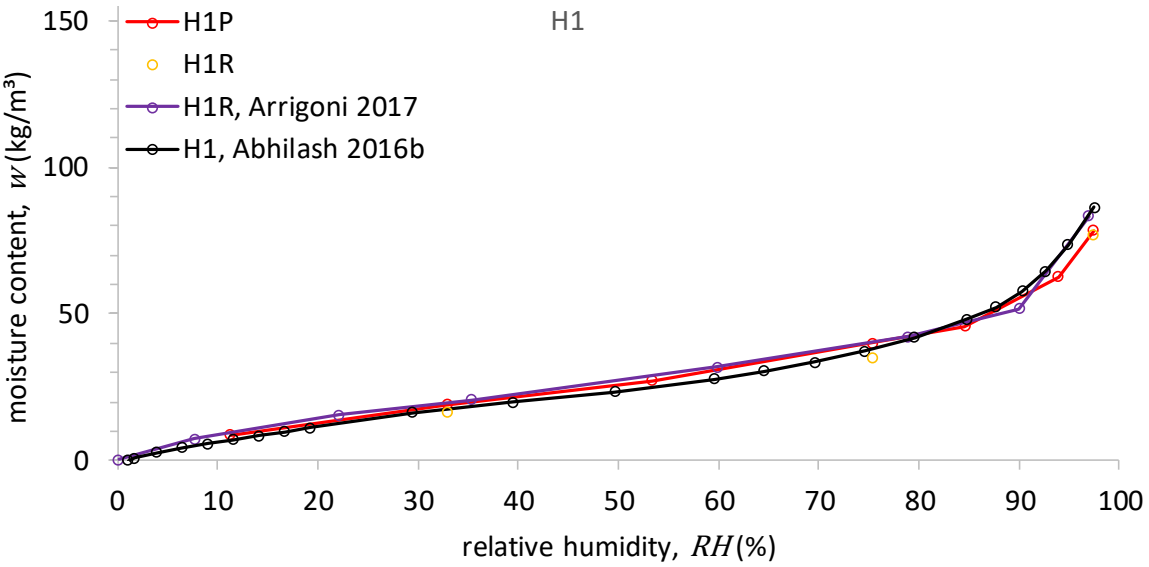

Fig. 3.11: Absorption isotherm for the material of house 1 from different sources.

3.3.1.4 Conclusion

In the sorption isotherm, two distinct types of hygroscopic behaviour are observed: the material of house 1 is strongly hygroscopic, whereas the authentic materials (houses 2 and 6) show more capillary condensation at relative humidities > 75%. Furthermore, the authentic materials are considerably more heterogenous in moisture storage as the relative humidity increases further.

3.3.2 Moisture retention curve

3.3.2.1 Introduction

The main wetting moisture retention curve is the equilibrium relation between the capillary pressure and the moisture content describing the wetting of an initially dry material up to the capillary saturation state. So, it indicates the actual moisture storage capacity of the material. This in contrast to the main drainage curve which can include ink-bottle effects (Roels et al., 2001) and is therefore not necessarily representative for the intended moisture retention curve. Hence, the purpose is to determine the main wetting curve for the selected rammed earth materials.

3.3.2.2 Test setup and method

In order to determine to which extent the mercury intrusion porosimetry results obtained in Section 3.2.3 are useful, they are compared with main wetting data. For this, they are brought together with the already collected results of the sorption isotherm (Section 3.3.1), complemented by psychrometry (Feng & Janssen, 2019) measurements in the intermediate range. The finally retained curve is cut off at the capillary moisture content determined in Section 3.4.2 and fitted by van Genuchten forms, Eq. (3.5), wherein w_{sat} is replaced by w_{cap}.

The psychrometry is performed on samples of 3.1 cm in diameter by 0.3 cm to 0.6 cm in height. This sample size is determined by the inner dimensions of 3.7 cm diameter and 0.9 cm height of the metal sample cups used for the measurement. Three samples per material are tested. The initially dry samples, provided with a plexiglass (PMMA) sample holder to avoid crumble loss and touching impact, are put above pure water in a closed container with a fan for accelerating the process, Fig. 3.12 (a). About once every two weeks, the absorption process is interrupted by sealing the samples into the metal cups for the equilibration of the moisture content and the capillary pressure before the measurement. It is assumed that 12 hours of isolation is sufficient in order to reach this internal equilibrium. Next, the metal cup with the sample is inserted into the WP4C psychrometer test device, Fig. 3.12 (b), where it is sealed against a sensor block.

The principle consists of measuring the vapour pressure of the air in this chamber caused by the equilibrated water evaporation from the sample, by means of the chilled mirror dew point technique. At the same time, the sample temperature is measured by means of infrared thermometry, and hence, the capillary pressure is derived (Kelvin). The corresponding moisture content is determined by weighing the sample, using the sealed metal cup as a weighing jar.

(a)

(b)

Fig. 3.12: (a) Main wetting moisture retention test setup; (b) Psychrometer test device.

The WP4C psychrometer capillary pressure range is from 0 MPa to -300 MPa (i.e. $log_{10}(-p_c) =$ -∞ $\log_{10}$(Pa) to 8.48 $\log_{10}$(Pa) or RH =100% to 11.2%). The accuracy is ±0.05 MPa from 0 MPa to -5 MPa (the latter corresponds to $log_{10}(-p_c) = 6.7$ $\log_{10}$(Pa) or $RH = 96.42\%$) and ±1% from -5 MPa to -300 MPa (Decagon Devices, 2015). Hence, e.g., a measurement at -0.1 MPa (i.e. $log_{10}(-p_c) = 5$ $\log_{10}$(Pa) or $RH = 99.93\%$) has an accuracy of ±50% of the reading, so it can lie anywhere between 4.7 $\log_{10}$(Pa) and 5.2 $\log_{10}$(Pa). Thus although the psychrometer allows determining relative humidities near 100%, it is limited by accuracy in the wet end.

For each measurement round, a linear calibration curve is determined by measuring the capillary pressure for five different unsaturated KCl salt solutions for which the theoretical capillary pressure value is known, and for pure water, using a metal cup. Hence, the calibration ranges from 0 MPa to -0.22 MPa to -10.98 MPa (i.e. from $log_{10}(-p_c) =$ -∞ $\log_{10}$(Pa) to 5.34 $\log_{10}$(Pa) to 7.04 $\log_{10}$(Pa) or from 100% to 99.84% to 92.29% relative humidity).

3.3.2.3 Results and discussion

Fig. 3.13 to Fig. 3.15 show the results per rammed earth material. The absorption moisture content at 75% relative humidity is used to shift the porosimetry curve, as discussed in Section 3.2.3. Assuming hysteresis negligible at and below 75% relative humidity (Arrigoni et al., 2017), the porosimetry curve can be merged with the sorption isotherm data in this range.

Above 75% relative humidity, overall a fairly close agreement is found between the porosimetry and the main wetting data for the rammed material of house 1. For the material of house 2 and house 6 on the other hand, it is observed that the porosimetry does not reproduce the capillary condensation trend observed in the sorption isotherm correctly for most of the samples. It is presumed that the large observed discrepancy can be explained in four ways: material evolution

(as explained in Section 3.3.1), material dissolution, mercury intrusion porosimetry deformation effects, material heterogeneity, and (micro)cracks from sample sawing.

It is concluded that the mercury intrusion porosimetry results match sufficiently well with the absorption results to be used as main wetting data (considering that no ink-bottle effects are included) for the materials studied. For the authentic materials (H2, H6), the moisture retention curve is fitted in between the mercury intrusion porosimetry and the absorption results to make a compromise in the concerned range of discrepancy. The material of house 2 will eventually not be used further due to excessive heterogeneity (see Section 3.4.1). The material of house 6 will be used further. Table 3.5 gives the Van Genuchten parameters, cf. Eq. (3.5).

Table 3.5: Van Genuchten parameters for moisture retention curve fit of H1 & H6 rammed earth.

		drainage				wetting		
H1	f_i	-	0.340	0.532	0.128	0.184	0.658	0.158
	α_i	-	0.256	0.070	0.000436	0.180	0.071	0.000434
	n_i	-	4.003	1.556	1.768	5.488	1.568	1.768
H6	f_i	0.130	0.278	0.488	0.104	0.323	0.559	0.118
	α_i	2.278	0.630	0.028	0.000436	0.646	0.028	0.000431
	n_i	5.996	1.856	1.954	1.838	1.849	1.952	1.842

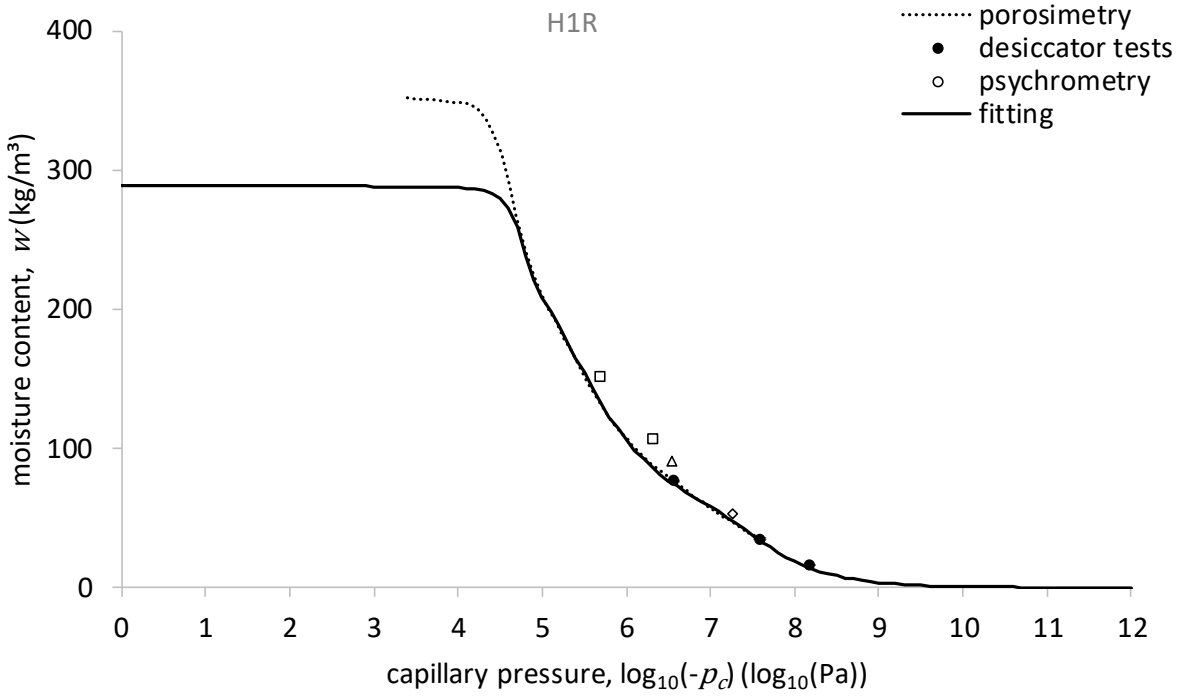

Fig. 3.13: Moisture retention data for the rammed material of house 1.

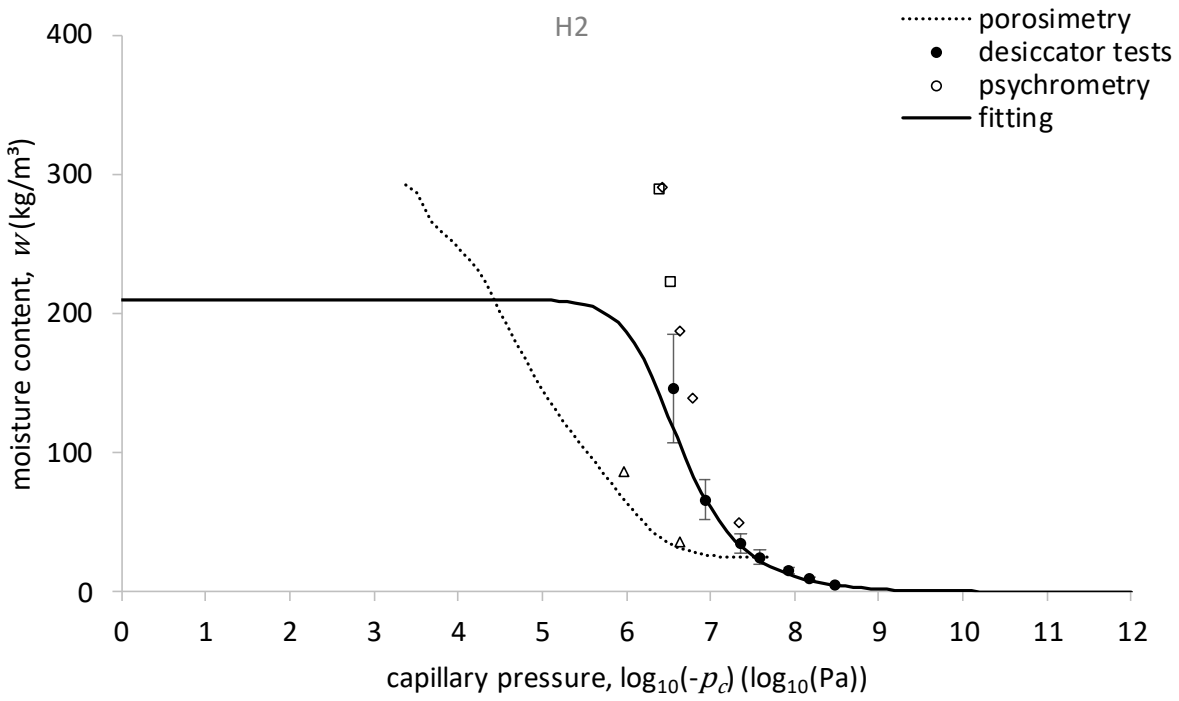

Fig. 3.14: Moisture retention data for the material of house 2.

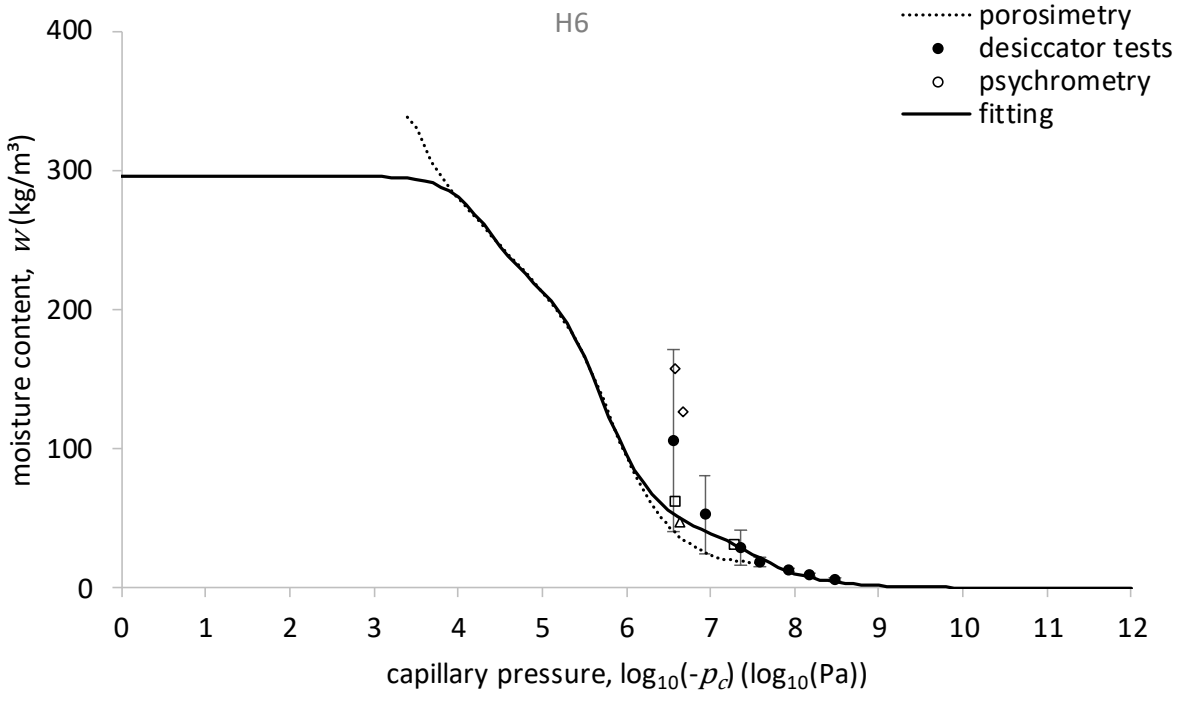

Fig. 3.15: Moisture retention data for the material of house 6.

Fig. 3.16 and Fig. 3.17 collect the resulting fitted complete main wetting moisture retention curve and pore volume distribution, respectively, for the different materials. It is observed that the share of the fine pores is relatively more important for the rammed material of house 1. For the material

of house 6 the (retained) curve is rather flat in this hygroscopic range from about 53% to 97% relative humidity. In the intermediate range, the material of house 6 has the more important pore system. Finally, in the most coarse pore range, the material of house 1 dominates again. The relatively low capillary moisture content for house 2 could be due to its heterogeneity or its more significant gravel content.

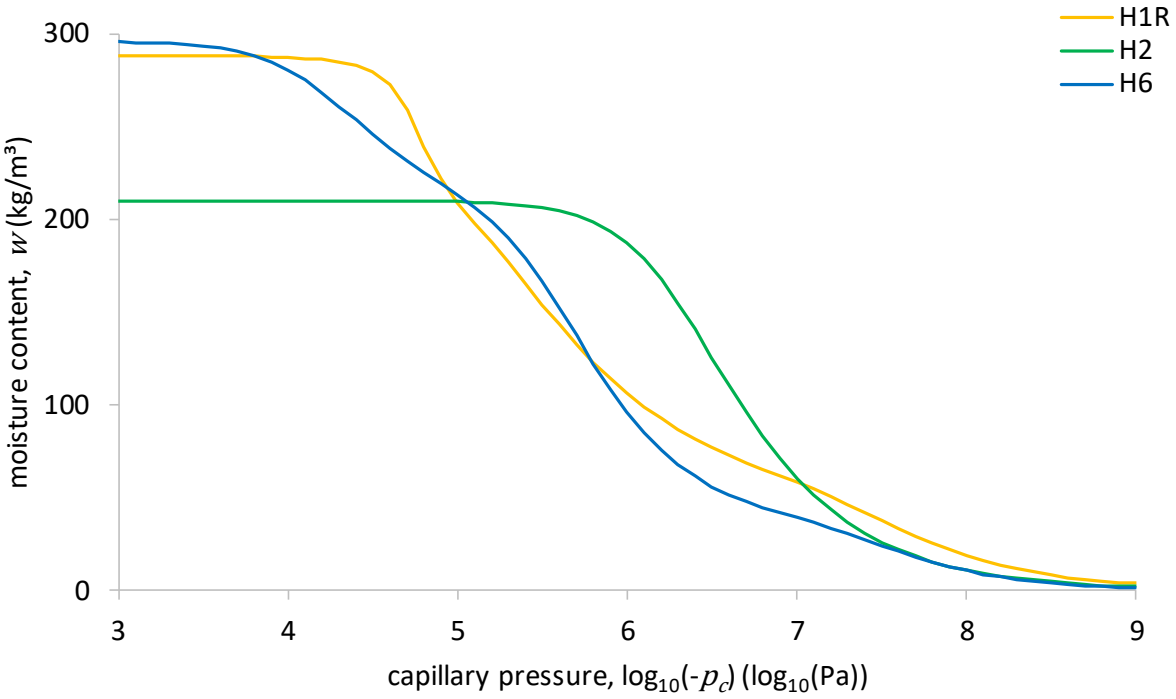

Fig. 3.16: Moisture retention curve retained for the material of house 1, house 2, and house 6.

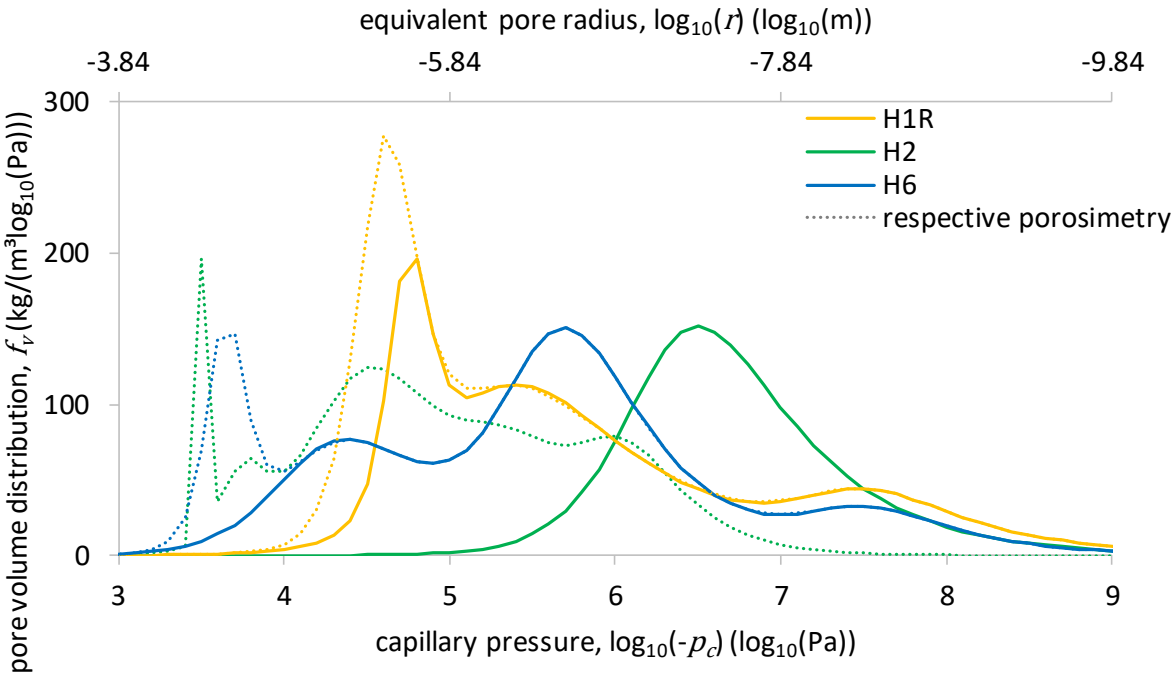

Fig. 3.17: Pore volume distribution corresponding to the main wetting moisture retention curve retained for the material of house 1, house 2, and house 6; and comparison with main drainage.

Fig. 3.18 shows the moisture retention curve of the H1 rammed earth from different sources. It is observed that the moisture retention curve from the present work matches the literature results in the hygroscopic range. The agreement is less close in the high overhygroscopic range. Such discrepancies in mercury intrusion porosimetry (Arrigoni et al., 2017) between different labs could be due to material inhomogeneity (cf. Fig. 3.4 (b) or the difference between H1P and H1R in Fig. 3.5) and measuring procedure (e.g. equilibration mode or scanning mode for increasing the pressure) (Roels et al., 2004); (Micromeritics, 2001).

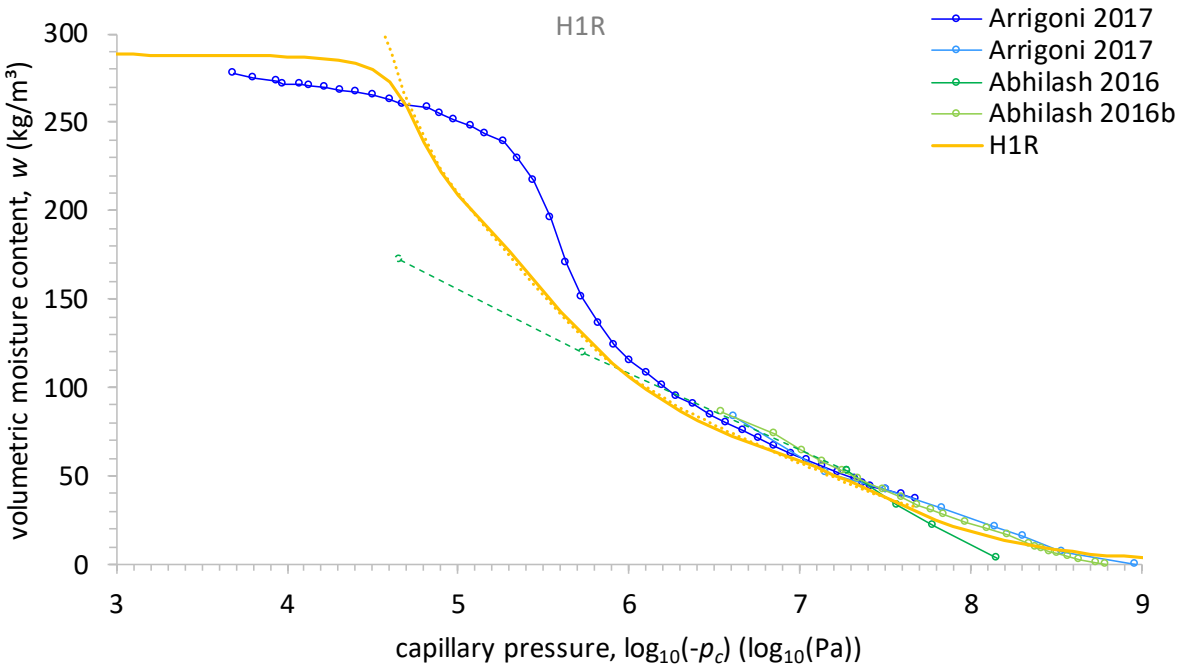

Fig. 3.18: Moisture retention curve for the material of house 1 from different sources.

3.3.2.4 Conclusion

For the complete moisture retention curve, the mercury intrusion porosimetry results are considered matching sufficiently well with the absorption results to be used as main wetting data. The observed differences between the porosimetry and the absorption results for the authentic material samples in the low range are bridged by making an average result. The moisture retention curve is cut off at the capillary moisture content in the high end. The result is fitted by Van Genuchten forms.

3.4 Moisture transport

3.4.1 Vapour permeability

3.4.1.1 Introduction

The vapour permeability of a building material influences the hygrothermal performance of a component (e.g. regarding the possibility to dry out, the risk on interstitial condensation). The equivalent vapour permeability is referred to when liquid water formed by pore wall adsorption or capillary condensation enhances the moisture transport. The goal is to measure this resulting moisture permeability in the hygroscopic range by cup tests at different humidities.

3.4.1.2 Test setup and method

Three samples per material are tested, but for the rammed material of house 1, only one sample per condition is tested. The sample diameter is 7 cm and the thickness 3 cm, which is a minimum, estimated based on available wet cup test results for rammed earth, in order to obtain an equivalent air layer thickness larger than 0.1 m, as recommended for the measurement accuracy (ISO 12572). (However, the recommendation of the sample thickness exceeding three times the largest particle size is not followed in this way for some samples of house 2 and house 6.)

Table 3.6 summarises the conditions for the three performed cup tests, wherein the relative humidity is regulated by saturated salt solutions (ISO 12571). The samples are initially dry each time. The ventilated test closet, Fig. 3.19 (a), forms a double chamber and the airflow velocity near the fan measures 4 m/s which gives a negligible exterior surface resistance in the data processing, Eq. (3.7). Since the balance is outside this conditioned environment, a weighing box is used, Fig. 3.19 (b). Fig. 3.20 shows a detail of the test assembly. (The space between the saturated salt solution and the sample is ca. 3 cm high, in contrast to the prescribed (15 ± 5) mm in (ISO 12572).)

(a) (b)

Fig. 3.19: (a) Cup test setup; (b) Cup test weighing.

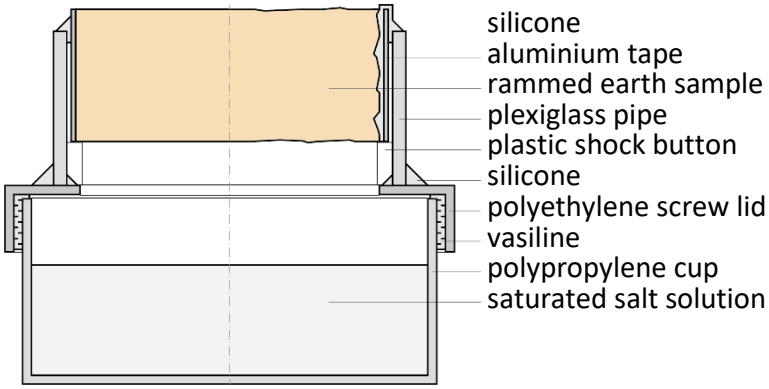

Fig. 3.20: Cup design and sealing for smooth sample (left half, H1); for rough sample (right half).

Table 3.6: Conditions in the cup tests; [a] measured, [b] according to (ISO 12571).

cup test name	temperature (°C) [a]	cup relative humidity (%) [b]	closet relative humidity (%) [b]
dry	23.5	11.3 (LiCl)	53.3 ($Mg(NO_3)_2.6H_2O$)
intermediate	25	52.9 ($Mg(NO_3)_2.6H_2O$)	84.3 (KCl)
wet	25	93.6 (KNO_3)	84.3 (KCl)

$$G_v = \frac{A\left(p_{v,e} - p_{v,i}\right)}{\frac{1}{\beta_e} + \frac{d_{mat}}{\delta_v} + \frac{d_{air}}{\delta_{air}}} \overset{Eq.\ (C.3)\ in\ Eq.\ (C.33)}{\approx} \frac{A\left(p_{v,e} - p_{v,i}\right)}{\frac{d_{mat}}{\delta_v} + \frac{d_{air}}{\delta_{air}}} \Leftrightarrow \delta_v = \frac{d_{mat}}{\frac{A\left(p_{v,e} - p_{v,i}\right)}{G_v} - \frac{d_{air}}{\delta_{air}}} \quad (3.7)$$

G_v	vapour flow	kg/s
A	surface area	m²
p_v	vapour pressure	Pa
β	convective surface moisture transfer coefficient	s/m
d	thickness	m
δ_v	(equivalent) vapour permeability	kg/(Pa m s)
$e/i/mat$	exterior/interior/material	

The (average) moisture content of the sample at the measured (equivalent) vapour permeability is obtained by weighing the sample in the detachable lid after the test. This moisture content is further used to find the corresponding actual average relative humidity / capillary pressure via the moisture retention curve (Section 3.3.2) (it is verified whether this falls within the test conditions).

3.4.1.3 Results and discussion

Fig. 3.21 shows the results of the (equivalent) vapour permeability as a function of the (average) moisture content for the different materials. It is found that the H2 material is highly heterogenous - one quasi non-hygroscopic versus two clearly hygroscopic samples -, even with this larger sample

size, cf. Section 3.3.2, whence it is chosen to be discarded and not discussed/characterised further.

The dry cup vapour resistance factor, μ (-), indicating how many times more vapour tight the material is than air, amounts to 7.7 for the rammed material of house 1 and 8.2 (± 8.8%) for house 6 (with an actual average relative humidity of 52% and 54%, respectively), which reflects the open porosity trend (Section 3.2.3). The permeability hardly increases in the intermediate cup test (at 77% and 73% actual average relative humidity, respectively) as the transport continues similarly.

The wet cup permeability in contrast is greater than the intermediate, by a factor 3 for house 1 and 2 for house 6. This reflects the hygroscopicity trend (Section 3.3) and indicates that, at the actual average relative humidity of 89% and 84%, respectively, the liquid islands formed play a part in the transport.

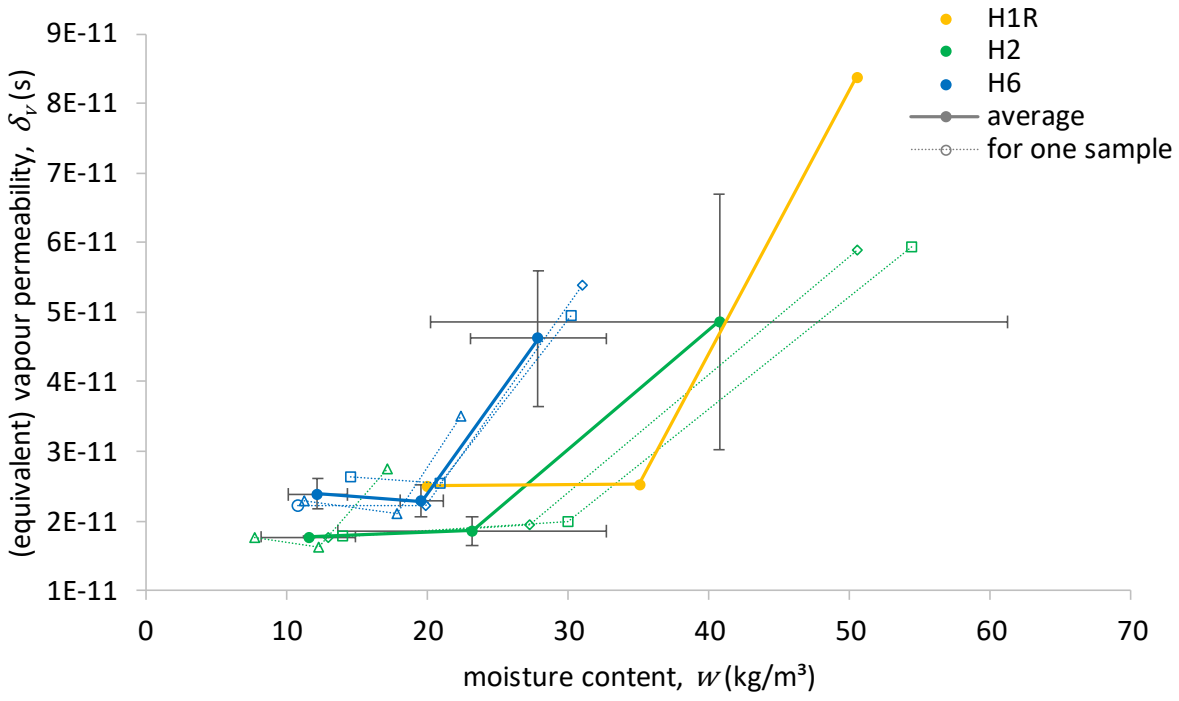

Fig. 3.21: Cup test results for the rammed earth material of house 1, house 2, and house 6. The error bars represent standard deviations.

3.4.1.4 Conclusion

A clear link between the (equivalent) vapour permeability and the open porosity and the hygroscopicity is observed. The results per sample confirm that the material of house 2 is highly heterogenous after all, whence this material is further discarded.

3.4.2 Capillary absorption

3.4.2.1 Introduction

A capillary building material absorbs water actively, which influences the building wall's insulatability (e.g. via rain penetration, moisture buffering, moisture redistribution). Hence, the capillary absorption coefficient and the capillary moisture content are important material properties, indicating the transport and the storage of the capillary moisture, respectively. Both properties are determined by the capillary absorption test. Moreover, this test forms the basis for determining the moisture permeability (Section 3.4.3). For the investigated rammed earth materials which are unstable to water, the test's method is adapted.

3.4.2.2 Test setup and method

Since the capillary absorption test in this work is especially used in view of the moisture permeability determination, most of the samples are X-ray formatted: 1.4 cm thick (d), 6.4 cm wide (W), and 6 cm high (H). For the rammed material of house 1, the samples are 9 cm high due to the larger capillary absorption coefficient and also a 7 cm diameter (D) sample is tested. For each material additionally a 2.2 cm high prismatic sample is used. Table 3.7 gives an overview of the samples. The temperature is ca. 22.6 °C (average room and water temperature).

Table 3.7: Overview of confined composite rammed earth samples for capillary absorption test.

Material	H1 rammed earth				H6 rammed earth			
	Sample 1	Sample 2	Sample 3	Sample 4	Sample 1	Sample 2	Sample 3	Sample 4
	lab	X-ray	X-ray	lab	lab	X-ray	X-ray	lab
H (cm)	8.6	9.3	9.2	2.2	6.0	6.2	6.0	2.2
W (cm)	7.0 (D)	6.6	6.4	6.3	6.4	6.4	6.4	6.4
d (cm)	-	1.4	1.4	1.4	1.4	1.5	1.4	1.4
H_{wick} (cm)	1.0	1.0	1.0	0.3	1.0	1.0	1.0	0.3
paper type	blotting	blotting	filter	filter	filter	filter	filter	filter

The measured sample dimensions that are needed separately in the data processing of the capillary absorption test are corrected for roughness (Section 3.2.2). When the bulk density of a sample is similar to that of other samples of the same material, the correction factor as determined by Eq. (3.8) is applied, assigning the material bulk density to the sample. Otherwise, a typical correction factor for the concerned material is applied, allowing the sample's aberrant bulk density.

$$(d_{cal} + \delta)(W_{cal} + \delta)(H_{cal} + \delta) = d_{cal} W_{cal} H_{cal}\, \rho_{bul,cal}/\rho_{bul} = d\, W\, H \tag{3.8}$$

δ	dimensional correction factor (typically negative)	m
d	thickness	m
W	width	m
H	height	m
ρ	density	kg/m³
$_{cal/bul}$	caliper / bulk	

As discussed in Section 3.2.4, the material unstability leads to the test setup developments of the wick addition and the confining sealing application, Fig. 3.22. Herein, the sample is attached to the wick - which is why, like the sample, the wick is initially dry, and hence a composite case applies. In (Wilson et al., 1995), it is shown how the absorption properties of the second medium of a bilayer composite are determined (based on a sharp front model): the first medium's presence impact diminishes as the time increases, and the absorption rate of the second medium is retrieved at sufficiently long times - sooner for a shorter first medium with similar or greater permeability.

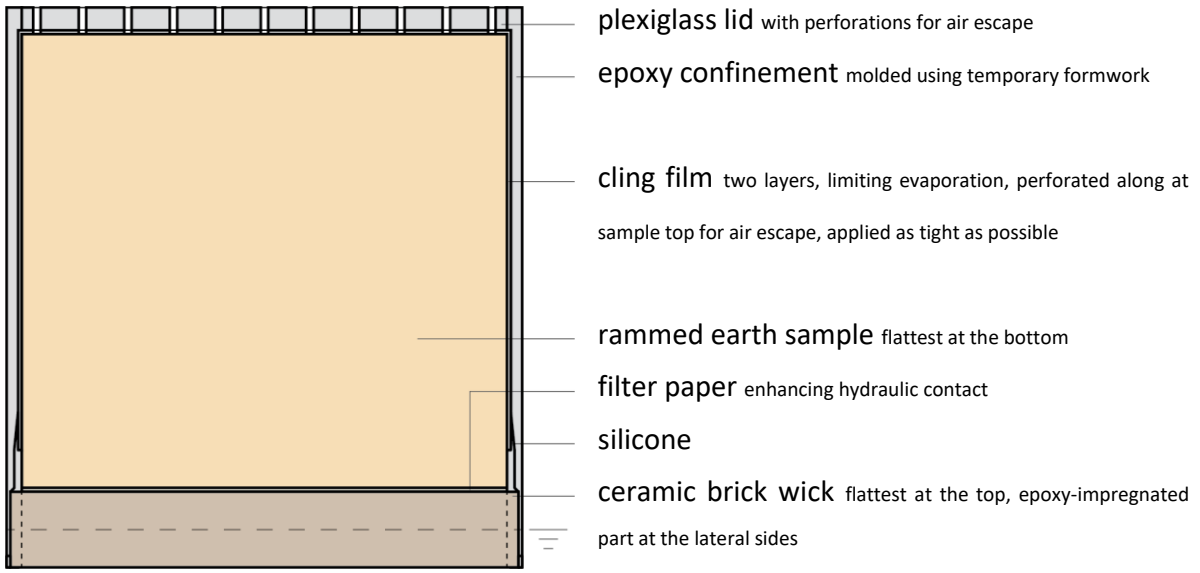

Fig. 3.22: Capillary absorption test assembly.

The wick is 1 cm high, except for the 2.2 cm short samples it is 0.3 cm high. Relevant properties of the selected (strong and stable) ceramic brick material for the wick are the bulk density of 1818 kg/m³, the vacuum saturation moisture content of 326 kg/m³, the capillary moisture content of 210 kg/m³, and the capillary absorption coefficient of 0.61 kg/(m² $s^{0.5}$) (Feng & Janssen, 2018).

Fig. 3.23 shows the capillary absorption process for a sample of this ceramic brick material in two different configurations. Firstly, the reference data in grey result from a test using the (12 cm high) sample alone. It is observed that the capillary absorption pattern is ideal - a linear relation between the moisture mass and the square root of time in the first stage - and the intercept is zero. Secondly, the blue curve are the raw measurement data from a composite test, wherein the assembly is composed of the ceramic brick sample plus a (1 cm high ceramic brick) wick, with a filter paper at the interface. It is observed that the reference capillary absorption coefficient is retrieved but the new intercept is negative, indicating that the interface causes a delay in an early part of the first stage after which the reference behaviour is recovered. (The work of Wilson learns that this curve needs to be shifted vertically for coinciding with the reference.)

According to the literature, the capillary absorption coefficient of rammed earth materials typically amounts to about 0.3 kg/(m² $s^{0.5}$), which indicates a lower permeability than the ceramic brick. For a composite with a rammed earth sample at the top hence the influence of the interface is expected to be less pronounced (for the same quality of the contact at the interface). Furthermore, the ceramic brick wick impacts the process in the opposite sense in this case.

Resultantly, the influence of the wick and the accompanying interface is presumed to be limited to an early part of the first stage for the cases studied. Moreover, since a reference test without wick is not an option for the rammed earth materials, it is in the first instance assumed that the materials have an ideal capillary absorption pattern. All things considered, it is presupposed that the latest retrieved linear part of the first stage gives the correct capillary absorption coefficient.

For the moisture mass in the top part alone, a constant moisture mass of the wick is subtracted, Fig. 3.23, estimated at the average of the vacuum saturation and the capillary moisture content (the wick is half-immersed; the filter paper is neglected). Although this implies that the hence determined intended capillary moisture content is not quite independent of the wick's (actual) properties, tests with detachable wick show that the 268 kg/m³ is a good approximation.

Where the envisaged capillary absorption coefficient (A_c, kg/(m² $s^{0.5}$)) is retrieved, the target top sample behaves physically as if it were preceded by a certain length of itself. Assuming that the intercept of the first stage fitting is zero for the target material alone reference, and that the fictitious preceding sample part is capillary saturated, this length is determined by Eq. (3.9), as illustrated in Fig. 3.23. This equivalent height, capturing the influence of the wick and the interface,

is used for adjusting the Boltzmann transformation of the X-ray capillary absorption test results in Section 3.4.3.

$$H_{equ} = m_{equ}/w_{cap} \tag{3.9}$$

m	moisture mass	kg/m²
w	moisture content	kg/m³
$_{equ/cap}$	equivalent / capillary	

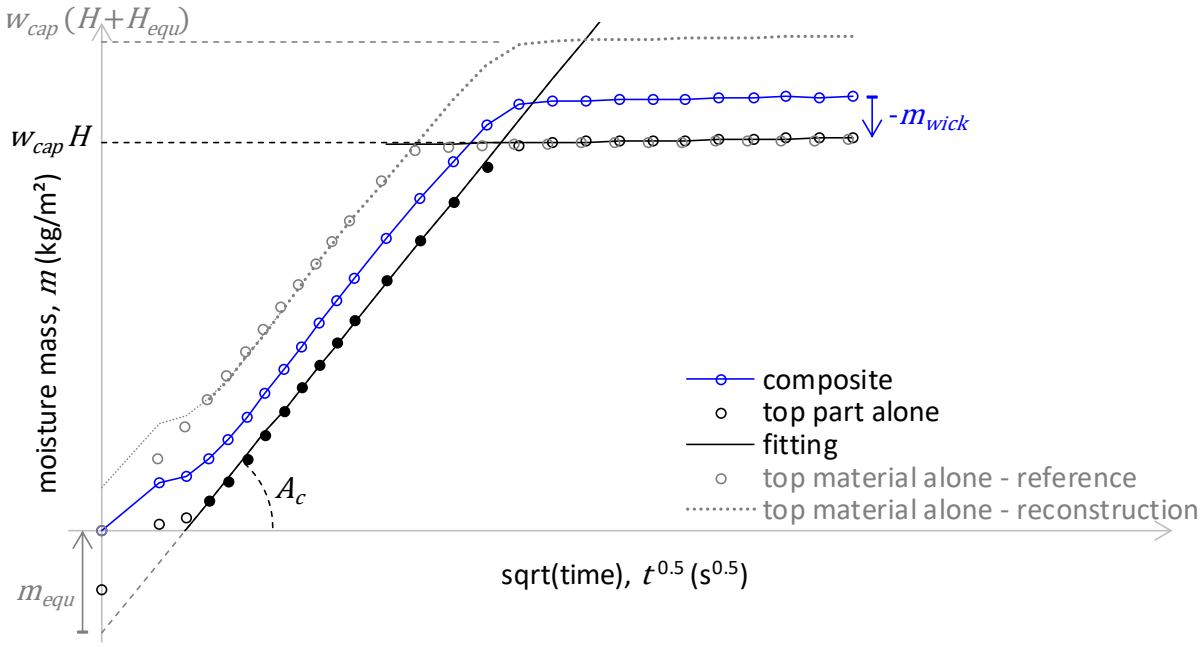

Fig. 3.23: Data processing method illustration using ceramic brick capillary absorption test results.

3.4.2.3 Results and discussion

Fig. 3.24 and Fig. 3.25 show the capillary absorption process in the rammed earth part alone of four samples per material for the rammed earth material of house 1 and house 6, respectively. Filled markers indicate the data used for the first stage fitting, supported by the coefficient of determination that remains > 0.999. And markers that are moreover crossed, indicate X-ray data selected to form the characteristic profile in Section 3.4.3.

It is observed that a persistent linear pattern is retrieved after a while, which confirms the assumption of the rammed earth materials behaving ideally and proves that the proper capillary absorption coefficient is retrieved. Where the target behaviour is retrieved, the top sample behaves as if it were preceded by a certain length of its own material that equals the equivalent height corresponding to the intercept value. This equivalent height is usually not greater than the wick height (except for sample 2 of the H6 material).

Table 3.8 collects the determined properties. For the rammed material of house 1, the results of different samples are similar (they are always from the same layer, with a consistent direction). For house 6, on the other hand, the capillary absorption coefficient is found to vary between 0.142 kg/(m² $s^{0.5}$) and 0.220 kg/(m² $s^{0.5}$) due to heterogeneity.

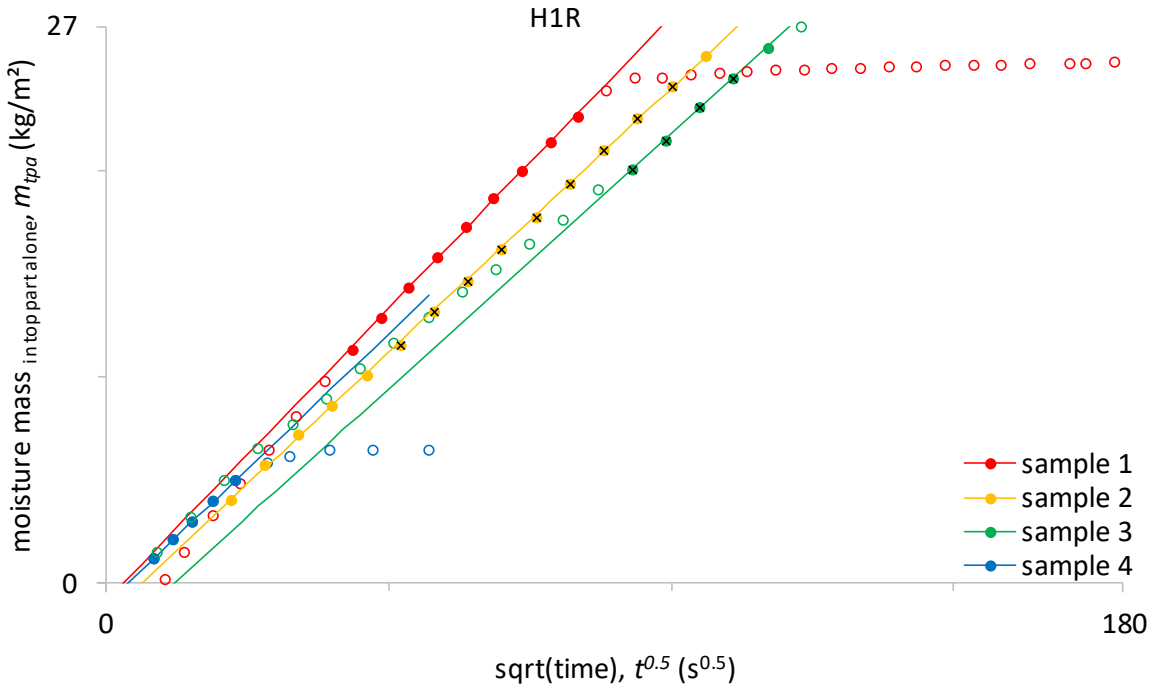

Fig. 3.24: Capillary absorption process for house 1's rammed material (9 cm or 2.2 cm high).

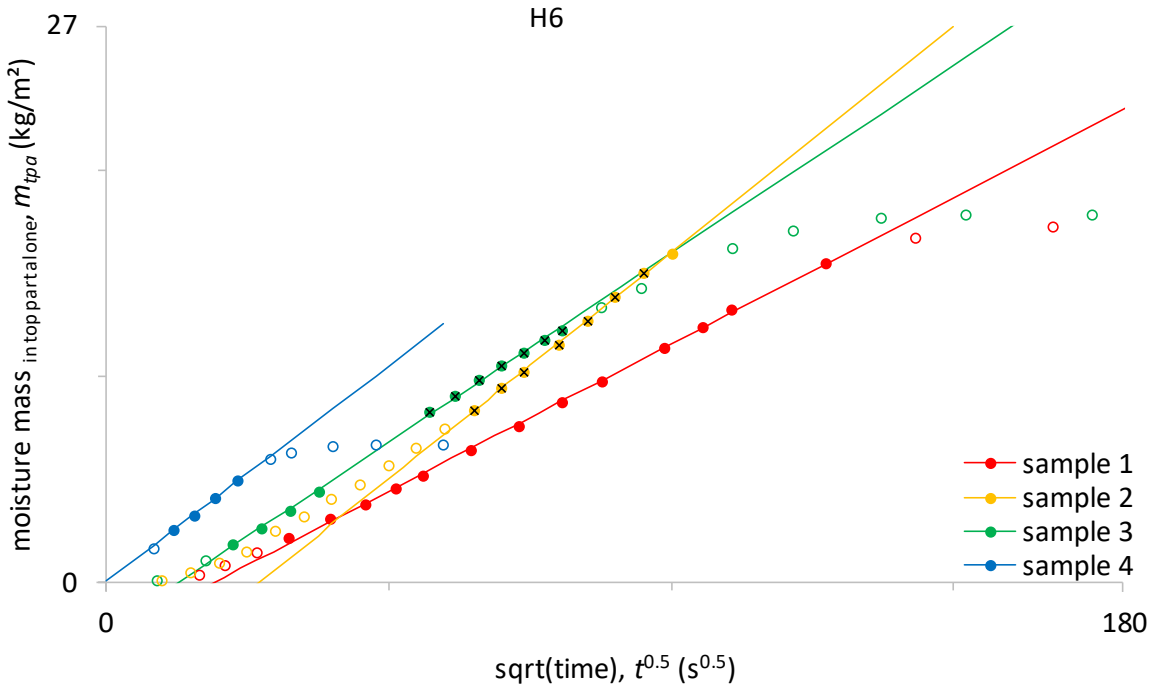

Fig. 3.25: Capillary absorption process for house 6 samples (6 cm or 2.2 cm high).

Table 3.8: Capillary absorption coefficient and capillary moisture content of target materials.

	H1R	H6
capillary absorption coefficient (kg/(m² $s^{0.5}$))	0.262 (±5.7%)	0.188 (±18.1%)
capillary moisture content (kg/m³)	288 (±1.5%)[a]	296 (±3.2%)

[a] Deviation instead of standard deviation because only two results are involved.

3.4.2.4 Conclusion

The capillary absorption test forms the basis for determining the moisture permeability. Moreover, it provides the capillary moisture content and the capillary absorption coefficient. Since the rammed earth materials studied expand and liquefy upon contact with water, the test's method is adapted. For avoiding the liquefaction, a thin permeable wick is introduced (with a filter paper at the sample-wick interface for enhancing the hydraulic contact), and for impeding the expansion, a confining sealing is applied. It is found that the resulting influence of the wick and the paper on the capillary absorption process is limited to an early part of the first stage. After that, the capillary absorption rate of the rammed earth material is retrieved and the rammed earth part behaves then as if it were preceded by an equivalent rammed earth length.

3.4.3 Moisture diffusivity

3.4.3.1 Introduction

The moisture diffusivity is determined with the aim of obtaining the moisture permeability curve. It is defined as the ratio of the moisture permeability to the moisture capacity, and it thus indicates how easily a local moisture content (or capillary pressure) change spreads over the material. The theoretical background for its experimental determination follows from the moisture mass conservation equation, formulated with the moisture diffusivity describing the moisture transport using the moisture content as the governing variable (Carmeliet et al., 2004); (Roels & Carmeliet, 2006):

$$\frac{\partial w}{\partial t} = -\frac{\partial}{\partial x}\left(-k_m \frac{\partial p_c}{\partial x}\right) = -\frac{\partial}{\partial x}\left(-\frac{k_m}{\frac{\partial w}{\partial p_c}}\frac{\partial w}{\partial x}\right) = -\frac{\partial}{\partial x}\left(-D_m \frac{\partial w}{\partial x}\right) \tag{3.10}$$

w	moisture content	kg/m³
t	time	s
x	position	m
k_m	moisture permeability	s
p_c	capillary pressure	Pa
D_m	moisture diffusivity	m²/s

Provided that the porous medium can be considered homogeneous, semi-infinite, initially at a uniform moisture content, and, subsequently, exposed to a constant boundary condition at one surface, and provided that the investigated resulting moisture transfer process in it behaves linearly with the square root of time, the above partial differential equation Eq. (3.10) - with the moisture content as a function of the time and the position - can - by substituting the Boltzmann variable Eq. (3.11) in it - be reduced to an ordinary one Eq. (3.12) which has one solution:

$$\lambda = \frac{x}{\sqrt{t}} \tag{3.11}$$

$$\frac{-\lambda}{2}\frac{dw}{d\lambda} = -\frac{d}{d\lambda}\left(-D_m \frac{dw}{d\lambda}\right) \tag{3.12}$$

with the initial Eq. (3.13) and boundary Eq. (3.14), Eq. (3.15) conditions:

$t = 0$ (and $x > 0$) → $\lambda \to \infty$: $w = w_0$ (3.13)

$t > 0$ and $x = 0$ → $\lambda = 0$: $w = w_B$ (3.14)

$t > 0$ and $x \to \infty$ → $\lambda \to \infty$: $w = w_0$ (3.15)

λ	Boltzmann variable	m/s$^{0.5}$
$_0$	initial	
$_B$	boundary	

Hence, the Boltzmann conditions fulfilled, the transformed transient moisture content profiles - scaled to square root of time - collapse to form one single w-λ profile. Integration of Eq. (3.12) gives the expression for the moisture diffusivity as a function of the moisture content and shows that the diffusivity is obtained by integrating and differentiating this Boltzmann transformed profile:

$$D_m = \frac{-\frac{1}{2}\int_{w_0}^{w} \lambda \, dw}{\frac{dw}{d\lambda}\Big|_w} \tag{3.16}$$

In what follows, moisture content profiles for determining the moisture diffusivity are measured during a capillary absorption test. Although the associated imposed boundary condition is rather unusual for building components exposed to real climatic conditions and this test does not necessarily give accurate results for the diffusivity in the low and intermediate range, it does reliably deliver the moisture diffusivity in the high range (Carmeliet et al., 2004).

3.4.3.2 Test setup and method

The sample size and preparation and the conditions for the capillary absorption test are as described in Section 3.4.2. Instead of weighing the sample like in the lab test, the experimental procedure consists of monitoring the moisture content profiles by means of X-ray projectional radiography using Tomohawk software. For this, the sample is positioned between an X-ray source, which is set for 80 kV energy and 215 µA current each time, and a detector (the distance source-sample is ca. 107 cm, the detector is 21x21 cm², the iris position is 0.85). In order to reduce the noise in the acquired images, several (256) projections (85 ms exposure) taken at the same time (in 22 s) are averaged. The resulting greyscale images are 1024x1024 pixels. For each pixel,

an intensity value is stored. The matrix form radiation files are read using Matlab software.

The intensity indicates the number of X-ray photons ('counts' or 'hits'). The data processing method for obtaining moisture content profiles from these radiography measurements is based on the Beer-Lambert law:

$$I = I_0 e^{-\mu d} \tag{3.17}$$

I	transmitted intensity	-
I_0	incident intensity	-
μ	attenuation coefficient	m^{-1}
d	thickness of the sample	m

Applying Eq. (3.17) to a water-containing porous medium using the typical separation concept (Roels & Carmeliet, 2006), gives the following attenuation relation:

$$I_{wet} = I_{dry} e^{-\mu_{wat} d_{wat}} = I_0 e^{-\mu d} e^{-\mu_{wat} d_{wat}} \tag{3.18}$$

$_{wat}$	water

Herein, d_{wat} is the fictitious water layer thickness which is in agreement with the medium's moisture content, i.e. resulting in the wet transmitted intensity. The relation between the moisture content and this equivalent water thickness is given by:

$$w = \frac{\rho_{wat} d_{wat}}{d} \tag{3.19}$$

Hence, by rewriting of Eq. (3.18) to replace d_{wat} in Eq. (3.19), it is found that the moisture content at each position can be quantified by logarithmically subtracting the reference image of the dry sample from the images of the wet sample:

$$w = -\frac{\rho_{wat}}{\mu_{wat} d} \ln\left(\frac{I_{wet}}{I_{dry}}\right) \tag{3.20}$$

In (Roels & Carmeliet, 2006), it is demonstrated that the resolution in this moisture content can be used to determine an optimal sample thickness and X-ray energy. The choice of the used

sample thickness (and X-ray energy) in this work is based on this literature, assuming that the rammed earth materials' attenuation coefficient is similar to the ceramic brick material's presented there.

The effective (Pease et al., 2012) water attenuation coefficient is determined (using Eq. (3.20)) by setting the average moisture content of the sample according to the final wet image equal to the final moisture content measured immediately after this last image by weighing the sample:

$$\mu_{wat} = -\frac{\rho_{wat}}{w_{fin} d} \ln\left(\frac{I_{wet,fin}}{I_{dry}}\right) \tag{3.21}$$

$_{fin}$ final

The estimated real edges (Roels & Carmeliet, 2006) are used as the sample borders in the image - only the rammed earth part is considered. For the 'dry' reference image, the first (wet) image taken as soon as possible after the water touches the sample is used. This usually is at ca. 36 s (yet the original times are kept further) and causes a boundary zone wherein the calculated moisture contents are incorrect. (For the water attenuation coefficient and for the capillary absorption process (cf. below), these values are replaced by a linear connection to the material's capillary moisture content at the boundary.)

In order to reckon with the instability of the X-ray source over time, for each wet image a linear calibration curve is determined by means of dummies (Vereecken, 2013). These are small dry samples which are included in the setup as a reference and give attenuated intensities in a range that covers the target sample. Besides, the calibration curve is forced to go through the origin (cf. the source is off). (The resulting slope becomes a multiplication factor for I_{wet} in the equations.) In order to increase the precision, the data in the middle 20x20 pixels of a dummy are averaged. Analogously, in order to reduce the scatter, the data in the target sample's middle 20 pixels wide column are averaged for the moisture content profiles (and their water attenuation coefficient).

In addition to the moisture content profiles, the capillary absorption process is plotted via the X-ray data - the full sample width is used for this - in order to supply the hydraulically equivalent height of the lower parts (wick and paper), see Eq. (3.9). This equivalent height is used in the Boltzmann transformation of application for the composite case as following:

$$\lambda^* = \frac{x_{tpa} + H_{equ}}{\sqrt{t}} \tag{3.22}$$

λ^*	adapted Boltzmann variable	m/s$^{0.5}$
H	height	m
$_{tpa/equ}$	top part alone / equivalent	

The characteristic profile falls in the middle of the scatter band and is approximated smoothly using the tangent formula (Evangelides et al., 2018), Eq. (3.23), in order to facilitate the derivation of the moisture diffusivity (Eq. (3.16), wherein λ is replaced by λ^*). The tangent formula woks with the boundary conditions Eq. (3.24) and Eq. (3.25) and with the requirement that the surface area under the characteristic profile is fitted correctly. This surface area corresponds to the capillary absorption coefficient, Eq. (3.26). Since the characteristic profile is as a material property, the capillary moisture content is assigned to the fictitious boundary - as if the sample were effectively taller by H_{equ}. In that way, the data-less zone resulting from the adapted Boltzmann transformation is bridged. It is verified that the determined diffusivity reproduces the capillary absorption behaviour of the sample via numerical hygrothermal simulation using Delphin software (Section 2.3.1). The diffusivity is used directly as material liquid water diffusivity input for this. In Appendix D, the characteristic profile from the ruler method (Ren et al., 2019) is compared.

$$\lambda^*(w) = \frac{1}{b}\left(\tan\left(-\frac{w + w_{cap}}{a}\right) - c\right) \tag{3.23}$$

$$w = w_{cap} : \lambda^* = 0 \tag{3.24}$$

$$w = 0 : \lambda^* = \lambda_f^* \tag{3.25}$$

a, b, c	fitting parameters	
w_{cap}	capillary moisture content	kg/m³
λ_f	average boundary lambda value	m/s$^{0.5}$

$$A_{c,C} = \int_{w_{0,C}}^{w_{B,C}} \lambda^* \, dw = \int_{0}^{w_{cap,C}} \lambda^* \, dw \tag{3.26}$$

A_c	capillary absorption coefficient	kg/(m² s$^{0.5}$)
$_c$	of the top material C for the tri-layer composite of application	

3.4.3.3 Results and discussion

Fig. 3.26 (a) and (b) capture the selection of the resulting transformed moisture content profiles (the incorrect data in the boundary zone are discarded) for the rammed earth material of house 1 and house 6, respectively. It is observed that the transformed data collapse into a single characteristic profile. The characteristic profile moreover reproduces the capillary absorption coefficient for both materials. Hence, it is concluded that the X-ray method with the adapted Boltzmann transformation is valid for the cases studied - rammed earth sample plus wick and paper. Fig. 3.27 (a) and (b) show the corresponding determined moisture diffusivity.

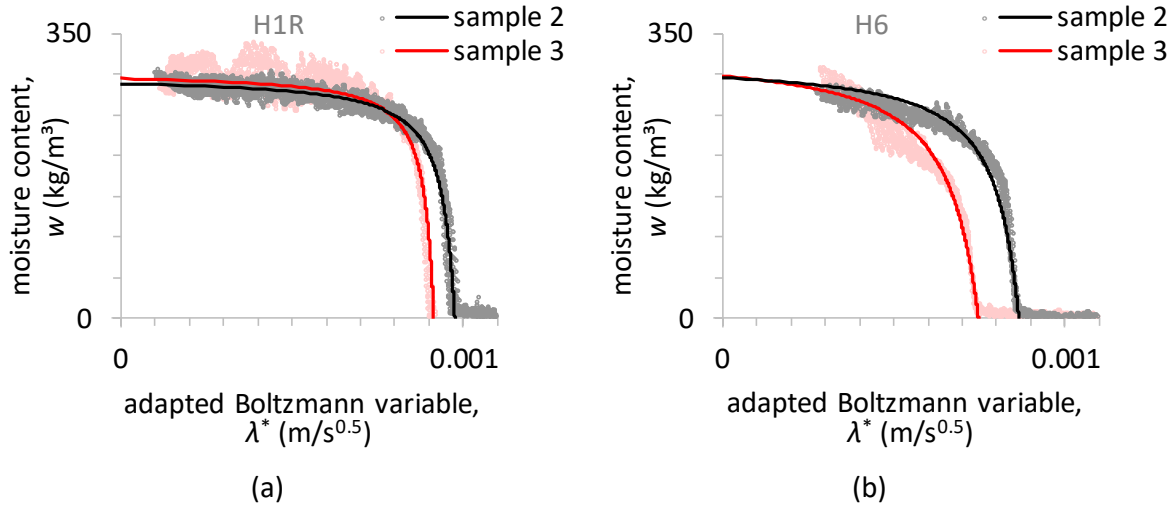

Fig. 3.26: Characteristic profile fitting and underlying Boltzmann transformed moisture content profiles (a) for H1 rammed earth samples and (b) for H6 rammed earth samples.

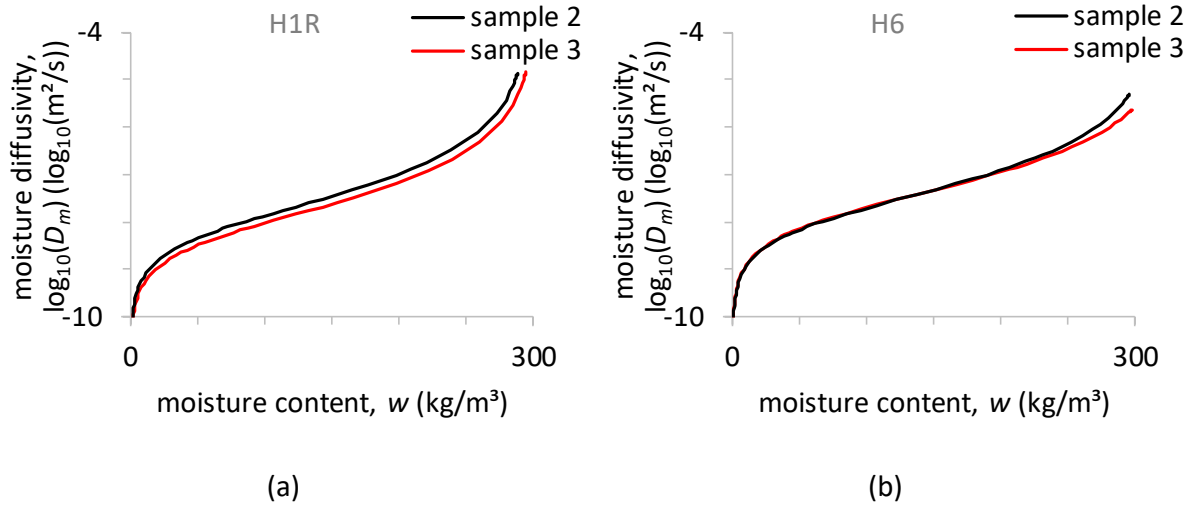

Fig. 3.27: Moisture diffusivity (a) for H1 rammed earth samples and (b) for H6 rammed earth samples.

3.4.3.4 Conclusion

The moisture diffusivity of rammed earth is determined with the X-ray technique for monitoring moisture content profiles within the sample during the capillary absorption test. The applied Boltzmann transformation for this is adapted to take into account the influence of the wick and paper via their equivalent height.

3.4.4 Moisture permeability

3.4.4.1 Introduction

The moisture permeability is a crucial hygric property describing the moisture transport in porous building materials. This transport property uses the capillary pressure as driving potential.

3.4.4.2 Method

The moisture permeability is obtained by the product of the moisture diffusivity (Section 3.4.3) and the moisture capacity (Section 3.3.2): Eq. (2.25), cf. Eq. (3.10). The limited accuracy in determining the moisture capacity when nearing capillary saturation yields an unphysically decreasing permeability in that range (Carmeliet et al., 2004). It is therefore corrected enforcing a constant permeability. The numerical simulation of the capillary absorption test is performed again (cf. Section 3.4.3.2) with the permeability as input this time to verify that the same behaviour is still reproduced. If necessary, the upper limit of the permeability is slightly adjusted (lowered, in practice) to fit this reproduction. The resulting permeability is used as the liquid water permeability.

3.4.4.3 Results and discussion

Fig. 3.28 (a) and (b) collect the resulting liquid permeability curves for the rammed earth material of house 1 and house 6, respectively. The vapour permeability curves using the capillary pressure as driving potential are included as well. This vapour permeability is calculated using Eq. (2.24) and Eq. (2.11) in combination with Kelvin equation Eq. (2.15):

$$k_v = \frac{\delta_{air}}{\mu}\left(1 - \frac{w}{w_{sat}}\right) p_{v,sat} exp\left(\frac{p_c}{\rho_l R_v T}\right) \frac{1}{\rho_l R_v T} \tag{3.27}$$

k_v vapour permeability, with capillary pressure as driving potential s

δ_{air}	vapour permeability of air, 1.9 x 10^{-10} s at 20 °C and sea level pressure		s
μ	vapour resistance factor (from dry cup test)		-
w	moisture content		kg/m³
w_{sat}	vacuum saturation moisture content		kg/m³
$p_{v,sat}$	saturation vapour pressure		Pa
p_c	capillary pressure		Pa
ρ_l	liquid water density	1000	kg/m³
R_v	specific gas constant of water vapour	461.52	J/(kg K)
T	temperature		K

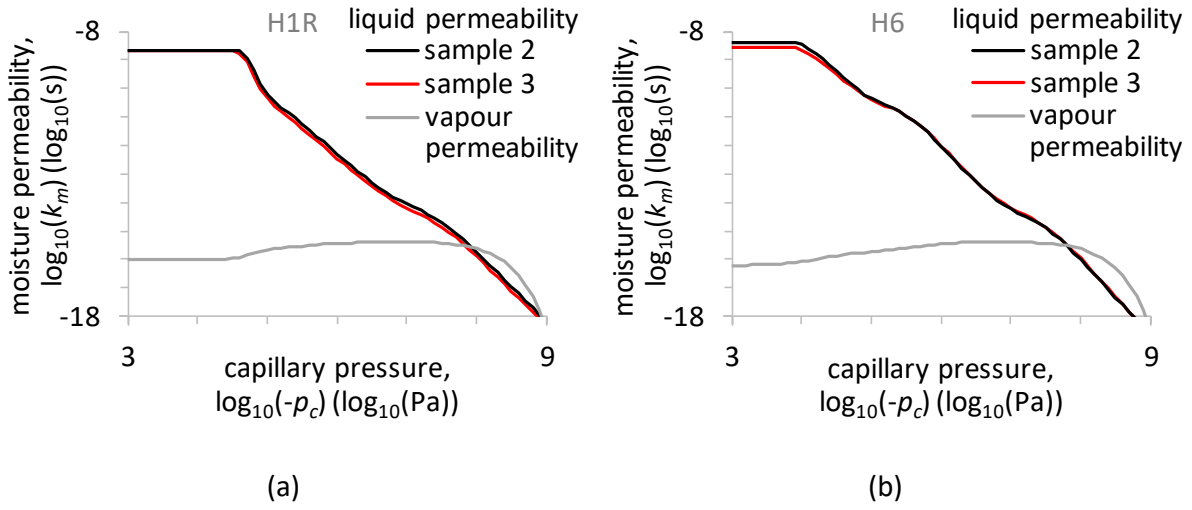

(a) (b)

Fig. 3.28: Liquid permeability and vapour permeability (a) for H1 rammed earth samples and (b) for H6 rammed earth samples.

Fig. 3.29 shows, (a) for the H1 rammed earth and (b) for the H6 rammed earth, the moisture permeability curve as the sum of the liquid- and the vapour permeability to enable comparison with the cup test results that are included as well. It is observed that the results are not identical, particularly for the intermediate and wet cup: the obtained moisture permeability is usually above the permeability from the cup tests. The moisture permeability is not adjusted though in the present work.

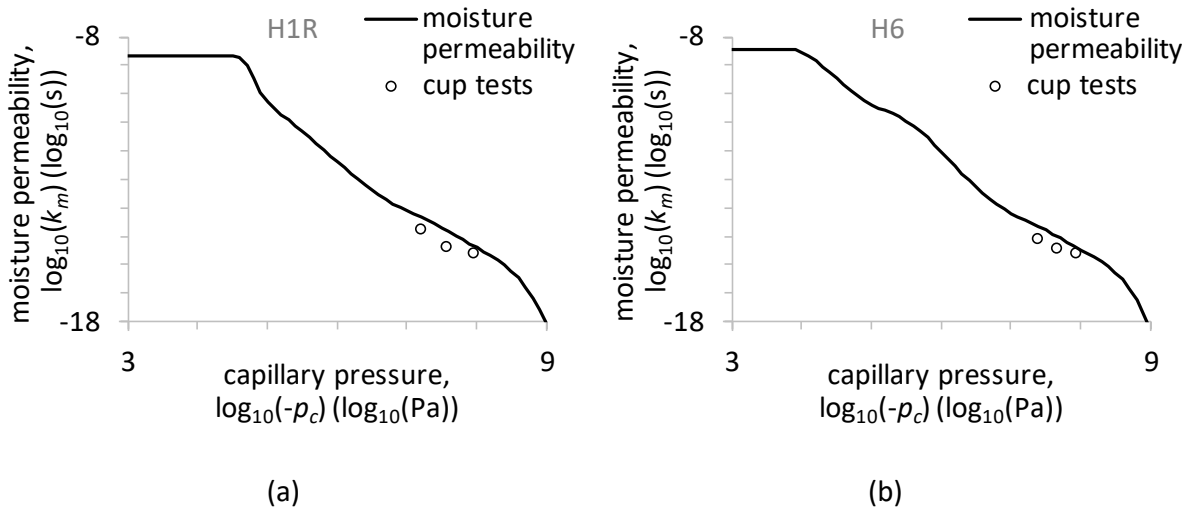

Fig. 3.29: Moisture permeability (a) for H1 rammed earth and (b) for H6 rammed earth.

Fig. 3.30 shows the average liquid permeability of the duplicate samples and the vapour permeability for the H1 rammed earth and for the H6 rammed earth. The characteristic profile from a simulation with these properties falls in between the characteristic profiles of the duplicate samples for both materials. The target characterisation is hereby completed.

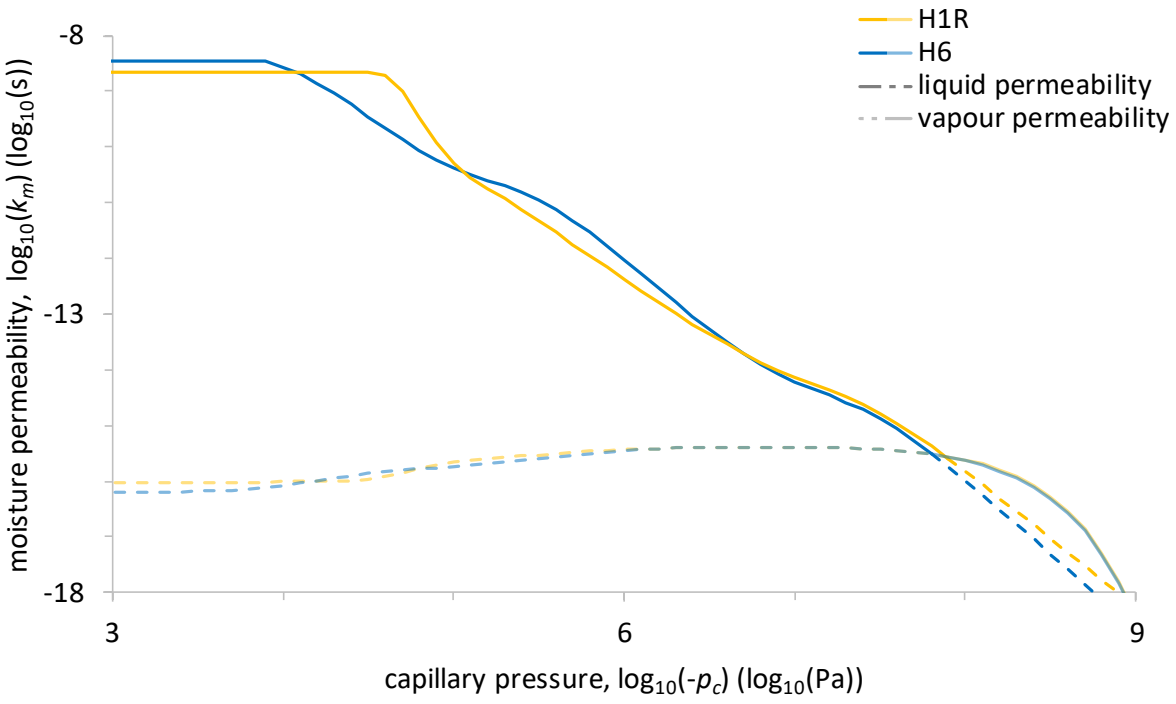

Fig. 3.30: Moisture permeability of rammed earth target materials H1 and H6.

3.4.4.4 Conclusion

The modified capillary absorption test under the X-ray with the adapted Boltzmann transformation results in a reliable moisture permeability in the high range. To which extent this is sufficient to determine the complete moisture transport behaviour that is representative for the material, could be verified by means of additional tests (e.g. isothermal drying, partial capillary absorption).

3.5 Conclusion

The complete hygric characterisation is performed for two different rammed earth materials. Their moisture retention curve is determined by means of a combination of desiccator testing and mercury intrusion porosimetry. Comparison of the mercury intrusion porosimetry with measurements in absorption showed that ink-bottle effects are negligible, whence the mercury intrusion porosimetry result is interpreted as the proper moisture storage capacity. For the main wetting curve, the mercury intrusion porosimetry result is cut off at the capillary moisture content.

The vapour permeability of the rammed earth materials is determined according to the standard cup test method. Their liquid permeability curve is obtained from the moisture diffusivity determined through the redeveloped capillary absorption test for rammed earth materials with X-ray radiography. Herein, the capillary absorption test set-up is modified in two ways: a thin brick wick and filter paper are introduced and a confining sealing is utilised. The Boltzmann transformation method is adjusted for the impact of the wick and paper through their equivalent height in the capillary absorption.

4 Performance indicators

4.1 Introduction

The destruction of rammed earth buildings consequent to interior insulation is the biggest concern in retrofit actions. Despite this, no performance criteria have yet been developed for this that can be applied in the hygrothermal performance analysis.

The objective is thus to develop a series of mechanical performance indicators that cover the mechanical risks involved in the interior insulation of rammed earth walls.

Existing damage cases are studies for this, to come to a selection of the most relevant failure mechanisms. These are then developed into indicators, similarly as thermal and hygric.

4.2 Indicator development

4.2.1 Overall strength and stiffness

With increasing moisture content, materials swell, and their strength and stiffness decrease. This is especially pronounced for clay-bound materials, such as rammed earth (Gallipoli et al., 2022); (Brinkmann & Wiehle, 2023). The relevance and significance of this hygromechanical aspect in the hygrothermal performance analysis of rammed earth walls is reflected by the numerous severe moisture/stability failure events seen in practice, Fig. 1.2, Fig. 4.1 (Morris, 2012). In (Scarato, 2014), it is estimated that more than a thousand rammed earth building walls disappear per year in the Rhône-Alpes Region, of which the main cause is typically rising damp in that region. In the present work, it is assumed that rising damp is by all means excluded and it is investigated how under these conditions the addition of interior insulation could still induce structural damage risks.

2013 inhabited 2018 declared uninhabitable '19 collapse-ready

(a)

(b) (c) (d)

Fig. 4.1: Damage cases under mechanical load and/or moisture, with following presumable explanations: (a) becoming uninhabitable by structural deterioration consequent to interior water leak and/or rising damp; (b) compression failures along façade; (c) damage consequent to rising damp and/or bending plus roof water leak and/or differential settlements; (d) buckling end elevation on low stem wall.

A building construction element needs to be sufficiently strong and stiff to bear its mechanical load. Rammed earth materials typically having superior strength in compression (yet still poor compared to other building materials) and poor strength in tension and shear, a well-designed rammed earth mass walling element is primarily loaded in compression (Maniatidis & Walker, 2003). To evaluate its overall mechanical performance hence, the relative fracture stress and the relative buckling stress need to be monitored, of which the maxima are determined by the compressive strength and the bending stiffness, wall fixings and height, wall loading form, and Poisson's ratio, respectively (and which are influenced by the moisture content or capillary pressure).

The normal stresses by compression are the greatest at the bottom of a rammed earth wall. Their magnitude is estimated on the basis of an exemplary building geometry with prescribed additional mechanical loads, Fig. 4.2 (a).

The geometry considered (Maniatidis & Walker, 2003); (Livradois-Forez, 2011); (Genis, 2018); (Morris, 2012) is a rammed earth house of 6 m by 6 m floor plan. The rammed earth walls are 6.5 m high. The walls are built on the foundation's stem wall that extends 0.6 m above the exterior cleared ground level. Two stories are present besides the ground floor: the first floor and the attic floor. The rammed earth wall material is considered homogeneous with a bulk density of 1850 kg/m³. It is for simplicity assumed that the moisture content is already included in this value, and this with a uniform distribution. The walls are 0.5 m thick and this constantly, for simplicity; in practice, the thickness may vary from ca. 0.4 m at the top to ca. 0.65 m at the bottom. The first

and attic floor and the pitched roof are constructions of wood with a bulk density of 500 kg/m³. The floor beams have a section of 0.4 m x 0.1 m and a center-to-center distance of 0.6 m. It is assumed that a soundproofing floor is applied (Reppel b.v., 2020) for acoustical comfort. The roof beams have a section of 0.225 m x 0.075 m. Three trusses are present: one in the middle of the building and one of half section at each end elevation. The rafters on the purlins have a center-to-center distance of 0.6 m. It is assumed that the roof is already thermally insulated (not drawn). Ceramic roof tiles are applied (WTCB, 2001). The roof overhang is 0.5 m (protects upper wall part).

The mechanical loads considered (CSTS EN 1991-1-1, 2015) are only the vertical loads (so snow and vertical use besides self-weight, but no wind load e.g.). Fig. 4.2 (b) shows the structural model under the symmetric loading. A clamped boundary is considered since any rotation at the bottom surface is limited as the rammed earth wall is 0.5 m wide. Fig. 4.2 (c) shows the free body diagram of the structure, with simplified equivalent roof construction, used to calculate first the (internal and external) reaction forces and next the section forces in the rammed earth wall. Fig. 4.2 (d) shows the result of the normal force along the rammed earth wall height. The compressive normal stress in the rammed earth wall at its bottom amounts to 0.171 MPa, using the wall section surface area of 0.5 m by 6.5 m, 69% of which is its self-weight.

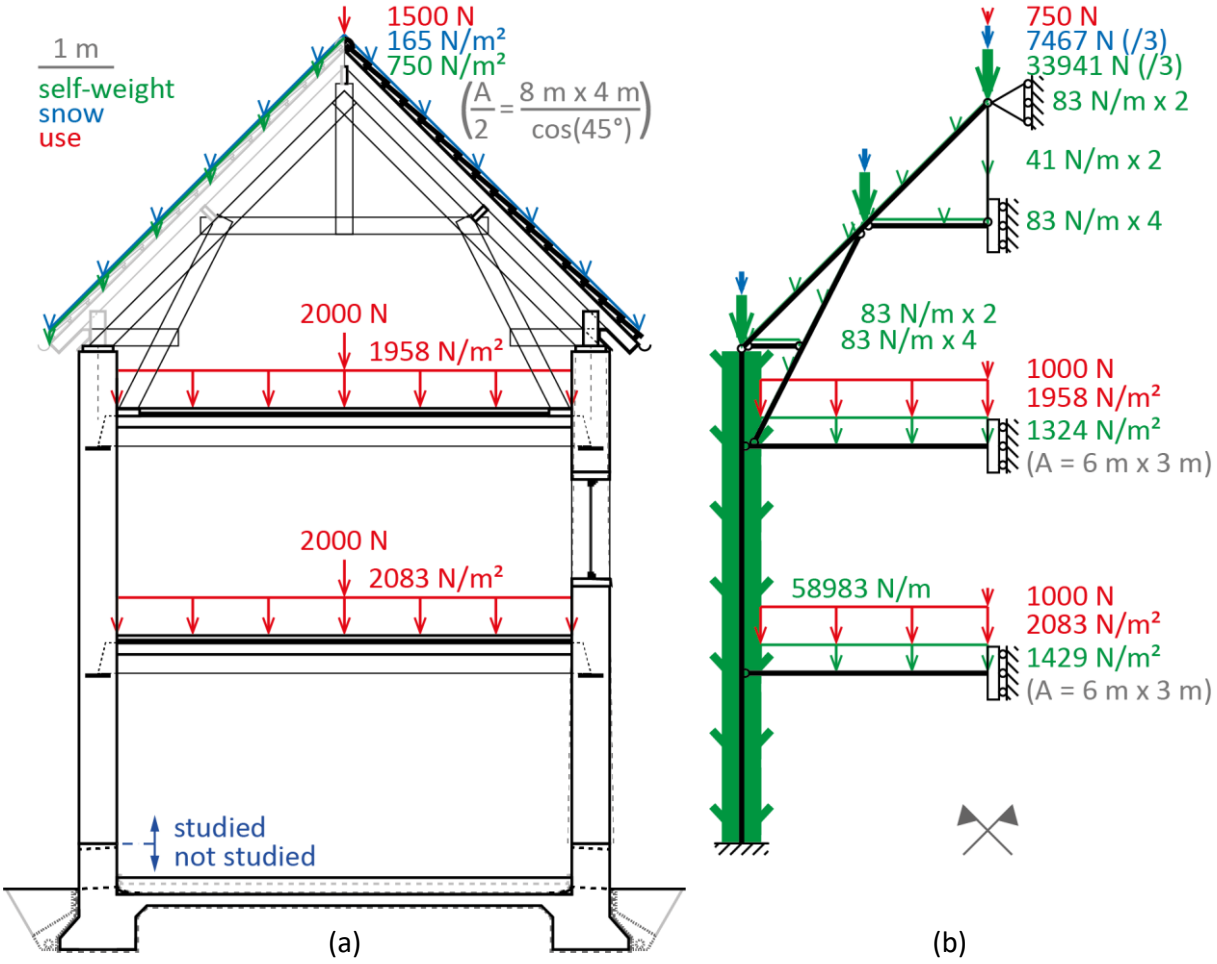

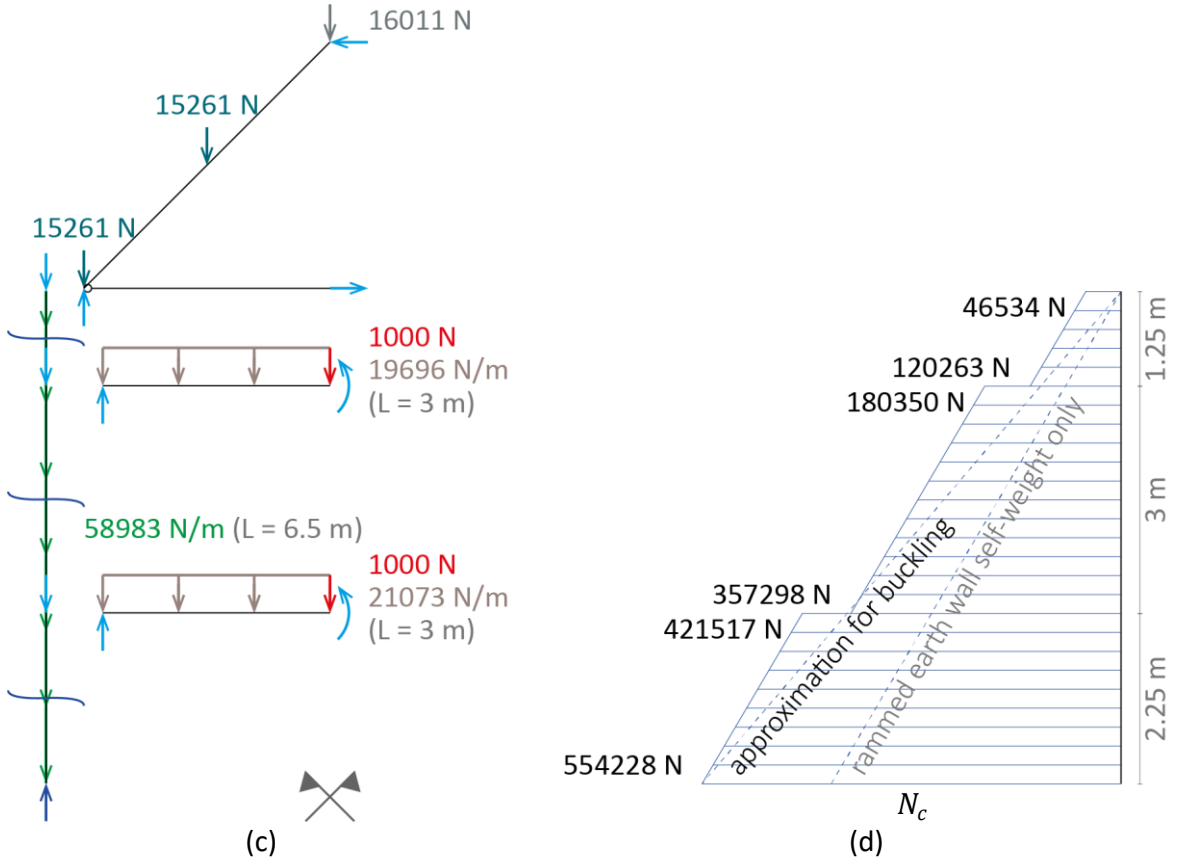

Fig. 4.2: Rammed earth (a) construction; (b) model; (c) free body diagram; (d) wall normal force.

Besides this structural mechanical load, normal stresses of hygric origin add when the associated movement is hindered, Eq. (4.1). In the present work, it is assumed that all expansion relative to the transient stability equilibrium state at the average relative humidity or capillary pressure of the wall is fully suppressed in the height and width direction (Gonzalez & Scherer, 2004); (Scherer, 2006); (TERA, 2018). The magnitude of the hygric stress is estimated in Section 4.2.2: through Hooke's law, it is related to the associated deformation via the stiffness modulus and the Poisson's ratio. The example of the hygric stress for the H1 material as a function of the capillary pressure using the average relative humidity in the non-insulated wall over the year as reference (cf. Fig. 4.7) is also included in Fig. 4.3 (a). Thermal stresses are not investigated in the present work.

$$\sigma = \sigma_c + \sigma_{hygric} \; (+\sigma_{thermal}) \tag{4.1}$$

σ_c compressive stress, from self-weight and external structural mechanical loads Pa

Fig. 4.3 (a-c) show the compressive strength, the stiffness modulus, and the Poisson's ratio of a few rammed earth materials as a function of the logarithmic capillary pressure. Two effects are at play in the decrease of the strength and the stiffness from dry to wet conditions. The first, suction

(or capillary) effect is similar as for other porous building materials (Carmeliet & Van Den Abeele, 2004). The second, clay swelling, additionally contributes significantly herein as follows: the more water molecules penetrate in and between the clay particles, the smaller the cohesion of the material (Scherer, 2006). The electrostatic weakening and expansion of the clay is directly translated into softening of the rammed earth material. It is assumed that the reduced strength and stiffness of wetted rammed earth is completely reversible in the present work.

The rammed earth material of (El Nabouch, 2017) (Dagneux, France), see Fig. 4.3 (a,b), is the same as the H1 material used in the present work. Based on similarities in composition, moisture retention curve, and mechanical properties (, and also lab connections), it is presumed that the material of (Bui et al., 2014) is also (practically) the same, and these mechanical properties are used further. Bui measured the compressive strength, the stiffness modulus, and the Poisson's ratio by means of unconfined compression tests as a function of the moisture content, as well as the moisture retention curve by means of the filter paper method, in desorption from the manufacturing moisture content.

First however, Bui did not perform an in lab calibration of the filter papers used to measure the capillary pressure curve. In (Abhilash, 2016a), it is shown that this can lead to significant errors (cf. Fig. 2.12) and this is also reflected in Fig. 4.3 (a-c). Herein, the properties as a function of Bui's capillary pressure are shown on the one hand, and on the other the moisture retention curve (MRC) of the H1 material determined in the present work is used to get Bui's results as a function of the correct intended capillary pressure. It is found that a polynomial function fits closely the resultant data set. Due to the lack of measurement data near capillary saturation, for the compressive strength and the stiffness modulus, another polynomial function is used in that range to form the connection with the estimated constant property values at capillary saturation. The value of the compressive strength at capillary saturation is estimated to be 0.0019 MPa based on the observation that a 9.1 cm high sample undergoes some fracture failure at its bottom by the end of an unconfined capillary absorption test. The value of the stiffness modulus at capillary saturation is estimated to be 31.65 MPa through the measured strain, see Fig. 4.6, Eq. (4.8). For the Poisson's ratio, a constant value is used directly to extrapolate towards the higher moisture contents, from a critical point on. Towards the dry state, the properties are extrapolated as a constant from a critical point on for the strength and stiffness, or an inflection point for the Poisson's ratio.

Second however, Bui's published stiffness modulus values represent the secant modulus that is only representative for stresses below 20% of the maximum stress. Beyond that stress level, the stress-strain curve goes from linear elastic regime to increasing elasto-plastic behaviour of the

material. The tangent modulus, which is of interest for a more dependable assessment of the mechanical behaviour (Carmeliet & Van Den Abeele, 2004); (Roels et al., 2006), is estimated starting from the available stress-strain curve of another of Bui's rammed earth materials. Continuing a suggestion in Bui's publication, it is found that the following six-point scheme fits the curve closely: secant modulus at 20% of the maximum stress, 20% reduced secant modulus at 40% of the maximum stress, 40% reduced secant modulus at 60% of the maximum stress, and so on. The same scheme is applied to reconstruct the presumed stress-strain curve of the H1 material, and this for each capillary pressure at which the secant modulus is measured (the exact corresponding maximum stress at the same capillary pressure is calculated by means of the determined expression Fig. 4.3 (a)). The result (not shown) is in reasonable agreement with the stress-strain curve of (Abhilash, 2016a) and (Al Haffar, 2017) for the H1 material. Subsequently, the Ramberg-Osgood relation with the Hollomon parameters is used to fit each curve and hence determine the strength coefficient (K_1, Pa) and the inverse of the strain hardening coefficient ($K_2(=1/k_2)$, -) as a function of the log capillary pressure. These parameter functions are next fitted linearly: y=0.459x and y=-0.067x+5.692, respectively. And hence, the inverse of the derivative of the Ramberg-Osgood relation gives the tangent modulus as a function of the capillary pressure and the stress, Eq. (4.2). By using the hygric (rather than the total) stress herein, the tangent modulus becomes exclusively a function of the capillary pressure (and not of the wall height e.g.). The hygric stress and the tangent modulus are determined together in Section 4.2.2. The tangent modulus resulting is shown in Fig. 4.3 (b).

$$E_{(tangent)} = (d\varepsilon/d\sigma)^{-1} = \left(1/E_{secant} + K_2 {\sigma_{hygric}}^{K_2-1}/{K_1}^{K_2}\right)^{-1} \quad (4.2)$$

E	stiffness modulus	Pa
ε	strain	m/m
$K_{1/2}$	fitting parameters	

Additionally, a second rammed earth material is illustratively included in Fig. 4.3 (a,b): that of (Gerard et al., 2015) and (François et al., 2017) (Marche-Les-Dames, Belgium), of which a rather complete mechanical characterisation is available as well. However, all the signs are that the filter papers used to measure the capillary pressure at the manufacturing moisture content were not calibrated in the lab again. Besides, also a higher moisture content was addressed, however, an arbitrary suction was assigned to this point. The stiffness modulus measured at this higher moisture content was not published owing to plastic behaviour of the specimens. Resultantly, only reliable data in the hygroscopic range remain. Only the influence of the bulk density on the

compressive strength (Gerard et al., 2015) is hence still discussed here. It appears that the greater bulk density yields, besides a greater compressive strength, a steeper decrease of the strength with increasing moisture content, which can probably be linked to a greater swelling. The bulk densities of the other materials are for information also mentioned in Fig. 4.3 (a).

While the compressive strength can be used directly for fracture, the stiffness modulus, as well as the Poisson's ratio and the hygric strain via the hygric stress, is used to determine the buckling strength as per Eq. (4.3). This equation is based on Euler's critical load formula. The full wall height is used herein for the worst-case buckling scenario (intermediate floor supports are disregarded, like is the case for an end elevation), and unsupported sides are considered. A factor $1/\sqrt{2}$ is present for the effective length with fixed-pinned ends. As compared to the basic formula of Euler's critical load for buckling of a column under a concentrated concentric axial load, a factor $(1-\nu^2)$ is additionally present for a wall (with similar width and height dimensions) because its strain is zero in the width-direction and consequently also smaller in the height-direction (Rees, 2009); (Bulson, 1970). Besides and more importantly, a factor that varies between 1 for a point load and 5.32 for a uniform distributed load for the clamped-hinged case appears in the formula (Girgin & Girgin, 2011); (Teifouet et al., 2017); (Teifouet et al., 2019). The linear structural normal force approximation implied is shown in Fig. 4.2 (d). The section's average total normal stress at the wall bottom should be compared with the buckling strength. Fig. 4.3 (d) illustratively shows the buckling strength for a uniformly distributed moisture content over the wall section as a function of the capillary pressure. The first curve utilises a zero hygric stress, so a uniform distributed load only, leading to the maximum buckling strength. The second curve utilises the exemplary hygric stress relative to the average relative humidity in the non-insulated H1 wall over the year.

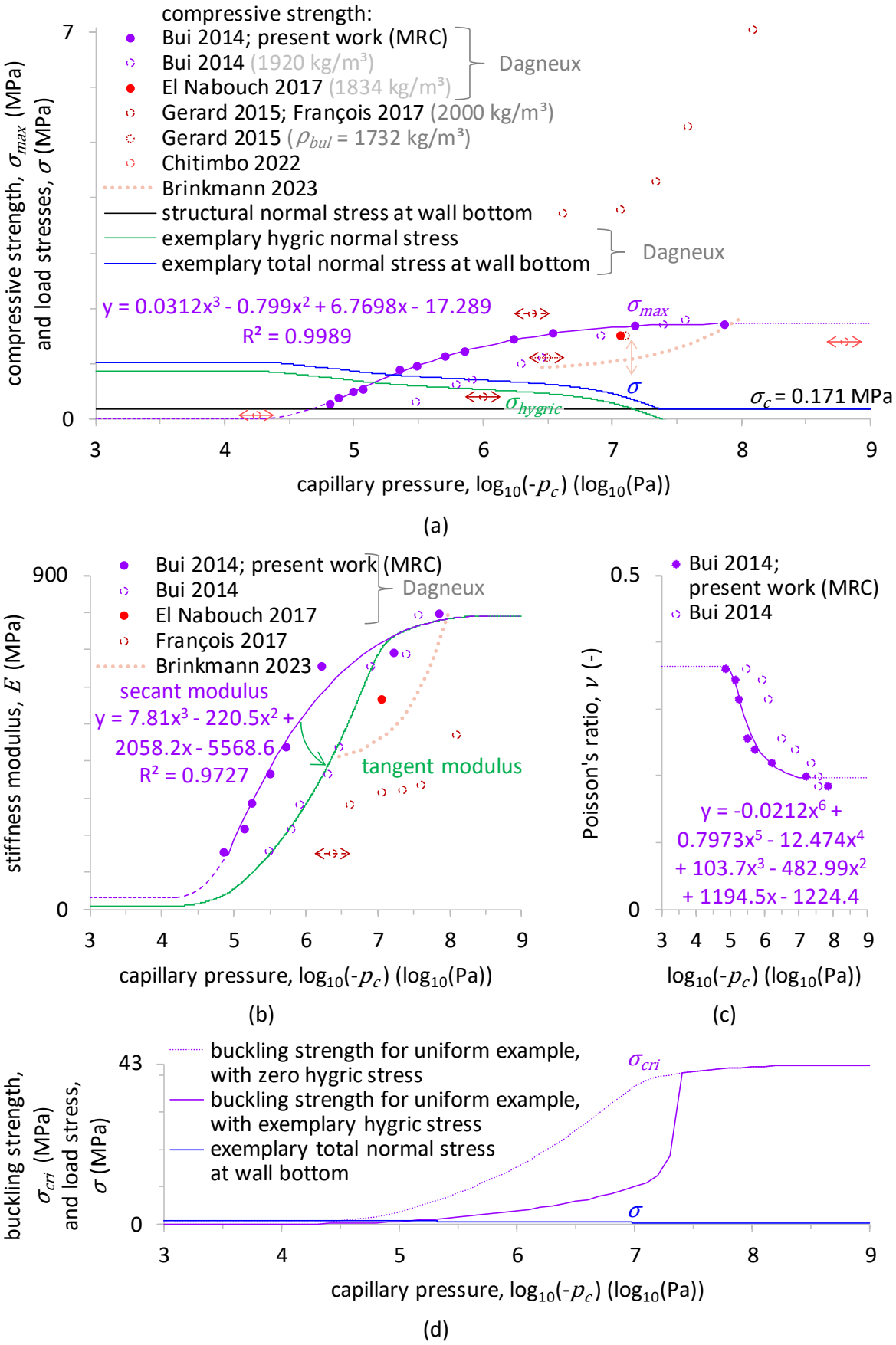

Fig. 4.3: Rammed earth (a) compressive strength and load stresses; (b) stiffness modulus; (c) Poisson's ratio; (d) buckling strength for uniform example; as a function of capillary pressure.

$$\sigma_{cri} = \frac{N_{cri}}{bh} = \frac{5.32 \times \pi^2 E_{avg} I}{\left(1 + 4.32 \times \frac{N_{hygric,avg}}{N_c + N_{hygric,avg}}\right)\left(1 - {\nu_{avg}}^2\right)\left(L/\sqrt{2}\right)^2 bh} = \frac{52.504 \times E_{avg} bh^3}{\left(1 + 4.32 \times \frac{\sigma_{hygric,avg} bh}{N_c + \sigma_{hygric,avg} bh}\right)\left(1 - {\nu_{avg}}^2\right)\left(L/\sqrt{2}\right)^2 bh \times 12} \quad (4.3)$$

σ_{cri}	buckling strength	Pa
N_{cri}	critical buckling normal force (always evaluated at wall bottom)	N
b	wall width	m
h	wall thickness	m
I	area moment of inertia	m^4
ν	Poisson's ratio	-
L	wall height	m
$_{avg}$	average over wall section	

The risk on structural failure by compression fracture is indicated by the load-bearing section loss S (%), of which the determination method is illustrated in Fig. 4.4. This failure mechanism is evaluated at the bottom of the rammed earth wall, since this is where the greatest compressive stresses are expected to occur and the mechanical resistance thus to be lost first and foremost. Using the total normal stress at the wall bottom and the compressive strength that vary with the moisture content profile, the relative stress profile is determined, Eq. (4.4) for each position i in the wall along its thickness. Where the relative stress equals or exceeds unity, the section is presumed to become non-load-bearing by fracture failure and the stress is set to zero. The structural compressive mechanical load is for simplicity not subsequently redistributed over the remaining reduced wall section surface area, and so the relative stress profile is also not further updated accordingly. The load-bearing section loss is hence determined, Eq. (4.5), and its maximum value over the simulation period is retained as the fracture risk.

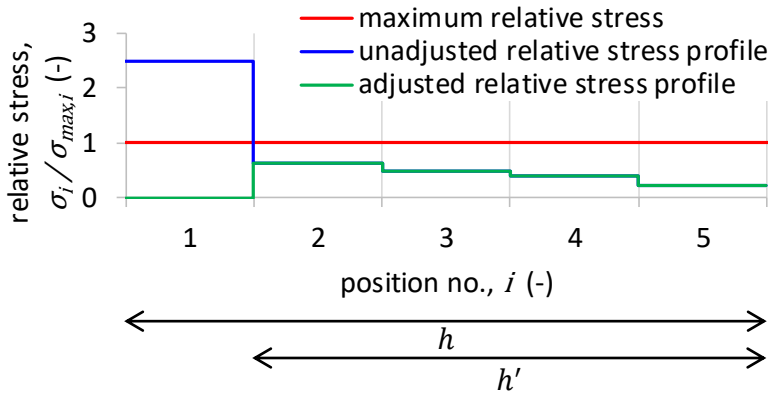

Fig. 4.4: Illustration of relative stress profile for fracture and load-bearing section loss, with coarse grid.

$$1 > \frac{\sigma_i}{\sigma_{max,i}} = \frac{\sigma_c + \sigma_{hygric,i}}{\sigma_{max,i}} = \frac{N_c/A + \sigma_{hygric,i}}{\sigma_{max,i}} = \frac{N_c/(bh) + \sigma_{hygric,i}}{\sigma_{max,i}} \tag{4.4}$$

$$S = (A - A')/A \times 100 = (h - h')/h \times 100 \tag{4.5}$$

σ_{max}	compressive strength	Pa
S	load-bearing section loss	%
A	(original) wall section surface area	m²
A'	remaining load-bearing wall section surface area	m²
$_i$	position no.	

The risk on buckling failure is indicated by the relative buckling stress B (%), Eq. (4.6). The average total normal stress at the wall bottom is used in the numerator, the buckling strength Eq. (4.3) in the denominator, and the fracture failure is taken into account in a simplified way (‘). The maximum value of the relative buckling stress over the simulation period is retained as the buckling risk.

$$\begin{aligned} B = \frac{\sigma'}{\sigma_{cri}'} \times 100 &= \frac{\sigma_c' + \sigma_{hygric,avg}'}{\frac{5.32 \times \pi^2 E_{avg}' bh'^3}{\left(1 + 4.32 \times \frac{N_{hygric,avg}'}{N_c + N_{hygric,avg}'}\right)\left(1 - \nu_{avg}'^2\right)\left(L/\sqrt{2}\right)^2 bh' \times 12}} \times 100 \\ &= \frac{N_c/A' + \sum_{i=1}^{n'} \sigma_{hygric,i}/n'}{\frac{5.32 \times \pi^2 E_{avg}' bh'^3}{\left(1 + 4.32 \times \frac{\sigma_{hygric,avg}' A'}{N_c + \sigma_{hygric,avg}' A'}\right)\left(1 - \nu_{avg}'^2\right)\left(L/\sqrt{2}\right)^2 bh' \times 12}} \times 100 \\ &= \frac{N_c/(bh') + \sum_{i=1}^{n'} \sigma_{hygric,i}/n'}{\frac{5.32 \times \pi^2 E_{avg}' bh'^3}{\left(1 + 4.32 \times \frac{\sum_{i=1}^{n'} \sigma_{hygric,i}/n'\, bh'}{N_c + \sum_{i=1}^{n'} \sigma_{hygric,i}/n'\, bh'}\right)\left(1 - \nu_{avg}'^2\right)\left(L/\sqrt{2}\right)^2 bh' \times 12}} \\ &\times 100 \end{aligned} \tag{4.6}$$

B	relative buckling stress	%

4.2.2 Differential hygrothermal stresses and strains and clay swelling damage

Temperature and humidity differences (gradients and fluctuations) in building components cause working of the materials. The wanted but restricted differential movement of adjacent connected layers or parts causes stresses that can lead to damage in the form of cracks. All the four examples of hygrothermal stresses and strains damage pattern mechanisms shown in Fig. 4.5 can invigorate upon interior insulation. Since while the wall was equally exposed to the exterior and the milder interior conditions before the retrofit, it becomes more isolated from the interior climate and so more heavily hygrothermally loaded by the harsher exterior climate. Moreover, interstitial condensation can add. Only the third mechanism (c) is studied in the present work, that is the hygric clay swelling damage by repeated shear that can be (and is presumed to be in the picture) followed by buckling of a surface layer of the rammed earth wall (Wangler & Scherer, 2009); (Gallipoli et al., 2022).

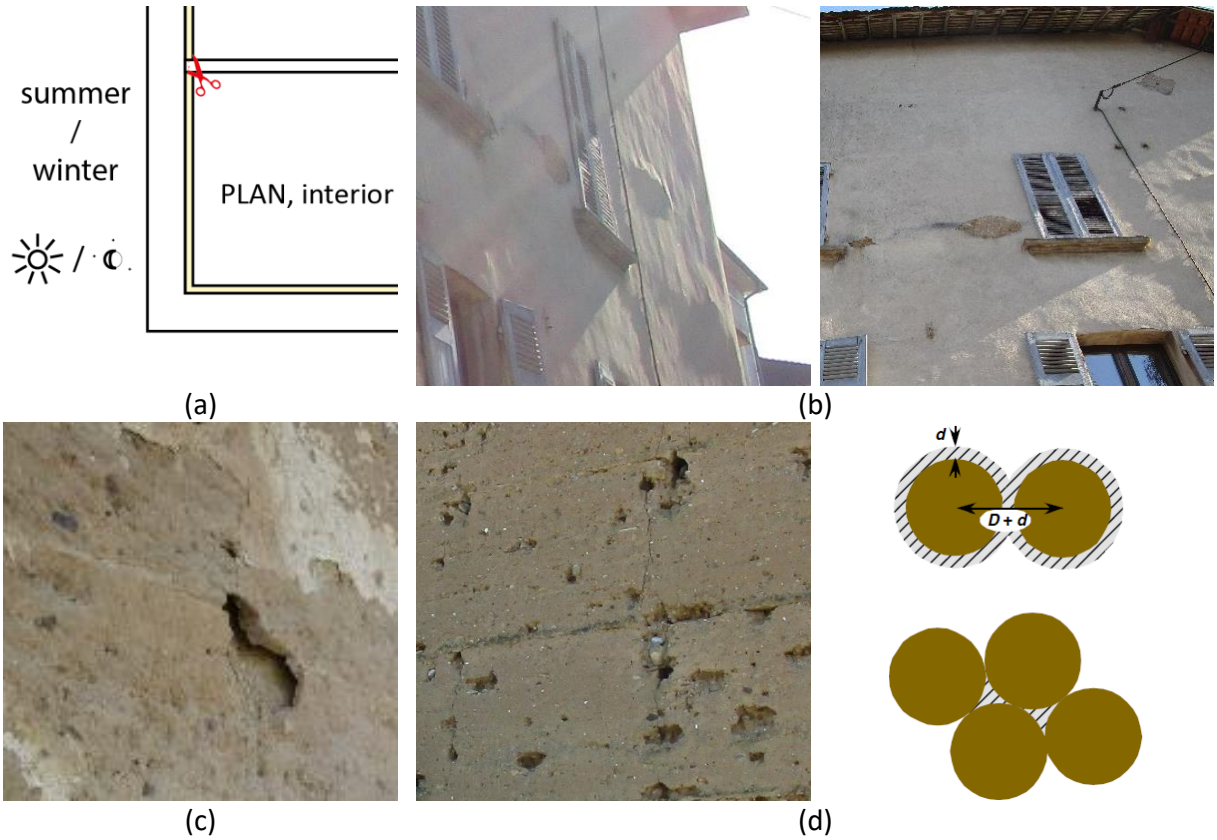

Fig. 4.5: (a) Thermal working of load-bearing construction and its tearing off and down; (b) differential working of rammed earth wall and plaster layer upon (hygro)thermal loading, delamination and cracking of plaster, wind-driven rain water infiltration, and blistering and bursting of plaster and increased hygric loading of rammed earth surface; (c) clay swelling and shear and buckling; (d) local out-of-plane or microscopic clay swelling damage (Scherer, 2006).

Hygrothermal stresses and strains should be limited in such a way that the consequential damage in the form of cracking does not affect the functions of envelope parts or the looks of finishing layers. Hygric shear and buckling clay swelling damage to a wall such as in Fig. 4.5 (c) should hence be avoided for the following reasons explained in more detail.

Even if only the shear failure occurs, the wall performance is already strongly affected. A detrimental capillary break that interrupts the hydraulic continuity is created within the massive wall by the shear crack. Moisture redistribution by conduction towards the underlying bulk material is hereby disabled, which leads for the delaminated surface layer to a more heavy hygric loading, higher moisture contents, and a sooner reaching of saturation storage capacity. At the exterior surface, the risks on forms of moisture damage such as rot of wooden lintels, buckling of the surface layer, frost damage, and erosion are consequently invigorated; this latter moreover by an increased amount of wind-driven rain water runoff upon capillary saturation. The increased moisture content of the interior surface layer from interstitial condensation when interior insulation is applied, invigorates the risks on reduced insulation quality, mould growth, wooden floor beam rot, and fracture failure of the surface layer.

If moreover buckling occurs of the exterior surface layer, with detachment of the buckled material, the appearance is additionally disturbed and the function even more as well, as following. The excess wind-driven rain that drains as runoff over the exterior surface can reach the wall internally through the hole and e.g. run off at the interior surface of the exterior surface layer. The bulk wall can hence become more hygric loaded as well. This water penetration in combination with the reduced drying ability and the reduced wall thickness (by the shear failure already) lead to increased risks on structural buckling failure and fracture failure (Section 4.2.1).

The cracks whereby the wall is hydraulically as well as mechanically no longer a whole in which the clay swelling damage by buckling to a wall originates, can be caused in several ways. First example, shear failure cracks caused by differential hygric normal stresses by moisture gradients. As long as no fracture failure is reached, the hindered expansion during moistening increases the compressive stress. The difference in normal stress between two adjacent material cells generates shear. In this way, the swelling pressure can induce fatigue shear damage (Scherer & Gonzalez, 2005); (Gonzalez et al., 2008), also already at low moisture contents (see Fig. 4.7). Second, shear failure cracks caused by differential normal stresses by fracture failure. Upon wetting, consequent to fracture failure at the bottom of the wall with less than 100% reduced section, shear stresses develop in a plane at the maximum depth of the fracture failure in the wall starting at the bottom because the normal stresses are reduced to zero at the failed bottom section. When the wall redries and the fracture failure disappears, the concerned section becomes also load-bearing

again. In this way, after a few times, shear failure can be developed and subsequently buckling of the separated layer can make an appearance. And third, yet further not considered in the present work, buried flaws, e.g. caused by frost (Appendix B) or salt (Scherer, 2006).

The magnitude of the swelling pressure is estimated by means of Hooke's law under equibiaxial plane stress conditions considering the hygric load only Eq. (4.7). In the lab, this formula holds e.g. for the maximum stress that occurs when the swelling layer is very thin relative to the sample thickness, so that its expansion is completely suppressed by the bulk material that determines the actual strain (Gonzalez & Scherer, 2004); (Moonen & Wangler, 2015); (Livermore, 2007). In building practice, the actual hygric equibiaxial plane strain is supposed to be determined by the average relative humidity state of the wall (cf. Section 4.2.1). Besides, compressive stresses only are considered in the present work; tensile stresses are disregarded and set to zero. All remaining (compressive) stresses are hence made positive for simplicity. The subscript 'free' of the hygric strain is further left behind as well.

$$\sigma_{hygric} = \frac{E\left(\varepsilon_{actual} - \varepsilon_{(free)}\right)}{1-\nu} \approx \frac{E\left(\varepsilon_{p_{c,avg}} - \varepsilon_{(free)}\right)}{1-\nu} \overset{compression\ only}{=} \left|\min\left(0; \frac{E\left(\varepsilon_{p_{c,avg}} - \varepsilon_{(free)}\right)}{1-\nu}\right)\right| \tag{4.7}$$

E	stiffness modulus (of wet material part)	Pa
ν	Poisson's ratio (for wet material)	-
ε	one-dimensional (free swelling) strain	m/m

Fig. 4.6 shows the one-dimensional free swelling strain defined with reference to the oven dry state (consistently with all other hygric properties) of two rammed earth materials. In the present work, this reference oven (70°C) dry state (Section 3.2.2) is presumed to be at a relative humidity of 0.939% ≈ 1% (Feng et al., 2013) which corresponds to a capillary pressure of - $10^{8.8}$ Pa = - 630957344 Pa (Section 3.3). The hygric strain of (Gerard et al., 2015) is hence recalculated using linear extrapolation - entirely hypothetical - as a function of the logarithmic capillary pressure between the two lowest points towards zero strain. Besides, a few points are included of the H1 material in the present work based on measurements in the hygroscopic (by means of laser scanning during the psychrometer test, Section 3.3.2) and in the capillary range (Section 3.2.4). The lowest point corresponds to the oven dry state; the second lowest is at 96.4% relative humidity. The second highest point is the average expansion at the moment the water front

reaches the sample top during an unconfined capillary absorption test. Immediately upon this, a swell boom occurs, which comes to rest at the highest point. The capillary pressures of these two high points are estimated with respect to the moisture retention curve.

To determine a somewhat physically dependable course of the hygric strain curve for the H1 material based on these limited data available, the formula of the poroelastic concept is used for the hygric stress in Eq. (4.8) (Roels et al., 2006). The integral of the moisture saturation curve is calculated manually from the reference oven dry capillary pressure and in small steps of capillary pressure corresponding to 0.001 $\log_{10}$(Pa). The coupling coefficient scaling factor is fitted using the measured data of the second lowest point. Since the stresses are limited during the direct measurement of the free swelling strain concerned, with which stress-free conditions are associated, it is assumed that the use of the secant modulus available is acceptable herein. The resulting curve course assigned is shown in Fig. 4.6. It appears that a constant scaling factor that amounts to 0.055188 gives a reasonable approximation for the whole range. E.g., in (Hens, 2011), it is shown that the increase in hygric strain with increasing humidity is typically greater at lower moisture contents, in the hygroscopic range, and that this derivative stabilises towards zero at capillary saturation. Rammed earth materials usually evolve significantly more above the manufacturing moisture content, of which the capillary pressure is presumed to amount to ca. -$10^{5.3}$ Pa for the H1 material in the present work, which corresponds to 0.1 kg/kg.

$$\varepsilon \overset{(Hooke's\ law)}{=} \frac{\sigma_{hygric}}{E_{secant}} = \frac{-C \int_{p_c} S(p_c) dp_c}{E_{secant}} \tag{4.8}$$

C	Biot's poroelastic coupling coefficient scaling factor	-
S	degree of moisture saturation	kg/kg

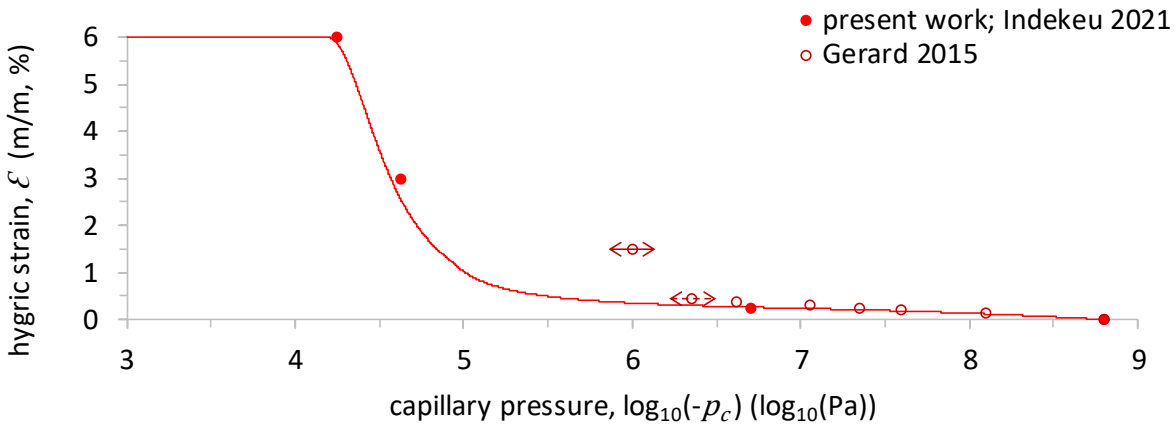

Fig. 4.6: Rammed earth one-dimensional free hygric strain as a function of capillary pressure.

The resulting swelling pressure or hygric stress from Eq. (4.7) is shown in Fig. 4.7 for an example in which the actual strain used corresponds to the average relative humidity in the non-insulated wall over the year ($RH_{avg} = 83.94\%$ or $\log_{10}(-p_{c,avg}) = 7.375$ $\log_{10}$(Pa)). Three variants are included. The first hygric stress curve is still determined by means of the secant modulus. While its order of magnitude is similar as for other examples (Wangler et al., 2012), its course seems to be overestimating at higher moisture contents (Roels et al., 2006); (Gerard et al., 2015) and it gets remarkably great as compared to the compressive strength. The dependency of the stiffness modulus on the relative stress, using the hygric stress only (cf. Section 4.2.1), is addressed to improve this.

The second hygric stress curve hence uses the tangent modulus that is determined by means of Eq. (4.2) Section 4.2.1 from the first positive hygric stress on using small steps of 0.001 $\log_{10}$(Pa) capillary pressure. The next hygric stresses are each step calculated using the previously determined tangent modulus and as the maximum of the actual and the previous hygric stress to avoid oscillations of the tangent modulus and the hygric stress. Once the tangent modulus is fully determined in this way (shown in the figure inset), the hygric stresses are once more recalculated at the fully correct capillary pressures. The resulting hygric stress curve has a more acceptable magnitude but is found to decrease and diminish to zero unreasonably in the higher moisture range. For if one would measure the swelling pressure confined (Madsen & Müller-Vonmoos, 1989) which corresponds more closely to the conditions in practice, the material is not able to expand and soften that much and remains more or less stable whereby the increasing swelling pressure is expected to approach a constant value at higher moisture contents like in the examples from the literature (cf. above).

The third hygric stress curve is hence determined as the maximum of the previous and the actual hygric stress. The tangent modulus is subsequently recalculated once more as well based on this adjusted hygric stress curve, using Eq. (4.7), and the definitively kept property is shown in Fig. 4.3 (b). It is found that the resulting modulus hence decreases less at higher moisture contents, see Fig. 4.7 inset. This trend is also consistent with the acousto-elastic effect (Carmeliet & Van Den Abeele, 2004). Unlike the hygric stress curve, which is recalculated hourly in the simulations according to the transient average relative humidity state, this tangent modulus function is further retained and not recalculated (also for other (insulated) wall configurations that may yield a different yearly average relative humidity). The tangent modulus data are used directly (as a function of the log capillary pressure with an accuracy of 0.001 $\log_{10}$(Pa)), rather than a fitting, to be exact. The resultant swelling stresses have a significant magnitude that can go up to 5 times greater than the structural compressive normal stress at the wall bottom, Fig. 4.8. For the

exemplary hygric stress curve, i.e. relative to the average capillary pressure in the non-insulated H1 wall over the year, the total stress exceeds the compressive strength at a capillary pressure of ca. 5.3 $\log_{10}$(Pa), see Fig. 4.7, which corresponds to the manufacturing moisture content of the H1 rammed earth in the present work. The hygric stresses are already taken into account in Section 4.2.1 besides the structural mechanical loading.

The shear stresses for clay swelling damage are quantified in a simplified way as per Eq. (4.9). Herein, the differential normal stresses are considered per 1 mm thick material layer (rather than per infinitely small volume (Hens, 2011)), which is the minimum grid dimension in the simulation program Delphin used, and the surface area for shear is taken 1 mm high as well. As a result, the shear stress simply equals the difference in normal stress between each incremental position.

$$\tau_{imm} = \tau_{i/i+1} = \frac{\Delta F_{imm}}{A_{shear}} = \frac{\Delta F_{i/i+1}}{0.001m \times b} = \frac{F_i - F_{i+1}}{0.001m \times b} = \frac{\sigma_i A_i - \sigma_{i+1} A_{i(+1)}}{0.001m \times b} = \frac{0.001m \times b \times (\sigma_i - \sigma_{i+1})}{0.001m \times b} = \sigma_i - \sigma_{i+1} \tag{4.9}$$

τ	shear stress	Pa
F	normal force	N
A	surface area	m²
b	wall width	m
σ	normal stress	Pa
$_i$	depth from exterior to interior surface or position no.	mm or -

The shear strength of the H1 material in monolithic form is measured by (El Nabouch, 2017); the result of her shear box test is included in Fig. 4.7. In accordance with the conditions in practice for clay swelling damage, this is the shear strength with zero normal stress on the failure plane and thus simply the cohesion of the Mohr-Coulomb equation, Eq. (4.10). In absence of experimental data, the shear strength of rammed earth is usually approximated as a constant fraction of the compressive strength (NZS 4297:1998). The used factor 0.1 for this is of typical magnitude (T. T. Bui et al., 2014) and the resulting curve fits the measured data point closely.

$$\tau_{max} \overset{(Mohr-Coulomb\ equation)}{=} c + \sigma_z \tan\varphi \overset{if\ \sigma_z=0}{=} c \approx 0.1 \times \sigma_{max} \tag{4.10}$$

τ_{max}	shear strength	Pa

c	cohesion or cohesive strength	Pa
σ_z	normal stress on failure plane	Pa
φ	internal friction angle	°
σ_{max}	compressive strength	Pa

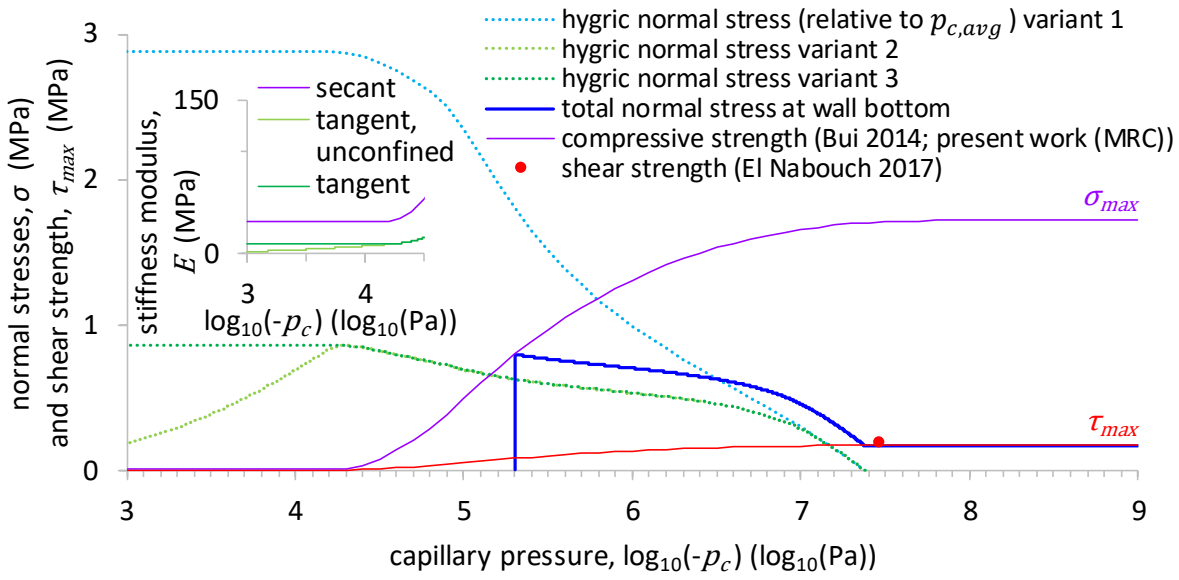

Fig. 4.7: Rammed earth hygric normal stress component (two trials and third one definitive), total normal stress at wall bottom, and shear strength as a function of capillary pressure.

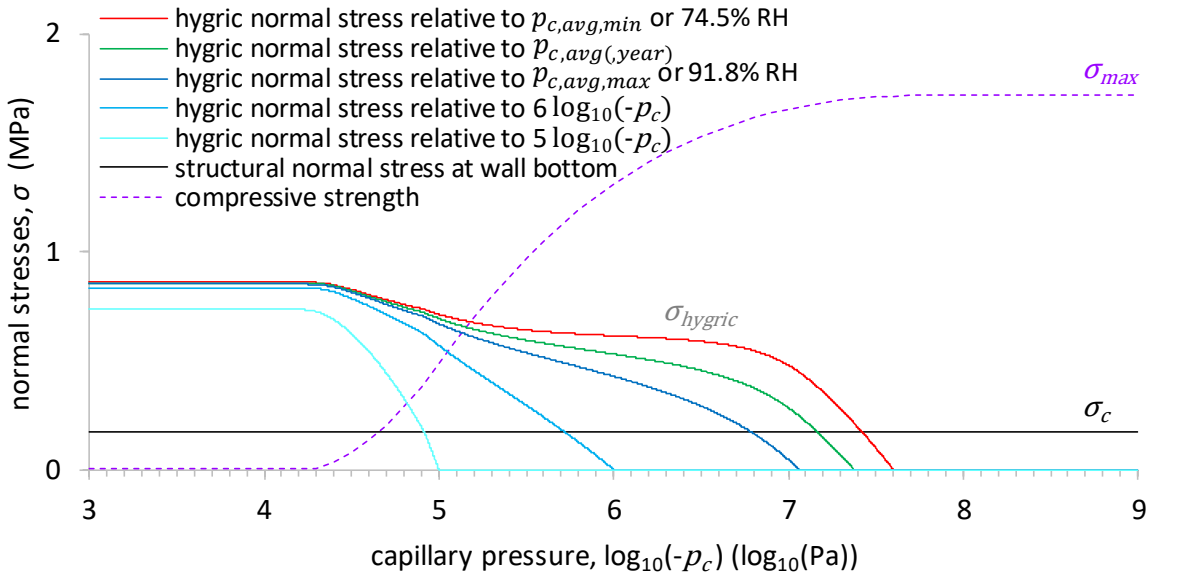

Fig. 4.8: Hygric stress curve examples.

The risk on clay swelling damage is indicated by the number of swelling cycles, which is determined at each position along the thickness (mm) in the wall at the bottom by the number of times that

the absolute value of the shear stress equals or exceeds the shear strength, Eq. (4.11), and the shear stress is positive for the exterior surface or negative for the interior surface or fracture failure occurs. A current swelling cycle ends when the absolute value of the shear stress rebecomes smaller than the shear strength or the shear stress becomes negative for the exterior surface or positive for the interior surface and this is not caused by fracture failure. The greatest number of swelling cycles at a certain depth is counted separately at the exterior surface of the wall (or rather, the outer half) and at the interior surface (inner wall half). It is checked which share of the number of clay swelling cycles is caused by fracture failure or by excessive wetting moisture gradients.

$$1 \leq \frac{|\tau_{imm}|}{\tau_{max,imm}} = \frac{|\sigma_i - \sigma_{i+1}|}{0.1 \times \frac{\sigma_{max,i} + \sigma_{max,i+1}}{2}} \tag{4.11}$$

4.2.3 Erosion

Erosion by intense wind-driven rains is a destructive natural action most specific to rammed earth elements, Fig. 4.9. In turn, typical architectural details to protect the traditional rammed earth construction against this erosion are relatively great sloped roof module heights (wind-blocking effect) and relatively great roof overhang lengths (shelter effect) (Blocken & Carmeliet, 2002); (Bui et al., 2009); (Mohaddes et al., 2014), as well as integrated (sand-/trass-lime mortar) erosion breaks (Livradois-Forez, 2011); (Rauch, 2015), or exterior renderings (Morel, 2012). (Note, however, that narrowing the walls upwards may counteract these effects, as obtusely inclined surfaces catch more rain.) The erosion stresses (compression, tension, shear) result from the raindrop impact pressure and the consequent radial flow (Engel, 1958). The erosion resistance of materials thus concerns their fracture toughness (strength and deformability, shatter resistance, crack propagation resistance), hardness (permanent plastic deformation or yield resistance, abrasion resistance), and cohesion (Hockey et al., 1978).

Wind-driven rain erosion necessitates simultaneous windward wind and rain on the wall surface exposed. Since a quantification of the impact loading (conservation of energy, Newton's second law) and other forces exerted by the raindrops (Abuku et al., 2009b); (Erkal et al., 2012) falls out of the scope of the present work, the risk on erosion damage is assessed in a simplified way, as following. For erosion damage, it is required that the moisture content of the exterior wall surface exceeds 80% of the capillary moisture content (which comes out greater than the manufacturing moisture content), in addition to the positive wind-driven rain load requirement. By this, it is implied that the erosion resistance is low (the mechanical properties of rammed earth

are typically significantly reduced near capillary saturation Section 4.2.1 Fig. 4.3 (a,b), Fig. 4.7), the chances of runoff (Blocken et al., 2013) which contributes to erosion (Kinnell, 2005) are relatively high, and the wind-driven rain event is intense (Vereecken & Roels, 2013); (Abuku et al., 2009a); (Janssen et al., 2007b); (Janssen et al., 2007a). The number of hours during the simulation period that these two conditions are met indicates the erosion risk.

(a) (b) (c)

Fig. 4.9: Erosion damage by wind-driven rain: (a) edge erosion breaks, frost damage (Appendix B); (b) frost damage and erosion; (c) invigorated damage around impermeable hard gravel.

4.3 Conclusion

Four mechanical performance indicators are developed for the interior insulation of rammed earth walls: fracture failure, buckling failure, clay swelling damage, and erosion. These can be added to the well-established list of hygrothermal performances for the analysis. This makes a total of twelve evaluation criteria (besides thermal insulation quality, thermal transient response, interior mould growth, interstitial mould growth, dripping moisture, wood decay, hygric transient response, and frost damage). In this way, it is enabled to draw crucially comprehensive conclusions regarding the insulatability of rammed earth walls.

For the hygrothermal analysis, consequently, also the mechanical properties and their moisture-dependency are needed, in the post-processing. Specifically, the compressive strength, the stiffness modulus, the free swelling strain curve and/or the swelling pressure curve relative to different states, the Poisson's ratio, and eventually the shear strength are required. Besides, it is necessary to assume a building geometry to calculate the mechanical loads on the wall, as well as to determine the buckling strength.

5 Interior insulation analysis

5.1 Introduction

Rammed earth walls need to be insulated to improve their thermal performance. For historical rammed earth buildings with valuable non-plastered façades, interior insulation is the applicable post-insulation technique. Applying interior insulation however modifies the hygrothermal performance of the wall and, as a consequence, can induce a risk on several damage patterns such as suboptimal thermal insulation quality, biological deterioration, and stresses. Owing to the numerous failure events in practice and the lack of scientific research analysing the interior insulatability of rammed earth walls, there is nowadays a reluctance to adopt this technique.

The goal is thus to gain insight into the possibilities to thermally retrofit rammed earth constructions with interior insulation. The associated research question is: 'What is the impact of interior insulation on the hygrothermal performance of rammed earth walls?'.

Numerical simulation is used to enable this interior insulation analysis prior to the retrofit within a reasonable time span (in contrast to hygrothermal monitoring). In Section 5.2, the hygrothermal simulation model setup is explained. In Section 5.2.1, the hygrothermal component simulation software is presented. In Section 5.2.2, first, an overview of the wall configurations and material properties is given. Next, the exterior and interior climate conditions are presented. In Section 5.2.3, the hygrothermal performance/risk indicators to be quantified are defined: the thermal insulation effectiveness, the hygro-thermal insulation quality, the thermal transient response, the interior mould growth, the interstitial mould growth, the dripping moisture, the wood decay of embedded floor beams, the hygric transient response, the fracture failure, the buckling failure, the clay swelling damage, the frost damage, and the erosion. In Section 5.3, the results of the deterministic hygrothermal performance analysis are presented and interpreted. In Section 5.3.1, the non-insulated reference wall is treated. In Section 5.3.2, the impact of five different 10 cm thick interior insulation systems on the hygrothermal performance is investigated. In Section 5.3.3, the influence of four different insulation thicknesses is considered. In Section 5.3.4, the influence of the hygric rammed earth material properties is studied. In Section 5.3.5, the influence of the rammed earth wall thickness is regarded. In Section 5.3.6, the influence of the wall orientation is explored. And in Section 5.3.7, finally, the influence of the mechanical properties is evaluated.

5.2 Model setup

5.2.1 Software

Delphin software (DELPHIN, 2021) is used for the hygrothermal component simulations. The software is based on the control volume method. The hygrothermal transfer equations (Section 2.3.1) are already implemented (Nicolai & Grunewald, 2006). The program is already validated by means of Benchmarks (Sontag et al., 2013).

Fig. 5.1 shows the user interface of the Delphin software with an exemplary wall geometry. One-dimensional heat and moisture transfer are considered (no air, no ice, and no material evolution). The wooden beams are not simulated to evaluate the wood decay risk, for simplicity. The stem wall is not simulated since the analysis focuses on the interior insulatability of rammed earth walls above the stem wall. Rising damp is not considered. An equidistant grid with element size 1 mm is used, which is simply the minimum grid element size in Delphin. This facilitates addressing specific locations in the construction and it is appropriate for the mechanical performance indicators post-processing (specifically clay swelling damage).

The initial temperature and relative humidity conditions are taken 20 °C and 50 %, respectively. Equilibration - which means that no more yearly increase in moisture content is found - with the imposed simulation year boundary conditions and materials takes a couple of years. The results discussed come from the year(s) after this equilibration period.

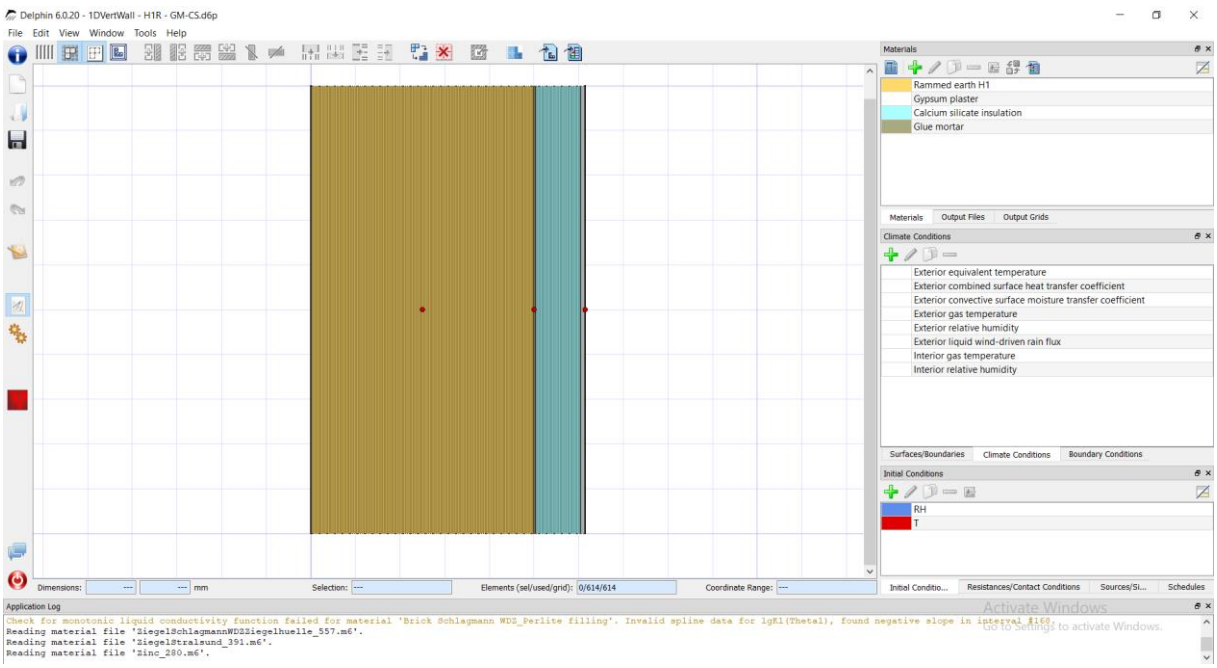

Fig. 5.1: Delphin software user interface with exemplary wall geometry.

5.2.2 Input parameters

5.2.2.1 Materials

Table 5.1 shows the composition of the different wall assemblies. The reference is a homogeneous exteriorly uncoated rammed earth wall. The two rammed earth materials considered, that of house 1 (H1) and H6, have different hygric properties: the H1 rammed earth is more hygroscopic and more capillary active than the H6 rammed earth. Investigated is the influence of five different conventional interior insulation options applied to this wall: two different vapour tight (VT), one vapour open (VO), and two different capillary active (C) (- one vapour neutral (VN), since it is equally vapour permeable as rammed earth, and one vapour open) insulation systems. The first vapour tight insulation system is a vapour tight extruded polystyrene (XPS) insulation layer. The second vapour tight insulation system is a vapour open mineral wool (MW) insulation layer combined with a vapour barrier (VB) at the inside. The vapour open insulation system is a mineral wool insulation layer. The first capillary active insulation system is a wood fibre (WF) insulation layer. The second capillary active insulation system is a calcium silicate (CS) insulation layer, that is typically applied with a glue mortar (GM) that has a vapour retarding function (Vereecken & Roels, 2016). In the present work, all the insulation systems are assumed to be applied with the same glue mortar except for the soft mineral wool insulation boards. The interior finishing layer is a gypsum plaster (GP) or a gypsum board (GB) (for the soft mineral wool insulation systems). The rammed earth wall is 50 cm thick, the glue mortar layer 4 mm, the insulation layers 10 cm, the plaster layer 10 mm, and the gypsum board 12 mm.

Table 5.1: Overview of wall assemblies with different interior insulation systems.

<table>
<tr><td>reference</td><td rowspan="6">outside</td><td rowspan="6">rammed earth wall
H1/H6</td><td colspan="3">gypsum plaster</td><td rowspan="6">inside</td></tr>
<tr><td>VT</td><td>GM</td><td>XPS</td><td>gypsum plaster</td></tr>
<tr><td>VT</td><td colspan="2">Mineral wool + VB</td><td>gypsum board</td></tr>
<tr><td>VO</td><td colspan="2">Mineral wool</td><td>gypsum board</td></tr>
<tr><td>(VN-)C</td><td>GM</td><td>Wood fibre</td><td>gypsum plaster</td></tr>
<tr><td>(VO-)C</td><td>GM</td><td>Calcium silicate</td><td>gypsum plaster</td></tr>
</table>

Table 5.2 gives an overview of the basic hygric and thermal properties of the materials concerned. The symbols herein stand for the bulk density (ρ_{bul}, kg/m³), the specific heat capacity (c, J/(kg K)), the thermal conductivity (λ, W/(m K)), the thermal conductivity moisture content factor (a, W m²/(kg K)), the open porosity (Ψ_o, m³/m³), the capillary moisture content (w_{cap}, kg/m³), the vapour resistance factor (μ, -), the saturated liquid permeability ($k_{l,sat}$, s), and the capillary absorption coefficient (A_c, kg/(m² s$^{0.5}$)). The hygric properties of the rammed earth materials are determined

in Section 3. The thermal properties of the rammed earth materials are derived in Section 2.4.2. The properties of the other materials are mainly taken from the Delphin database (they are slightly adjusted where necessary). Fig. 5.2 shows the moisture retention curves of the materials involved and Fig. 5.3 shows the moisture permeability curves.

Table 5.2: Basic thermal and hygric properties of involved materials.

	ρ_{bul}	c	λ	a	Ψ_o	w_{cap}	μ	$k_{l,sat}$	A_c
H1	1757	900	0.6	0.0038	0.352	288	7.7	$2.1\text{x}10^{-9}$	0.262
H6	1708	900	0.6	0.0038	0.338	296	8.2	$3.4\text{x}10^{-9}$	0.188
XPS[a]	35	1500	0.027	0	0.91	3	225	0	$8\text{x}10^{-6}$
MW[b]	67	840	0.040	0	0.92	0.138	1	0	0
WF[c]	197	1684	0.064	$3.4\text{x}10^{-4}$ [h]	0.926	240	12.9	$9.6\text{x}10^{-9}$	0.292
CS[d]	270	1158	0.069	$5.6\text{x}10^{-4}$	0.91	830	3.8	$2.3\text{x}10^{-8}$	1.115
GM[e]	1473	1018	0.918	$5.6\text{x}10^{-4}$	0.444	255	38.4	$2.2\text{x}10^{-11}$	0.008
GP[f]	1043	1047	0.261	$5.6\text{x}10^{-4}$	0.606	350	11.3	$5.5\text{x}10^{-9}$	0.367
GB[g]	850	850	0.2	$5.6\text{x}10^{-4}$	0.65	400	10	$6.3\text{x}10^{-9}$	0.277
VB	-	-	-	-	-	-	10^5	-	-

Delphin ID: [a] PolystyreneBoardExtruded_189, [b] MineralWool67_645, [c] HolzwolleleichtbauplattePavatexPaHWLIHeight_516, [d] CalsithermCalciumsilikatHamstad_571, [e] CalsithermKPKleber_407, [f] GipsputzMAXIT71korr_799, [g] GypsumBoard_81. [h] Taken from (Troppová et al., 2015).

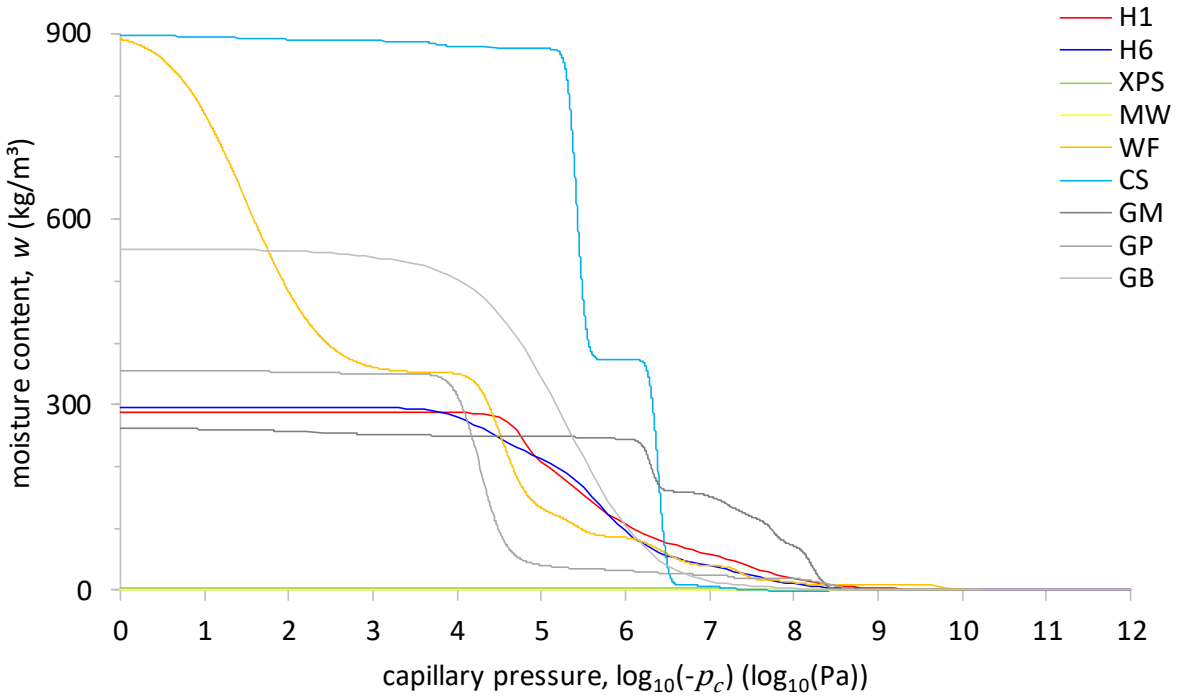

Fig. 5.2: Moisture retention curve of involved materials.

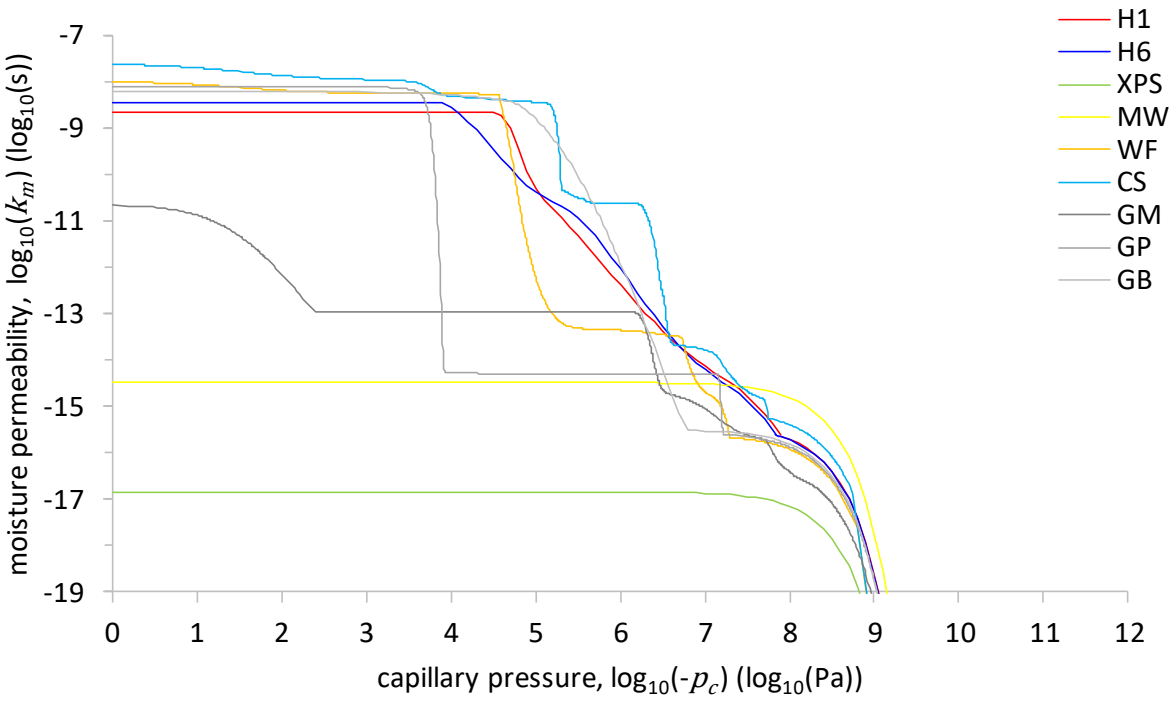

Fig. 5.3: Moisture permeability curve of involved materials.

In the manual post-processing concerning the mechanical performance indicators, the mechanical properties of the rammed earth materials are needed as an input. These mechanical properties are only available for the H1 rammed earth material and they are derived in Section 4. Besides, a variant of the mechanical properties (compressive strength and free swelling strain) is considered. This variant "2" corresponds to what would be a realistic assumption of the mechanical properties for the H2 rammed earth, cf. its moisture retention curve. Its compressive strength curve has 'the steepness of Gerard and Brinkmann', see Appendix E. Fig. 5.4 shows the compressive strength curve and the stiffness modulus curve and Fig. 5.5 shows the free swelling strain curve and the Poisson's ratio curve. The building geometry that is assumed to calculate the mechanical loads on the wall is described in Section 4.2.1. The resultant structural normal force/stress at the wall bottom amounts to 554228 N / 0.171 MPa, respectively. The wall is 0.5 m thick, 6.5 m wide, and 6.5 m high. The calculation of the buckling strength is also treated in Section 4.2.1.

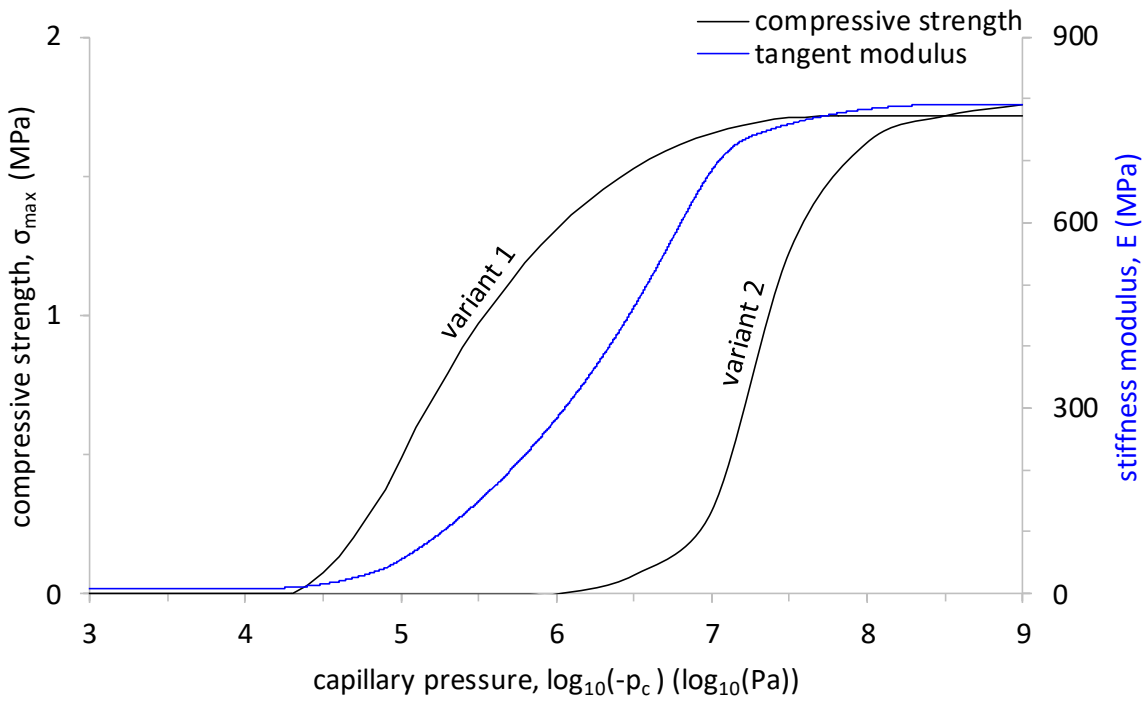

Fig. 5.4: Compressive strength curve and stiffness modulus curve of H1 rammed earth material.

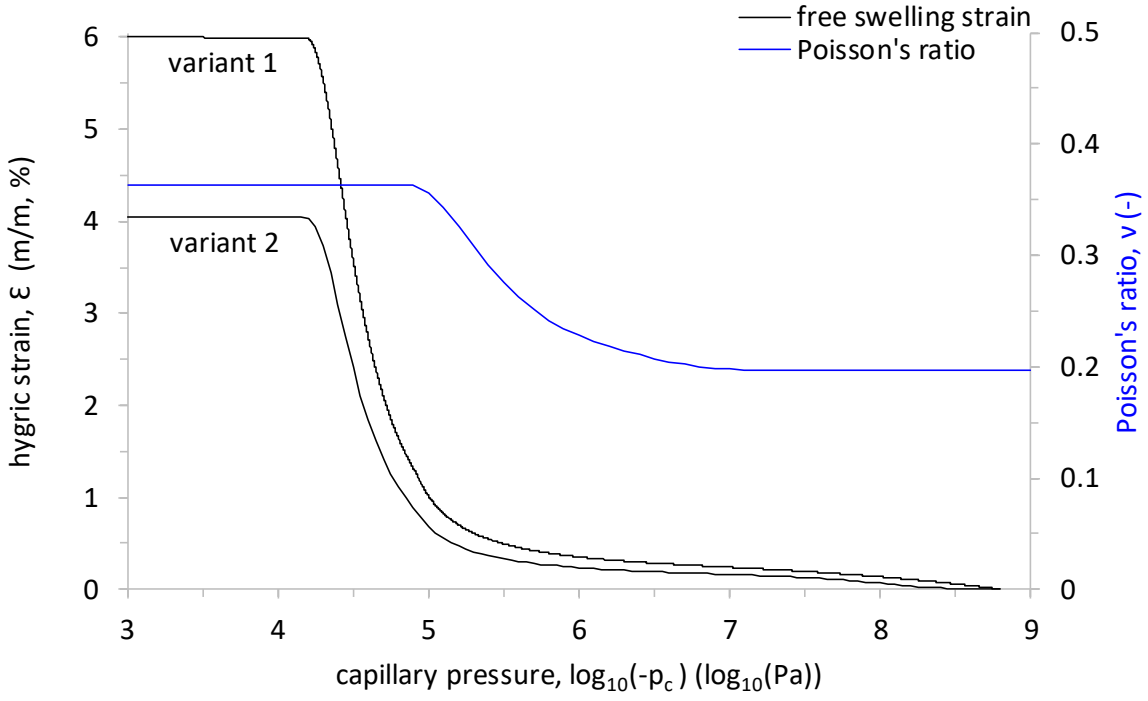

Fig. 5.5: Free swelling strain curve and Poisson's ratio curve of H1 rammed earth material.

5.2.2.2 Climate conditions

Table 5.3 summarises the exterior climate conditions. The symbols herein stand for the exterior equivalent temperature ($T_{e,equ}$, °C), the exterior vapour pressure ($p_{v,e}$, Pa), the wind-driven rain intensity (R_{wdr}, kg/(m² y)), the exterior gas temperature (T_e, °C), the exterior relative humidity (RH_e, %), the wind speed (U_{10}, m/s), the horizontal rainfall intensity (R_h, kg/(m² y)), the cloudiness (c, -), the short-wave direct horizontal radiation ($q_{S,dir,h}$, kWh/m²), the short-wave diffuse horizontal radiation ($q_{S,dif,h}$, kWh/m²), the exterior convective surface heat transfer coefficient ($h_{conv,e}$, W/(m² K)), the exterior radiative surface heat transfer coefficient ($h_{rad,e}$, W/(m² K)), and the exterior convective surface moisture transfer coefficient (β_e, s/m). The climate database of Météo-France (Météo France, 2020) is used and that of ENTPE (ENTPE, 2020) for the short-wave radiation. The climate of Lyon(-Saint-Exupéry) is chosen from a selection of five candidate cities with a weather station in the Auvergne-Rhône-Alpes Region where most of France's rammed earth heritage is located (Dorothée, 2018); (Leylavergne, 2012), because it is the most moisture-severe location regarding wind-driven rain, see Appendix F. From the years 2010 to 2014, the year 2014 is chosen as the moisture reference year based on the wind-driven rain load, see Appendix G. Fig. 5.6 shows (a) the wind rose and (b) the wind-driven rain rose for 2014 in Lyon. The wind comes mainly from the South and then the North. The reference wall orientation is chosen South, as the wind-driven rain in Lyon in 2014 comes mainly from the South.

Table 5.3: Lyon 2014 exterior environmental conditions and surface transfer coefficients.

	$T_{e,equ}$ [a]	$p_{v,e}$	R_{wdr} [a]	T_e	RH_e	U_{10}	R_h	c	$q_{S,dir,h}$	$q_{S,dif,h}$	$h_{conv,e}$ [a]	$h_{rad,e}$	β_e [a]
average	16	1108	154[b]	13	71	3	1091[b]	0.63	702[b]	539[b]	13.4	5[c]	10.4[d]
maximum	53	2120		35	100	17		1			58.4		45.0[d]
minimum	-9	303		-6	16	0		0			7.0		5.4[d]

[a] For 180° South oriented façade. [b] Total (instead of average). [c] Standard value, constant. [d] x 10^{-8}.

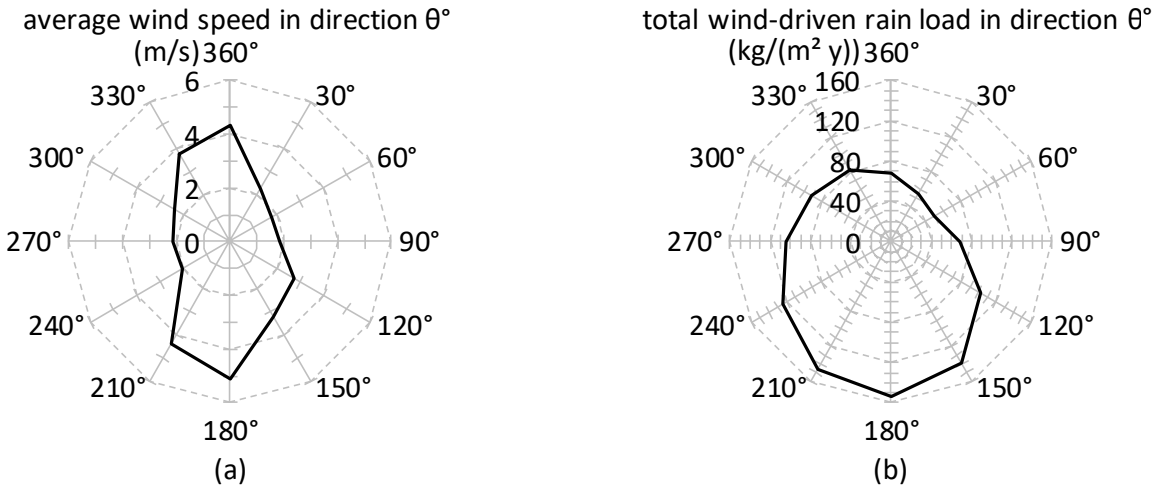

Fig. 5.6: Directional roses for (a) wind speed and (b) wind-driven rain load in 2014 in Lyon.

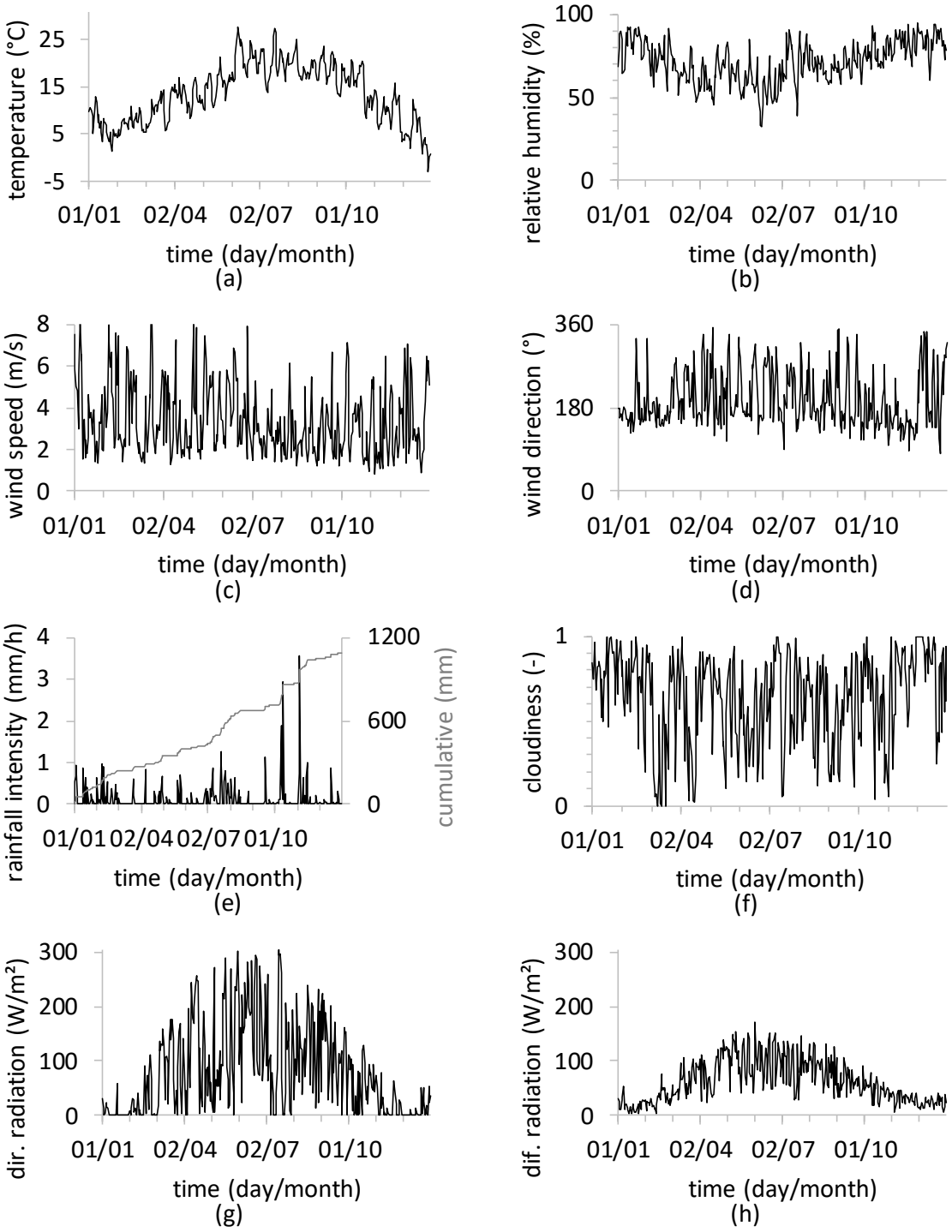

Fig. 5.7: Daily averaged raw exterior climate data over the year: (a) exterior gas temperature, (b) exterior relative humidity, (c) wind speed, (d) wind direction, (e) horizontal rainfall intensity, (f) cloudiness, (g) short-wave direct horizontal radiation, and (h) short-wave diffuse horizontal radiation.

Fig. 5.7 shows the daily averaged raw exterior climate data over the year: the exterior gas temperature, the exterior relative humidity, the wind speed, the wind direction, the horizontal rainfall intensity, the cloudiness, the short-wave direct horizontal radiation, and the short-wave diffuse horizontal radiation. The hourly raw exterior climate data figures are included in Appendix H. Fig. 5.8 shows the hourly exterior equivalent temperature, Fig. H.9 in Appendix H shows the hourly exterior convective surface heat and moisture transfer coefficients, and Fig. 5.9 shows the hourly wind-driven rain load for the South oriented façade. The theoretical background for calculating these boundary conditions is given in Appendix C. The short-wave absorptivity of the exterior surface ($\alpha_{S,se}$, -) is taken 0.675. The long-wave emissivity of the exterior surface ($e_{L,se}$, -) is taken 0.9 (plays a role in the standard value for the exterior radiative surface heat transfer coefficient). The exterior convective surface heat transfer coefficient is calculated using Sharples (Janssen et al., 2007) for taking into account the effect of the wind speed and sense. Lewis is used for moisture. The building is assumed to be situated in farm land and the investigated envelope part is assumed to be at 7.1 m height above the ground, horizontally in the centre of a two stories high building with a sloped roof (- whereby the wall factor becomes 0.4). The resulting wind-driven rain coefficient (α, s/m) amounts to 0.0837 s/m.

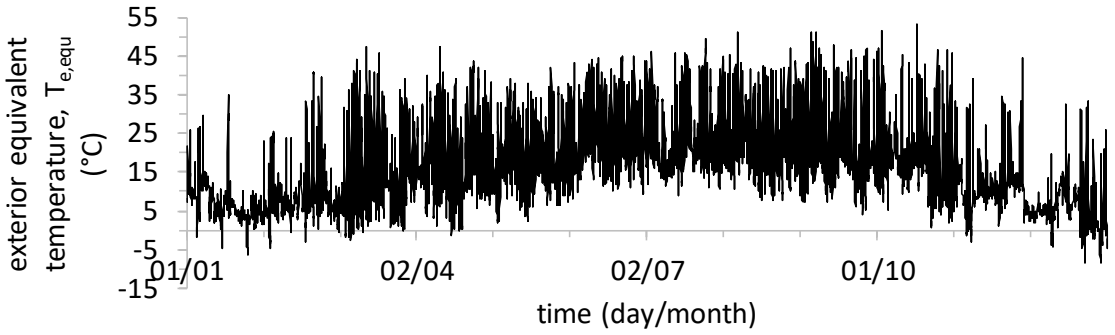

Fig. 5.8: Hourly exterior equivalent temperature over the year 2014 for South orientated façade in Lyon.

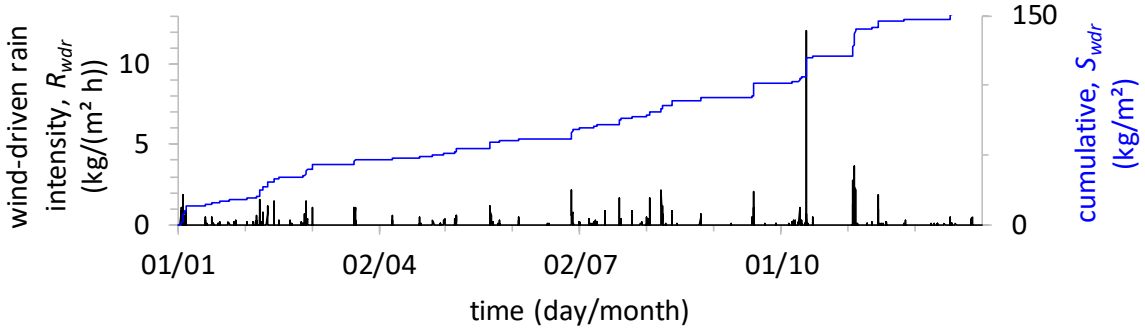

Fig. 5.9: Hourly wind-driven rain load and cumulative amount over the year 2014 for South orientated façade in Lyon.

Table 5.4 summarises the interior climate conditions. The subscript 'i' stands for interior. The interior climate conditions are determined in accordance with (EN 15026). The imposed interior temperature varies on a daily basis depending on the daily mean exterior temperature. It amounts to 20 °C for exterior temperatures from -20 °C to 10 °C, then increases linearly to 25 °C for exterior temperatures from 10 °C to 20 °C, and finally remains constant at 25 °C for exterior temperatures between 20 °C and 30 °C. Fig. 5.10 (a) shows the resulting interior temperature for Lyon in 2014. In (Tijskens et al., 2017), it is shown for an example in Bremerhaven, Germany, that a close agreement is found between the standard imposed interior temperature and the interior temperature calculated from the heat balance at zone level Eq. (2.1). The imposed interior relative humidity varies also on a daily basis depending mainly linearly on the daily mean exterior temperature. The interior relative humidity level for high (versus normal) occupancy of the building is selected. Fig. 5.10 (b) shows the resulting interior relative humidity for Lyon in 2014. Fig. 5.11 shows the resulting interior vapour pressure besides the exterior vapour pressure.

Table 5.4: Lyon 2014 interior environmental conditions and surface transfer coefficients.

	T_i (°C)	$p_{v,i}$ (Pa)	RH_i (%)	$h_{conv,i}$ (W/(m² K))	$h_{rad,i}$ (W/(m² K))	β_i (s/m)
average	22	1708	63	3.5[a]	4.5[a]	2.695 x 10^{-8} [a]
maximum	25	2216	70			
minimum	20	1098	47			

[a] Standard value, constant.

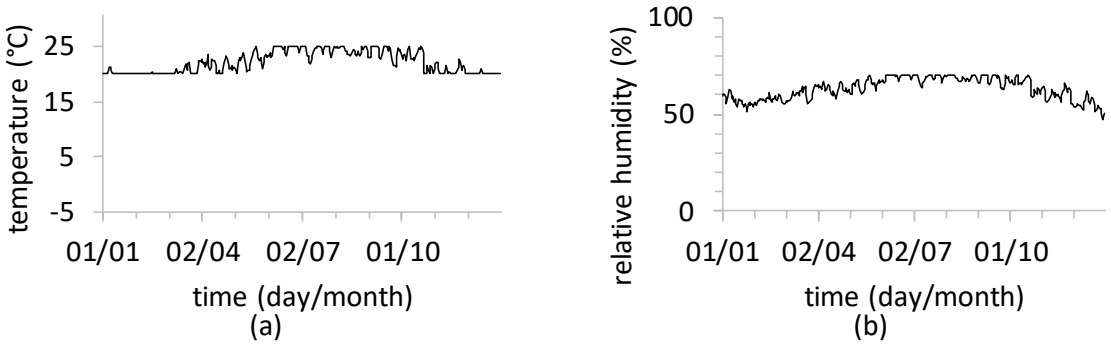

Fig. 5.10: Interior temperature (a) and interior relative humidity (b) over the year 2014 in Lyon.

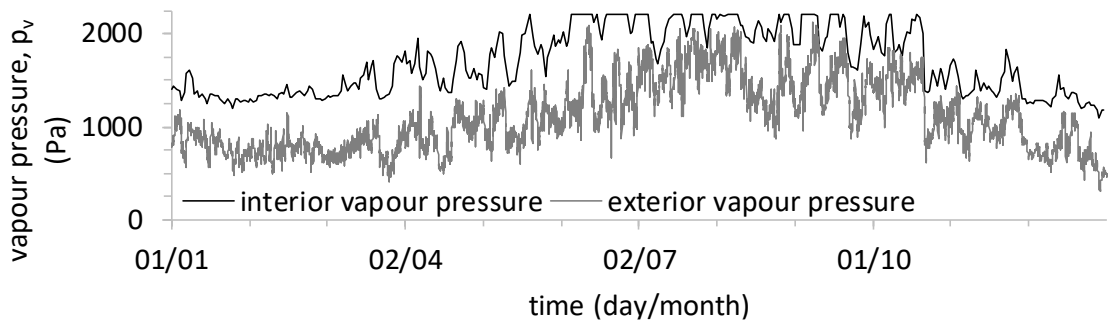

Fig. 5.11: Interior vapour pressure and exterior vapour pressure over the year 2014 in Lyon.

5.2.3 Outputs

5.2.3.1 Thermal insulation quality and hygro-thermal insulation quality

The stationary U-value in practice (U_{stat}, W/(m² K)), that can be compared with the requirement of $U \leq 0.3$ W/(m² K) (Section 2.2.1), is defined as the average heat flux in time divided by the average temperature difference in time, Eq. (5.1) (Janssen et al., 2004). To find out how much energy one saves, the thermal insulation quality is indicated by the total heat loss by transmission, Eq. (5.2). Considering only transmission through the envelope, this equals the energy consumption for space heating Eq. (2.1) to maintain an interior temperature of 20 °C at the least (EN 15026). Besides, Eq. (5.3) is used to verify to which extent the insulation is kept sufficiently dry. The dry U-value herein is calculated in the same way as the stationary U-value, but the dry thermal conductivity of the insulation material is used in the simulation.

$$U_{stat} = \frac{average(|q_{trans}|)}{average(|T_{i,equ} - T_{e,equ}|)} \overset{Eq.\ (2.6)\ (b)}{=} \frac{average(|q_{si}|)}{average(|T_{i,equ} - T_{e,equ}|)} \tag{5.1}$$

$$\begin{aligned} q_{trans,loss,total} \times 1\text{h} &= \int_{time_{total}} q_{trans,loss} \underbrace{d(time)}_{1\text{h}} = \int_{t_{total}} \max(0; q_{trans})\, dt \\ &= 1\text{h} \times \sum_{1\text{h}}^{24\text{h}\times 365} \max(0; q_{trans}) \end{aligned} \tag{5.2}$$

$$\frac{\Delta U_{moisture}}{U_{dry}} = \frac{U_{stat} - U_{dry}}{U_{dry}} \leq 0.1 \tag{5.3}$$

5.2.3.2 Thermal transient response

The thermal transient response concerning summer comfort is evaluated qualitatively by means of the heat flux in and out of the interior surface. This evaluation is only done for the month of June, which has the highest average and peak daily mean temperature for the year 2014 in Lyon.

5.2.3.3 Interior mould growth

The mould growth risk at the interior surface is indicated by the maximum value of the mould index (M, -) over a ten-year simulation period considered. The calculation of the mould index is explained in Appendix A.

5.2.3.4 Interstitial mould growth

The mould growth risk at interfaces is indicated by the maximum value of the mould index (M, -) (Appendix A) over a ten-year simulation period considered. It is evaluated at both sides of the insulation layer. The most critical side is retained.

5.2.3.5 Dripping moisture

The dripping moisture risk (DM, %) is evaluated as the fraction of time that the relative humidity exceeds 97 % at non-absorbing locations in the construction. The risk on dripping moisture is only evaluated for the insulation system mineral wool plus vapour barrier, at the interface between these two non-absorbent materials.

5.2.3.6 Wood decay

The wood decay risk for floor beam ends is indicated by the total wood mass loss (Section 2.2.3.3) after a ten-year simulation period considered (ML, %). The wooden elements are not modelled for operational reasons in the present work. The floor beam wood decay risk is evaluated at two depths in the wall: at 25 cm from the rammed earth interior surface (at the beam end) and at the rammed earth interior surface (i.e. at the interface between the wall and the plaster or the insulation system). The most critical depth is retained.

5.2.3.7 Hygric transient response

The moisture buffering performance is evaluated qualitatively in terms of the vapour flux from the interior in and out of the interior surface. This evaluation is only done for the most humid and the driest month of the year qua interior vapour pressure, i.e. June and December, respectively.

5.2.3.8 Fracture failure

The risk on fracture failure is indicated by the maximum load-bearing section loss (S, %) over the simulation year. The load-bearing section loss is determined by the ratio of the total stress to the compressive strength. It is evaluated at the bottom of the rammed earth wall, with an accuracy of 1 cm wall width (thickness).

5.2.3.9 Buckling failure

The risk on buckling failure is indicated by the maximum relative buckling stress (B, %) over the simulation year. The relative buckling stress is determined as the ratio of the total average stress to the buckling strength. Both are calculated at the wall bottom and fracture failure is taken into account in a simplified way.

5.2.3.10 Clay swelling damage

The risk on clay swelling damage is indicated separately for the exterior and the interior surface layer by the maximum total number of clay swelling cycles ($\#CSC$, -) at the same depth in the wall over the simulation year. A greater depth is considered more critical for the same number of clay swelling cycles. The clay swelling cycles are determined by the shear stress exceeding the shear strength, which can be caused by fracture failure or excessive wetting moisture gradients. The clay swelling damage risk is evaluated at the bottom of the rammed earth wall, per 1 cm wall thickness.

5.2.3.11 Frost damage

The risk on frost damage is indicated by the total number of frost-thaw cycles ($\#F\text{-}TC$, -) at the most critical position in the wall over the simulation year. The frost-thaw cycles are determined by means of the Gibbs-Thomson relation, Appendix B. The frost damage risk is evaluated per 1 mm wall thickness.

5.2.3.12 Erosion

The erosion risk (ER, h) is indicated by the time that the moisture content of the exterior wall surface exceeds 80 % of the capillary moisture content. And at the same time, the wind-driven rain load must be greater than zero.

5.3 Results and discussion

5.3.1 Reference wall

5.3.1.1 Introduction and general results

Before assessing the impact of insulation, the hygrothermal behaviour of the non-insulated reference wall is investigated. Since it was commonly assumed that the hygrothermal response of rammed earth walls concerns only hygroscopic regimes, the moisture content at 97 % relative humidity, i.e. 72 kg/m³ for the H1 rammed earth, is used as the upper limit of the hygroscopic range to verify this assumption. Fig. 5.12 shows the hourly moisture content profile evolution in the H1 rammed earth wall over the year in (a) 3D, (b) front, and (c) side view. It is observed that overhygroscopic states are addressed 24 % of the time and especially during winter and autumn; they occur at the exterior side of the wall consequent to wind-driven rain events.

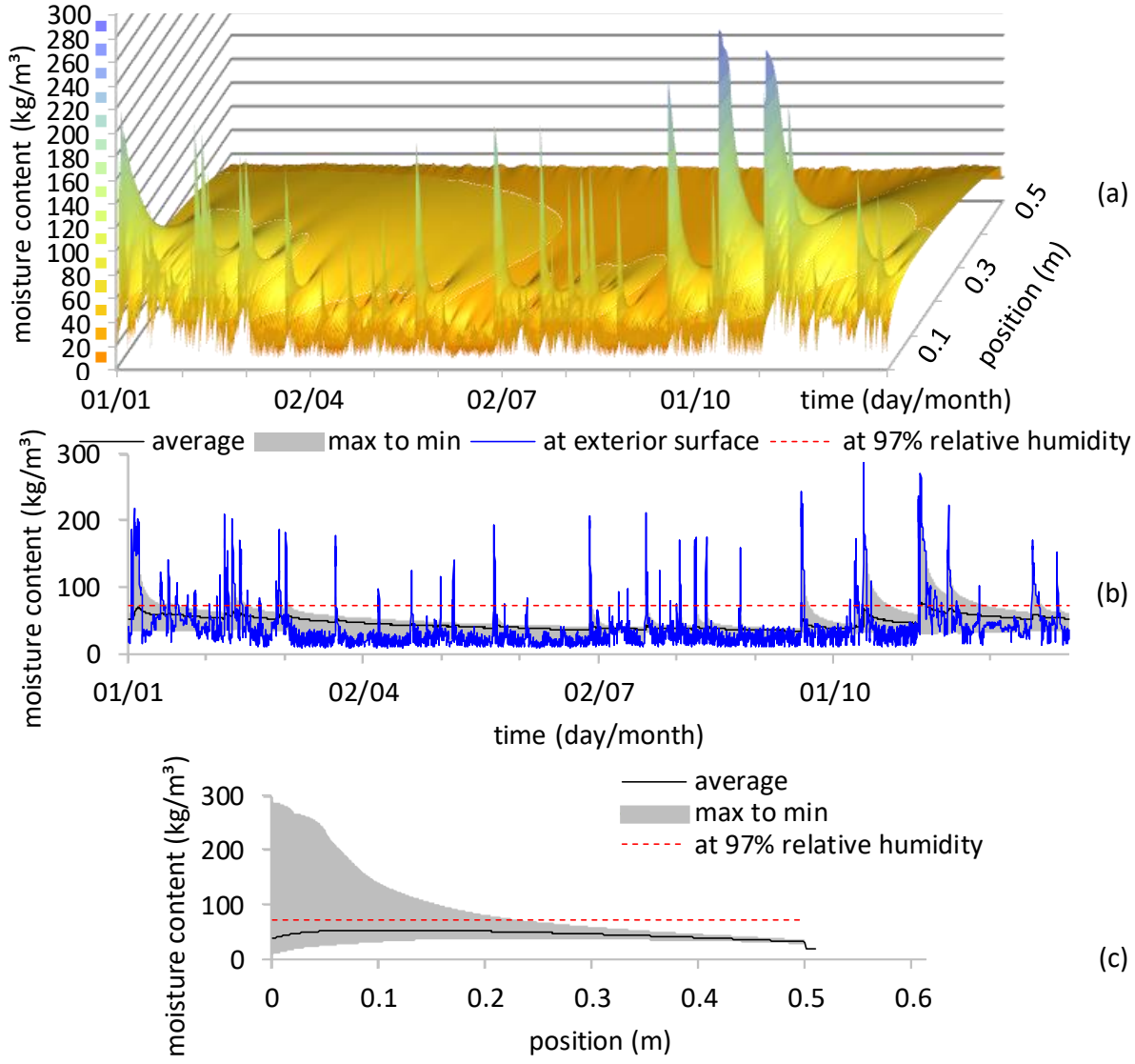

Fig. 5.12: Hourly moisture content profile evolution in H1 rammed earth wall (3D, front, side).

5.3.1.2 Thermal insulation quality

The stationary U-value in practice for the non-insulated H1 rammed earth wall amounts to 0.82 W/(m² K), which largely exceeds the maximum allowed value of 0.3 W/(m² K). The total transmission heat loss amounts to 72 kW h/m²; Fig. 5.13 shows the temporal distribution over the year. It is observed that the greatest heat losses occur during winter and autumn.

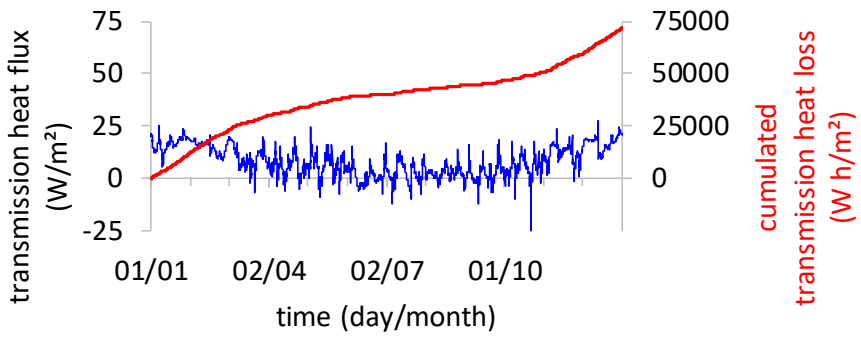

Fig. 5.13: Temporal distribution of hourly transmission heat flux and cumulated loss for non-insulated H1 rammed earth wall.

5.3.1.3 Thermal transient response

Fig. 5.14 shows the heat flux at the interior surface for the non-insulated H1 rammed earth wall and the interior temperature for June. It is observed that a sudden rise/fall in temperature results in a large heat uptake/release. This can be linked to the great thermal effusivity of (the gypsum plaster and) the rammed earth material: (534 J/(m² K $s^{0.5}$) and) 974 J/(m² K $s^{0.5}$).

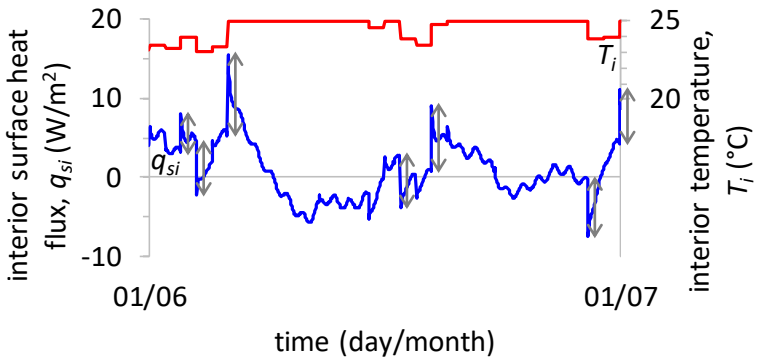

Fig. 5.14: Heat flux from interior to interior surface for non-insulated H1 rammed earth wall and interior temperature for June.

5.3.1.4 Interior mould growth

The interior mould growth risk is zero for the non-insulated H1 rammed earth wall according to the VTT model. This is because the interior surface relative humidity never reaches the 80 % threshold value (Appendix A).

5.3.1.5 Interstitial mould growth

For the non-insulated wall, the risk on interstitial mould growth is evaluated between the rammed earth wall and the plaster layer. This interstitial mould growth risk amounts to zero.

5.3.1.6 Wood decay

Only a minor wood decay risk of 1.1 % wood mass loss after ten years in the middle of the wall is found for the non-insulated H1 rammed earth wall. No wood decay risk is found at the side of the wall because the relative humidity does not exceed the 95 % threshold value (Section 2.2.3.3).

5.3.1.7 Hygric transient response

Fig. 5.15 shows the vapour flux at the interior surface for the non-insulated H1 rammed earth wall and the interior vapour pressure (a) for June and (b) for December. It is observed that a sudden rise/fall in vapour pressure results in a large vapour uptake/release. This is consistent with the moisture buffering effect. Besides, the vapour flux is most of the time in the direction out of the interior surface towards the interior environment, as the vapour pressure at the interior surface is higher than the interior vapour pressure. This is explained by the wind-driven rain load.

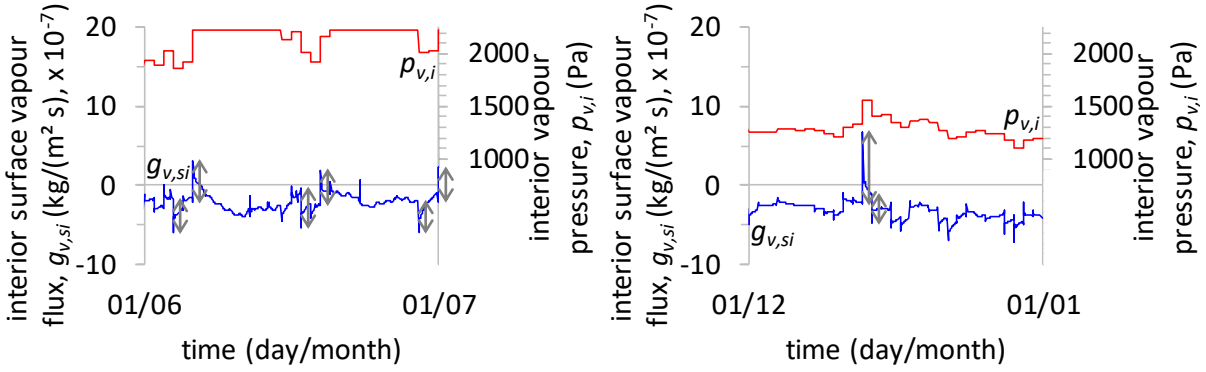

Fig. 5.15: Vapour flux from interior to interior surface for non-insulated H1 rammed earth wall and interior vapour pressure (a) for June and (b) for December.

5.3.1.8 Frost damage

No frost damage risk is found for the non-insulated H1 rammed earth wall. The temperature at each position remains greater than the frost temperature at the corresponding capillary pressure in time.

5.3.1.9 Erosion

The erosion risk amounts to 13 hours for the non-insulated H1 rammed earth wall. This is only 0.15 % of the time.

5.3.1.10 Conclusion

The hygrothermal performance of the non-insulated reference wall is evaluated. Preliminarily, it is found that overhygroscopic states up to the capillary moisture content are attained in the wall, demonstrating the importance of the full-range material characterisation. Further, it is found that only the thermal insulation quality is problematic for this case. No risk on interior mould growth, interstitial mould growth or frost damage is found, and only an insignificant risk on wood decay. Furthermore, nothing unusual is observed for the risk on erosion, nor for the thermal or the hygric transient response. The question thus remains with which interior insulation system and thickness the thermal insulation quality can be improved without invigorating the hygrothermal risks.

5.3.2 Influence of insulation systems

5.3.2.1 Introduction and general results

The application of interior insulation modifies the hygrothermal performance of the wall. The lower temperatures of the wall result in a reduced drying potential towards the exterior. The extra moisture resistance by the interior insulation systems hinders the inward drying. And interstitial condensation adds when vapour diffusion reaches a cold zone in the wall assembly. Hence, by applying interior insulation, the moisture levels in the wall increase.

Fig. 5.16 shows the hourly average moisture content in the H1 rammed earth wall for the different insulated wall assemblies as compared to for the non-insulated reference wall over the year. Fig. 5.17 shows the relative humidity at the interface between the rammed earth wall and the insulation system or the plaster. And Fig. 5.18 - Fig. 5.21 show the moisture content profile in 3D. It is observed that the different insulated wall assemblies have different moisture responses, that reflect the hygric properties of the insulation systems. Four behaviours are distinguished.

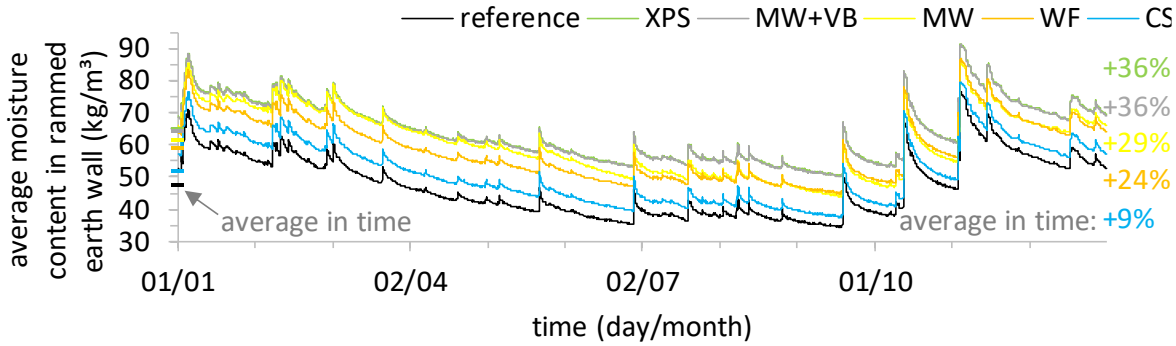

Fig. 5.16: Accumulated moisture in H1 rammed earth wall for different insulation systems.

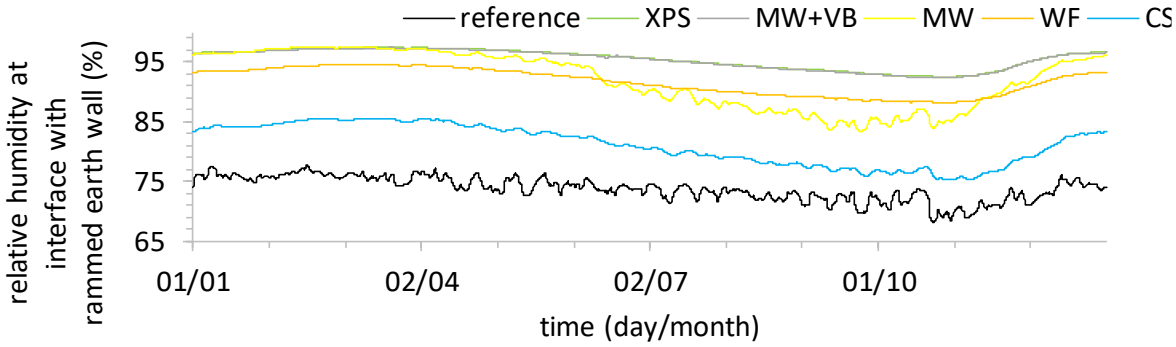

Fig. 5.17: Relative humidity at interface between H1 rammed earth wall and interior layers for non-insulated reference wall and for insulated wall assemblies with different insulation systems.

First, the vapour tight XPS and mineral wool with vapour barrier insulation systems give the largest reduced inward drying ability. This leads to the greatest moisture accumulation in the rammed earth wall of the absorbed wind-driven rain. As a result, overhygroscopic states are reached 56 % of the time and they can occur over the full wall thickness. Second, the vapour open mineral wool insulation system performs equally poor in moisture accumulation as the vapour tight systems during winter. This can be explained by the combination of wind-driven rain and interstitial condensation and the fact that mineral wool enables inward drying only through vapour diffusion. During summer, the wall can dry better, leading to lower moisture levels. Third, the vapour neutral capillary active wood fibre insulation system enables overhygroscopic drying and buffers and/or avoids interstitial condensation. It gives a harder drying during summer because the material is less vapour permeable than mineral wool. And fourth, the vapour open highly capillary active calcium silicate insulation system enables an optimal inward drying and buffers interstitial condensation. This results in moisture levels closest to the original wall, cf. Fig. 5.12. More detailed figures are included in Appendix I.

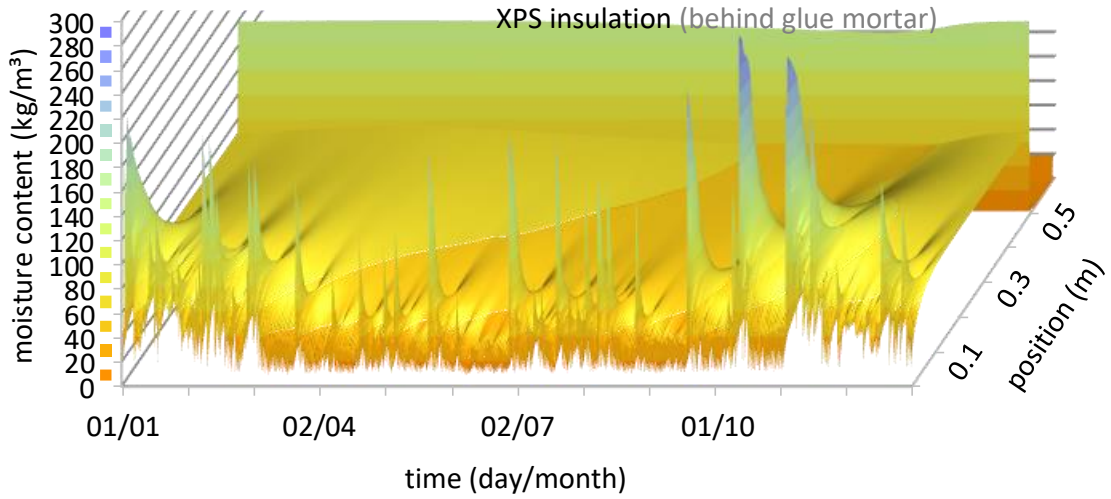

(a)

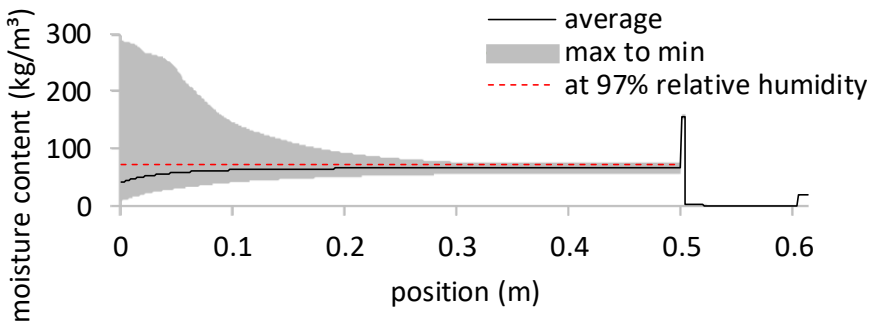

(b)

Fig. 5.18: Hourly moisture content profile in XPS insulated H1 rammed earth wall (a) 3D, (b) side.

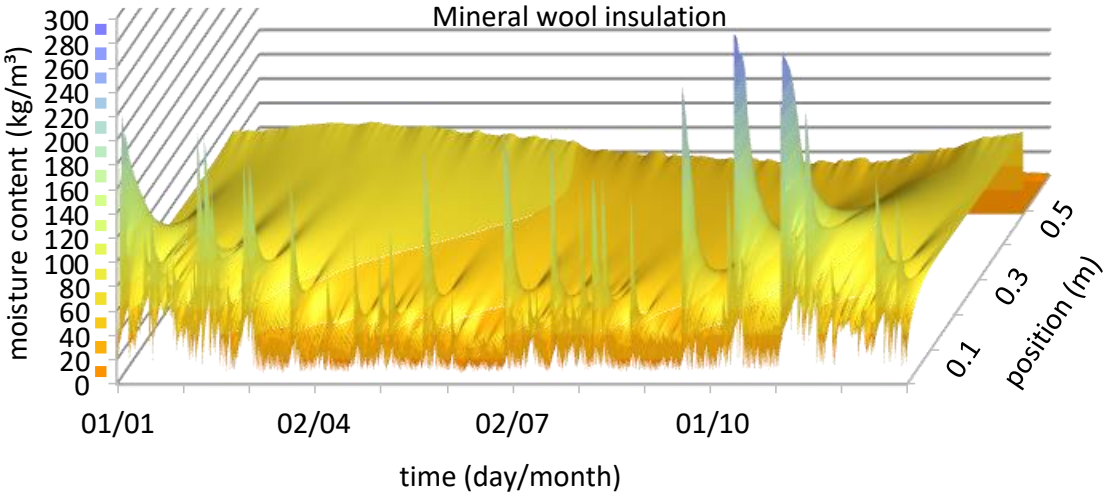

Fig. 5.19: Hourly moisture content profile in MW insulated H1 rammed earth wall in 3D.

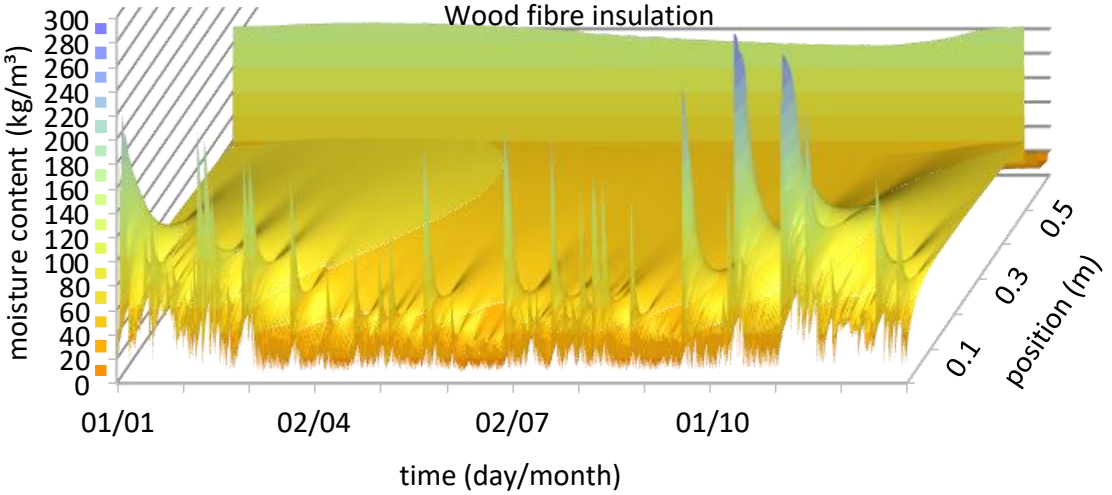

Fig. 5.20: Hourly moisture content profile in WF insulated H1 rammed earth wall in 3D.

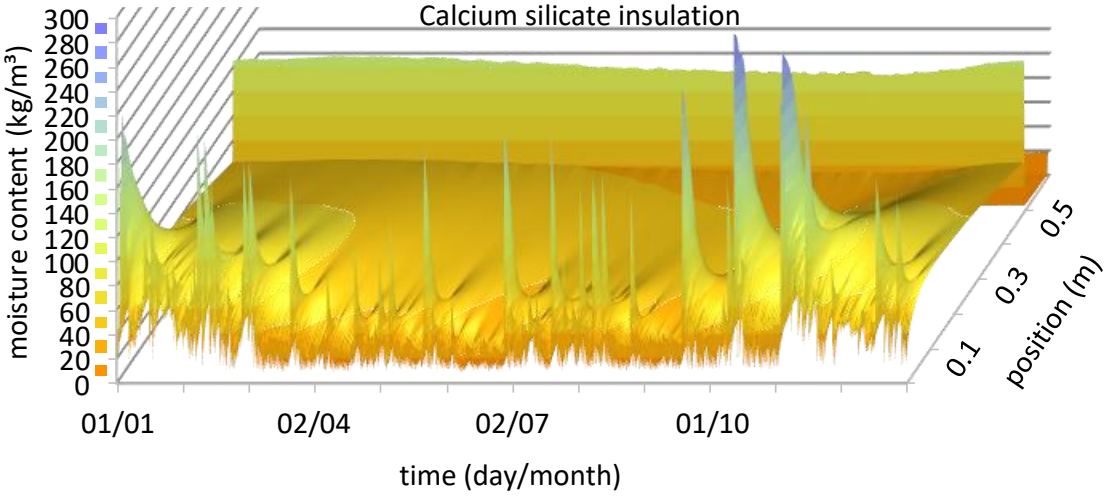

Fig. 5.21: Hourly moisture content profile in CS insulated H1 rammed earth wall in 3D.

5.3.2.2 Thermal insulation quality and hygro-thermal insulation quality

Fig. 5.22 (a) shows the stationary U-value in practice for the different insulated wall assemblies as well as for the non-insulated reference wall. It is observed that 10 cm insulation thickness is overall sufficient to meet the maximum U-value requirement of 0.3 W/(m² K). The difference in U-value between the insulation systems can mainly be explained by the dry thermal conductivity of the insulation materials, see Table 5.2. For the wood fibre and calcium silicate systems, moisture in the insulation additionally plays, Fig. 5.22 (b). The increase in U-value is greater for the wood fibre system because it is more hygroscopic and less permeable, leading to a higher moisture content, and the moisture content factor is greater. The XPS system performs the best regarding the thermal insulation quality. This is also reflected by the total transmission heat loss, Fig. 5.22 (c).

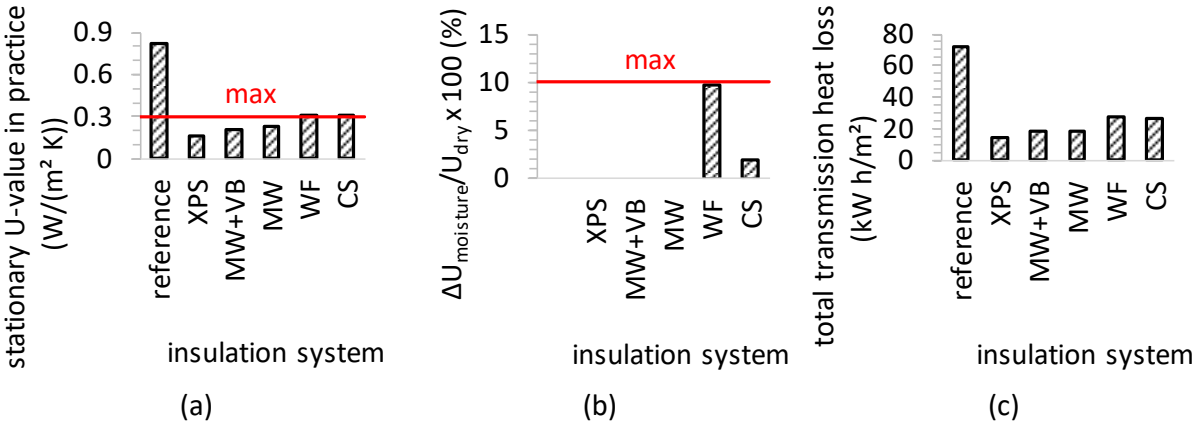

Fig. 5.22: Thermal insulation quality of reference wall and insulated wall assemblies: (a) practical stationary U-value, (b) increase in U-value by moisture, and (c) total transmission heat loss.

5.3.2.3 Thermal transient response

Fig. 5.23 shows the heat flux at the interior surface for June. It is observed that the admittance decreases in line with the thermal effusivity of the insulation materials: the wood fibre and calcium silicate systems perform slightly better than the XPS and mineral wool systems.

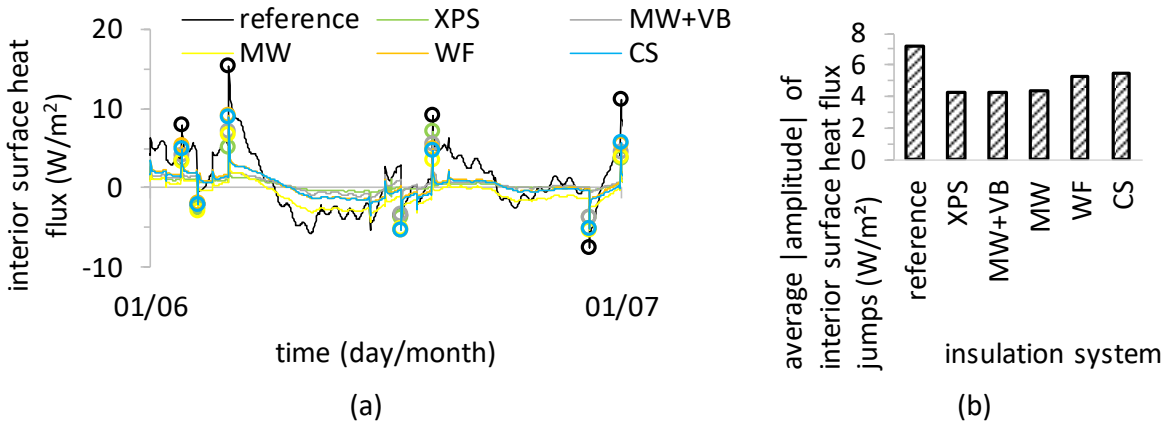

Fig. 5.23: Thermal transient response of non-insulated reference and insulated wall assemblies.

5.3.2.4 Interior mould growth

Like for the reference wall, and even more pronounced, the interior surface relative humidity never reaches 80 % for the different insulation systems. The mould growth conditions are hence never favourable and the mould index remains smaller than zero at the interior surface.

5.3.2.5 Interstitial mould growth

Fig. 5.24 shows the mould index for interstitial mould growth in time at the exterior side (worst case) of the insulation system, for the different insulation systems involved. It is observed that moderate growth (Vereecken & Roels, 2012) occurs for the vapour tight and vapour open insulation systems as well as for the wood fibre insulation system (clearly less though). This is due to the accumulated wind-driven rain in the wall (cf. Fig. 5.17). For the calcium silicate insulation system, no mould growth occurs, like for the non-insulated reference wall (Section 5.3.1). At the interior side of the insulation layer, no mould growth occurs for the different insulation systems.

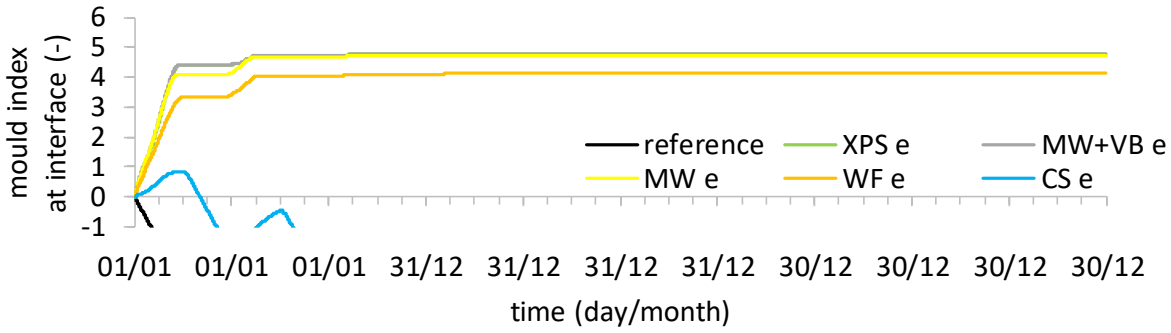

Fig. 5.24: Interstitial mould growth risk at exterior (e) side of insulation system for different insulation systems over ten years. The curves of the vapour tight insulation systems (XPS and MW+VB) overlap.

5.3.2.6 Dripping moisture

The time that the relative humidity exceeds 97 % at the interface between the mineral wool insulation layer and the vapour barrier amounts to 319 hours or 3.6 % of the time. These dripping moisture risk hours occur during late spring, summer, and early autumn, and point to summer condensation.

5.3.2.7 Wood decay

Fig. 5.25 shows the wood decay risk for the different insulated wall assemblies, as well as for the non-insulated reference wall, at the most critical of both investigated positions. It is observed that the wood decay risk can be ranked according to the drying ability of the different insulation systems, cf. Fig. 5.16. For the capillary active calcium silicate insulation system, the lowest wood mass loss is found: it starts after 12.6 months and reaches 37 % after ten years. For the other insulation systems, the wood mass loss starts after less than two months. For the capillary active wood fibre insulation system, it reaches 98 % after ten years. For the vapour open mineral wool insulation system, it reaches 100 % after 7.4 years. For the vapour tight insulation systems, it reaches 100 % after 6.3 years. For the vapour tight and vapour open insulation systems, the side of the wall is the most critical, in contrast to the middle for the other wall assemblies. This can generally be linked to where the average moisture content in time is the greatest, cf. Appendix I.

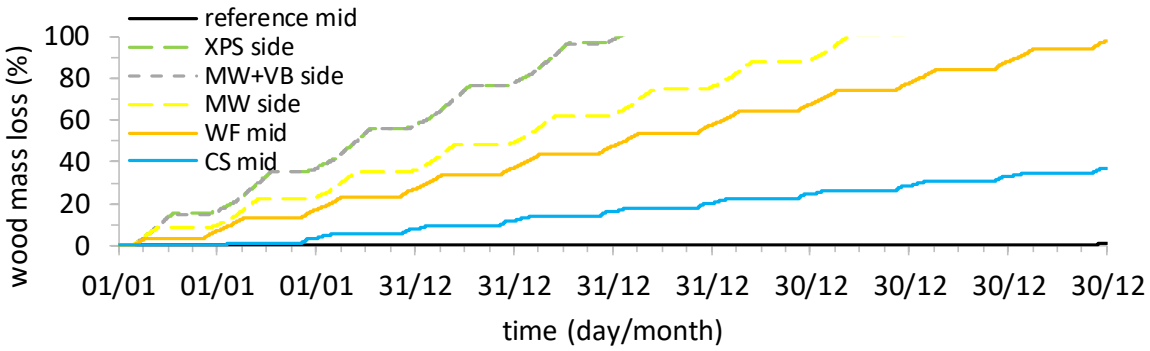

Fig. 5.25: Wood decay risk for the different insulated wall assemblies over ten years.

5.3.2.8 Hygric transient response

Fig. 5.26 shows the impact of the different insulation systems on the moisture buffering performance. It is observed that the hygric inertia decreases for the XPS and for the capillary active systems. It increases for the mineral wool systems, to be explained by the interior finishing layer.

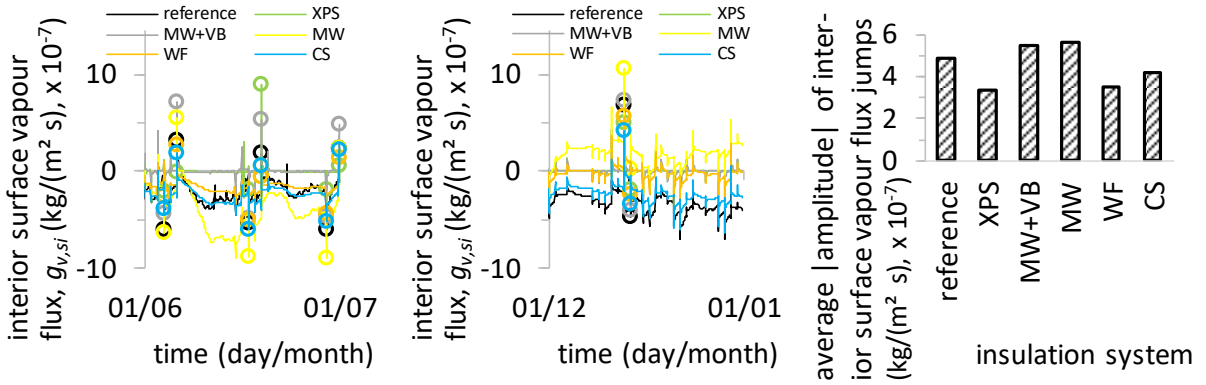

(a) (b) (c)

Fig. 5.26: Hygric transient response of non-insulated reference and insulated wall assemblies.

5.3.2.9 Frost damage

Fig. 5.27 shows the number of frost-thaw cycles at each position in the wall for the different insulated wall assemblies, as well as for the non-insulated reference wall. It is observed that the frost damage risk increases for the insulated wall assemblies as compared to for the reference wall. This is because the wall is colder and wetter after interior insulation. The maximum number of frost-thaw cycles is the same and amounts to 2 for the different insulation systems. It occurs up to 4.8 cm depth in the wall for the vapour tight XPS insulation system. This depth decreases for the other insulation systems in line with their thermal resistance and with their inward drying disability, down to 2.7 cm depth for the capillary active calcium silicate insulation system.

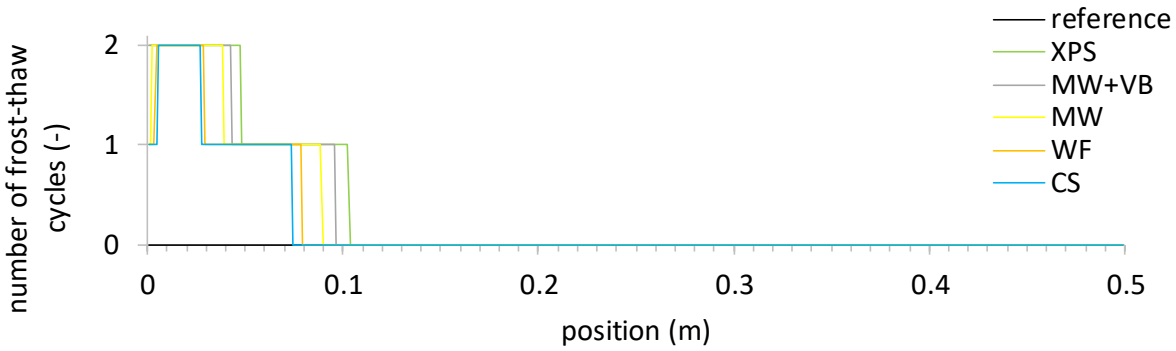

Fig. 5.27: Frost damage risk for different insulated wall assemblies.

5.3.2.10 Erosion

The erosion risk amounts to 13 hours for the reference wall and for the capillary active wood fibre and calcium silicate insulation systems and it increases to 14 hours for the other insulated wall assemblies. This is because the moisture content at the exterior surface slightly increases due to the reduced drying ability.

5.3.2.11 Conclusion

The impact of five different 10 cm thick interior insulation systems on the hygrothermal performance of the wall is evaluated. Table 5.5 summarises the results. Regarding the thermal insulation quality, about 10 cm insulation thickness is sufficient for the wood fibre and calcium silicate insulation systems. For the XPS and mineral wool insulation systems, even a smaller

insulation thickness is required. The increase in U-value by moisture in the insulation is greater for the wood fibre than for the calcium silicate insulation system, but it remains acceptable. The thermal transient response invigorates for all insulation systems. No interior mould growth risk is found for the different insulation systems. For all insulation systems except the calcium silicate - for which no mould growth occurs -, mould grows moderately at the exterior side of the insulation system. For the mineral wool insulation system with vapour barrier, besides, a risk on dripping moisture is found. The risk on wood decay remains the lowest with the capillary active calcium silicate insulation system, which yields the lowest moisture contents in the rammed earth wall. For the other insulation systems, a more significant risk on wood decay is found. The hygric transient response invigorates except for the mineral wool insulation systems with gypsum board interior finishing layer. The frost damage risk slightly increases for the different insulation systems. The erosion risk, finally, only slightly increases for the vapour tight and for the vapour open insulation systems. Resultantly, the capillary active calcium silicate insulation system is promoted because it yields the lowest moisture damage risks.

Table 5.5: Overview of hygrothermal performances for non-insulated reference H1 rammed earth wall and for 10 cm thick insulation systems. Colour code: red = extreme or hazardous, orange = requires special attention, green = acceptable.

	reference	XPS	MW+VB	MW	WF	CS
Stationary U-value in practice (W/(m² K))	0.82	0.16	0.21	0.23	0.32	0.31
ΔU-value by insulation moisture (%)	NA	0	0	0	9.8	2.0
Thermal transient response						
Interior mould growth (-)	0	0	0	0	0	0
Interstitial mould growth (-)	0	4.8 e [a]	4.8 e	4.7 e	4.1 e	0.9 e
Dripping moisture (%)	NA	NA	3.6	NA	NA	NA
Wood decay (%)	1.1 m [b]	201 s [c]	200 s	128 s	98 m	37 m
Hygric transient response						
Frost damage (-)	0	2	2	2	2	2
Erosion (h)	13	14	14	14	13	13

[a] e: at the exterior side of the insulation system; [b] m: in the middle of the wall; [c] s: at the side of the wall

5.3.3 Influence of insulation thickness

5.3.3.1 Introduction and general results

Besides the insulation system material properties, the thickness of the insulation layer can influence the hygrothermal performance of the wall assembly, primarily as following. With increasing insulation thickness, the inward drying ability of the wall decreases (besides its temperature), resulting in higher moisture contents, as shown in Fig. 5.28 and Fig. 5.29. The improved thermal performance must thus be balanced against an increased risk of moisture problems for an increased insulation thickness. Four insulation thicknesses are considered to study this: 2 cm, 5 cm, 10 cm and 20 cm.

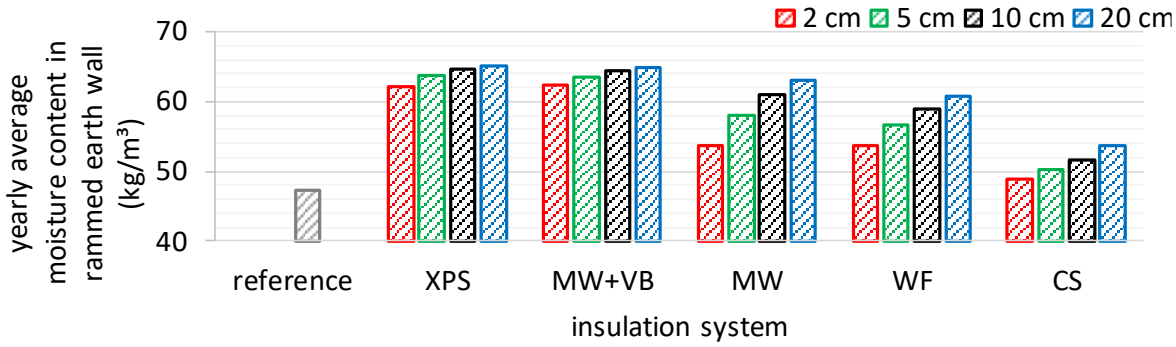

Fig. 5.28: Yearly average moisture content in rammed earth wall for non-insulated reference wall and for insulated wall assemblies with different insulation systems and with different insulation thicknesses.

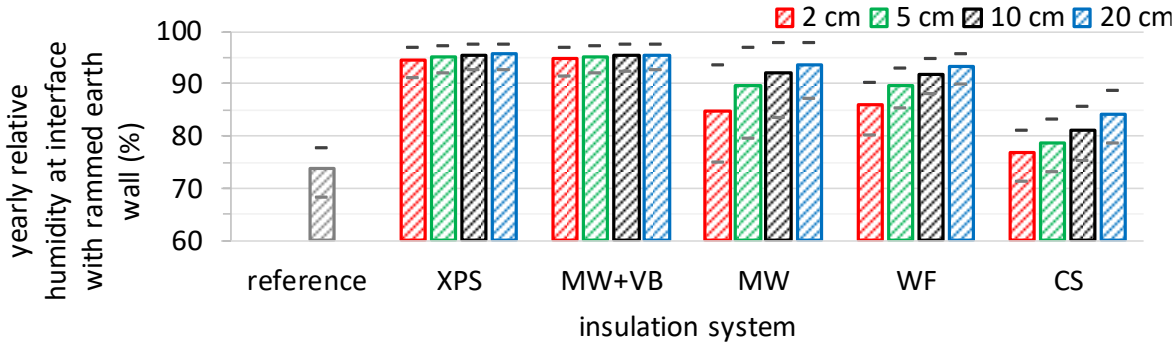

Fig. 5.29: Yearly average, maximum & minimum relative humidity at interface between rammed earth wall and ensemble of interior layers for non-insulated reference wall and for insulated wall assemblies with different insulation systems and with different insulation thicknesses.

5.3.3.2 Thermal insulation quality and hygro-thermal insulation quality

Fig. 5.30 shows the thermal insulation quality risk in terms of the stationary U-value in practice for the reference wall and for the different insulated wall assemblies. It is observed that 2 cm insulation thickness has already a significant impact on the heat losses. The thermal transmittance further decreases with increasing insulation thickness. With the vapour tight XPS insulation system, 5 cm insulation thickness is sufficient to meet the maximum U-value requirement, owing to the low thermal conductivity of the insulation material. With the other insulation systems, > 5 cm insulation thickness is required, and 10 cm is considered sufficient.

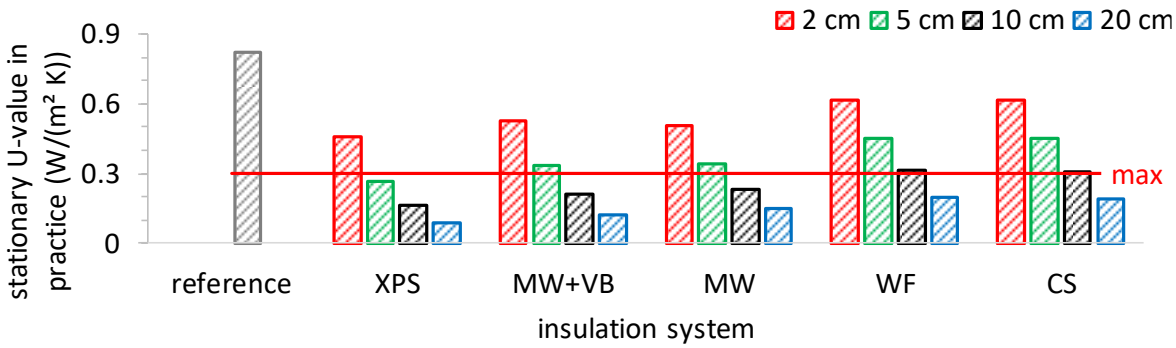

Fig. 5.30: Stationary U-value in practice for non-insulated reference wall and for insulated wall assemblies with different insulation systems and with different insulation thicknesses.

Fig. 5.31 (a) shows the increase in U-value by moisture in the insulation for the two capillary active insulation systems. It is observed that the increase in U-value increases with increasing insulation thickness. This can be linked to the increasing moisture content in the insulation layer, Fig. 5.31 (b). The increase in U-value by insulation moisture is unacceptable for 20 cm wood fibre insulation.

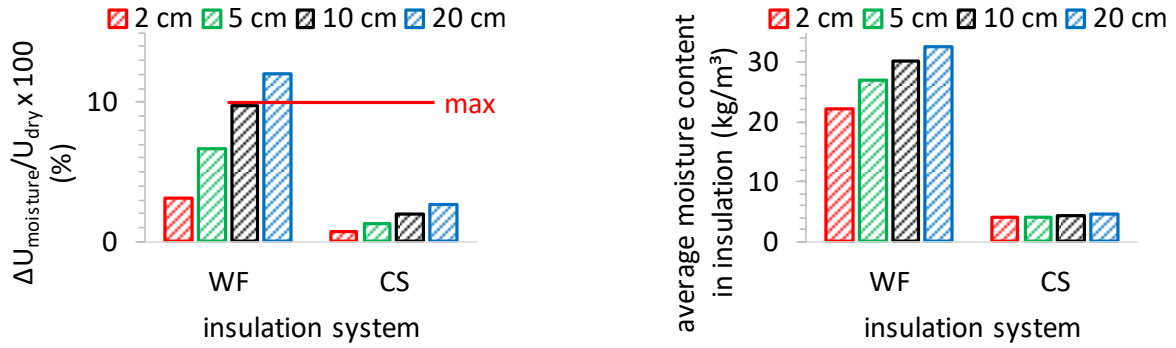

(a) (b)

Fig. 5.31: (a) Increase in U-value by moisture and (b) average moisture content in insulation.

5.3.3.3 Thermal transient response

Fig. 5.32 shows the average absolute value of the amplitude of the interior surface heat flux jumps indicated in Fig. 5.14. It is observed that especially the difference in thermal inertia between the non-insulated reference wall and the insulated wall assemblies is large. The slight increase in thermal inertia for the 2 cm thick insulation systems could indicate that the rammed earth material beneath the insulation system still contributes to the thermal inertia. The outlier for the 5 cm thick XPS insulation system is not logical.

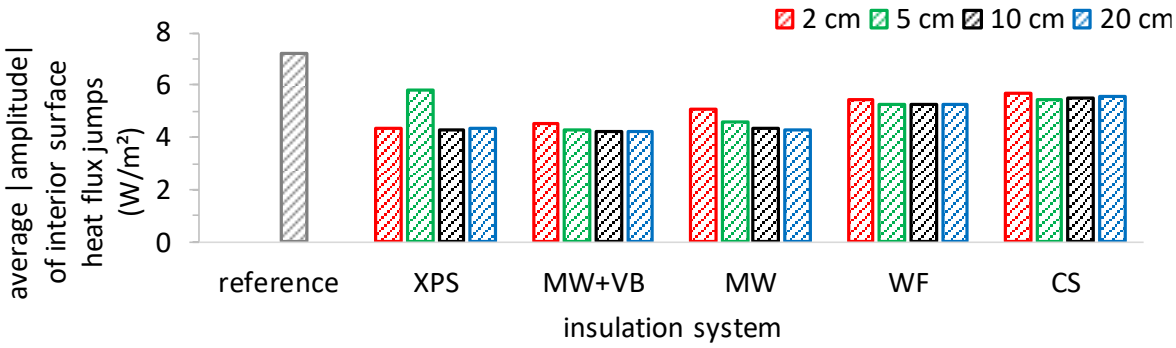

Fig. 5.32: Average absolute value of amplitude of main interior surface heat flux jumps in June.

5.3.3.4 Interior mould growth

Fig. 5.33 shows that the interior surface relative humidity never reaches the lower limit for mould growth (80 %). It is further observed that it decreases for the insulated wall assemblies as compared to for the reference wall. For the capillary active insulation systems, it is somewhat higher than for the other systems. It slightly decreases with increasing insulation thickness. This could be linked to the interior surface temperature.

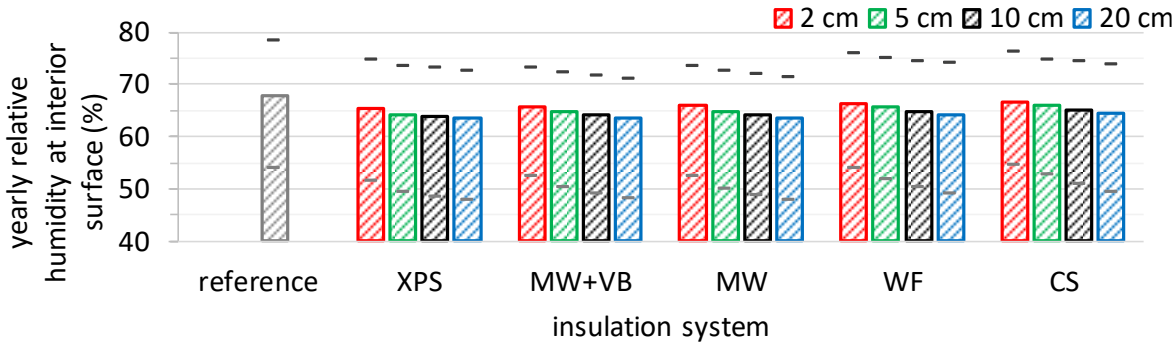

Fig. 5.33: Yearly average, maximum & minimum relative humidity at interior surface for non-insulated reference wall and for insulated wall assemblies with different insulation systems and with different insulation thicknesses.

5.3.3.5 Interstitial mould growth

Fig. 5.34 shows for the different insulation systems and thicknesses the maximum mould index over ten years at the interface between the rammed earth wall and the insulation system. It is observed that the insulation thickness has quasi no influence on the outcomes for the vapour tight insulation systems. For the vapour open and the capillary active insulation systems, the interstitial mould index decreases with decreasing insulation thickness. This can be linked to the drying ability.

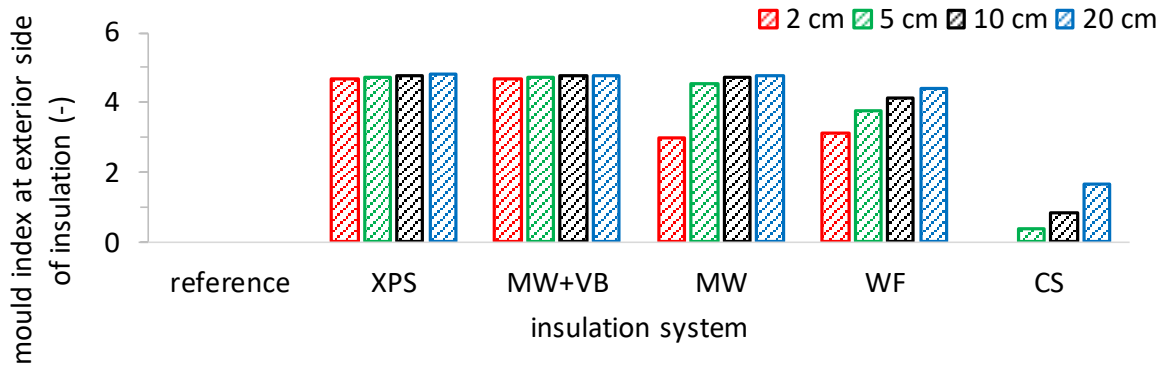

Fig. 5.34: Interstitial mould growth risk at exterior side of insulation for different insulation systems with different insulation thicknesses over ten years.

5.3.3.6 Dripping moisture

Fig. 5.35 shows the total number of dripping moisture risk hours per year at the interface between the mineral wool insulation and the vapour barrier. It is observed that the dripping moisture risk increases with increasing insulation thickness from 2 cm to 5 cm, which can be linked to the temperature, and decreases from 5 cm to 20 cm thick insulation, which can be linked to the vapour resistance.

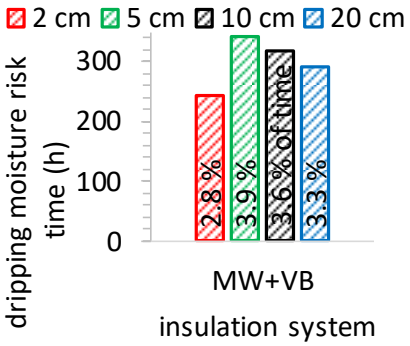

Fig. 5.35: Dripping moisture risk at interface between mineral wool insulation and vapour barrier.

5.3.3.7 Wood decay

Fig. 5.36 shows the total wood mass loss after ten years for the different insulation systems and thicknesses at the most critical of the two investigated positions (beam end (middle of the wall) or interface (side of the wall)). It is observed that the wood mass loss increases with increasing insulation thickness, which can be explained by the reduced drying ability that leads to higher moisture levels in the construction. The wood mass loss remains the lowest for the capillary active calcium silicate insulation systems. For the vapour tight insulation systems, on the other hand, there is always >100% wood mass loss. The other insulation systems perform in between.

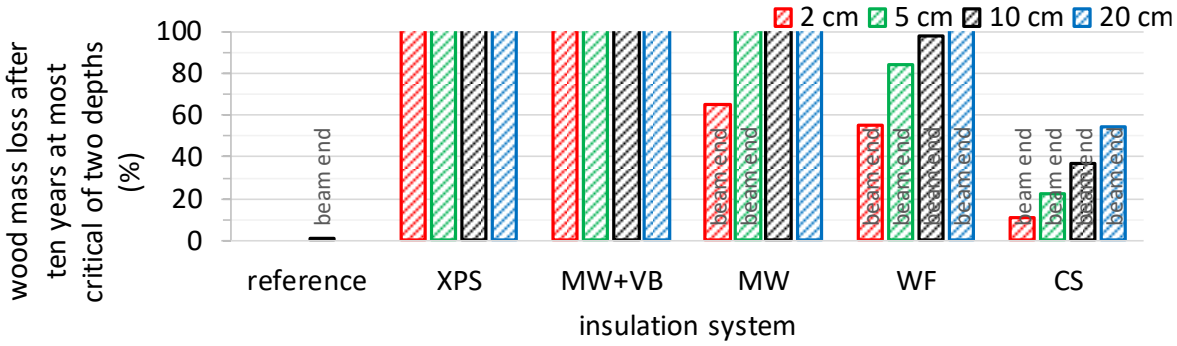

Fig. 5.36: Wood decay risk for different insulation systems with different insulation thicknesses.

5.3.3.8 Hygric transient response

Fig. 5.37 shows the average absolute value of the amplitude of the interior surface vapour flux jumps indicated in Fig. 5.15. It is observed that for the insulated wall assemblies, especially the difference in hygric inertia between gypsum board and gypsum plaster as interior finishing layer is large. The aberrant result for the 5 cm thick XPS insulation system is not logical.

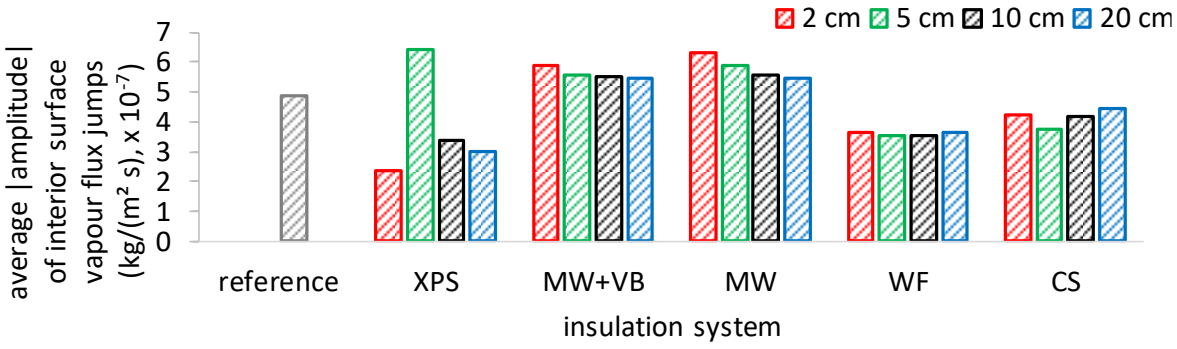

Fig. 5.37: Average absolute value of amplitude of interior surface vapour flux jumps for June and December for different insulation systems with different insulation thicknesses.

5.3.3.9 Frost damage

Fig. 5.38 shows the total number of frost-thaw cycles at the most critical depth in the wall for the different insulation systems with the different insulation thicknesses. It is observed that, as compared to the results for 10 cm insulation thickness, the frost damage risk increases for 20 cm insulation thickness for the vapour tight insulation systems. Besides, the frost damage risk decreases for the 2 cm thick capillary active insulation systems. This evolution can be explained in the same way as in Section 5.3.2.9: by the drying (dis)ability. The frost damage risk remains only zero for the non-insulated reference wall.

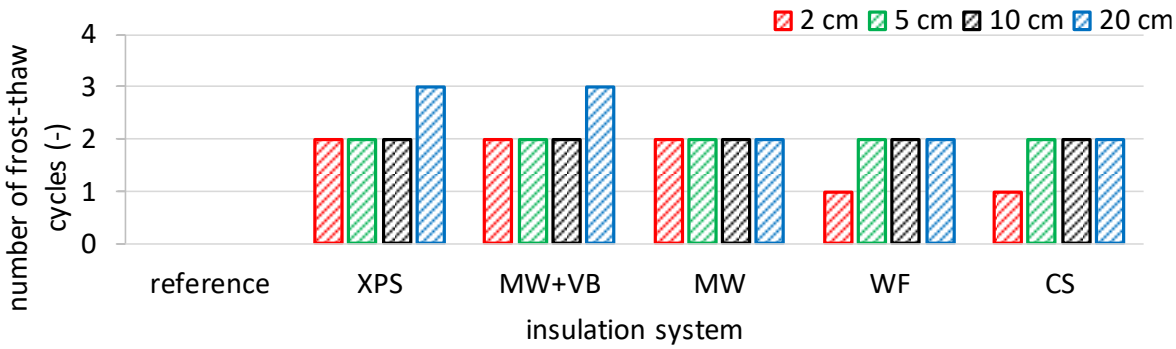

Fig. 5.38: Frost damage risk for different insulation systems with different insulation thicknesses.

5.3.3.10 Erosion

Fig. 5.39 shows the erosion risk for the different insulated wall assemblies with varying insulation thicknesses. it is observed that, except for the vapour open capillary active calcium silicate insulation system, the number of erosion risk hours slightly increases with increasing insulation thickness. This can be linked to the drying disability, leading to higher moisture contents at the exterior surface.

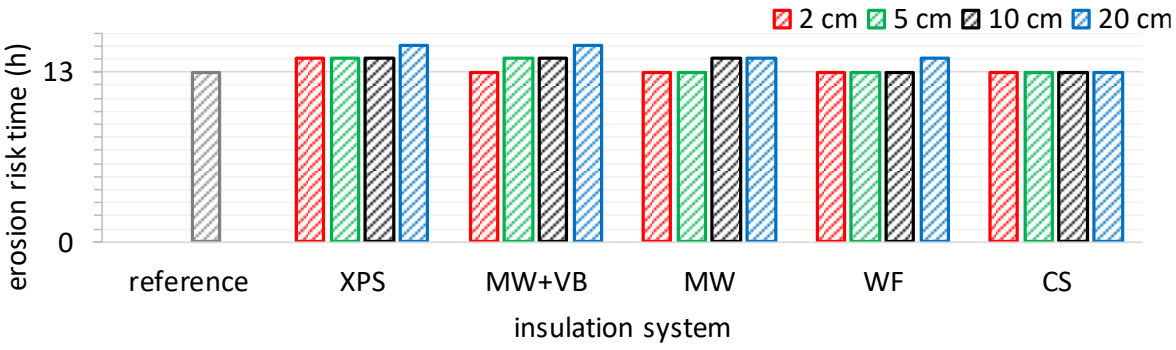

Fig. 5.39: Erosion risk for different insulation systems with different insulation thicknesses.

5.3.3.11 Conclusion

The influence of four different insulation thicknesses on the hygrothermal performance is evaluated. Table 5.6 gives an overview of the results. It is concluded that the moisture damage risks do not decrease sufficiently with decreasing insulation thickness to promote another insulation system than calcium silicate or a smaller insulation thickness than 10 cm. It remains that the capillary active calcium silicate insulation system outperforms the other insulated configurations since it leads to a lower increased risk on wood decay and interstitial mould growth. Furthermore, the increased risk on frost damage (and erosion) remains more limited for the capillary active insulation systems.

Table 5.6: Overview of hygrothermal performances for studied configurations. Colour code: red = extreme or hazardous, orange = requires special attention, green = acceptable.

	ref.	XPS				MW+VB				MW				WF				CS			
ins. thick. (cm)	-	2	5	10	20	2	5	10	20	2	5	10	20	2	5	10	20	2	5	10	20
U^{a} (W/(m²K))	0.82	0.46	0.27	0.16	0.09	0.53	0.34	0.21	0.12	0.51	0.34	0.22	0.14	0.62	0.45	0.32	0.20	0.62	0.45	0.31	0.19
ΔU_{moist} [b] (%)	NA	0	0	0	0	0	0	0	0	0	0	0	0	3.2	6.6	9.8	12.1	0.8	1.3	2.0	2.6
M_{si} [c] (-)	0	0	0	0	0	0	0	0	0	0	0	0	0	0	0	0	0	0	0	0	0
M [d] (-)	0	4.7 e [h]	4.7 e	4.8 e	4.8 e	4.7 e	4.7 e	4.8 e	4.8 e	3 e	4.5 e	4.7 e	4.8 e	3.1 e	3.7 e	4.1 e	4.4 e	0 e	0.4 e	0.9 e	2 e
Drip [e] (%)	NA	NA	NA	NA	NA	2.8	3.9	3.6	3.3	NA	NA	NA	NA	NA	NA	NA	NA	NA	NA	NA	NA
Wood [f] (%)	1 m [i]	166 s [j]	191 s	201 s	205 s	186 s	194 s	200 s	204 s	65 m	104 m	128 s	146 s	55 m	84 m	98 m	115 m	11 m	23 m	37 m	54 m
Frost [g] (-)	0	2	2	2	3	2	2	2	3	2	2	2	2	1	2	2	2	1	2	2	2
Erosion (h)	13	14	14	14	15	13	14	14	15	13	13	14	14	13	13	13	14	13	13	13	13

[a] Stationary U-value in practice; [b] ΔU-value by insulation moisture; [c] Interior mould growth; [d] Interstitial mould growth; [e] Dripping moisture; [f] Wood decay; [g] Frost damage; [h] e: at the exterior side of the insulation system; [i] m: in the middle of the wall; [j] s: at the side of the wall.

5.3.4 Influence of rammed earth material

5.3.4.1 Introduction and general results

Traditional rammed earth is an original material per site. The impact of the hygric properties of a second, different, rammed earth material on the hygrothermal performance of the non-insulated reference wall and of the different 10 cm thick insulated wall assemblies is studied. Fig. 5.40 shows the average moisture content in the rammed earth wall over the year for the H1 rammed earth and for the H6 rammed earth. It is observed that the average moisture content is significantly smaller, 28 % on average, for the H6 rammed earth. This is explained by the hygroscopically flatter course of the moisture retention curve of the H6 rammed earth. The impact of the rammed earth material on the accumulated moisture is e.g. greater than the impact of the wall orientation studied in Section 5.3.6, cf. Fig. 5.47. Fig. 5.41 shows the average moisture content profile over the year. The greater capillary absorption coefficient of the H1 rammed earth promotes moisture redistribution towards the inside.

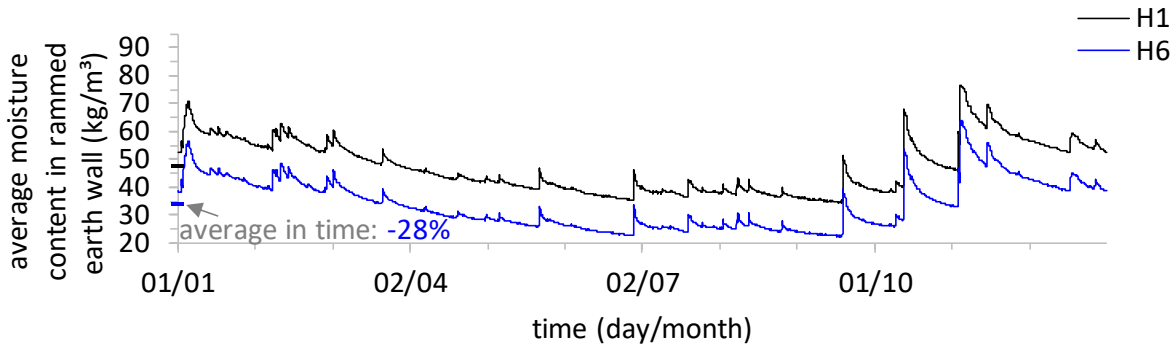

Fig. 5.40: Accumulated moisture in rammed earth wall for different rammed earth materials.

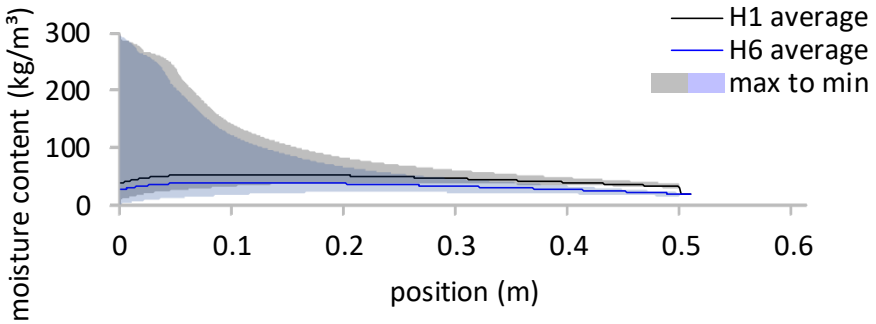

Fig. 5.41: Moisture content profile in rammed earth wall assembly for different rammed earth materials.

Although the moisture content in the rammed earth wall decreases for the H6 rammed earth as compared to for the H1 rammed earth, the relative humidity increases. Fig. 5.42 shows the average relative humidity profile over the year. This increase in relative humidity for the H6 rammed earth is explained by the different course of the moisture retention curve of both materials, where the H6 rammed earth is less hygroscopic, presenting more wide pores instead.

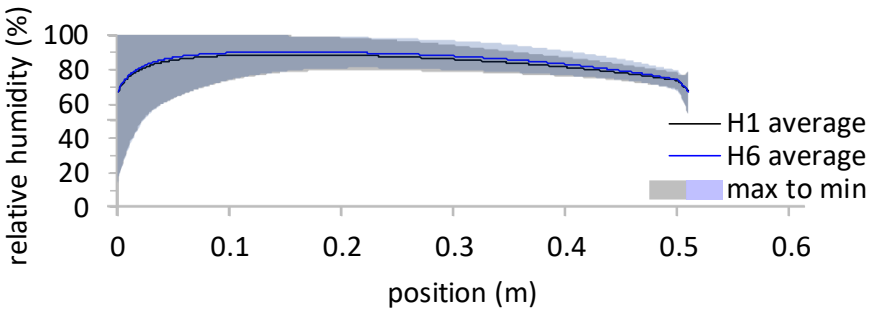

Fig. 5.42: Relative humidity profile in rammed earth wall assembly for different rammed earth materials.

5.3.4.2 Thermal insulation quality and hygro-thermal insulation quality

The U-values of the H6 rammed earth wall assemblies are slightly smaller than those of the H1 rammed earth wall assemblies. This is because the moisture contents in the H6 rammed earth wall are smaller. The increase in U-value by moisture in the insulation, on the other hand, is greater for the H6 rammed earth wall assemblies. This is explained by the higher relative humidity at the interface between the rammed earth wall and the interior layers for the H6 rammed earth wall, whereby the moisture content in the wood fibre and calcium silicate insulation materials increases.

5.3.4.3 Interior mould growth

The interior mould growth risk remains zero for the H6 rammed earth wall assemblies, like for the H1 rammed earth wall assemblies.

5.3.4.4 Interstitial mould growth

The interstitial mould growth risk increases for the insulated H6 rammed earth wall assemblies as compared to for the insulated H1 rammed earth wall assemblies. The increase in interstitial mould growth risk is explained by the higher relative humidity at the interface between the rammed

earth wall and the interior layers for the H6 rammed earth wall, which also leads to slightly more summer condensation for the mineral wool insulation system with vapour barrier.

5.3.4.5 Dripping moisture

The dripping moisture risk for the mineral wool insulation system with vapour barrier increases slightly for the H6 rammed earth wall as compared to for the H1 rammed earth wall. This is explained by the higher relative humidity at the interface between the rammed earth wall and the interior layers for the H6 rammed earth wall.

5.3.4.6 Wood decay

The wood decay risk increases significantly for the non-insulated H6 rammed earth wall as compared to for the non-insulated H1 rammed earth wall. This is because the relative humidities in the H6 rammed earth wall are greater, cf. Fig. 5.42. The same holds for the insulated wall assemblies. Only for the capillary active calcium silicate insulation system, the wood mass loss after ten years remains smaller than 100 % (87 %). For the vapour tight, the mineral wool, and the wood fibre insulation systems, the wood mass loss reaches 100 % after 3.4 years, 5.2 years, and 7.1 years, respectively. The wood mass loss starts within 11 months for the non-insulated H6 rammed earth wall and within one to two months for the insulated H6 rammed earth wall assemblies. House 6 in practice is oriented differently, so that the wooden beams are embedded in the 50 ° North-East and in the 230 ° South-West oriented façade, where the wind-driven rain load is generally lower, see Fig. 5.6 (b) and Fig. G.2 in Appendix G.

5.3.4.7 Frost damage

The number of frost-thaw cycles increases for the H6 rammed earth wall assemblies as compared to for the H1 rammed earth wall assemblies. This increase is less pronounced for the capillary active insulation systems. The increase in the number of frost-thaw cycles for the H6 rammed earth wall could be explained by the smaller capillary absorption coefficient of the H6 rammed earth material. For the smaller the water penetration coefficient (which is proportional), the more moisture is stored near the outer surface, which could induce more frost-thaw cycles. This trend is also observed in (Vereecken et al., 2015). Moreover, the H6 rammed earth having overall wider pores, lower moisture contents are required for freezing in the main temperature range.

5.3.4.8 Erosion

The number of erosion risk hours decreases for the H6 rammed earth wall assemblies as compared to for the H1 rammed earth wall assemblies. Given that the capillary moisture content of both materials is similar, this could be explained by the smaller capillary absorption coefficient of the H6 rammed earth material whereby the moisture content at the exterior surface remains overall lower in time for the H6 rammed earth wall assemblies because moisture that remains closer to the exterior surface can also dry out more easily.

5.3.4.9 Conclusion

Table 5.7 shows the results of the hygrothermal performance criteria for the H6 rammed earth wall assemblies. Although the H6 rammed earth wall absorbs wind-driven rain less fiercely, most moisture performance worsens as compared to for the H1 rammed earth wall. This is due to the shape of the moisture retention curve of the H6 rammed earth material in the hygroscopic range, leading to higher relative humidities. Since the impact can be significant, it is important to properly determine all the hygric properties involved.

Table 5.7: Overview of hygrothermal performances of H6 rammed earth wall assemblies for 10 cm thick insulation systems. Colour code: red = extreme or hazardous, orange = requires special attention, green = acceptable.

	reference	XPS	MW+VB	MW	WF	CS
Thermal insulation quality (W/(m² K))	0.78	0.16	0.21	0.23	0.31	0.30
ΔU-value by insulation moisture (%)	NA	0	0	0	10.3	2.1
Interior mould growth (-)	0	0	0	0	0	0
Interstitial mould growth (-)	0	4.9 e [a]	4.9 e	4.9 e	4.4 e	1.1 e
Dripping moisture (%)	NA	NA	4.2	NA	NA	NA
Wood decay (%)	66 m [b]	289 s [c]	290 s	193 m	142 m	87 m
Frost damage (-)	1	3	3	3	2	2
Erosion (h)	7	7	7	7	7	7

[a] e: at the exterior side of the insulation system; [b] m: in the middle of the wall; [c] s: at the side of the wall

5.3.5 Influence of rammed earth wall thickness

5.3.5.1 Introduction and general results

Rammed earth walls in practice are mostly 65 cm to 40 cm thick. To study the influence of the rammed earth wall thickness, a 80 cm thick and a 30 cm thick H1 rammed earth wall is simulated. Fig. 5.43 shows the average moisture content in the rammed earth wall over the year. It is observed that the 30 cm thick rammed earth wall dries out easier during spring and summer, while the average moisture content increases during the more rainy autumn and winter, owing to the higher rain penetration. The thicker the rammed earth wall, the flatter the course of the average moisture content over time. Fig. 5.44 shows the moisture content profiles for 80 cm and 50 cm.

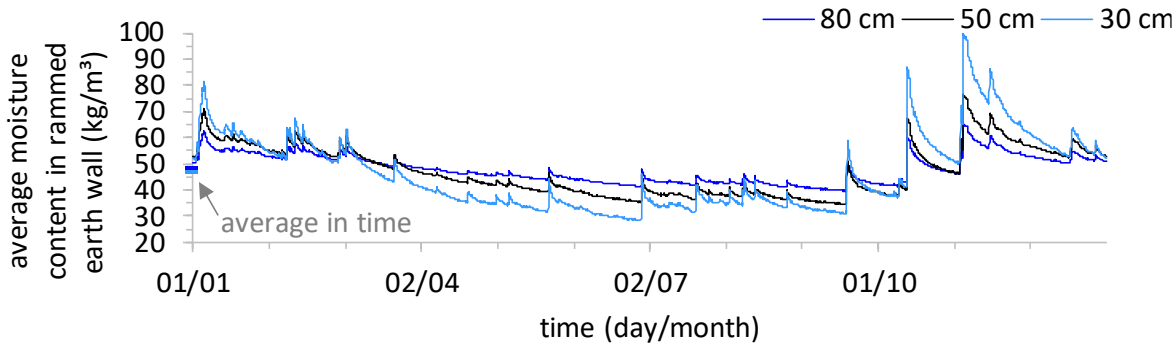

Fig. 5.43: Accumulated moisture in rammed earth wall for different wall thicknesses.

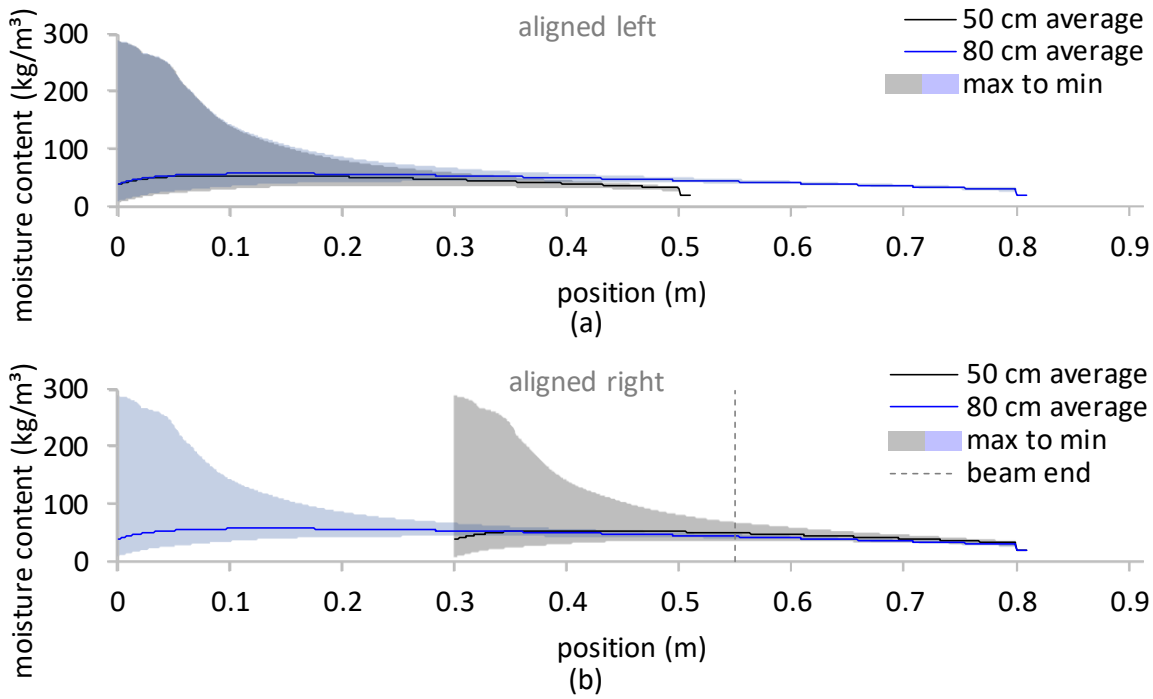

Fig. 5.44: Moisture content profile in rammed earth wall for different wall thicknesses.

5.3.5.2 Thermal insulation quality and hygro-thermal insulation quality

For the 80 cm thick rammed earth wall as compared to the 50 cm thick rammed earth wall, the thermal insulation quality increases for the non-insulated reference wall (as well as for the vapour tight and vapour open insulated wall assemblies) due to the extra material and due to the lower average moisture content during winter and autumn. For the capillary active insulated wall assemblies, moreover, the insulation remains drier because the absorbed wind-driven rain stays further away from the interior rammed earth wall surface, Fig. 5.44 (b).

5.3.5.3 Interstitial mould growth

With the thicker rammed earth wall for the different insulation systems, the mould index at the exterior side of the insulation decreases because of the lower moisture levels in the wall near the interior surface, Fig. 5.44 (b).

5.3.5.4 Dripping moisture

The number of dripping moisture risk hours reduces to zero for the 80 cm thick wall. This is again explained by the moisture levels remaining lower near the interior wall surface, Fig. 5.44 (b).

5.3.5.5 Wood decay

The wood decay risk reduces to zero for the non-insulated wall and for the walls insulated with wood fibre or calcium silicate, and almost zero for the mineral wool insulation system without vapour barrier. This is owing to the combination of the lower rain penetration - the beam end is 30 cm farther away from the exterior surface, Fig. 5.44 (b) - and the provision of enough inward drying ability. For the walls insulated with a vapour tight insulation system on the other hand, the wood mass loss remains > 100 % and invigorates. This is because with the vapour tight insulation systems, the moisture that is transported inward cannot dry out at the interior surface and the outward drying resistance has increased owing to the larger wall thickness.

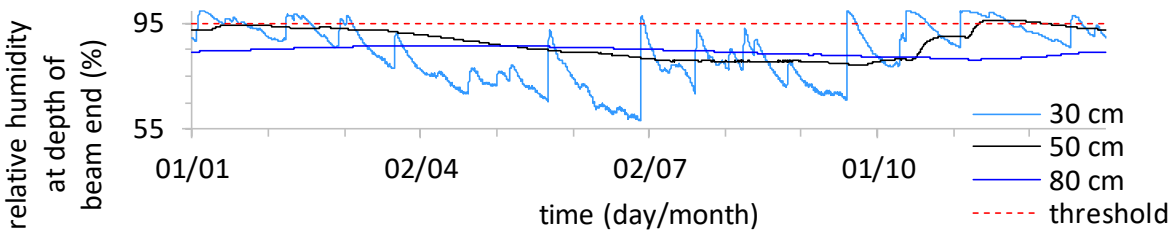

Fig. 5.45: Relative humidity at 25 cm from the interior rammed earth wall surface over time for different wall thicknesses and threshold relative humidity value for wood decay.

Fig. 5.45 shows for the non-insulated reference wall configurations the relative humidity at the depth of the wooden floor beam end, i.e. at 25 cm from the interior rammed earth surface, for the different wall thicknesses. It is observed that the smaller the rammed earth wall thickness, the more the course of the relative humidity over time can be linked to the exterior climate conditions and hygrothermal states. For the non-insulated 30 cm thick H1 rammed earth wall, the total wood mass loss increases to 60 % after ten years.

5.3.5.6 Frost damage

The frost damage risk increases slightly for the non-insulated 80 cm thick rammed earth wall as compared to for the non-insulated 50 cm thick rammed earth wall. This is because the moisture contents near the exterior surface are slightly higher owing to the reduced inward drying ability, Fig. 5.44 (a).

5.3.5.7 Conclusion

Table 5.8 summarises the hygrothermal performance results for the 80 cm thick rammed earth wall. It is concluded that a thicker rammed earth wall overall favours the insulatability of rammed earth walls. In particular the wood decay risk (besides summer condensation, as well as interstitial mould growth) decreases significantly - except for the vapour tight insulation systems - for a larger rammed earth wall thickness because of the lower rain penetration.

Table 5.8: Overview of hygrothermal performances of 80 cm thick H1 rammed earth wall assemblies for 10 cm thick insulation systems. Colour code: red = extreme or hazardous, orange = requires special attention, green = acceptable.

	reference	XPS	MW+VB	MW	WF	CS
Stationary U-value in practice (W/(m² K))	0.59	0.15	0.19	0.20	0.27	0.27
ΔU-value by insulation moisture (%)	NA	0	0	0	6.8	1.5
Interior mould growth (-)	0	0	0	0	0	0
Interstitial mould growth (-)	0	4.6 e [a]	4.6 e	4.1 e	3.5 e	0
Dripping moisture (%)	NA	NA	0	NA	NA	NA
Wood decay (%)	0	231 s [b]	228 s	10 m [c]	0	0 [d]
Frost damage (-)	1	2	2	2	2	2
Erosion (h)	13	14	14	14	13	13

[a] e: at the exterior side of the insulation system; [b] s: at the side of the wall; [c] m: in the middle of the wall; [d] Also verified and valid for H6 rammed earth wall.

5.3.6 Influence of wall orientation

5.3.6.1 Introduction and general results

Besides the materials, the climate conditions influence the hygrothermal response. The different boundary conditions per wall orientation yield a different hygrothermal response. Fig. 5.46 shows the cumulative wind-driven rain load over the year for each of the four main different wall orientations, cf. Fig. 5.6 (b). Besides the wind-driven rain, the solar heat gains differ, as well as the exterior convective surface heat and moisture transfer coefficients. Fig. 5.47 shows the hourly average moisture content in the H1 rammed earth wall over the year for the different orientations. It is observed that the moisture contents for the North are greater than for the East, which is explained by the lower exterior equivalent temperatures for the North that lead to a reduced outward drying potential (Janssen et al., 2007b); (Zhou et al., 2016). Furtheron, the impact of the wall orientation on the thermal insulation quality is regarded. Furthermore, the frost damage risk is evaluated for the North orientation, which is the coldest. Last but not least, the impact of interior insulation on the hygrothermal performance of an East oriented wall, which has the lowest wind-driven rain load, is studied for different insulation systems.

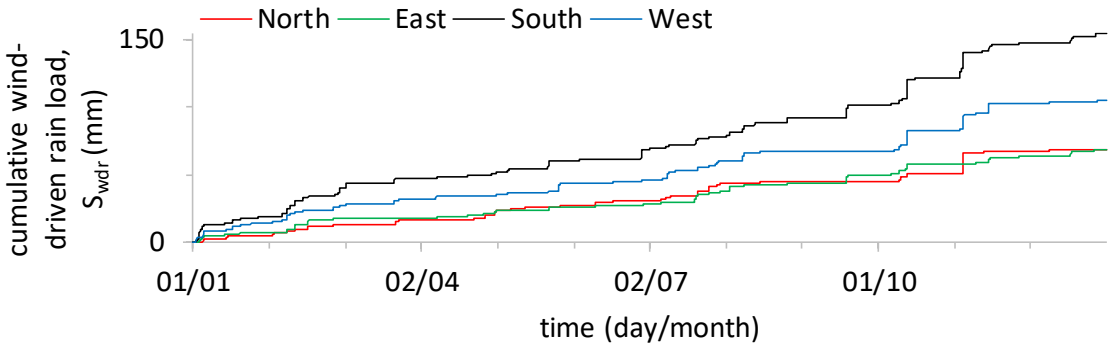

Fig. 5.46: Cumulative wind-driven rain load over the year 2014 for different wall orientations.

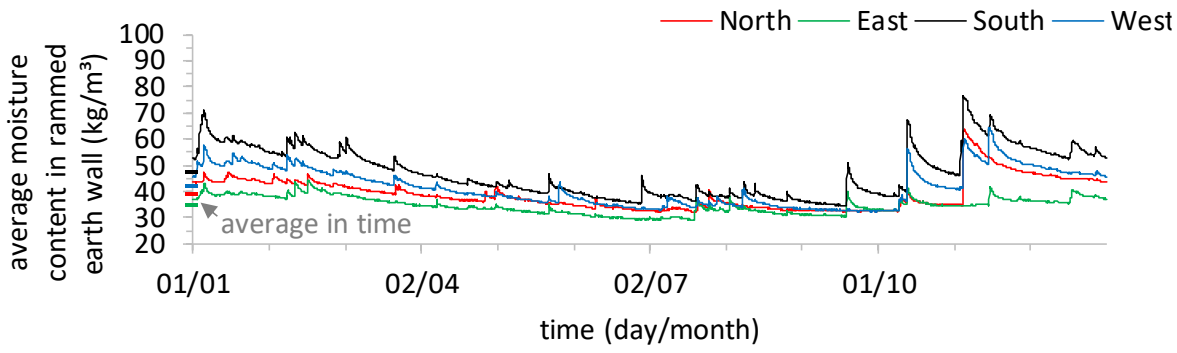

Fig. 5.47: Accumulated moisture in H1 rammed earth wall for different wall orientations.

5.3.6.2 Thermal insulation quality

Fig. 5.48 shows the stationary U-value in practice for the four different wall orientations for the non-insulated reference wall and for different 10 cm thick insulated wall assemblies. (The results for the vapour tight mineral wool insulation system with vapour barrier are not included.) For the non-insulated reference wall, it is observed that the U-value varies with the wall orientation from the lowest U-value for the South orientation over the East and then the West to the highest U-value for the North orientation. The increase in U-value for the North orientation as compared to the South orientation amounts to 28 %. The same order is found, with lower U-values, but with more equally distributed differences in U-value between the different orientations when the dry thermal conductivity of the rammed earth material is used. So this order is mainly explained by the solar heat gains. The increase in U-value by moisture is the greatest for the South oriented wall, which is explained by the greatest wind-driven rain load. For the capillary active wood fibre and calcium silicate insulation systems, a slightly larger insulation thickness than 10 cm may be required for most of the wall orientations to meet the maximum U-value requirement.

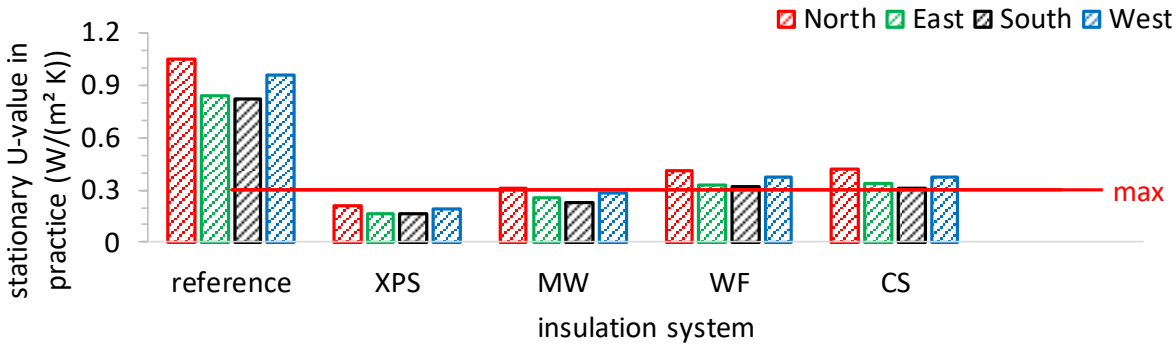

Fig. 5.48: Stationary U-value in practice for different wall orientations for non-insulated reference H1 rammed earth wall and for insulated wall assemblies with different insulation systems.

5.3.6.3 Frost damage

Fig. 5.49 shows the number of frost-thaw cycles for the non-insulated reference wall and for the different insulated wall assemblies for the South and for the North oriented façade. It is observed that the number of frost-thaw cycles decreases for the North orientation as compared to for the South orientation. This indicates that, for the frost damage, the lower wind-driven rain load for the North than for the South is more important than the lower exterior equivalent temperatures.

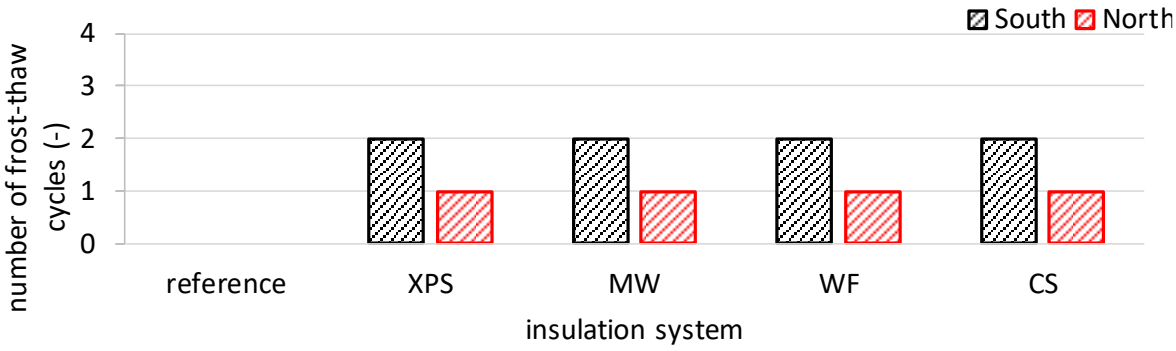

Fig. 5.49: Frost damage risk for different wall orientations with different insulation systems.

5.3.6.4 Insulatability

Table 5.9 shows the impact of interior insulation on the hygrothermal performance of an East oriented wall for different insulation systems. It is observed that all the insulation systems give acceptable risks for the East orientation with the low wind-driven rain load. This is in contrast with the South orientation with the high wind-driven rain load where the calcium silicate system is the only recommendable insulation system. There is no wood decay risk for this East orientation and interstitial condensation is more important than the wind-driven rain load. All together, the choice of the insulation system can depend on the wall orientation through the wind-driven rain load.

Table 5.9: Overview of hygrothermal performances of East oriented H1 rammed earth wall assemblies for 10 cm thick insulation systems. Colour code: red = extreme or hazardous, orange = requires special attention, green = acceptable.

	reference	XPS	MW+VB	MW	WF	CS
Stationary U-value in practice (W/(m² K))	0.84	0.17	0.22	0.26	0.33	0.34
ΔU-value by insulation moisture (%)	NA	0	0	0	6	2
Interior mould growth (-)	0	0	0	0	0	0
Interstitial mould growth (-)	0	1.1 e [a]	1.0 e	3.0 e	1.2 e	0
Dripping moisture (%)	NA	NA	0	NA	NA	NA
Wood decay (%)	0	0	0	0	0	0
Frost damage (-)	0	1	1	1	0	0
Erosion (h)	0	0	0	0	0	0

[a] e: at the exterior side of the insulation system

5.3.6.5 Conclusion

The North orientation is the most severe for the thermal insulation quality. This is because the North orientation has the lowest incident direct short-wave radiation from the sun, leading to a lower exterior equivalent temperature, and hence an increased heat loss. Although the North is colder, the frost damage risk for the North is smaller than for the South orientation (in 2014). This is explained by the smaller wind-driven rain load for the North. Finally, the choice of the insulation system can depend on the wall orientation through the wind-driven rain load. For example, whereas for the South orientation with the high wind-driven rain load the calcium silicate system is the only recommendable insulation system, all the investigated insulation systems give acceptable risks for the East orientation with the low wind-driven rain load. Besides, for a smaller wind-driven rain load, interstitial condensation can become a more important moisture load.

5.3.7 Influence of fracture failure, buckling failure, and clay swelling damage

5.3.7.1 Introduction

Relative to Section 5.3.2, the influence of three additional mechanical performance indicators on the hygrothermal risk assessment is evaluated. It concerns the load-bearing section loss for fracture failure, the relative buckling stress for buckling failure, and the number of clay swelling cycles for clay swelling damage. Moreover, the influence of two variants of the mechanical properties is determined (cf. Section 5.2.2.1).

5.3.7.2 Mechanical response with variant 1 of the mechanical properties

Table 5.10 shows the results of the impact of the five different 10 cm thick interior insulation systems on the hygrothermal performance of the wall (cf. Section 5.3.2) including the results of the mechanical response with variant 1 of the mechanical properties. Nothing unusual is observed for the risks on fracture failure, buckling failure, and clay swelling damage for the non-insulated reference wall. Moreover, these risks remain quasi unchanged upon interior insulation. The results are discussed in more detail in Appendix J. In Appendix K, the influence of not taking into account the hygric stress is demonstrated.

Table 5.10: Overview of hygrothermal performances for non-insulated reference H1 wall and with insulation systems, with variant 1 of the mechanical rammed earth properties. Colour code: red = extreme or hazardous, orange = requires special attention, green = acceptable.

	reference	XPS	MW+VB	MW	WF	CS
Stationary U-value in practice (W/(m² K))	0.82	0.16	0.21	0.23	0.32	0.31
ΔU-value by insulation moisture (%)	NA	0	0	0	9.8	2.0
Interior mould growth (-)	0	0	0	0	0	0
Interstitial mould growth (-)	0	4.8 e [a]	4.8 e	4.7 e	4.1 e	0.9 e
Dripping moisture (%)	NA	NA	4	NA	NA	NA
Wood decay (%)	1.1 m [b]	201 s [c]	200 s	128 s	98 m	37 m
Fracture failure (%)	15.2	15.2	NE [d]	15.2	NE	15.4
Buckling failure (%)	4.4	3.9	NE	4.0	NE	4.3
Clay swelling damage (-)	10	8	NE	9	NE	8
Frost damage (-)	0	2	2	2	2	2
Erosion (h)	13	14	14	14	13	13

[a] e: at exterior side of insulation system; [b] m: in middle of wall; [c] s: at side of wall; [d] Not evaluated.

5.3.7.3 Mechanical response with variant 2 of the mechanical properties

This outcome is completely different when variant 2 of the mechanical properties is assumed. Fig. 5.50 shows the results for the fracture failure, buckling failure, and clay swelling damage for the different insulation systems. It is observed that structural collapse occurs for the vapour tight, the vapour open, and the wood fibre insulation systems as the load-bearing section loss and/or the relative buckling stress reaches or exceeds 100 %. Only the calcium silicate system remains usable.

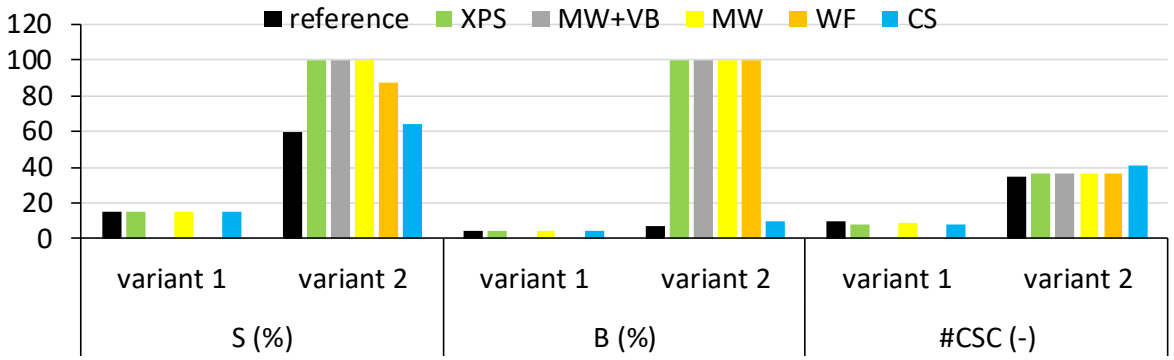

Fig. 5.50: Mechanical risks for non-insulated reference wall and for insulated wall assemblies with two variants of the mechanical properties.

Table 5.11: Overview of hygrothermal performances for non-insulated reference H1 wall and with insulation systems, with variant 2 of the mechanical rammed earth properties. Colour code: red = extreme or hazardous, orange = requires special attention, green = acceptable.

	reference	XPS	MW+VB	MW	WF	CS
Stationary U-value in practice (W/(m² K))	0.82	0.16	0.21	0.23	0.32	0.31
ΔU-value by insulation moisture (%)	NA	0	0	0	9.8	2.0
Interior mould growth (-)	0	0	0	0	0	0
Interstitial mould growth (-)	0	4.8 e [a]	4.8 e	4.7 e	4.1 e	0.9 e
Dripping moisture (%)	NA	NA	4	NA	NA	NA
Wood decay (%)	1.1 m [b]	201 s [c]	200 s	128 s	98 m	37 m
Fracture failure (%) *with variant 2*	59.8	100	100	100	87.8	63.8
Buckling failure (%) *with variant 2*	7.0	> 100	> 100	> 100	> 100	9.2
Clay swelling damage (-) *with variant 2*	35 [d]	36 [d]	36 [d]	36 [d]	36 [d]	41 [d]
Frost damage (-)	0	2	2	2	2	2
Erosion (h)	13	14	14	14	13	13

[a] e: at exterior side of insulation system; [b] m: in middle of wall; [c] s: at side of wall; [d] exterior side.

5.3.7.4 Conclusion

Whether the mechanical risks of fracture failure, buckling failure, and clay swelling damage invigorate upon interior insulation is related to assumptions of mechanical properties. It is shown that with a realistic assumption of the mechanical properties, it is possible that severe structural damage will occur. This is possible for all the investigated insulation systems except for the calcium silicate. So this needs to be investigated further in future research.

5.4 Conclusion

The interior insulatability of rammed earth walls above the stem wall is investigated. Five different interior insulation systems are considered: a vapour tight XPS, a vapour tight mineral wool plus vapour barrier, a vapour open mineral wool, a capillary active wood fibre, and a capillary active calcium silicate insulation system.

Whereas the XPS and mineral wool insulation systems perform better in thermal insulation quality, they cause the most moisture problems. So, for all studied cases on the South wall with the high wind-driven rain load, in particular the vapour tight insulation systems, but also the vapour open mineral wool insulation system and besides also the wood fibre insulation system to a less extent (unless the rammed earth wall is sufficiently thick), are rejected because they lead to hazardous amounts of wood decay of embedded floor beams and significant interstitial mould growth. In order to keep these risks to a minimum, it is best to use a capillary active calcium silicate insulation system enabling optimal drying inwards. Besides, the wood fibre insulation system yields a higher risk on by moisture reduced thermal insulation quality than the calcium silicate insulation system. Moreover, summer condensation can occur for the mineral wool insulation system with vapour barrier, with dripping moisture problems as a consequence. The XPS and mineral wool insulation systems also tend to induce a higher risk of frost damage and erosion than the capillary active insulation systems, although the risk of these damage patterns remains limited (under the investigated climate conditions). On the East wall with the low wind-driven rain load, all the insulation systems give acceptable risks.

When the mechanical risks are also taken into account, finally, all except the capillary active calcium silicate insulation system can cause collapse by fracture failure and/or buckling failure. Whether this is possible depends *inter alia* on the mechanical properties of the rammed earth material. With a rammed earth material that maintains its strength throughout the hygroscopic

range (i.e. until 97 % relative humidity), none of the insulation systems causes mechanical issues. But with a rammed earth material that loses its strength sharply in the high hygroscopic range, the calcium silicate is the only insulation system that does not lead to structural collapse for the South oriented wall.

6 Conclusion

6.1 Conclusions

State of the art

The state of the art study showed that two preliminary objectives needed to be tackled to get to the evaluation of the insulatability: the complete hygric material characterisation and the mechanically completed set of performance indicators enabling a comprehensive evaluation.

Material characterisation

For the complete hygric material characterisation, the moisture retention curve, the vapour permeability curve and the liquid permeability curve need to be determined. Furthermore, the bulk density and the capillary moisture content are necessary to determine the moisture retention curve. And the vacuum saturation moisture content is necessary to determine the vapour permeability curve. The full-range hygric characterisation is performed for two rammed earth materials that are extracted from traditional rammed earth buildings.

For the determination of the moisture retention curve, mercury intrusion porosimetry is performed. The saturation moisture content that is the necessary maximum value of the mercury intrusion porosimetry curve, is determined as the sum of the intruded mercury volume at the pressure corresponding to 75% relative humidity and the pore volume filled by moisture at the 75% relative humidity equilibrium moisture content. The bulk density that is used to express the moisture content volumetrically is determined by means of 70°C oven drying for the dry mass and immersion in mercury for the volume. The representativeness of the mercury intrusion porosimetry result for the moisture retention curve is approved by means of comparison with absorption data. Desiccator testing is performed to complete the moisture retention curve in the hygroscopic range. The capillary moisture content to curtail the moisture retention curve as to represent the main wetting curve in practice is determined through confined (composite) capillary absorption testing.

For the determination of the liquid permeability curve, the capillary absorption test is performed, with X-ray projection. The capillary absorption test for this purpose is adapted for rammed earth materials, that otherwise liquefy and expand upon contact with water. Hence, a thin permeable brick wick and contact filter paper are applied as lower sample parts, to counter the liquefaction, and a confining sealing is utilised, to counter the expansion. The capillary absorption coefficient and the capillary moisture content (after subtraction of the wick's moisture mass) obtained in this way are representative for the stable material. The characteristic profile that is necessary to derive the moisture diffusivity, is determined through the Boltzmann transformation, that is adapted for the hydraulic impact of the wick and paper via their equivalent height. This equivalent height is determined based on the capillary absorption process. Cup testing is performed for the determination of the vapour permeability.

Performance indicators

Four mechanical performance indicators have been developed, based on damage patterns observed in practice (excluding rising damp): fracture failure, buckling failure, clay swelling damage, and erosion. The fracture failure risk is indicated by the load-bearing section loss at the wall bottom when the total stress reaches or exceeds the compressive strength. The buckling failure risk is indicated by the ratio of the total average stress over the wall section at the wall bottom to the buckling strength of the wall. The clay swelling damage risk is indicated by the number of shear failure induced clay swelling cycles within the wall. And the erosion risk is indicated by the number of hours that the moisture content of the exterior wall surface exceeds 80% of the capillary moisture content while the wind-driven rain load is greater than zero. These four new mechanical performance indicators are added to the list of existing hygrothermal performance indicators for the analysis: thermal insulation quality, thermal transient response, interior mould growth, interstitial mould growth, dripping moisture, wood decay, hygric transient response, and frost damage.

Interior insulation analysis

The interior insulatability of unplastered rammed earth walls above the stem wall is investigated by means of hygrothermal numerical simulation. For low risk acceptability, the moisture reference

year and orientation that are most severe regarding wind-driven rain moisture build-up are used. The wind-driven rain load is imposed according to the standard. Rising damp is excluded.

Resultantly, it is found that the interior insulation of rammed earth walls can cause mechanical failure. This is the case when the compressive strength of the rammed earth material decreases rapidly in the hygroscopic range with increasing relative humidity, with all insulation systems except the capillary active calcium silicate insulation system. The second main risk to be avoided is the decay of embedded wooden floor beams. Also for this, a capillary active calcium silicate insulation system is most suitable. An insulation thickness of ca. 10 cm is fitted.

Under the investigated conditions, using a vapour tight XPS insulation system yields wood decay and interstitial mould growth as well as possibly fracture failure and buckling failure. A vapour tight mineral wool insulation system with vapour barrier yields wood decay, interstitial mould growth and dripping moisture, as well as possibly fracture failure and buckling failure. A vapour open mineral wool insulation system yields wood decay and interstitial mould growth as well as possibly fracture failure and buckling failure. A capillary active wood fibre insulation system yields wood decay, interstitial mould growth and a moderate risk on suboptimal thermal insulation quality, as well as possibly buckling failure. All the insulation systems (including the capillary active calcium silicate) induce a small risk of frost damage. For a wall orientation with a low wind-driven rain load, all the insulation systems yield acceptable risks, excluding possible risks related to the mechanical response.

Besides, the hygrothermal performance analysis points out that the complete hygric material characterisation is a must. This is because overhygroscopic regimes occur frequently and largely determine the research outcomes. Moreover, the exact shape of the hygric material property functions can significantly influence the hygrothermal performance.

6.2 Recommendations for improvements and further research

State of the art

The first hypothesis in hygrothermal modelling is that the material structure is invariable. To find out to which extent this assumption is valid for rammed earth materials, the impact of material evolution should be investigated.

Whereas in past research, the wind-driven rain load was not considered, in the present work, the wind-driven rain load is taken into account according to the standard. The wind-driven rain load in reality is presumably between zero and standard level, because rammed earth buildings often have a lager roof than standard buildings. Since the wind-driven rain load has a large impact on the insulatability of rammed earth buildings, the wind-driven rain load on rammed earth building walls should be investigated.

Material characterisation

The open porosity, used to vertically shift the mercury intrusion porosimetry curve and to determine the vapour permeability curve, should rather be measured independently, e.g., by means of helium pycnometry. The result could be compared with the presently determined open porosity based on the mercury intrusion porosimetry and desiccator testing.

More research should be done to determine the moisture retention curve more reliably, in particular for the rammed earth materials for which the mercury intrusion porosimetry and the absorption results diverge.

The reliability of the moisture permeability in the intermediate range should be evaluated, e.g., by means of isothermal drying test calibration. In doing so, proper attention should be paid to the avoidance of material evolution (like in the redeveloped capillary absorption test).

More rammed earth materials should be characterised and the hygric, thermal, and mechanical properties should be determined. The present work has shown that under certain circumstances, the interior insulation of rammed earth walls causes mechanical risks. This may also be the case

when an exterior plaster layer is present or when rising damp is included in the analysis (cf. below). For some houses, the ability to cope with more heterogenous materials should be provided.

Performance indicators

Rising damp should be investigated and a rising damp performance indicator should be developed. For this, the material properties of the stem wall should be determined as well.

Differential hygrothermal stresses and strains at the building level should be investigated, especially when an exterior plaster layer is present (cf. below).

The mechanical performance indicators should be validated in future research, including the magnitude and variation with capillary pressure of the hygric stress. More mechanical failure mechanisms could be considered, for example including the wind load or a seismic load.

Interior insulation analysis

While the present work focused on the interior insulation of rammed earth walls above the stem wall, the architecture of rammed earth buildings in practice always comprises a stem wall. This stem wall has to be thermally insulated too because otherwise it becomes a thermal bridge. The insulatability of the stem wall should hence be investigated. And this should go hand in hand with the rising damp analysis (cf. above). It could for example be proposed to insulate the stem wall exteriorly, also under the ground level, whereby rising damp is reduced.

Since the hygric properties of the H2 rammed earth are very different from those of H1 and H6, the present work could be improved by including the H2 rammed earth until the end of the material characterisation and until the end of the interior insulation analysis.

The same climate year is repeated ten times for the mould growth and the wood decay risk in the present work. In future research, ten successive future climate years could be used to obtain a representative climate loading for the risk evaluation. Moreover, the used climate year 2014 is not ideally representative or suited regarding typical wind-driven rain load in the different wind

directions and frost conditions. This could be improved by composing a hybrid climate year, e.g., consisting of elements of 2013 and 2014.

The wooden beams are not simulated in the present work. This could be improved in future research for a more reliable assessment of the wood decay risk.

The conclusions of the present work are based on assumptions of the mechanical properties. In order to come to definitive conclusions, more research is necessary, both concerning the validation of the mechanical performance indicators and the measurement of the mechanical properties of rammed earth materials.

The interior insulatability conclusions of the present work are based on a limited deterministic study. To facilitate a comprehensive analysis and investigating more parameters, such as the wind-driven rain load, …, an automatised probabilistic risk assessment tool could be used.

Since a significant part of the rammed earth heritage is exteriorly plastered, and these houses need to be insulated as well, the insulatability of these exteriorly plastered rammed earth walls should be investigated in case one does not want to remove the exterior plaster layer, see Fig. 1.2.

A Mould growth

The mould index M (-) calculated by the updated VTT model (on an hourly basis in the present work) can vary between 0: no mould growth, over inter alia 1: start of microscopic mould growth and 3: first visually detectable mould growth, and 6: heavy and dense mould growth. The parameter that determines whether mould growth conditions are favourable ($\Delta M/\Delta t > 0$) or unfavourable ($\Delta M/\Delta t \leq 0$) is the relative humidity of air near the surface. The critical surface relative humidity is defined as "the lowest humidity for mould growth if the material is exposed to it for a long enough period", Eqs. (A.1)-(A.6), Fig. A.1. These calculations are for materials belonging to the (mould growth) very sensitive class. The critical surface relative humidity (mainly) decreases with increasing temperature, roughly down to a minimum of 80% for very sensitive materials at or above 20 °C. However, all materials featured in the main text of this thesis are assumed to belong to the (mould growth) sensitive class (Vereecken & Roels, 2012) because this qualification is the more realistic one for rammed earth materials.

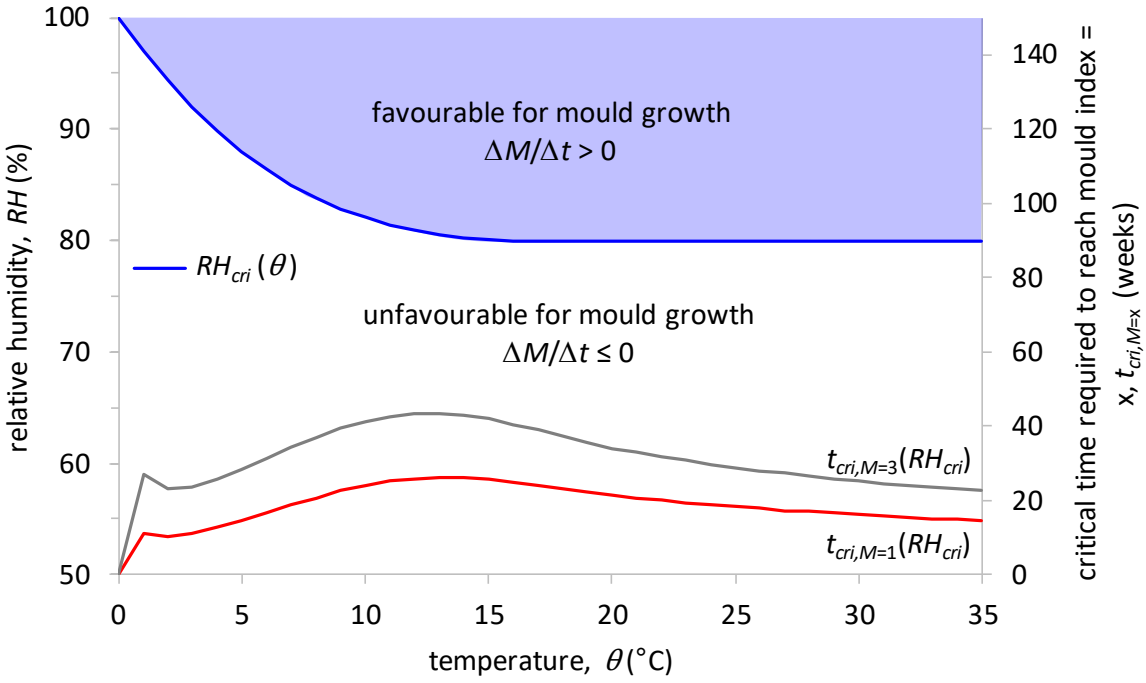

Fig. A.1: Mould growth conditions on materials classified as very sensitive. Lower curves with right vertical axis are added as example.

$$RH_{cri} = \begin{cases} -0.00267\theta^3 + 0.16\theta^2 - 3.13\theta + 100 & when\ \theta < 20\ °C \\ RH_{cri,min}^{(very\ sensitive)} = 80\% & when\ \theta \geq 20\ °C \end{cases} \quad \text{(A.1)}$$

$$M_{t+\Delta t} = M_t + \underbrace{\Delta t}_{1\mathrm{h}} \times \begin{cases} \dfrac{k_1 k_2}{24 \times 7 \times t_{cri,M=1}} (\theta_{t+\Delta t}, RH_{t+\Delta t}, M_t) \quad when\ favourable \\ -0.00133 \quad when\ unfavourable\ and\ t + \Delta t - t_0 \leq 6h \\ 0 \quad when\ unfavourable\ and\ 6h < t + \Delta t - t_0 \leq 24h \\ -0.000667 \quad when\ unfavourable\ and\ t + \Delta t - t_0 > 24h \end{cases} \tag{A.2}$$

$$t_{cri,M=1} \overset{(very\ sensitive)}{=} \exp(-0.68 \times \ln(\theta) - 13.9 \times \ln(RH) + 66.02) \tag{A.3}$$

$$k_1 \overset{(very\ sensitive)}{=} \begin{cases} 1 \quad when\ M < 1 \\ 2 \quad when\ M \geq 1 \end{cases} \tag{A.4}$$

$$k_2 = \max\left(1 - \exp\left(2.3 \times (M - M_{lim})\right); 0\right) \tag{A.5}$$

$$M_{lim} \overset{(very\ sensitive)}{=} \max\left(1 + 7\frac{RH_{cri} - RH}{RH_{cri} - 100} - 2\left(\frac{RH_{cri} - RH}{RH_{cri} - 100}\right)^2; 0\right) \tag{A.6}$$

RH	relative humidity	%
θ	temperature	°C
M	mould index	-
t	time	h
k	growth rate parameter	-
$t_{cri,M=1}$	critical time required to reach M=1 (start growth)	weeks
$t + \Delta t - t_0$	time exposed to unfavourable conditions	h
$_{cri/min/lim}$	critical / minimum / maximum limit	

B Frost damage

The expansion of pore water by 9% when freezing from 0 °C and lower temperatures on can lead to material frost damage. Five different mechanisms for the generation of frost stresses (during moist freezing) can be distinguished (Scherer, 2006): expansion pressure (freezing of ice-confined liquid), hydraulic pressure, crystallisation pressure (in fine pores), equilibration pressure (in large ice formations), and differential pressure (freezing of moist exterior wall surface layer). In each case (not used further), cracking occurs when the stresses exceed the tensile strength of the material (Zhou et al., 2017). The tensile strength of rammed earth is typically estimated as one-tenth of its compressive strength (Gerard et al., 2015). Besides, the quality of a material to resist frost damage is related to its deformability and its pore volume distribution (Hens, 2011).

The freezing point of water decreases in finer pores (this is the Gibbs-Thomson effect). Hence, frost occurs only at combinations of a low enough temperature and a high enough moisture content (or capillary pressure), which are interdependent frost-variables, Fig. B.1. Their relationship is determined by means of a combination of the Gibbs-Thomson equation (Koči et al., 2017) and the Young-Laplace equation: Eq. (B.1). The risk on frost damage is indicated by the maximum number of frost-thaw cycles at the same position in the wall by the end of the simulation period.

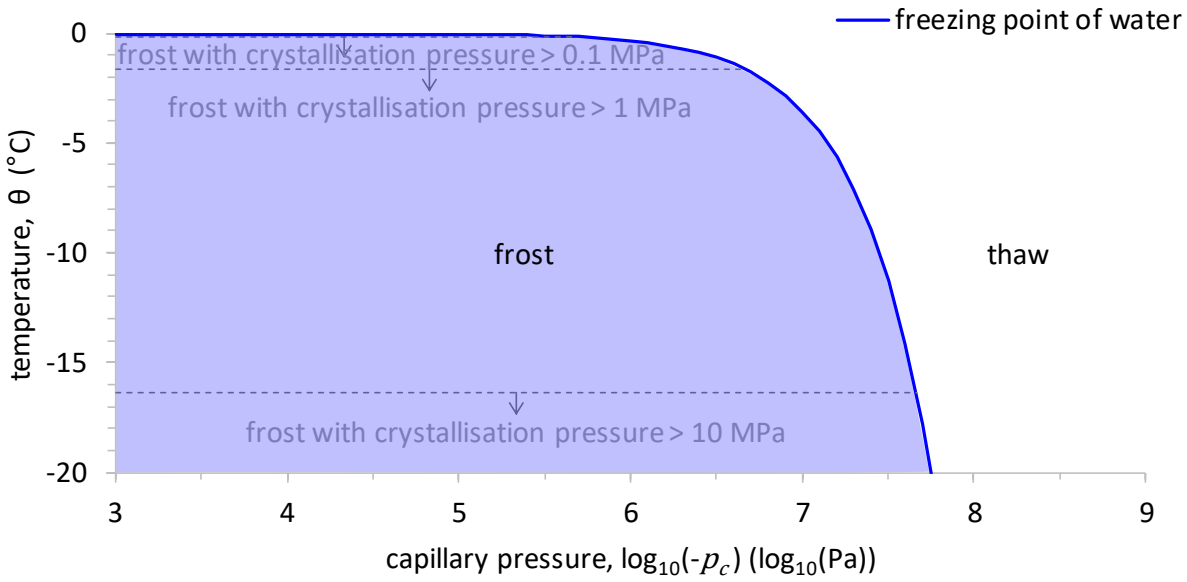

Fig. B.1: Frost conditions in porous materials. Crystallisation pressure lines (Chanvillard & Scherer, 2006) included for example (not further used in the present work) indicate already that the whole frost range is critical for materials with a poor tensile strength like rammed earth.

$$T_{frost} \overset{Gibbs-Thomson\ equation}{=} T_0 - \frac{2T_0\sigma_{l-i}}{L_{m,l}\rho_l r} \overset{Young-Laplace\ equation}{=} T_0 + \frac{T_0\sigma_{l-i}p_c}{L_{m,l}\rho_l\sigma_{l-a}\cos\vartheta} \qquad (B.1)$$

T_{frost}	freezing point of water in relation to pore radius		K
T_0	standard freezing point of water	273.15	K
σ_{l-i}	surface tension liquid water – ice	0.0317	N/m
$L_{m,l}$	latent heat of melting	333550	J/kg
ρ_l	density of liquid water	1000	kg/m³
r	equivalent pore radius		m
σ_{l-a}	surface tension liquid water – air	0.073	N/m
ϑ	contact angle	0	-
p_c	capillary pressure		Pa
$_{l/i/a}$	liquid / ice / air		

C Surface balances – Detailed theoretical background

The balance of the **heat** fluxes at the **exterior** wall surface (Fig. 2.10) is given by:

$$q_{se} = q_{conv,e} + q_{rad,e} - q_{solar} - q_{l,e} + q_{v,e} \quad \text{(C.1)}$$

$_{s/e/conv/rad}$ surface / exterior / convective / radiative

The **convective** heat exchange is described by use of a convective surface heat transfer coefficient which contains the full mass and heat flow interaction between the surface and fluid:

$$q_{conv,e} = h_{conv,e}\left(T_{se} - T_{e,conv}\right) = h_{conv,e}\left(T_{se} - T_{e,g}\right) \quad \text{(C.2)}$$

h surface heat transfer coefficient W/(m² K)

An average standard value for the exterior convective surface heat transfer coefficient is 20 W/(m² K) (Janssen et al., 2007a). In reality, this coefficient is influenced by a wide range of parameters (building surroundings and geometry, position on façade, façade roughness, wind speed and direction, local airflow pattern, and surface to gas temperature differences (Montazeri et al., 2015)). In order to take into account the wind speed effect, EN15026 states:

$$h_{conv,e} = (4 + 4v)\left(\frac{J}{m^3 K}\right) \quad \text{(C.3)}$$

Herein, the wind speed v (m/s) should be measured near the building surface, which is usually not to hand. Alternatively, Sharples, 1984 takes into account the wind speed and sense:

$$h_{conv,e} = 1.7V_{loc} + 5.1 \quad \text{(C.4)}$$

wherein

$$V_{loc} = 1.8U_{10} + 0.2 \quad \text{(windward)} \quad \text{(C.5)}$$

$$V_{loc} = 0.4U_{10} + 1.7 \quad \text{(leeward)} \quad \text{(C.6)}$$

V_{loc}	local wind velocity	m/s
U_{10}	reference wind speed, climate data	m/s

The **long-wave radiation** exchange between the exterior wall surface and its surrounding surfaces, which are considered to be the sky and ground surface, is given by:

$$\begin{aligned} q_{rad,e} &= F_{Rse-sky}\sigma\left({T_{se}}^4 - {T_{sky}}^4\right) + F_{Rse-ground}\sigma\left({T_{se}}^4 - {T_{ground}}^4\right) \\ &\approx e_{L,se}\sigma\frac{1}{2}\left(4\left(\left(T_{se}+T_{sky}\right)/2\right)^3\left(T_{se}-T_{sky}\right) + 4\left(\left(T_{se}+T_{e,g}\right)/2\right)^3\left(T_{se}-T_{e,g}\right)\right) \\ &\approx e_{L,se}\sigma 4\left(\left(T_{se}+T_{e,rad}\right)/2\right)^3\left(T_{se}-T_{e,rad}\right) = h_{rad,e}\left(T_{se}-T_{e,rad}\right) \end{aligned} \quad \text{(C.7)}$$

σ	Stefan-Boltzmann constant	5.67 x 10^{-8}	W/(m² K⁴)
F_R	radiation factor		-
e	emissivity		-
F	view factor		-
$_L$	long-wave		

A standard value for the exterior radiative surface heat transfer coefficient of 5 W/(m² K) is accepted, which follows from an exemplary calculation with average temperatures and $e_{L,se}$= 0.9. The following steps are applied in Eq. (C.7). The radiation factor for grey body exchange is given by:

$$F_{Ryz} = 1\Big/\left(\frac{\rho_{Ly}}{e_{Ly}} + \frac{1}{F_{yz}} + \frac{\rho_{Lz}A_y}{e_{Lz}A_z}\right) \quad \text{(C.8)}$$

ρ	reflectivity	-
A	surface area	m²

The application of Eq. (C.8) for the situation sketched above, where $A_y \ll A_z$, gives $F_{Ryz} \approx e_{Ly}F_{yz}$. The view factor stands for how surface z is seen by y and in this case, for a vertical wall, $F_{se-sky} = 1 - F_{se-ground} = 1/2$. The ground temperature is assumed to equal the gas temperature, $T_{ground} = T_{e,g}$. The exterior radiation temperature is the by-view-factor-weighted average of the sky- and ground temperature. The sky temperature is obtained by replacing it by a black body (Hens, 2011); the first or the second equality is used depending on the available climate data:

$$T_{sky} = \left(q_{L,sky,horizontal}/\sigma\right)^{1/4} \overset{or}{=} T_{e,g} - \Big(23.8 - 0.2025\big(T_{e,g} - 273.15\big)\Big)\,(1 - 0.87c) \qquad \text{(C.9)}$$

$q_{L,sky,horizontal}$	long-wave sky radiation on a horizontal surface, climate data	W/m²
c	cloud cover, climate data (or constant value assumed)	-

The **short-wave radiation** emanating from the sun which is incident on the exterior wall surface has a direct (from the sun), diffuse (from the sky) and reflected (e.g. ground albedo) component. The absorbed fraction of this total ((perpendicularly) incoming) short-wave radiation is given by:

$$q_{solar} = \alpha_{S,se} q_{S,se} = \alpha_{S,se}\big(q_{S,direct,se} + q_{S,diffuse,se} + q_{S,reflected,se}\big) \qquad \text{(C.10)}$$

α	absorptivity	-
$_S$	short-wave	

The direct radiation share is projected onto the surface normal by use of the incidence angle:

$$q_{S,direct,se} = \max\big(0, q_{S,direct,normal}\cos\chi_{se}\big) \qquad \text{(C.11)}$$

wherein (Hens, 2011)

$$\begin{aligned}\cos\chi = {} & \sin\delta\sin\varphi\cos s_s - \sin\delta\cos\varphi\sin s_s\cos a_s + \cos\delta\cos\varphi\cos s_s\cos\omega \\ & + \cos\delta\sin\varphi\sin s_s\cos a_s\cos\omega + \cos\delta\sin s_s\sin a_s\sin\omega\end{aligned} \qquad \text{(C.12)}$$

wherein (Hens, 2011)

$$\delta = \sin^{-1}\left(-\sin\left(\frac{\pi}{180}23.45\right)\cos\left(\frac{2\pi}{365.25}(day + 10)\right)\right)\frac{180°}{\pi} \qquad \text{(C.13)}$$

χ	sun incidence angle	°
δ	declination	°
φ	latitude	°
s	slope (horizontal surface 0°, vertical surface 90°)	°
a	surface's azimuth (degrees from south; south 0°, east 90°, north 180°, west -90°)	°
ω	time angle (0h -180°, noon 0°, 24h 180°)	°
day	number of days beyond December 31/January 1, at midnight	-

When horizontal radiation measurement data is provided, the normal radiation is calculated by:

$$q_{S,direct,normal} = \min\left(\max\left(0, \frac{q_{S,direct,horizontal}}{\cos\chi_{horizontal}}\right), q_{S,direct,max}\right) \quad \text{(C.14)}$$

The maximum value herein, introduced in order to suppress the otherwise unrealistically high normal radiation values when the sun is near the horizon, is calculated as following (Hens, 2011):

$$h_s > 0\ rad: q_{S,direct,max} = E\ exp(-\ m\ d_R\ Tu_{Atm});$$
$$h_s \leq 0\ rad: q_{S,direct,max} = 0 \quad \text{(C.15)}$$

wherein

$$h_s = \sin^{-1}(\sin\delta\sin\varphi + \cos\delta\cos\varphi\cos\omega) \quad \text{(C.16)}$$

$$E = 1367(W/m^2)\left(1 + 0.03344\cos\left(2\pi/365.25\ (day - 2.75)\right)\right) \quad \text{(C.17)}$$

$$m = (1 - 0.1\,z/1000)/(\sin h_s + 0.15(h_s + 3.885)^{-1.253}) \quad \text{(C.18)}$$

$$d_R = 1.4899 - 2.1099\cos h_s + 0.6322\cos(2h_s) + 0.0253\cos(3h_s) - 1.0022\sin h_s + 1.0077\sin(2h_s) - 0.2606\sin(3h_s) \quad \text{(C.19)}$$

$$Tu_{Atm} = 3.372 + 3.037h_s - 0.296\cos(0.5236\ month) \quad \text{(C.20)}$$

h_s	solar height, calculation Eq. (C.16) or climate data	-
E	solar constant	W/m²
m	air factor (tempering absorption by the atmosphere)	-
z	height above the sea level	m
d_R	optic factor (scattering reflection by the atmosphere)	-
Tu_{Atm}	turbidity of the atmosphere on a clear day with mean air pollution	-
$month$	month's ranking (1 for January and 12 for December)	-

The diffuse radiation (from the sky) that reaches the exterior wall surface is given by:

$$q_{S,diffuse,se} = 1/2\, q_{S,diffuse,horizontal} \tag{C.21}$$

The reflected radiation comprises the direct and diffuse radiation from the reflection by the ground (considering no other surrounding surfaces) and is given by (typically $\rho_{S,ground}$= 0.2):

$$q_{S,reflected,se} = 1/2\, \rho_{S,ground}\left(q_{S,direct,horizontal} + q_{S,diffuse,horizontal}\right) \tag{C.22}$$

The **sensible heat transfer by the wind-driven rain load** is given by:

$$q_{l,e} = h_l g_{l,e} = c_l\left(T_l - T_{ref,h}\right)g_{l,e} = c_l\left(T_{e,g} - T_{ref,h}\right)g_{l,e} \tag{C.23}$$

$T_{ref,h}$	reference temperature for heat	0	K

Herein, the temperature of the rain is assumed to equal the exterior gas temperature, $T_l = T_{e,g}$. The liquid water mass flux is elaborated below Eq. (C.29).

The **sensible and latent heat transport by evaporation** (or condensation) is given by:

$$q_{v,e} = h_v g_{v,e} = \left(c_v\left(T_{v,se} - T_{ref,h}\right) + L_v\right)g_{v,e} = \left(c_v\left(T_{se/e,g} - T_{ref,h}\right) + L_v\right)g_{v,e} \tag{C.24}$$

By using one and the same vapour flux for both the sensible and latent heat, it is assumed that the entire amount of water vapour exchange undergoes the transformation liquid water-water vapour at the surface. This is supported by the fact that moisture in a porous material is mainly accumulated in the form of liquid water (adsorption, capillary condensation, or rain absorption), hence contributing entirely to the (sensible and) latent (share of the) heat flow. The water vapour temperature at the surface equals the surface temperature or the gas temperature depending on the direction of the vapour flux. The water vapour mass flux is elaborated below Eq. (C.32).

The **total heat balance** at the exterior wall surface becomes:

$$\begin{aligned} q_{se} &= h_{conv,e}\left(T_{se} - T_{e,g}\right) + h_{rad,e}\left(T_{se} - T_{e,rad}\right) - \alpha_{S,se} q_{S,se} - c_l\left(T_{e,g} - T_{ref,h}\right)g_{l,e} \\ &\quad + \left(c_v\left(T_{se/e,g} - T_{ref,h}\right) + L_v\right)g_{v,e} \\ &= h_e\left(T_{se} - T_{e,equ}\right) - c_l\left(T_{e,g} - T_{ref,h}\right)g_{l,e} + \left(c_v\left(T_{se/e,g} - T_{ref,h}\right) + L_v\right)g_{v,e} \end{aligned} \tag{C.25}$$

wherein

$$h_e = h_{conv,e} + h_{rad,e} \tag{C.26}$$

and

$$T_{e,equ} = \frac{h_{conv,e} T_{e,g} + h_{rad,e} T_{rad,e} + q_{solar}}{h_e} \tag{C.27}$$

$_{equ}$ equivalent

The **moisture** balance at the **exterior** wall surface (Fig. 2.10) is given by:

$$g_{m,se} = -g_{l,e} + g_{v,e} \tag{C.28}$$

The liquid water mass flux is determined by the amount of wind-driven rain impinging on the surface (the leeward wind-driven rain load is assumed zero) (Janssen et al., 2007b):

$$g_{l,e}\ 3600(s/h) = R_{wdr} = \rho_l \alpha\ U_{10} \left(\frac{R_h/\rho_l}{1\ mm/h}\right)^{0.88} \cos(\theta - \varphi)\ (1\ mm/h) \tag{C.29}$$

R_{wdr}	wind-driven rain intensity		kg/(m² h)
ρ_l	density of liquid water	1000	kg/m³
α	wind-driven rain coefficient		s/m
R_h	unobstructed horizontal rainfall intensity, climate data		kg/(m² h)
θ	wind direction (degrees from north)		°
φ	surface normal (degrees from north)		°

The wind-driven rain coefficient, if no computational fluid dynamics simulation is applied, is determined as a constant by means of the ISO model (Blocken & Carmeliet, 2010):

$$\alpha = 2/9 \left(\frac{S}{m}\right) C_R\ C_T\ O\ W \tag{C.30}$$

$2/9$	ratio corresponding to Lacy's free-field α	s/m
C_R	roughness coefficient	-
C_T	topography coefficient	-
O	obstruction factor	-
W	wall factor	-

The roughness coefficient takes into account the change of the mean wind speed at the site due to the upstream roughness of the terrain and the height above the ground. It is given by:

$$C_R = K_R \ln(max(z_{min}, z)/z_0) \tag{C.31}$$

K_R	terrain factor (given as a function of the terrain category)	-
z_{min}	minimum height (given as a function of the terrain category)	m
z	height above the ground	m
z_0	aerodynamic roughness length (given as a function of the terrain category)	m

The given parameter values in Eq. (C.31) are determined according to four distinguished terrain categories: rough open sea (K_R=0.17, z_{min}=2, z_0=0.01), farm land (K_R=0.19, z_{min}=4, z_0=0.05), suburban area (K_R=0.22, z_{min}=8, z_0=0.3) and urban area (K_R=0.24, z_{min}=16, z_0=1). E.g., at 5 m height, the roughness coefficient equals 1.056, 0.875, 0.722 and 0.665 for the respective terrains and from 0 m to 4 m height, the first of the latter three becomes 0.833 while the other two remain unchanged. The ISO gives a more detailed description of the different terrain categories.

The topography coefficient takes into account the increase of the approach-flow mean wind speed over escarpments and isolated hills. It is not applied in the present work, but to give an idea: it varies from 1 for buildings situated at more than half way up the slope of a hill with less than 5% inclination to 1.6 in the case of steep cliffs.

The obstruction factor takes into account the shelter of the wall by the nearest obstacle that is at least as high as the wall, along the line of sight from the wall. This line of sight is defined as the ‘‘horizontal view away from the wall, over a sector spanning about 25 ° either side of the normal to the wall’’. The obstruction factor may vary at different points along a wall. Whereas not taken into account in the present study, ignoring obstructions may lead to a significant overestimation of the wind-driven rain load: values of the obstruction factor as a function of the distance of the obstruction from the façade vary from 0.2 for 4 m to 8 m, to 0.3 up to 15 m, 0.4 up to 25 m, 0.5 up to 40 m, 0.6 up to 60 m, 0.7 up to 80 m, 0.8 up to 100 m, 0.9 up to 120 m, and 1.0 for over 120 m. However, if the layout of the built environment is likely to funnel wind towards the wall, the obstruction factor should be taken equal to one, irrespective of the presence of obstructions.

The wall factor takes into account the modified wind-driven rain intensity due to the building itself. It is defined as the ratio of the wind-driven rain load on the wall of the building to the wind-driven

rain load passing through an imaginary vertical plane, without the building present. Hence, the influence of the wind-blocking effect by the building and the impact of a roof overhang on the wind-driven rain exposure and its variation across the surface are included, admittedly in a simplified way. (The wind-blocking effect refers to the disturbance of the wind-flow pattern by the presence of the building.) The wall factors made available in the Standard vary from 0.2 to 0.5, depending on the wall type (number of stories, roof overhang) and the position on the building façade. Average values include, inter alia, 0.4 for a three-storey wall with roof overhang and 0.3 for a two-storey wall with roof overhang.

The **convective** water vapour transport from the exterior surface to the atmosphere enables evaporative drying, which is taking up the main moisture removal role for permeable building façades. It is described by use of a convective surface moisture transfer coefficient:

$$g_{v,e} = g_{v,conv,e} = \beta_e\left(p_{v,se} - p_{v,e}\right) = \beta_e\left(exp\left(p_{c,se}/(\rho_l R_v T_{se})\right)p_{v,sat,se} - \varphi_e p_{v,sat,e}\right) \qquad \text{(C.32)}$$

β	convective surface moisture transfer coefficient	s/m

Since for the convective surface moisture transfer coefficients, empirical data are limited, it is commonly preferred to derive them from their thermal counterparts, based on the 'Lewis analogy' (Janssen et al., 2007a). This theory assumes that the thermal and hygric boundary layers are similarly shaped and sized, in which case the convective surface moisture transfer coefficient can be assumed proportional to the convective surface heat transfer coefficient:

$$\beta_e \underset{(Lewis)}{=} h_{conv,e}\ 7.7\ \times 10^{-9}\left(\frac{mKs}{W}\right) \qquad \text{(C.33)}$$

When implemented as a constant, independent of the wind conditions, an exemplary standard value for the exterior convective surface moisture transfer coefficient is 15.4 x 10^{-8} kg/(Pa m² s). However, in reality, it is similarly varying as the convective surface heat transfer coefficient. Moreover, in (Janssen et al., 2007b), it is shown that the moisture responses of permeable components are fairly sensitive to the exterior convective surface moisture transfer coefficient and that the wind speed-dependence should be taken into account when modelling evaporative drying.

The **total moisture mass balance** at the exterior wall surface becomes:

$$g_{m,se} = -\frac{\rho_l \alpha U_{10} \left(\frac{R_h/\rho_l}{1\ mm/h}\right)^{0.88} \cos(\theta - \varphi)\,(1\ mm/h)}{3600\left(\frac{s}{h}\right)} + \beta_e\left(exp\left(p_{c,se}/(\rho_l R_v T_{se})\right)p_{v,sat,se} - \varphi_e p_{v,sat,e}\right) \quad \text{(C.34)}$$

The **heat** balance at the **interior** wall surface (Fig. 2.10) is expressed as:

$$q_{si} = q_{conv,i} + q_{rad,i} + q_{v,i} = q_i + q_{v,i} \quad \text{(C.35)}$$

The **convective** heat exchange at the interior wall surface is given by:

$$q_{conv,i} = h_{conv,i}\left(T_{i,g} - T_{si}\right) \quad \text{(C.36)}$$

A standard value for the interior convective surface heat transfer coefficient is 3.5 W/(m² K) for a vertical wall. In reality, it is a function of the surface to gas temperature difference, the position on the wall (Abuku et al., 2009) and the eventual presence of radiators or ventilation.

The **radiative** heat exchange at the interior wall surface is given by:

$$q_{rad,i} = F_{Rsurf-si}\sigma\left(T_{i,surf}^4 - T_{si}^4\right) \approx F_{Rsurf-si}\sigma 4\left(\left(T_{i,surf} + T_{si}\right)/2\right)^3\left(T_{i,surf} - T_{si}\right) = h_{rad,i}\left(T_{i,surf} - T_{si}\right) \approx h_{rad,i}\left(T_{i,g} - T_{si}\right) \quad \text{(C.37)}$$

A standard value for the interior radiative surface heat transfer coefficient is 4.5 W/(m² K), which can be accepted for 'normal' temperatures and configurations, in the case where $e_{L,si}$>0.8 and $e_{L,surf}$>0.8. Normal is herein defined as the average temperature ranging from 273 K to 303 K and, assuming that the interior wall surface is fully enclosed by isothermal surfaces, the view factor equal to one (in both transport directions) and the area of both of the surfaces involved in the radiation exchange assumed to be equal. Besides, it is assumed that the temperature of the interior surrounding surfaces equals the interior gas temperature. The two latter assumptions are especially useful in component simulations given that these parameters (A_{surf} and $T_{i,surf}$) are otherwise unknown. Furthermore, the assumption of the area of the surface of the radiative heat flow to equal that of the convective heat transport and the use of the interior gas temperature (for the interior surrounding surfaces) are also necessary conditions for the commonly used combined expression for the interior convective and radiative heat transport.

The **sensible and latent heat transport by condensation** (or evaporation) is given by:

$$q_{v,i} = h_v g_{v,i} = \left(c_v\left(T_{v,si} - T_{ref,h}\right) + L_v\right)g_{v,i} = \left(c_v\left(T_{i,g/si} - T_{ref,h}\right) + L_v\right)g_{v,i} \quad \text{(C.38)}$$

Analogous as with the evaporative heat transport at the exterior surface, all water vapour is assumed to condense (or evaporate) in the open material pores at the surface. The water vapour temperature at the surface equals the gas temperature or the surface temperature depending on the direction of the vapour flux. The moisture transport by the convective water vapour exchange is elaborated below Eq. (C.41).

The **total heat balance** at the **interior** wall surface becomes:

$$\begin{aligned} q_{si} &= h_{conv,i}\left(T_{i,g} - T_{si}\right) + h_{rad,i}\left(T_{i,g} - T_{si}\right) + \left(c_v\left(T_{i,g/si} - T_{ref,h}\right) + L_v\right)g_{v,i} \\ &= h_i\left(T_{i,g} - T_{si}\right) + \left(c_v\left(T_{i,g/si} - T_{ref,h}\right) + L_v\right)g_{v,i} \end{aligned} \quad \text{(C.39)}$$

The **moisture** flow at the **interior** wall surface is expressed as:

$$g_{m,si} = g_{v,i} \quad \text{(C.40)}$$

The **convective** water vapour exchange at the interior wall surface is given by:

$$g_{v,i} = g_{v,conv,i} = \beta_i\left(p_{v,i} - p_{v,si}\right) = \beta_i\left(\varphi_i p_{v,sat,i} - p_{v,sat,si} exp\left(p_{c,si}/(\rho_l R_v T_{si})\right)\right) \quad \text{(C.41)}$$

A standard value for the interior convective surface moisture transfer coefficient is 2 x 10^{-8} kg/(Pa m² s), but it is again similarly varying as its thermal counterpart. Assuming the thermal and hygric boundary layers at the interior surface to be similar in shape and size, it is assumed that the same proportionality as at the exterior surface holds between the interior convective surface moisture transfer coefficient and the interior convective surface heat transfer coefficient. Therefore, the interior convective surface moisture transfer coefficient is commonly preferred as determined by using the Lewis relation (cf. Eq. (C.33)), which gives:

$$\beta_i = h_{conv,i} 10^{-9} 7.7(mKs/W) = 3.5(W/(m^2K)) 10^{-9} 7.7(mKs/W) = 10^{-8} 2.695(s/m) \quad \text{(C.42)}$$

The **total moisture mass balance** at the **interior** wall surface becomes:

$$g_{m,si} = \beta_i\left(\varphi_i p_{v,sat,i} - p_{v,sat,si} exp\left(p_{c,si}/(\rho_l R_v T_{si})\right)\right) \quad \text{(C.43)}$$

D Moisture diffusivity – Comparison with ruler method

A detailed visualisation of the moisture content profiles with techniques such as X-ray radiography provides the most accurate results for the moisture diffusivity, but such experimental facilities are not always available in laboratories. In (Evangelides et al., 2018), a simplified method is presented wherein the average boundary lambda value λ_f (m/s$^{0.5}$), see Section 3.4.3.2, is determined by visual observation of the moisture front position (through discolouration). In this way, the characteristic profile can also be determined using the tangent formula based on knowledge of the capillary absorption coefficient and the capillary moisture content. In addition, the equivalent height must be known for the determination of the individual boundary lambda values, cf. Eq. (3.22), for in the case of the composite rammed earth samples with wick and paper.

Fig. D.1 shows the results of the characteristic profile for the two rammed earth materials and their duplicate samples. It is observed that the average boundary lambda value from the ruler method is usually smaller than that of the X-ray method. This is also observed in (Ren et al., 2019). If the ruler method were to be used, it would be recommended to test a large number of samples and to retain only those with the greatest average boundary lambda values.

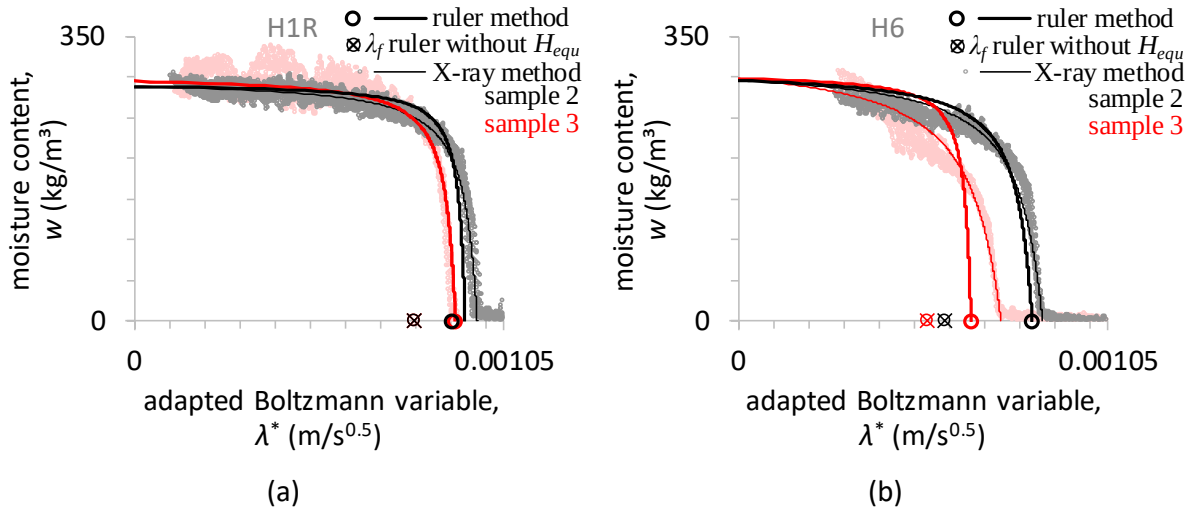

Fig. D.1: Characteristic profile from ruler method and X-ray method for samples of (a) H1 material and (b) H6 material.

E Mechanical material properties variant 2 comparison

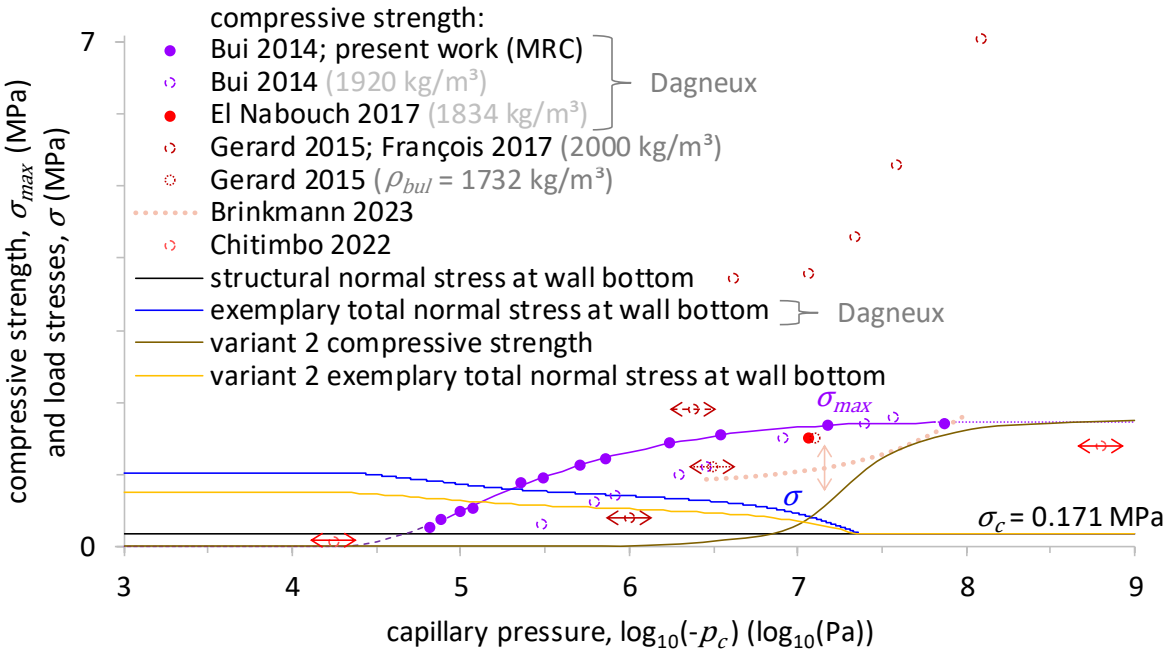

Fig. E.1: Rammed earth compressive strength and load stresses.

Variant 2 compressive strength:

$$y = \max(0; 0.63 \cdot \arctan(3.83 \cdot (x - 4.46) - 11.00) + 0.87)$$

F Interior insulation analysis – Climate location choice

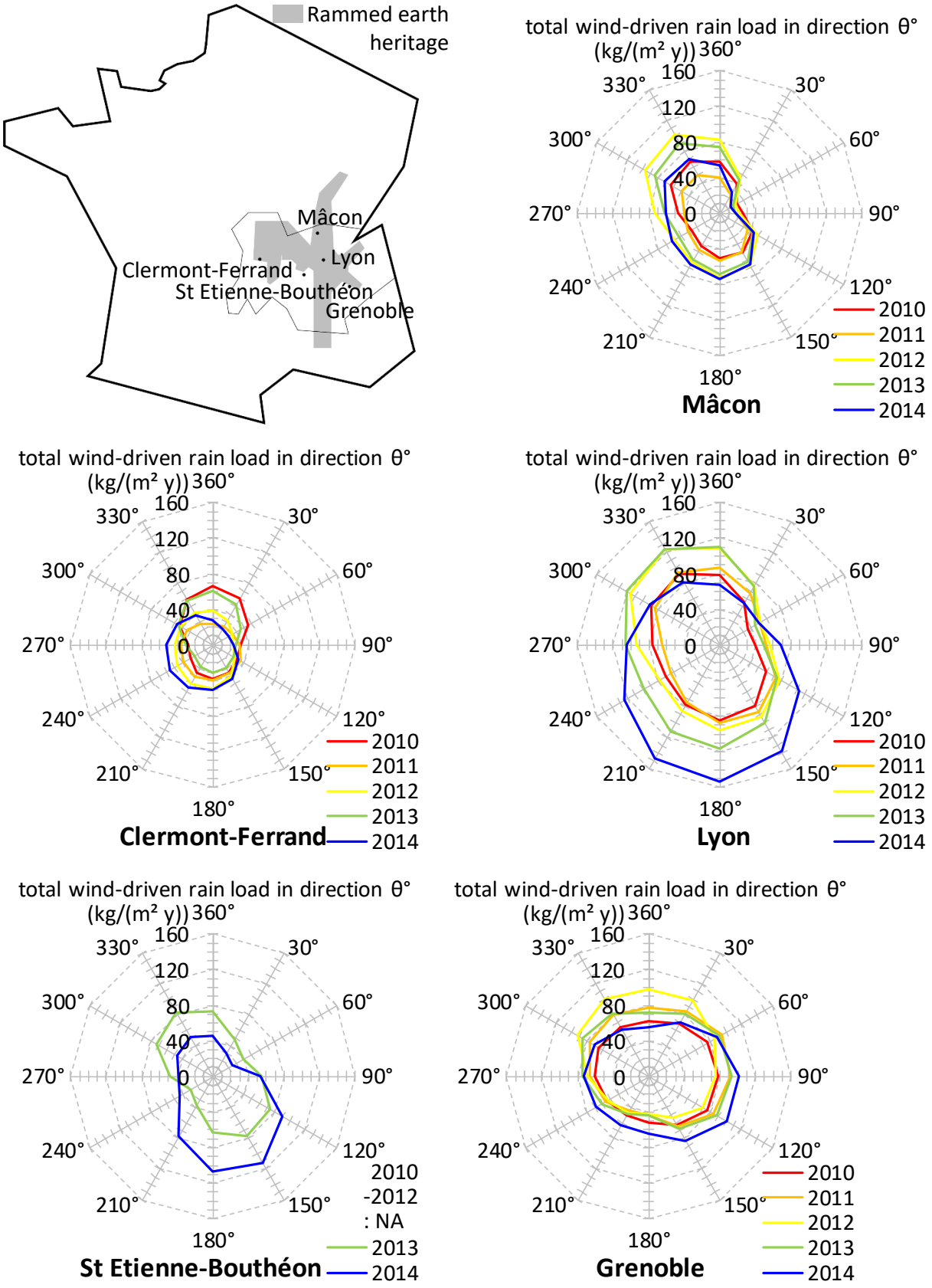

Fig. F.1: Directional roses for wind-driven rain load in 2010-2014 in different cities in France.

G Interior insulation analysis – Climate year choice

For the selection of the moisture reference year for hygrothermal simulation analysis, it is recommended to choose the most moisture-severe year of the past ten years (EN 15026); (Hens, 2011); (Zhou et al., 2016), which is appropriate for low risk acceptability. For the main problem being investigated (regarding the ensemble of performances studied), rain penetration, the most moisture-severe year yields the highest moisture built-up in the wall. Fig. G.1 shows that from 2010 to 2019, the years 2013 and 2014 have the greatest rainfall. Fig. G.2 shows the wind-driven rain roses for the years 2010 to 2014 in Lyon. It is observed that for the year(s) (2010 to) 2013, the 330° North(-West) orientation has the highest wind-driven rain load, whereas for the year 2014, the South orientation has the highest wind-driven rain load. Since besides the wind-driven rain load, the solar gains influence the moisture built-up, both the 2013 330° and the 2014 180° conditions are considered possible candidates for the moisture reference year (based on Fig. G.2).

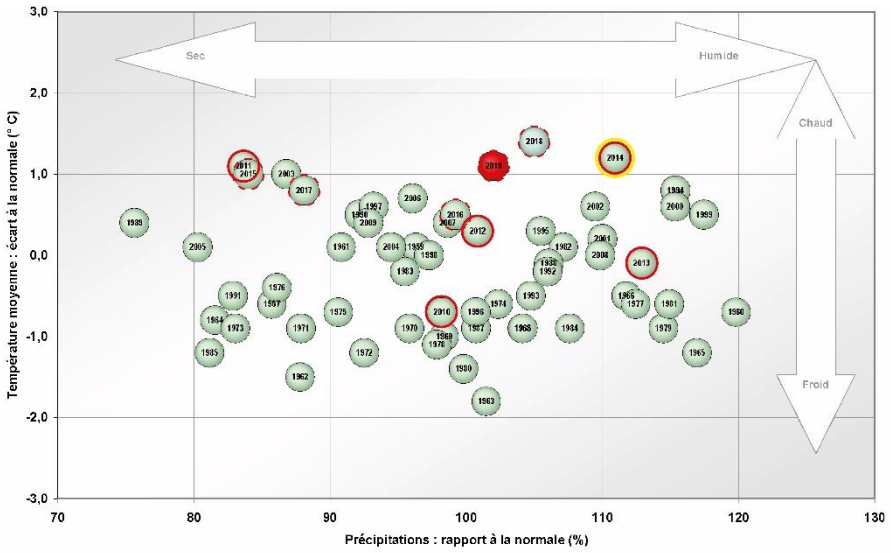

Fig. G.1: Temperatures and rainfall for the years 1959 to 2019 in France (Météo France, 2020).

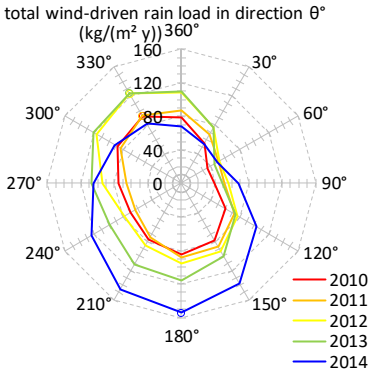

Fig. G.2: Directional roses for total wind-driven rain load for the years 2010 to 2014 for Lyon.

Fig. G.3 shows the temporal distribution of the main wind-driven rain load for the different climate years. It is observed that, while the wind-driven rain roses (2010-2013) have a rather similar shape, the wind-driven rain load for the 330° direction in 2013 has an aberrant course with a high concentration of wind-driven rain in spring. The wind-driven rain load for 2014 (as well as 2010-2012) on the other hand has a more equal distribution over time.

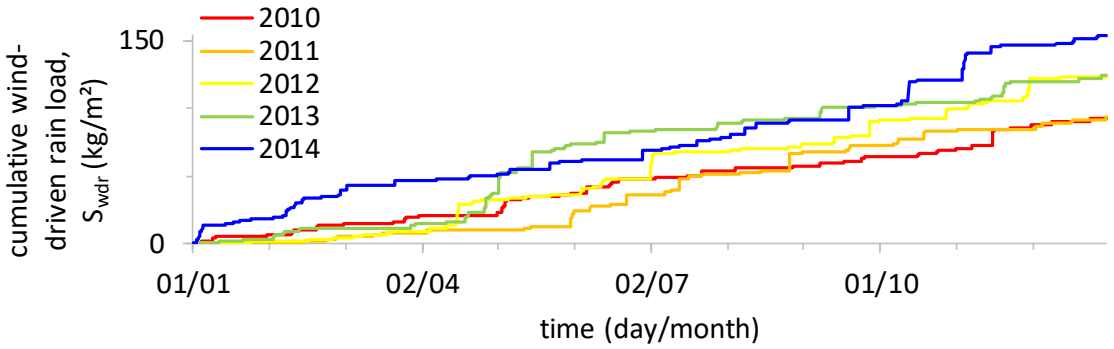

Fig. G.3: Hourly cumulative wind-driven rain load over the year for 2010 to 2014 for façade oriented in the main wind-driven rain direction.

Fig. G.4 shows the resulting moisture built-up in the wall for both candidate years. It is observed that the yearly average accumulated moisture is similar for both cases. The temporal distribution, on the other hand, is different, which reflects the wind-driven rain load. Although the year 2013 can as a result yield higher moisture damage risks, it is considered an exception due to the mentioned temporal wind-driven rain concentration, and hence the year 2014 is chosen as the moisture reference year. (Besides, the colder year 2013 would yield more frost damage, cf. Fig. G.1, but this is disregarded given global warming (Sanders, 2008)).

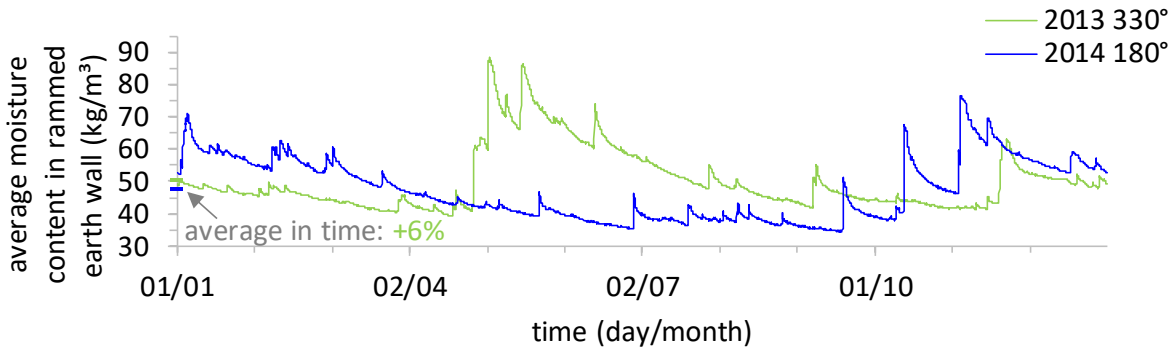

Fig. G.4: Accumulated moisture in H1 rammed earth wall for different climate years.

H Interior insulation analysis – Climate data figures

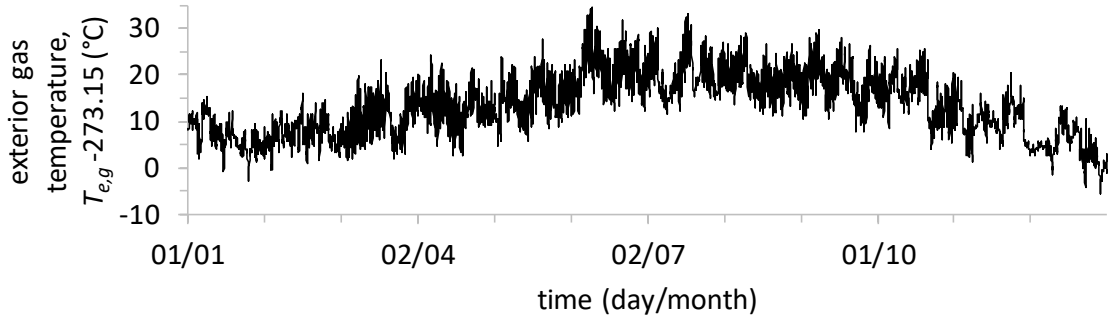

Fig. H.1: Hourly exterior gas temperature over the year 2014 in Lyon.

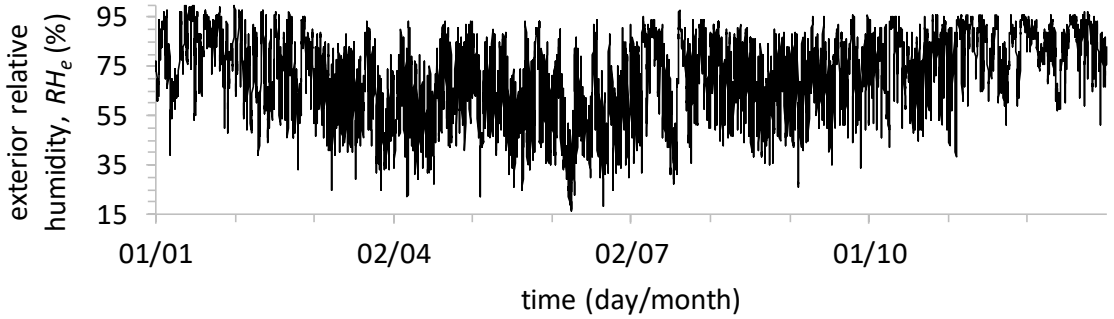

Fig. H.2: Hourly exterior relative humidity over the year 2014 in Lyon.

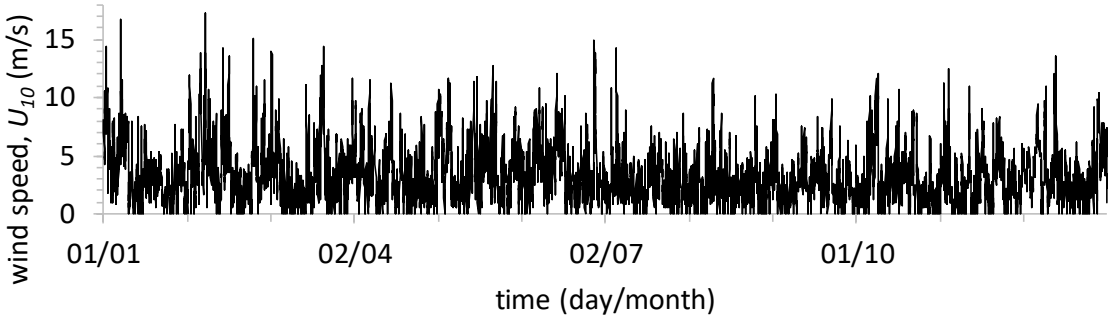

Fig. H.3: Hourly wind speed over the year 2014 in Lyon.

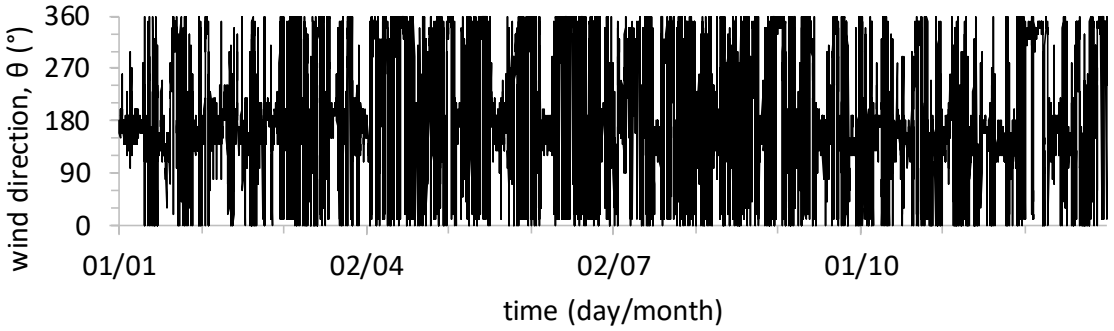

Fig. H.4: Hourly wind direction over the year 2014 in Lyon. Wind direction is set to zero when

wind speed is zero.

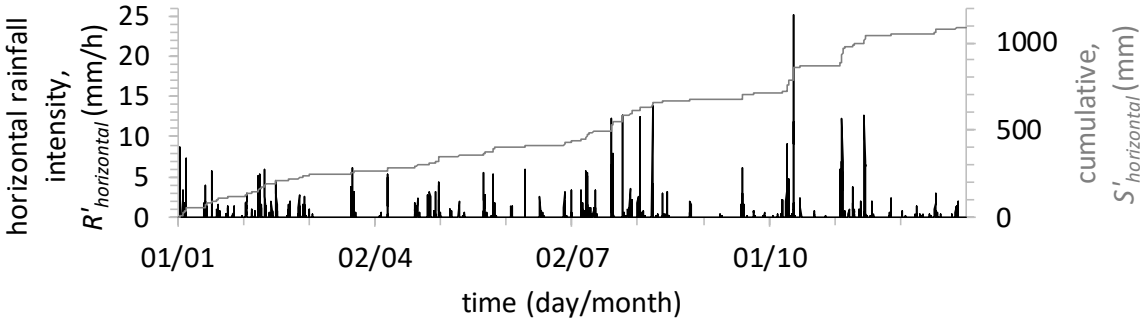

Fig. H.5: Hourly horizontal rainfall intensity over the year 2014 in Lyon.

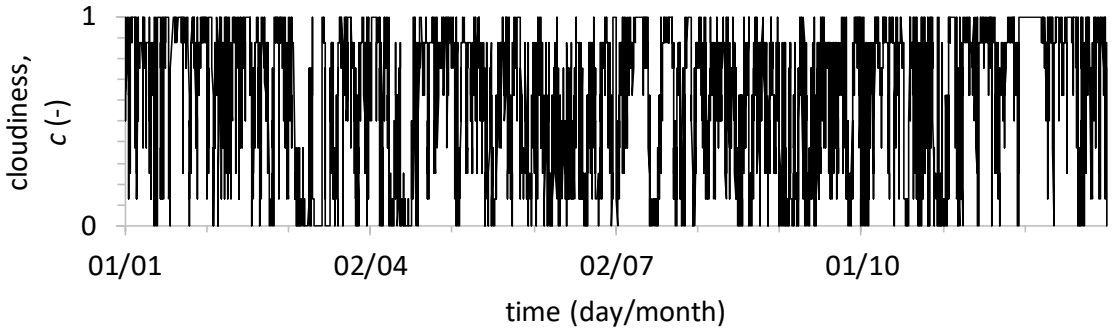

Fig. H.6: Hourly cloudiness over the year 2014 in Lyon.

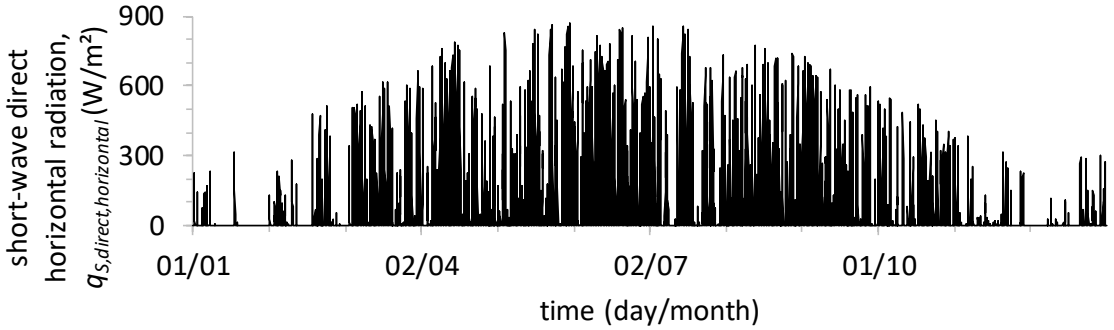

Fig. H.7: Hourly short-wave direct horizontal radiation over the year 2014 in Lyon.

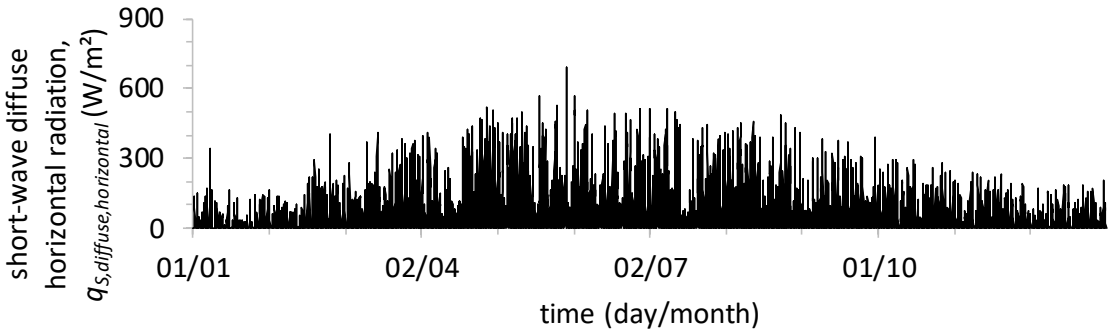

Fig. H.8: Hourly short-wave diffuse horizontal radiation over the year 2014 in Lyon.

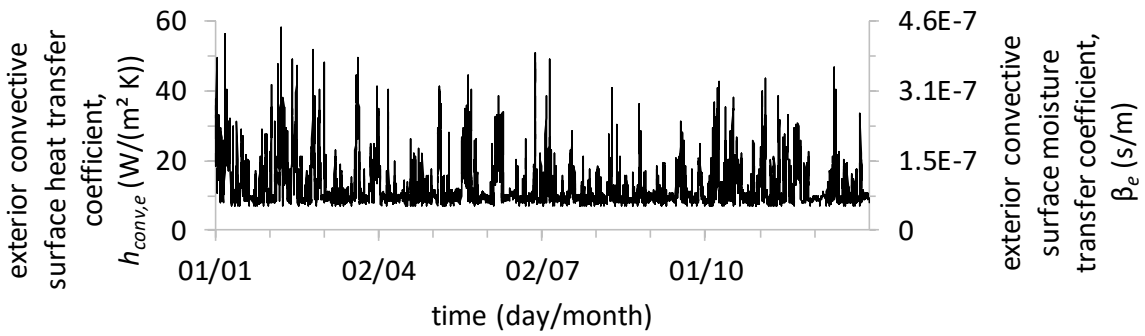

Fig. H.9: Hourly exterior convective surface heat and moisture transfer coefficient over the year 2014 for South orientated façade in Lyon.

I Interior insulation analysis – Insulation system Figs.

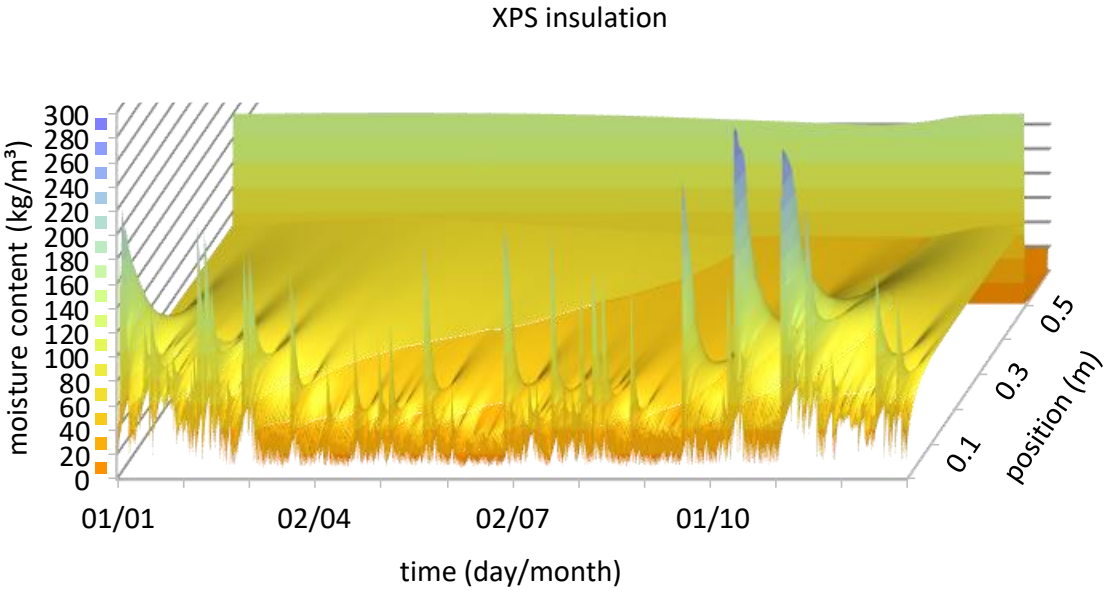

(a)

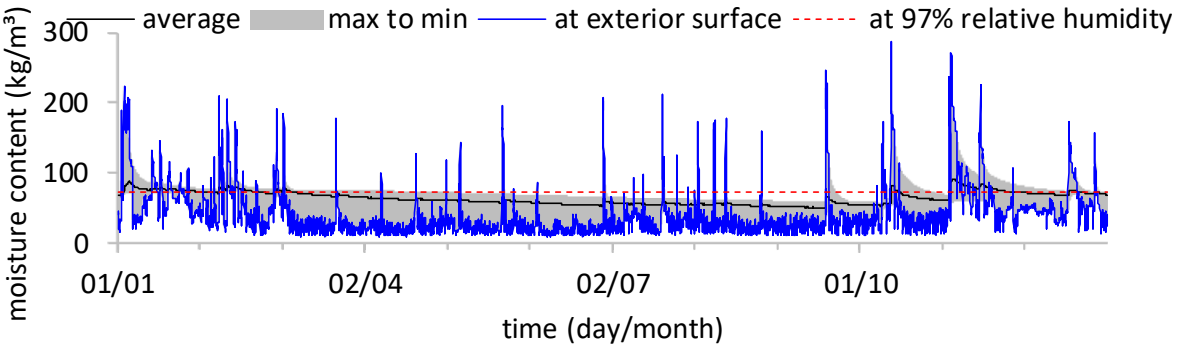

(b)

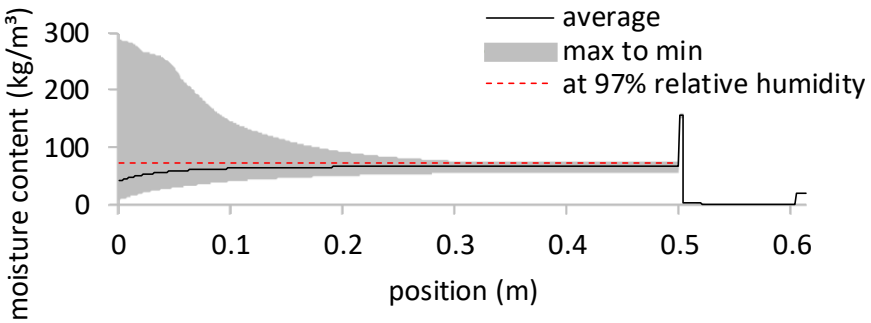

(c)

Fig. I.1: Hourly moisture content profile evolution in XPS insulated H1 rammed earth wall (a) 3D, (b) front, (c) side.

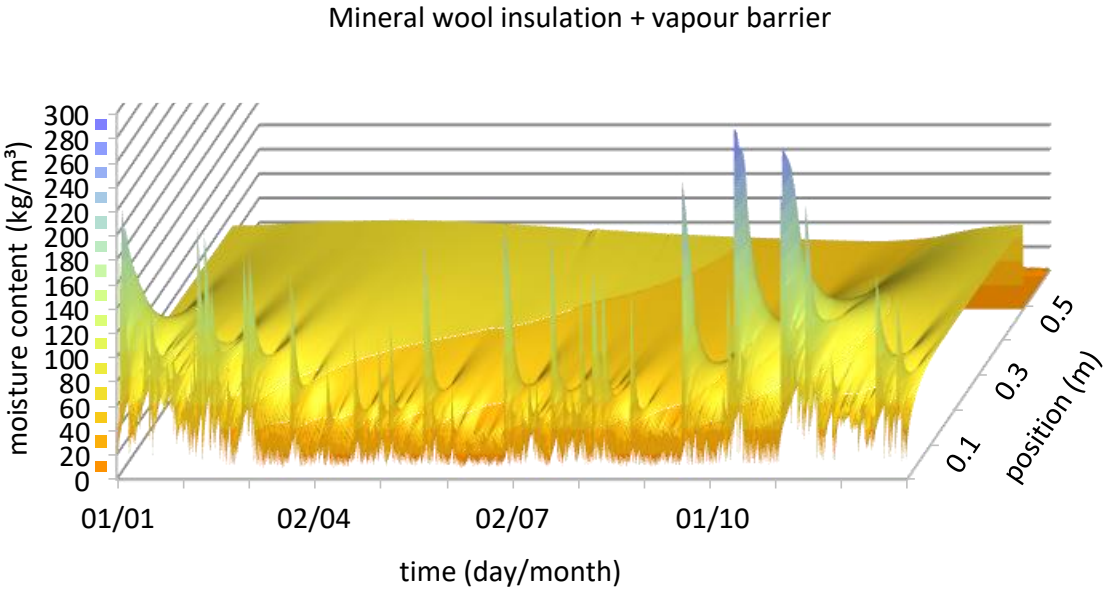

(a)

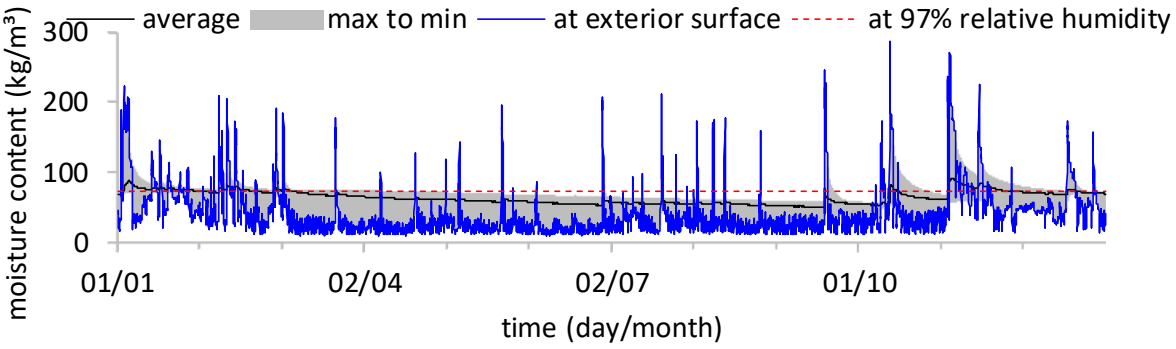

(b)

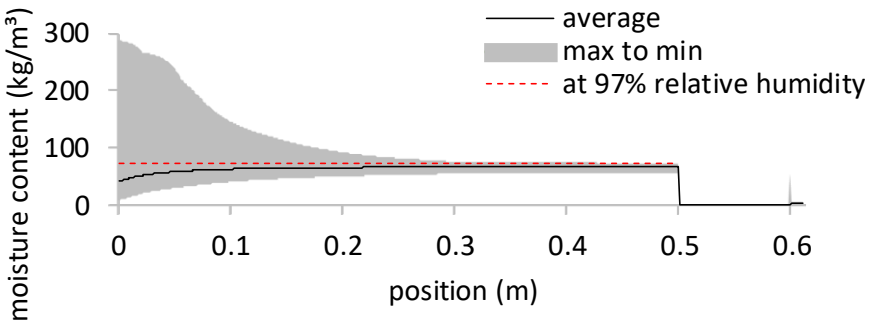

(c)

Fig. I.2: Hourly moisture content profile evolution in MW+VB insulated H1 rammed earth wall (a) 3D, (b) front, (c) side.

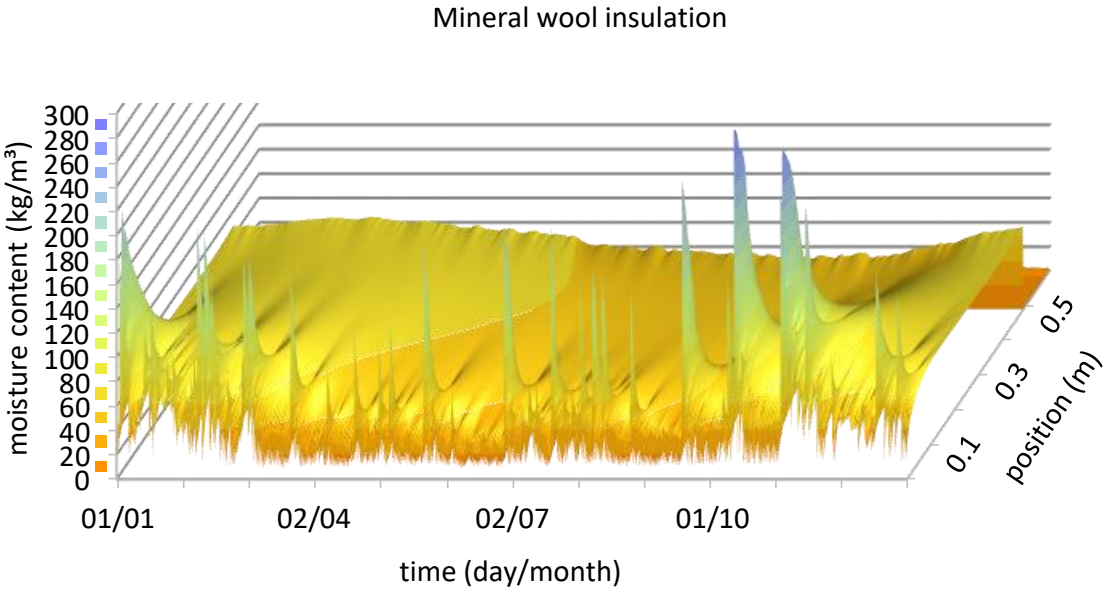

(a)

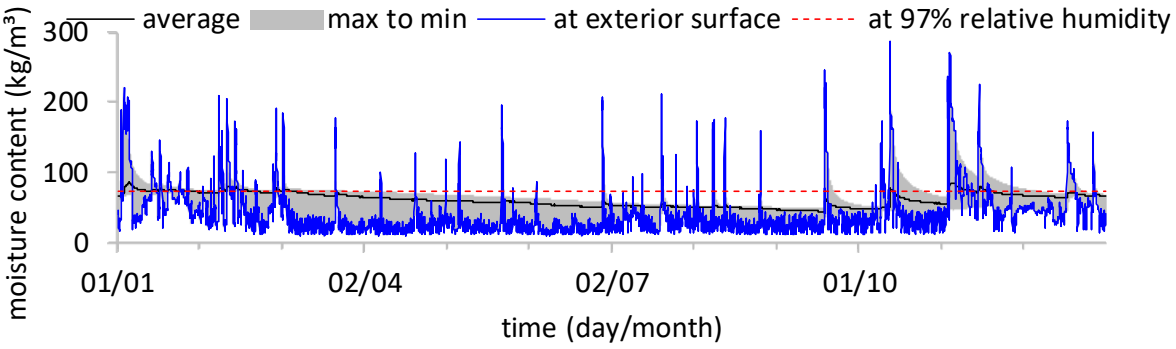

(b)

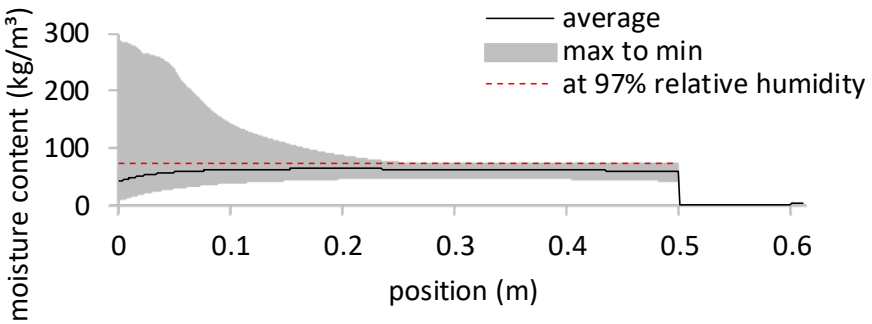

(c)

Fig. I.3: Hourly moisture content profile evolution in MW insulated H1 rammed earth wall (a) 3D, (b) front, (c) side.

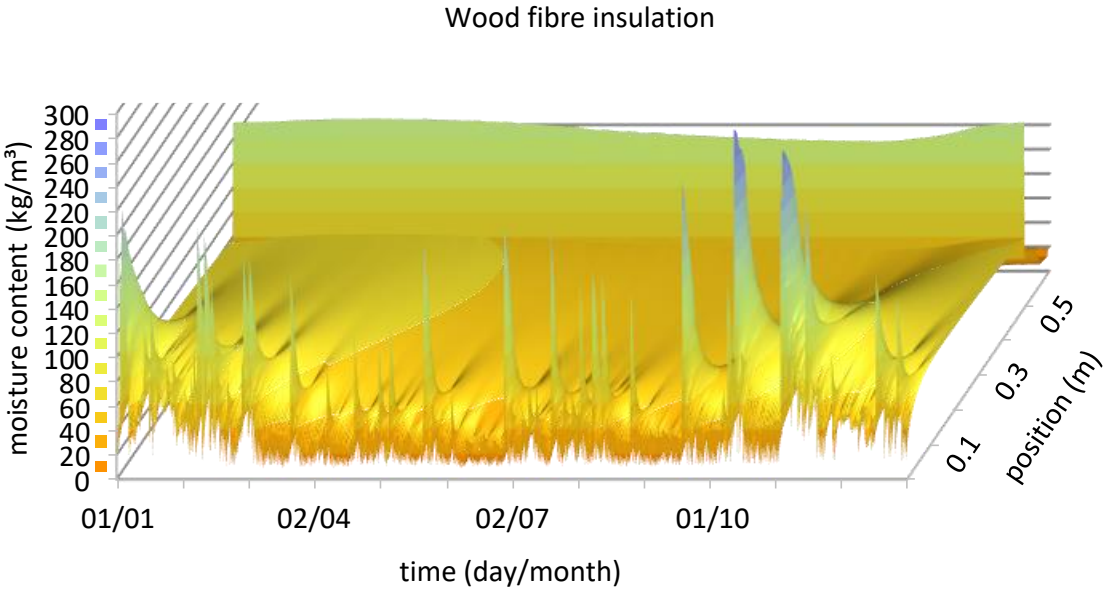

(a)

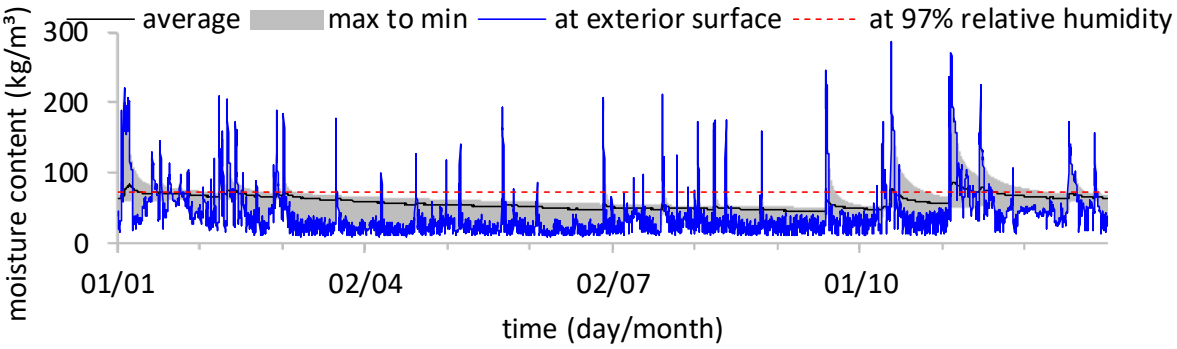

(b)

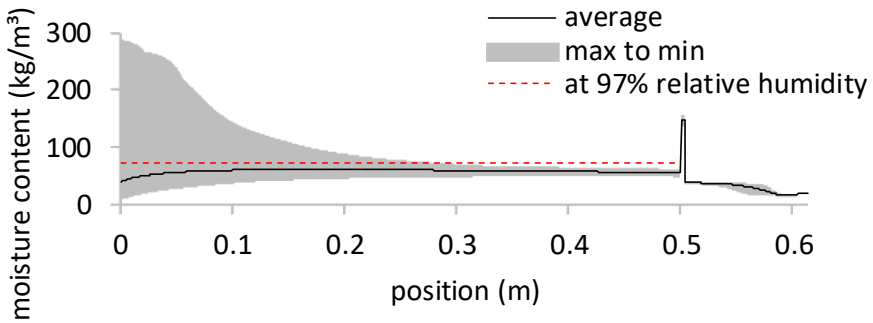

(c)

Fig. I.4: Hourly moisture content profile evolution in WF insulated H1 rammed earth wall (a) 3D, (b) front, (c) side.

Calcium silicate insulation

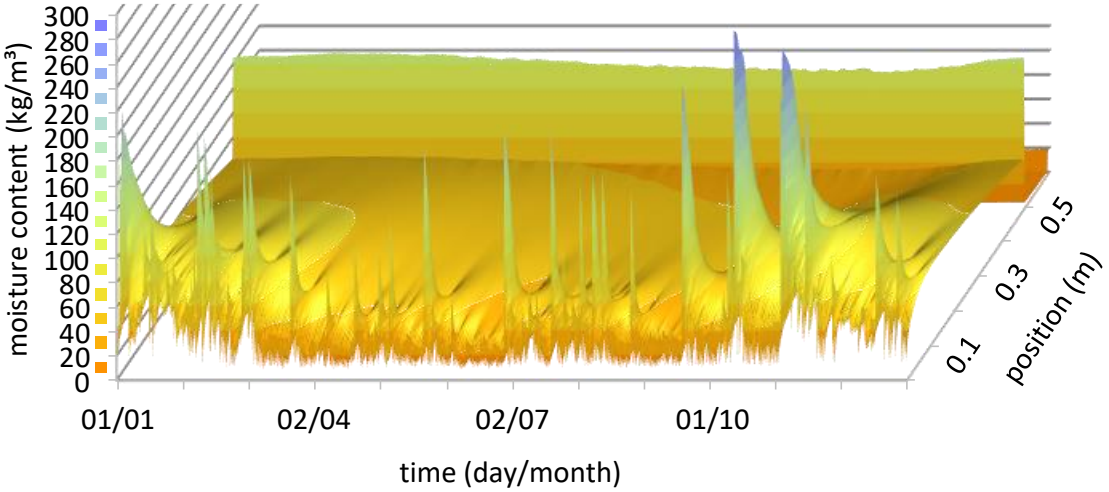

(a)

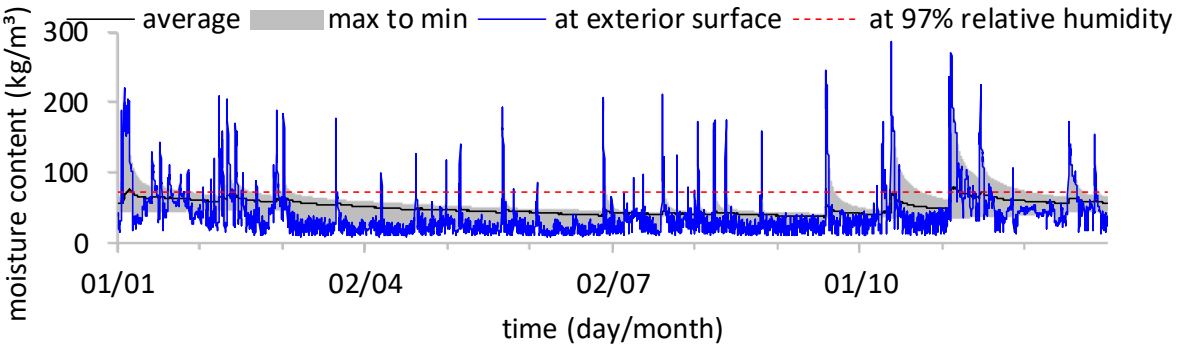

(b)

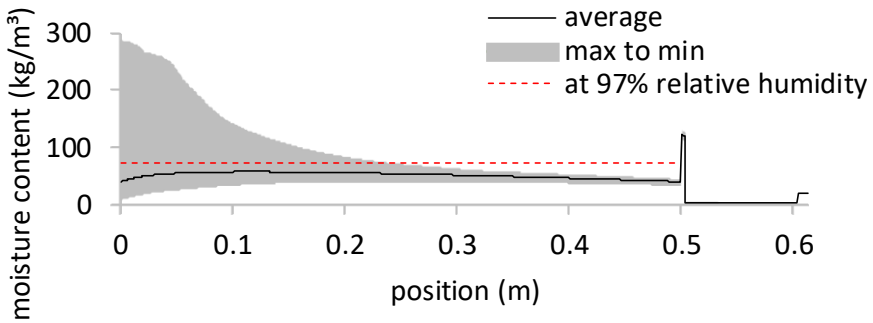

(c)

Fig. I.5: Hourly moisture content profile evolution in CS insulated H1 rammed earth wall (a) 3D, (b) front, (c) side.

J Interior insulation analysis – Mechanical response details

Reference wall

Fracture failure

The maximum load-bearing section loss over the year amounts to 15.2 % or 7.6 cm for the non-insulated H1 rammed earth wall. The fracture failure occurs at the exterior side of the wall. It occurs consequent to the wind-driven rain event in the beginning of November resulting in the second largest increase in cumulative wind-driven rain amount over the year, cf. Fig. 5.9.

Buckling failure

The maximum relative buckling stress over the year amounts to 4.4 % for the non-insulated H1 rammed earth wall. It occurs on November 15 at 2 p.m, after a wind-driven rain event.

Clay swelling damage

The maximum number of clay swelling cycles over the year amounts to 10 for the exterior wall side and 0 for the interior wall side for the non-insulated H1 rammed earth wall. The corresponding most critical position is at 8 mm from the exterior surface. All the swelling cycles at that position are caused by fracture failure; none of them is caused by excessive wetting moisture gradients. The swelling cycles occur spread over the year.

Influence of insulation systems

Fracture failure

Fig. J.1 shows the course of the load-bearing section loss over the year for the non-insulated reference wall and for three of the different insulated wall assemblies: the vapour tight XPS, the vapour open mineral wool, and the capillary active calcium silicate insulation system. The maximum load-bearing section loss is indicated. It is observed that the risk on fracture failure remains quasi unchanged for the different insulation systems as compared to for the reference wall. (In Appendix K, the influence of not taking into account the hygric stress is demonstrated.)

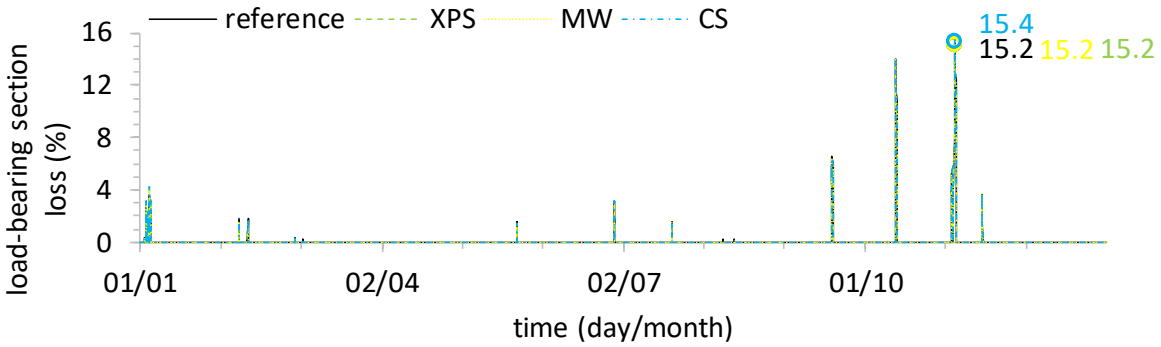

Fig. J.1: Fracture failure risk for non-insulated reference wall and for insulated wall assemblies.

Buckling failure

Fig. J.2 shows the course of the relative buckling stress over the year. It is observed that the maximum relative buckling stress does not increase for the different insulated wall assemblies as compared to for the non-insulated reference wall.

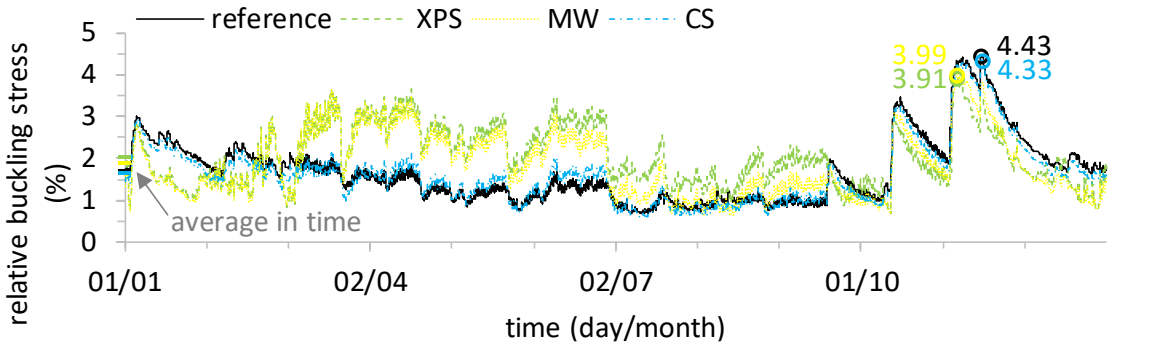

Fig. J.2: Buckling failure risk for non-insulated reference wall and for insulated wall assemblies.

Clay swelling damage

Fig. J.3 shows the number of clay swelling cycles at each position in the wall. The maximum number of clay swelling cycles is marked. It is observed that the risk on clay swelling damage does not increase for the different insulated wall assemblies as compared to for the non-insulated reference wall. The majority of the swelling cycles is caused by fracture failure.

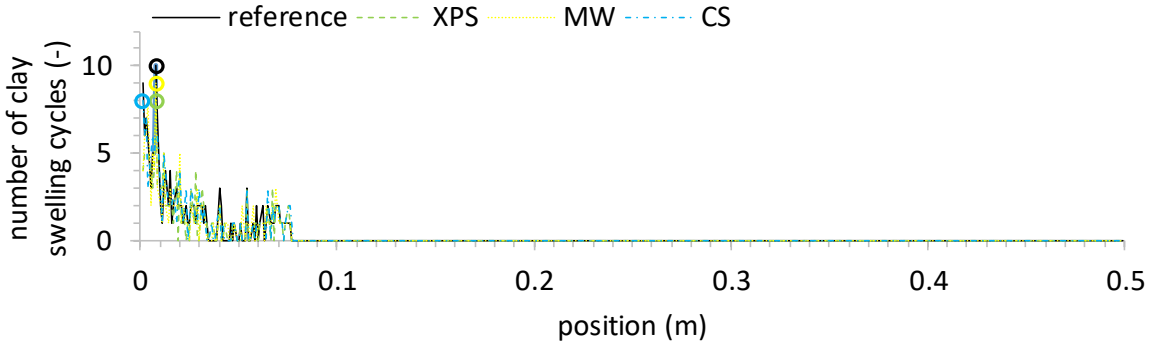

Fig. J.3: Clay swelling damage risk for non-insulated reference and insulated wall assemblies.

K Interior insulation analysis – Hygric stress influence

For the non-insulated reference H1 rammed earth wall, the maximum load-bearing section loss over the year amounts to 5% or 2.5 cm when the hygric stress is not taken into account. The risk on fracture failure slightly increases for the insulated wall assemblies relative to the reference wall. E.g., the load-bearing section loss amounts to 5.4% for the XPS insulation system and to 5.2% for the mineral wool insulation system without vapour barrier.

The maximum relative buckling stress over the year amounts to 0.57% without taking into account the hygric stress for the non-insulated reference H1 rammed earth wall. For the XPS and mineral wool without vapour barrier insulation systems, the maximum relative buckling stress over the year slightly increases relative to the reference wall, to 0.72% and 0.69%, respectively.

The maximum number of clay swelling cycles over the year amounts to 1 for the non-insulated reference H1 rammed earth wall when the hygric stress is not taken into account. The resulting swelling cycle is hence caused by fracture failure. It occurs at 25 mm from the exterior surface. For the XPS and mineral wool without vapour barrier insulation systems, the maximum number of clay swelling cycles over the year slightly increases relative to the reference wall, to 2 clay swelling cycles at 4 mm depth from the exterior surface. No clay swelling cycles are found for the interior wall side.

Résumé et tour d’horizon

1 Introduction

1.1 Contexte et énoncé du problème

Les maisons patrimoniales en pisé sont largement présentes en France. Les murs de ces bâtiments en pisé (dans lesquels les particules d'argile forment le liant naturel) ont généralement des « bottes », c'est-à-dire le soubassement, et un « chapeau », c'est-à-dire le toit. Ces bâtiments doivent être isolés pour réduire les déperditions de chaleur à travers l'enveloppe et ainsi économiser de l'énergie. L'isolation intérieure est adaptée à la rénovation thermique de ces enveloppes de bâtiment en pisé pour préserver l'aspect extérieur de la façade. L'isolation intérieure peut cependant entraîner des problèmes consécutifs à l'état hygrothermique modifié du mur, tels qu'un risque accru de pourriture du bois, de croissance de moisissures, de dommages par le gel et éventuellement d'effondrement structurel. Ces risques encourus doivent donc être analysés en amont afin d'orienter les décisions de rénovation.

1.2 Objectifs et question de recherche

En réponse aux questions brûlantes de la pratique de la rénovation, le présent travail vise à évaluer l'isolabilité intérieure des murs en pisé par simulation numérique. La question de recherche associée est : « Quel est l'impact des (différents) systèmes d'isolation intérieure sur les performances hygrothermiques des murs en pisé ? ». Deux sous-objectifs doivent être abordés pour cela. Tout d'abord, « Comment réaliser une caractérisation hygrique complète des matériaux en pisé ? », puisque les échantillons deviennent instables à des taux d'humidité élevés et que ces propriétés doivent encore être déterminées car les murs en pisé sont également exposés à la pluie poussée par le vent. Et deuxièmement, « Comment fournir un jeu complet d'indicateurs de performance pour le pisé ? », puisque le jeu actuel, composé d'indicateurs de performance hygriques et thermiques, n'intègre pas les performances mécaniques.

1.3 Méthodologie et structure

Dans la Section 2, l'**état de l'art** de l'isolabilité intérieure des murs en pisé est passé en revue. Cela concerne trois thèmes principaux à aborder : l'analyse des performances hygrothermiques, la modélisation de la simulation hygrothermique des composants et la caractérisation

hygrothermique des matériaux. Dans la Section 3, la **caractérisation des matériaux** hygrique complète de deux matériaux de construction en pisé traditionnel différents est élaborée en laboratoire. Cette caractérisation hygrique comprend la courbe de rétention d'humidité et la courbe de perméabilité à l'humidité, qui sont toutes les deux nécessaires comme données d'entrée dans les simulations de composants. Le test d'absorption capillaire est redéveloppé pour ce dernier. Dans la Section 4, les nouveaux **indicateurs de performance** mécaniques pertinents pour l'isolation intérieure des murs en pisé sont développés. La résistance et la rigidité globales, les contraintes et déformations hygrothermiques différentielles et l'érosion des murs en pisé sont abordées pour cela. Dans la Section 5, l'**analyse de l'isolation intérieure** des murs en pisé est effectuée au moyen de simulation numérique hygrothermique des composants. Dans un premier temps, les performances hygrothermiques du mur en pisé de référence non isolé sont évaluées. Ensuite, l'impact des différents systèmes d'isolation intérieure sur les performances hygrothermiques est quantifié. L'influence de l'épaisseur de l'isolant, du matériau en pisé, de l'épaisseur du mur en pisé et de l'orientation du mur est étudiée. Enfin, l'influence des indicateurs de performance mécanique de l'échec par fracture, de l'échec par flambement et de l'endommagement par gonflement de l'argile est évaluée, y compris l'impact des propriétés mécaniques sur l'évaluation des risques.

2 Technologie de pointe

2.1 Introduction

Concernant l'isolabilité intérieure des murs en pisé, il y a surtout beaucoup de questions dans la pratique et il y a un manque de recherche scientifique adéquate. L'objectif de cette étude de la littérature est d'identifier les lacunes spécifiques dans le domaine des connaissances qui doivent être résolues pour évaluer l'isolabilité intérieure des murs en pisé. De cette façon, les objectifs raffinés et les questions de recherche du présent travail sont déterminés. Tout d'abord, des informations sur l'analyse des performances hygrothermiques sont introduites. Cela inclut une revue des critères de performance hygrothermique au niveau de l'enveloppe. Ensuite, les équations physiques derrière la modélisation de la simulation hygrothermique des composants sont données. Celles-ci comprennent les équations de transfert et les bilans de surface. Et enfin, la caractérisation hygrothermique des matériaux est passée en revue pour les propriétés hygriques et thermiques qui sont nécessaires en entrée de simulation.

2.2 Analyse des performances hygrothermiques

Les quatre principaux critères de performance de confort, de durabilité, de santé et de viabilité selon lesquels la qualité physique d'un bâtiment est évaluée sont déterminés par la réponse hygrothermique du bâtiment (Hens, 2011); (Hens et al., 2006); (Janssen & Roels, 2009); (Tijskens et al., 2017). À partir de ces quatre critères de performance au niveau du bâtiment, plusieurs performances requises au niveau de l'enveloppe s'ensuivent : entre autres, qualité de l'isolation thermique, réponse transitoire thermique, développement de moisissures intérieures, développement de moisissures interstitielles, humidité dégouttante, pourriture du bois, réponse transitoire hygrique, résistance et rigidité globales, contraintes et déformations hygrothermiques différentielles, dommages causés par le gel, érosion, remontées capillaires, étanchéité à l'air et ponts thermiques. Par performance, un indicateur quantifiable est défini. L'analyse hygrothermique touchant l'isolabilité consiste essentiellement en une comparaison de ces valeurs d'indicateurs avant et après la rénovation pour chaque option d'isolation. Le système d'isolation offrant le meilleur équilibre entre les avantages et les risques de la rénovation doit être sélectionné (Vereecken et al., 2015). Concernant l'isolabilité des murs en pisé, le rapport de projet (HYGROBA, 2013a) est disponible, mais les conditions climatiques extérieures imposées (uniquement température et humidité relative) (François et al., 2017) et les propriétés du matériau en pisé (courbe de rétention d'humidité uniquement mesurée dans le domaine hygroscopique, approximation de la perméabilité à l'eau liquide par le logiciel de simulation) sont considérées comme inadéquates. De plus, les sorties ne comprennent que des critères de performance thermique (Hall & Allinson, 2008) et hygrique (Allinson & Hall, 2010), tandis que les performances mécaniques (Kianfar & Toufigh, 2016); (Fabbri et al., 2018) restent sans réponse. En outre, seuls les assemblages muraux enduits extérieurement sont étudiés. Les conclusions de ce rapport sont donc insuffisantes et les avis sur l'isolabilité intérieure des murs en pisé restent partagés (Heitz et al., 2015); (Galmiche, 2019); (Atelier Chevillotte, 2020); (Livradois-Forez, 2011); (Buzo et al., 2014).

2.2.1 Qualité de l'isolation thermique

La transmission thermique ou valeur U d'un mur d'enveloppe de bâtiment doit être d'environ 0.3 W/(m² K) maximum dans les pays européens à climat océanique tempéré (Hens, 2011), principalement pour l'efficacité énergétique. Les murs en pisé, qui ont généralement une épaisseur de 0.5 m avec une conductivité thermique de 0.6 W/(m K), doivent donc être isolés, avec env. 6 cm à 15 cm d'épaisseur d'isolant selon le matériau isolant. L'isolation intérieure est utilisée pour cela car elle est peu coûteuse et facile à appliquer et l'aspect extérieur est préservé. L'ajout d'une couche intérieure d'isolation thermique modifie cependant les performances

hygrothermiques du mur qui devient plus froid et plus humide. Des phénomènes tels que l'accumulation d'humidité par condensation interstitielle, une capacité de séchage réduite et des dommages accrus (Livradois-Forez, 2011); (Scarato, 2014); (Avons-Bariot, 2017) peuvent commencer à jouer et doivent être analysés avant la rénovation pour trouver des solutions d'isolation qui minimisent les risques de problèmes d'humidité (Vereecken et al., 2015); (Zhou et al., 2018). Trois classes de systèmes d'isolation intérieure sont distinguées. Les systèmes d'isolation étanches à la vapeur évitent la condensation interstitielle mais excluent le séchage vers l'intérieur de la pluie absorbée chassée par le vent (Janssen et al., 2007b); (Abuku et al., 2009a). Les systèmes d'isolation ouverts à la vapeur facilitent le séchage vers l'intérieur par diffusion de vapeur mais laissent libre cours à la condensation interstitielle. Les systèmes d'isolation actifs capillaires amortissent la condensation interstitielle (Vereecken, 2013) et facilitent le séchage vers l'intérieur par transport d'eau liquide. La qualité de l'isolation thermique diminue cependant à mesure que l'isolation s'humidifie (Vereecken & Roels, 2015) et il existe une exigence selon laquelle l'augmentation de la valeur U par l'humidité ne doit pas dépasser 10 % (Hens, 2011).

2.2.2 Réponse transitoire thermique

Par l'ajout d'une couche d'isolation thermique intérieure à un mur massif, l'admission (Hens, 2011); (Hens, 2010); (Hall & Allinson, 2008) diminue fortement, principalement parce que la masse thermique est éliminée. Le confort thermique (Hens, 2011); (Olesen & Parsons, 2002); (Olesen, 2005) pendant l'été peut donc être compromis par une surchauffe. L'évolution de la réponse transitoire thermique n'est pas exactement évaluable au moyen de simulations de composants qui utilisent une température intérieure imposée (EN 15026).

2.2.3 Détérioration biologique ou humidité dégouttante

2.2.3.1 Développement de moisissures intérieures

Le modèle empirique VTT mis à jour (Vereecken & Roels, 2012) est couramment utilisé pour l'évaluation du risque de développement de moisissures en termes d'indice de moisissure (M, -), à la surface intérieure. L'humidité relative critique pour le développement des moisissures est de 80 % dans le modèle.

2.2.3.1 Développement de moisissures interstitielles ou humidité dégouttante

Les moisissures peuvent également se développer de manière interstitielle là où l'air peut venir. En outre, l'humidité s'égouttant des interfaces en raison de la condensation où deux matériaux non capillaires sont impliqués doit être évitée.

2.2.3.1 Pourriture du bois structurel

Les constructions en pisé ont généralement (entre autres) des poutres de plancher en bois encastrées, pour env. 2/3 de leur hauteur (Livradois-Forez, 2011); (TERA, 2018). Le modèle empirique de pourriture du bois VTT (Viitanen et al., 2010) est couramment utilisé pour évaluer le risque de développement de la décomposition du bois par les moisissures géantes (champignons). La perte de masse (ML, %) des extrémités des poutres de plancher en bois est calculée par le modèle en fonction de la température et de l'humidité relative ambiante. Ce calcul comprend un processus d'activation et un processus de perte de masse, et l'humidité relative critique pour la pourriture du bois est de 95 %.

2.2.4 Réponse transitoire hygrique

Le risque sur l'inconfort de l'humidité intérieure (Hens, 2011); (Wolkoff, 2018) peut être quantifié comme le nombre d'heures pendant lesquelles l'humidité relative intérieure dépasse 70 % (Vereecken et al., 2015) ou tombe en dessous de 30 %. Dans la simulation de composants, cependant, l'humidité intérieure est généralement imposée conformément à la norme (EN 15026) et donc indépendante du tampon d'humidité (Wan et al., 2017); (Rode et al., 2005) par les éléments intérieurs (Janssen & Roels, 2009); (Abuku et al., 2009a); (Tijskens et al., 2017).

2.2.5 Réponse mécanique

En cas de pisé, les conséquences hygrothermiques potentielles de l'isolation intérieure incluent également les risques mécaniques concernant la résistance et la rigidité globales et les contraintes et déformations hygrothermiques différentielles (Fabbri et al., 2019); (Galmiche, 2019); (Scarato, 2014). Ceux-ci n'ont encore jamais été traduits en indicateurs de performance.

2.2.6 Dégâts de gel

Le nombre de cycles de gel-dégel peut être évalué de différentes manières (Vereecken et al., 2015); (Feng et al., 2019); (Koči et al., 2017); (Zhou et al., 2017).

2.2.7 Erosion

Une action naturelle destructrice plus spécifique aux murs en pisé est l'érosion par la pluie entraînée par le vent. Cela n'a d'ailleurs jamais encore été traduit en indicateur de performance.

2.2.8 Remontées capillaires

Les remontées capillaires ne sont généralement jamais explorées dans l'analyse de l'isolation intérieure car elles sont présumées nécessairement exclues a priori (TERA, 2018); (Heitz, 2014); (Livradois-Forez, 2011); (Hens, 2011); (Scarato, 2014).

2.3 Modélisation de la simulation hygrothermique des composants

2.3.1 Equations de transfert

L'outil de simulation numérique qui permet de simuler le comportement hygrothermique des éléments de construction repose physiquement sur deux équations de transfert : le bilan de masse hygrique, Eq. (1), et le bilan thermique, Eq. (2) (Carmeliet, 2006); (Hagentoft et al., 2004); (Nicolai & Grunewald, 2006). On suppose ici que le matériau de construction poreux reste stable. Pour le terme de stockage du bilan de masse hygrique, on suppose que la phase gazeuse ne contribue pas de manière marquée au stockage de l'humidité, que l'eau ne peut pas se transformer en glace et qu'aucune hystérésis ne se produit. La pression capillaire est définie par l'équation d'Young-Laplace pour un pore circulaire et est supposée indépendante de la température (via la tension superficielle). Pour les termes de transport du bilan massique d'humidité, la loi de Darcy est utilisée pour le transport advectif de l'eau liquide (on suppose entre autres que le matériau est isotrope) et la loi de Fick est utilisée pour le transport diffusif de la vapeur d'eau (on suppose entre autres qu'aucun transport d'humidité dû aux gradients thermiques ne se produit). La pression de vapeur est liée à l'équation de Kelvin pour un pore circulaire. Pour le bilan thermique, on suppose qu'il existe un équilibre thermique local entre les phases et la loi de Fourier est utilisée pour la conduction de la chaleur. (Les symboles sont définis dans la Nomenclature.)

$$\frac{\partial w_l}{\partial p_c}\frac{\partial p_c}{\partial t} = -\boldsymbol{\nabla}\cdot(-k_l\boldsymbol{\nabla}p_c - \delta\boldsymbol{\nabla}p_v) \tag{1}$$

$$\frac{\partial}{\partial t}(\rho_d c_d T + w_l c_l T + w_v(c_v T + L_v) + w_a c_a T) = -\boldsymbol{\nabla}\cdot\left(-\lambda\boldsymbol{\nabla}T + \boldsymbol{g}_l c_l T + \boldsymbol{g}_v(c_v T + L_v)\right) \tag{2}$$

2.3.2 Bilans de surface

Des conditions limites atmosphériques sous forme de flux d'humidité et de chaleur sont imposées à la surface extérieure Eqs. (3),(4) et intérieure Eqs. (5),(6) d'un élément de construction (Janssen et al., 2007a); (Nicolai & Grunewald, 2006). (**n** est un vecteur unitaire perpendiculaire à la surface du composant.) Ceux-ci forment les forces motrices pour le transfert dans le composant.

$$\boldsymbol{g}_{m,se} = \left(-\alpha U_{10} {R_h}^{0.88} \cos(\theta - \varphi)\,(1/3600 s/h) + \beta_e\left(p_{v,se} - p_{v,e}\right)\right) \cdot \boldsymbol{n} \tag{3}$$

$$\boldsymbol{q}_{se} = \left(h_e\left(T_{se} - T_{e,equ}\right) - c_l T_{e,g} g_{l,e} + \left(c_v T_{se/e,g} + L_v\right) g_{v,e}\right) \cdot \boldsymbol{n} \tag{4}$$

$$\boldsymbol{g}_{m,si} = \left(\beta_i\left(p_{v,i} - p_{v,si}\right)\right) \cdot \boldsymbol{n} \tag{5}$$

$$\boldsymbol{q}_{si} = \left(h_i\left(T_{i,g} - T_{si}\right) + \left(c_v T_{i,g/si} + L_v\right) g_{v,i}\right) \cdot \boldsymbol{n} \tag{6}$$

2.4 Caractérisation hygrothermique des matériaux

Les propriétés des matériaux qui sont nécessaires comme données d'entrée dans les simulations des composants hygrothermiques proviennent des équations de transfert : (la dérivée de) la courbe de rétention d'humidité ($w(p_c)$, kg/m³), la courbe de perméabilité à la vapeur (δ, s) , la courbe de perméabilité à l'eau liquide (k_l, s), la capacité calorifique (ρc, J/(m³ K)) et la conductivité thermique (λ, W/(m K)).

2.4.1 Propriétés hygriques

2.4.1.1 Stockage d'humidité

La courbe de rétention d'humidité des matériaux de construction stables est généralement obtenue à partir d'une série de tests expérimentaux tels que des mesures d'isotherme de sorption et des mesures de plaque de pression et/ou une analyse d'intrusion de mercure (EN 15026); (Feng & Janssen, 2019); (Carmeliet & Roels, 2002); (Carmeliet & Roels, 2001); (Feng & Janssen, 2020); (Feng & Janssen, 2021).

Pour les matériaux en pisé, l'examen des courbes de rétention d'humidité disponibles montre que trois tactiques de mesure peuvent être distinguées. La première tactique utilise une combinaison de porosimétrie par intrusion de mercure dans la plage surhygroscopique et de test de dessiccateur dans la plage hygroscopique (Arrigoni et al., 2017); (Hall et al., 2013). La deuxième tactique mesure la courbe de rétention d'humidité lors de la désorption à partir de la teneur en humidité de fabrication d'env. 0.08 kg/kg à 0.125 kg/kg, en utilisant des papiers filtres (Bui et al., 2014); (Gerard et al., 2015); (Jaquin et al., 2009). La troisième tactique fonctionne avec des échantillons fabriqués à différentes teneurs en humidité (Abhilash, 2016a); (Soudani, 2017); (Nowamooz & Chazallon, 2011). On observe que les matériaux en pisé sont typiquement hygroscopiques.

2.4.1.2 Transport d'humidité

La courbe de perméabilité à la vapeur est généralement déterminée en fonction de la perméabilité à la vapeur de la coupelle sèche, de la courbe de rétention d'humidité et de la teneur en humidité de la saturation sous vide, en utilisant une approche de faisceau de tubes (Scheffler & Plagge, 2010).

La courbe de perméabilité à l'eau liquide est généralement déterminée en fonction de la diffusivité de l'humidité et de la courbe de rétention d'humidité (Carmeliet et al., 2004). La diffusivité de l'humidité dans la plage haute est déterminée à l'aide du test d'absorption capillaire, par ex. avec projection de rayons X (Ren et al., 2019).

Pour les matériaux en pisé, le facteur de résistance à la vapeur en coupelle sèche varie généralement de 9 à 11 (Chabriac, 2014). Le coefficient d'absorption capillaire varie généralement d'environ 0.2 kg/(m² $s^{0.5}$) à 0.4 kg/(m² $s^{0.5}$) et le schéma d'absorption capillaire est idéal (Hall & Djerbib, 2004); (Hall & Allinson, 2009b); (Fabbri et al., 2019). La diffusivité de l'humidité (et donc la perméabilité à l'eau liquide) n'a cependant pas encore été mesurée.

2.4.2 Propriétés thermiques

La capacité calorifique spécifique des matériaux en pisé varie généralement de 650 J/(kg K) à 1100 J/(kg K) (Chabriac, 2014). La conductivité thermique (sèche) varie d'env. 0.25 W/(m K) à 1.0 W/(m K) (Chabriac, 2014). Et le facteur de teneur en humidité pour la conductivité thermique varie de 0.002 W m²/(kg K) à 0.0056 W m²/(kg K) (Hall & Allinson, 2009a); (Chabriac, 2014).

2.5 Conclusion

Trois lacunes, identifiées à travers l'examen de la technologie de pointe, seront abordées dans le présent travail. Dans un premier temps, en réponse à l'urgence des questions en pratique et au manque de recherche, l'isolabilité intérieure des murs en pisé (extérieurement non crépis) (au-dessus du soubassement) exposés à la pluie battante sera évaluée par simulation numérique. Dans un second temps, pour cela, des indicateurs de performances mécaniques seront développés en complément pour le pisé. Et troisièmement, de plus, les propriétés de transport hygrique dans le domaine capillaire seront déterminées pour les matériaux en pisé, grâce à des méthodes d'essai adaptées.

3 Caractérisation des matériaux

3.1 Introduction

Les propriétés hygriques des matériaux en pisé sont nécessaires pour étudier l'isolabilité des murs en pisé par simulation. L'objectif est d'effectuer une caractérisation hygrique complète de quelques matériaux cibles en pisé. L'atout majeur est de redévelopper le test d'absorption capillaire, incluant la méthode de transformation de Boltzmann, pour permettre son application correcte aux matériaux en pisé. En conséquence, la courbe de perméabilité à l'eau liquide des matériaux en pisé, manquante jusqu'à présent, est déterminée.

3.2 Informations sur les matériaux

3.2.1 Collection

Les matériaux en pisé candidats à la caractérisation sont extraits (au moyen de forages carottés) de constructions existantes sur six sites différents de la région Auvergne-Rhône-Alpes, France.

3.2.2 Masse volumique apparente

Alors que la détermination fiable de la masse sèche est la base pour caractériser les propriétés hygrothermomécaniques des matériaux de construction poreux, la masse volumique apparente est ensuite utile pour convertir les propriétés intensives en grandeurs volumétriques. La masse volumique apparente du pisé ne peut pas être déterminée au moyen de la pesée sous-eau saturée

sous vide standard, et par conséquent, elle est plutôt déterminée au moyen d'une immersion dans un liquide non mouillant (mercure), dans le cadre de la procédure de test de porosimétrie par intrusion de mercure. Par rapport à la méthode de détermination du volume au pied à coulisse (qui surestime le volume), le mercure donne des résultats plus fiables pour les échantillons de pisé en général relativement rugueux. Par conséquent, la masse volumique apparente de la porosimétrie par intrusion de mercure est conservée. En conséquence, la masse volumique apparente des matériaux de pisé collectés varie de 1540 kg/m³ à 1860 kg/m³ avec une moyenne de 1738 kg/m³. En outre, la masse volumique apparente obtenue à partir de deux méthodes de séchage est comparée puisque le séchage au four à 70 °C utilisé dans ce travail s'écarte des 105 °C utilisés dans la plupart des recherches antérieures sur le pisé. La différence de masse sèche correspondante est limitée.

3.2.3 Structure des pores

La structure poreuse d'un matériau de construction impacte ses propriétés hygriques. L'objectif est de sélectionner les quelques matériaux cibles à caractériser en fonction de leurs différences de structure poreuse. Pour cela, la répartition des volumes poreux des différents matériaux collectés est déterminée au moyen d'une porosimétrie à intrusion de mercure.

La porosimétrie par intrusion de mercure est réalisée sur deux à neuf échantillons par matériau, d'environ 1x1x2 cm³. La porosimétrie implique l'intrusion forcée de mercure dans un échantillon poreux sec et sous vide. L'augmentation progressive de la pression d'intrusion produit un volume de mercure introduit accru. La courbe de rétention de mercure qui en résulte est recalculée dans la courbe de rétention d'humidité du drainage principal à l'aide de l'équation de Young-Laplace et sur la base de la connaissance de la teneur en humidité de la saturation sous vide. Cette teneur en humidité à saturation sous vide est dans le présent travail estimée par la somme du volume de mercure intrus à la pression correspondant à 75% d'humidité relative et du volume des pores remplis par l'humidité lors de l'absorption isotherme jusqu'à 75% d'humidité relative (Section 3.3.1), puisque les pores les plus fins ne sont pas couverts par la plage de pression de l'appareil de porosimétrie à intrusion de mercure. Ce faisant, on suppose que l'hystérésis est négligeable à ce point d'humidité relative de 75%. Pour déterminer la distribution du volume des pores, dérivée de la courbe de rétention d'humidité, la courbe de rétention d'humidité est ajustée avec des formes de Van Genuchten.

Sur la base des résultats par échantillon, on constate que les matériaux collectés peuvent être considérés comme assez homogènes, à l'exception du pisé H4. La Fig. 1 montre la courbe de rétention d'humidité moyenne obtenue pour les différents matériaux. La porosité ouverte estimée des matériaux collectés varie de 0.293 m³/m³ à 0.406 m³/m³, avec une moyenne de 0.338 m³/m³. Sur la base des différences observées dans la structure des pores (et en écartant le pisé hétérogène H4), les pisés H1, H6 et H2 sont choisis pour être caractérisés davantage.

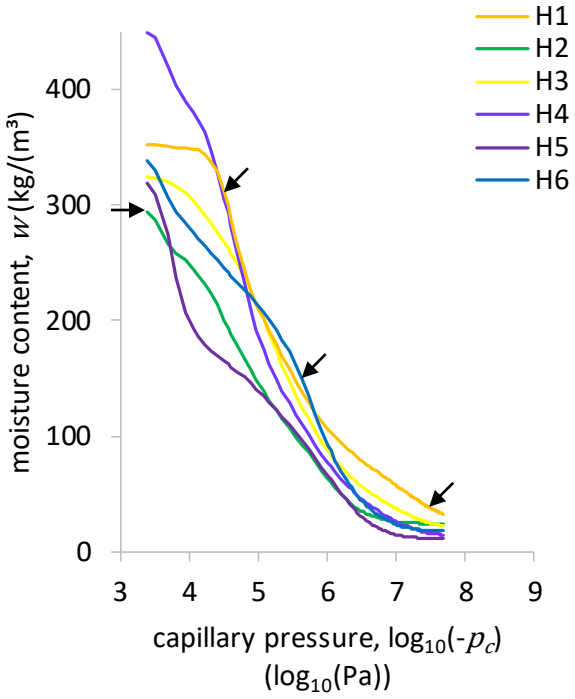

Fig. 1: Courbe moyenne de rétention d'humidité par porosimétrie par intrusion de mercure par matériau. Les flèches indiquent les critères de sélection des matériaux cibles.

3.2.4 Stabilité à l'eau

En préparation du plan de test global, un petit test de stabilité à l'eau non confiné est effectué, c'est-à-dire un test d'absorption d'eau dans lequel une mèche est utilisée pour contrer la liquéfaction et dans lequel le gonflement de l'échantillon de pisé est mesuré. Etant donné que ce gonflement est important, il est décidé d'utiliser en plus un scellement de confinement qui maintient l'échantillon mécaniquement stable dans la suite.

3.3 Stockage d'humidité

3.3.1 Isotherme de sorption

La courbe de rétention d'humidité de mouillage principal dans la plage hygroscopique est formée par l'isotherme d'absorption. L'essai au dessiccateur est utilisé pour mesurer cette isotherme d'absorption, pour trois échantillons par pisé cible et pour 11%, 33%, 53%, 75%, 85%, 94% et 97% d'humidité relative. Les isothermes de sorption résultantes sont d'abord concaves puis convexes par rapport à l'axe de l'humidité relative, ce qui est la forme normale. Deux comportements hygroscopiques distincts sont en outre observés : le pisé H1 est fortement hygroscopique dans la plage basse jusqu'à 75% d'humidité relative alors que les pisés H2 et H6 sont fortement hygroscopiques dans la plage haute au-delà de 75% d'humidité relative. Pour ces derniers, les écarts entre les échantillons augmentent significativement au-delà de 75% d'humidité relative.

3.3.2 Courbe de rétention d'humidité

Pour la courbe de rétention d'humidité de mouillage principal dans la plage surhygroscopique, les résultats de la porosimétrie par intrusion de mercure (Section 3.2.3) sont comparés aux données de mouillage principal. La psychrométrie dans la plage surhygroscopique faible est utilisée pour ces données de mouillage principal en plus des essais au dessiccateur (Section 3.3.1). De plus, le test d'absorption capillaire (Section 3.4.2) est utilisé pour déterminer la teneur en humidité capillaire, qui est utilisée pour raccourcir la courbe de rétention d'humidité dans la plage de surhygroscopie élevée.

Pour le pisé H1, un accord étroit est trouvé entre la porosimétrie d'intrusion de mercure et les données de mouillage principal. La courbe de porosimétrie par intrusion de mercure est donc utilisée pour former la courbe de rétention d'humidité de mouillage principal. Pour les pisés H2 et H6 en revanche, la porosimétrie d'intrusion de mercure et les données de mouillage principal divergent pour la plupart des échantillons à mesure que la teneur en humidité augmente, où la porosimétrie d'intrusion de mercure est inférieure aux données de mouillage principal. Cela peut s'expliquer de plusieurs manières : évolution du matériau, (micro)fissures de sciage d'échantillons, effets de déformation de la porosimétrie par intrusion de mercure, … Une courbe moyenne est donc réalisée dans le (grand) domaine hygroscopique élevé et la courbe de porosimétrie par intrusion de mercure est conservée dans la gamme surhygroscopique. Les courbes de rétention d'humidité complètes résultantes sont ajustées par des formes de Van Genuchten (pour fournir des dérivées continues). La Fig. 2 montre les résultats. Le résultat du pisé H1 est comparé aux sources de la littérature.

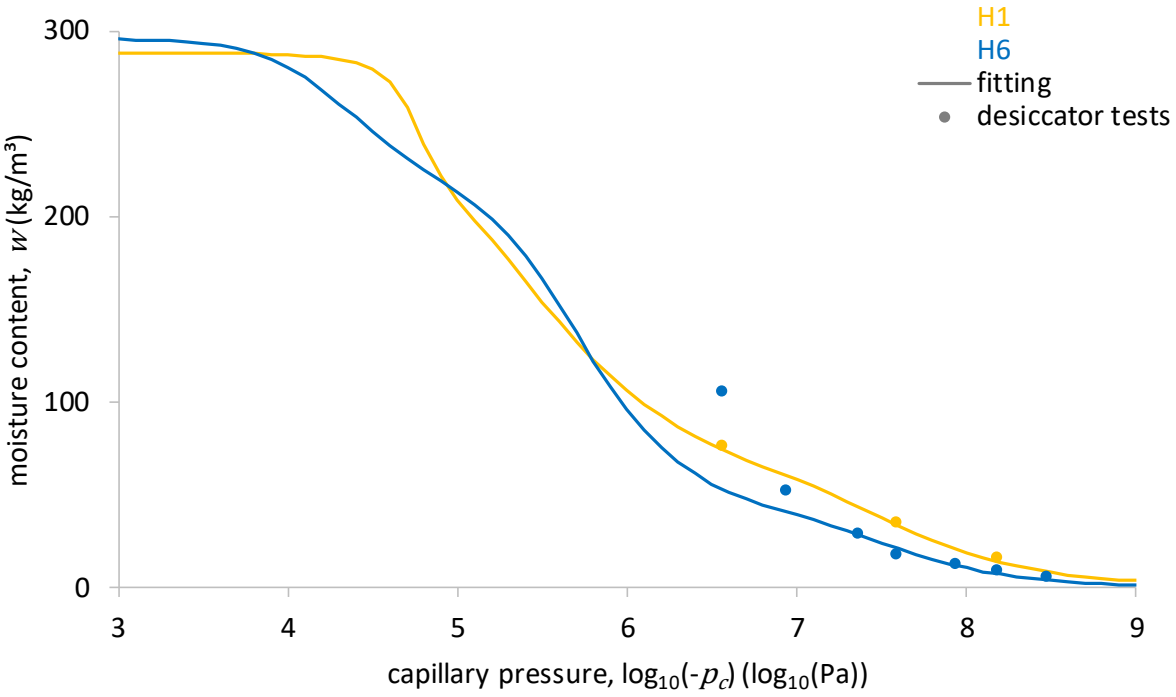

Fig. 2: Courbe de rétention d'humidité retenue pour les pisés H1 et H6. Le pisé H2 est écarté en raison de son hétérogénéité (Section 3.4).

3.4 Transport d'humidité

3.4.1 Perméabilité à la vapeur

Le facteur de résistance à la vapeur à partir duquel la courbe de perméabilité à la vapeur est calculée, ainsi que la perméabilité à l'humidité dans la plage hygroscopique, sont mesurés au moyen d'essais en coupelle. Un test en coupelle sèche (11% - 53% d'humidité relative (HR)), un test en coupelle intermédiaire (53% - 84% HR) et un test en coupelle humide (94% - 84% HR) sont effectués. Le facteur de résistance à la vapeur en coupelle sèche résultant est de 7.7 pour le pisé H1, de 8.2 pour le pisé H6 et de 10.9 pour le pisé H2. Cela reflète la tendance à la porosité ouverte. L'augmentation de la perméabilité à la vapeur (équivalente) dans le test de coupelle humide est la plus importante pour le pisé H1, ce qui reflète la tendance à l'hygroscopicité.

3.4.2 Absorption capillaire

Le test d'absorption capillaire constitue la base pour déterminer la perméabilité à l'humidité dans la plage surhygroscopique. Il fournit en outre le taux d'humidité capillaire (en plus du coefficient d'absorption capillaire). Par cible de pisé, deux échantillons sont testés en laboratoire et deux sous

rayons X. Le pisé H2 est considéré comme trop hétérogène pour être caractérisé davantage. Étant donné que les matériaux en pisé se liquéfient et se dilatent au contact de l'eau, la méthode d'essai standard est modifiée comme suit. Une fine mèche de brique perméable et un papier de contact sont appliqués en tant que parties inférieures de l'échantillon, pour contrer la liquéfaction, et un scellement de confinement est utilisé, contre l'expansion. Dans le traitement des données, Fig. 3, par conséquent, la masse d'humidité estimée des parties inférieures est soustraite pour permettre de déterminer la teneur en humidité capillaire. Comme la mèche et le papier sont initialement secs, l'absorption dans un composite s'applique. Le coefficient d'absorption capillaire est donc obtenu à partir du dernier motif de première étape linéaire persistant récupéré, soutenu par le coefficient de détermination. L'interception de cet ajustement de la première étape de la masse d'humidité dans la partie supérieure seule contre la racine carrée du temps, Eq. (7), correspond à la hauteur équivalente des parties inférieures.

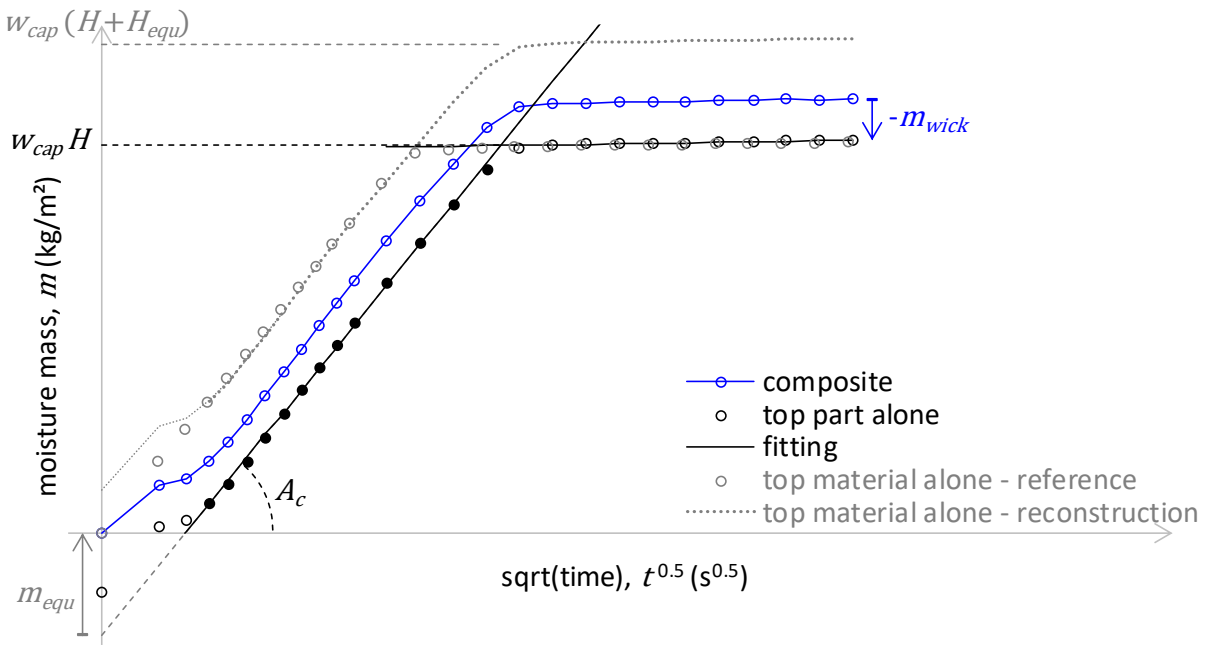

Fig. 3: Illustration de la méthode de traitement des données à l'aide des résultats des tests d'absorption capillaire en brique de céramique.

$$m_{tpa} = A_c\sqrt{t} - m_{equ} = A_c\sqrt{t} - w_{cap}H_{equ} \tag{7}$$

La teneur en humidité capillaire résultante s'élève à 288 kg/m³ pour le pisé H1 et à 296 kg/m³ pour le pisé H6 et le coefficient d'absorption capillaire s'élève à 0.262 kg/(m² s$^{0.5}$) pour le pisé H1 et à 0.188 kg /(m² s$^{0.5}$) pour le pisé H6. Les hauteurs équivalentes sont généralement similaires ou inférieures à la hauteur de mèche de 1 cm.

3.4.3 Diffusivité de l'humidité

Les profils de teneur en humidité pendant le test d'absorption capillaire sont mesurés au moyen d'une radiographie aux rayons X. La transformation de Boltzmann est appliquée à ces profils de teneur en humidité pour obtenir le profil caractéristique qui est utilisé pour déterminer la diffusivité de l'humidité. Étant donné que la méthode de transformation de Boltzmann exige normalement que l'échantillon soit suffisamment homogène et présente dès le départ le comportement d'absorption d'humidité racine carrée dans le temps idéal, elle est nécessairement redéveloppée pour le cas composite en question. La hauteur équivalente des parties inférieures est utilisée pour cela, Eq. (8). La Fig. 4 montre le résultat pour un échantillon de pisé H1. La diffusivité de l'humidité est obtenue en intégrant et en différenciant ce profil transformé caractéristique de Boltzmann.

$$\lambda^* = \frac{x_{tpa} + H_{equ}}{\sqrt{t}} \tag{8}$$

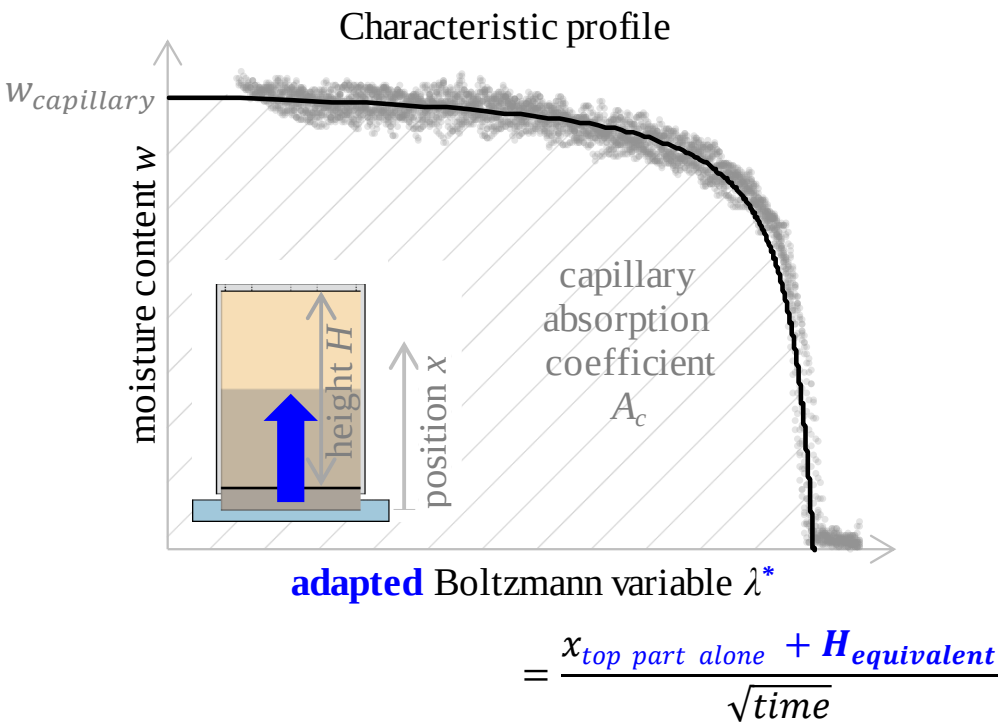

Fig. 4: Ajustement du profil caractéristique et profils de teneur en humidité transformés par Boltzmann sous-jacents pour l'échantillon de pisé H1.

3.4.4 Perméabilité à l'humidité

La perméabilité à l'humidité dans la plage surhygroscopique, c'est-à-dire la perméabilité à l'eau liquide, est obtenue par le produit de la diffusivité de l'humidité et de la capacité d'humidité, la dérivée de la courbe de rétention d'humidité. Il est vérifié que cette perméabilité reproduit le comportement d'absorption capillaire par simulation numérique. La Fig. 5 montre les résultats. La caractérisation cible est ainsi terminée.

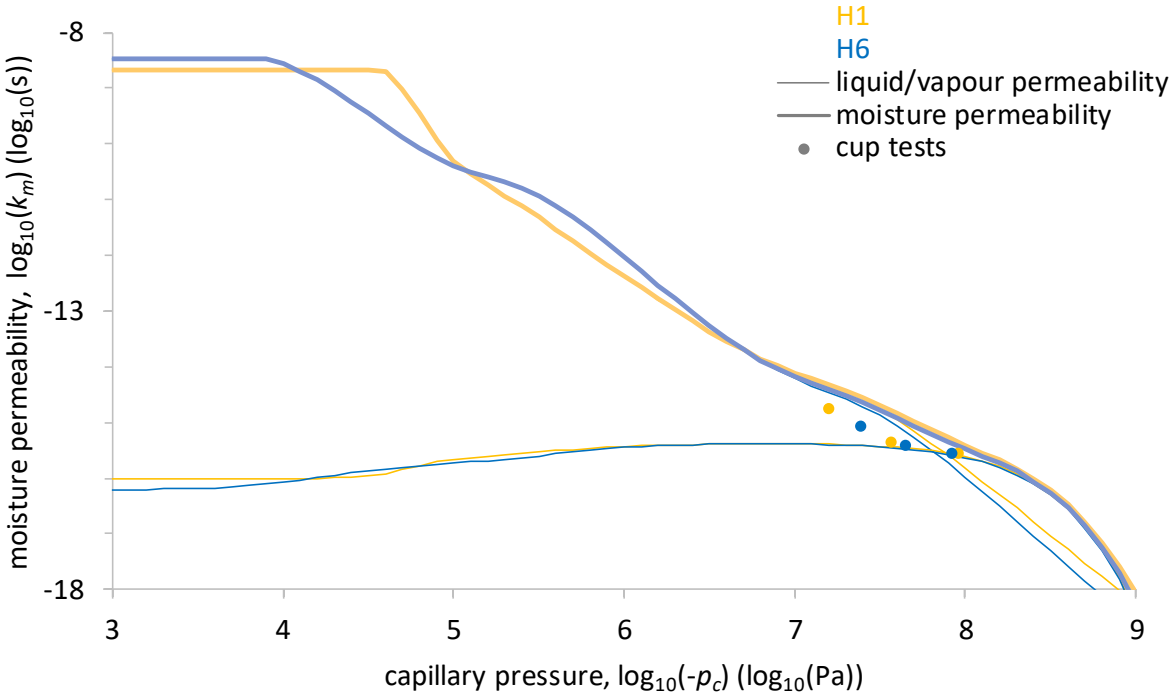

Fig. 5: Perméabilité à l'humidité des matériaux cibles en pisé H1 et H6.

3.5 Conclusion

La caractérisation hygrique complète est réalisée pour deux matériaux différents en pisé. Leur courbe de rétention d'humidité est déterminée au moyen d'une combinaison d'essais au dessiccateur, de porosimétrie par intrusion de mercure et d'essais d'absorption capillaire (réaménagés). Leur courbe de perméabilité à la vapeur est déterminée à l'aide du test standard de la coupelle. Et leur courbe de perméabilité à l'eau liquide est déterminée par le test d'absorption capillaire redéveloppé (composite confiné) avec radiographie aux rayons X.

4 Indicateurs de performance

4.1 Introduction

Pour permettre d'évaluer l'isolabilité intérieure des murs en pisé vis-à-vis des risques d'endommagement de la structure, des indicateurs de performance mécanique sont développés.

4.2 Développement d'indicateurs

4.2.1 Résistance et rigidité globales

Avec l'augmentation de la teneur en humidité, les matériaux gonflent et leur résistance et leur rigidité diminuent. Ceci est particulièrement prononcé pour les matériaux liés à l'argile, tels que le pisé. Pour évaluer les performances mécaniques globales des murs en pisé, la contrainte relative de fracture et la contrainte relative de flambement doivent être surveillées. Les contraintes normales de compression au bas d'un mur en pisé s'élèvent à env. 0.171 MPa, ce qui est estimé sur la base d'une géométrie de bâtiment exemplaire avec des charges mécaniques supplémentaires prescrites. Outre cette charge mécanique structurelle, des contraintes normales d'origine hygrique s'ajoutent lorsque le mouvement associé est entravé. Dans le présent travail, on suppose que toute expansion par rapport à l'état d'équilibre de stabilité transitoire à l'humidité relative ou la pression capillaire moyenne du mur est entièrement supprimée dans le sens de la hauteur et de la largeur. Les courbes de la résistance à la compression, du module de Young, de la déformation hygrique et du coefficient de Poisson du pisé H1 sont principalement obtenues à partir de sources bibliographiques. Alors que la résistance à la compression peut être utilisée directement pour la fracture, les trois autres propriétés sont utilisées en combinaison avec le moment quadratique, les fixations et la hauteur du mur, et la forme de chargement du mur, pour déterminer la résistance au flambement. Le risque de défaillance structurale par rupture par compression est indiqué par la perte de section portante, S (%). Ici, l'épaisseur restante de la section du mur porteur est celle où la contrainte de fracture relative reste inférieure à l'unité, Eq. (9). Le risque de rupture par flambement est indiqué par la contrainte de flambement relative, B (%), Eq. (10).

$$1 > \frac{\sigma_c + \sigma_{hygric,i}}{\sigma_{max,i}} \tag{9}$$

$$B = \frac{\sigma'}{\sigma_{cri}'} \times 100 = \frac{\sigma_c' + \sigma_{hygric,avg}'}{\left(1 + 4.32 \times \frac{N_{hygric,avg}'}{N_c + N_{hygric,avg}'}\right)\left(1 - \nu_{avg}'^2\right)\left(L/\sqrt{2}\right)^2 bh' \times 12} \times 100 \tag{10}$$

4.2.2 Contraintes et déformations hygrothermiques différentielles et dégâts de gonflement de l'argile

L'exemple de mécanisme d'endommagement des contraintes et déformations hygrothermiques qui est étudié dans le présent travail est les dégâts de gonflement de l'argile hygrique par cisaillement répété qui peuvent être suivis d'un flambage d'une couche superficielle de la paroi en pisé. De tels dommages doivent être évités car la discontinuité créée empêche la redistribution de l'humidité, ce qui augmente la teneur en humidité dans la couche de surface et, par conséquent, d'autres risques hygrothermiques peuvent également être renforcés. S'il se produit de surcroît un flambage de la couche de surface extérieure, avec détachement du matériau bouclé, l'apparence est en outre perturbée et la fonction encore plus, par la possible pénétration d'eau en combinaison avec la capacité de séchage réduite et l'épaisseur de paroi réduite. Les fissures de cisaillement peuvent être causées par des gradients d'humidité de mouillage excessifs ou par un échec de fracture. La contrainte hygrique est calculée au moyen de la loi de Hooke dans des conditions de contraintes planes équibiaxiales. La contrainte de cisaillement est égale à la différence de contrainte normale entre chaque position incrémentielle. La résistance au cisaillement est estimée à 0.1 fois la résistance à la compression. Le risque d'endommagement par gonflement de l'argile est indiqué par le nombre de cycles de gonflement de l'argile, c'est-à-dire le nombre de fois où la valeur absolue de la contrainte de cisaillement est égale ou supérieure à la résistance au cisaillement, Eq. (11), et la contrainte de cisaillement est positive pour la surface extérieure ou négative pour la surface intérieure ou un échec de fracture se produit.

$$1 \leq \frac{|\tau_{imm}|}{\tau_{max,imm}} = \frac{|\sigma_i - \sigma_{i+1}|}{0.1 \times \frac{\sigma_{max,i} + \sigma_{max,i+1}}{2}} \tag{11}$$

4.2.3 Erosion

Une quantification des contraintes d'érosion qui résultent de la pression d'impact des gouttes de pluie et de l'écoulement radial qui en résulte et de la résistance à l'érosion des matériaux en pisé sort du cadre du présent travail. Le risque de dommages causés par l'érosion est indiqué de manière simplifiée par le nombre d'heures pendant lesquelles la teneur en humidité de la surface du mur extérieure dépasse 80% de la teneur en humidité capillaire alors que la charge de pluie entraînée par le vent est positive, Eq. (12).

$$w_{se} > 0.8\, w_{cap}\ and\ R_{wdr} > 0 \tag{12}$$

4.3 Conclusion

Quatre indicateurs de performance mécanique sont développés pour l'isolation intérieure des murs en pisé : échec par fracture, échec par flambement, endommagement par gonflement de l'argile et érosion. Leur quantification nécessite des informations supplémentaires telles que les propriétés mécaniques des matériaux.

5 Analyse de l'isolation intérieure

5.1 Introduction

Pour contribuer à lever les incertitudes sur l'isolabilité intérieure des murs en pisé, l'impact de l'isolation intérieure sur les performances hygrothermiques des murs en pisé (non enduit) est analysé (au-dessus du soubassement et hors remontées capillaires), par simulation numérique. Les propriétés mécaniques seront négligées dans un premier temps. Ensuite, il sera examiné quel impact ceux-ci peuvent avoir.

5.2 Configuration du modèle

5.2.1 Logiciel

Le logiciel de simulation de composants hygrothermique Delphin est utilisé. Les transferts unidimensionnels de chaleur et d'humidité sont pris en compte (Section 2.3). La taille de l'élément de grille est prise égale à 1 mm.

5.2.2 Paramètres d'entrée

5.2.2.1 Matériaux

Le Tableau 1 présente la composition des différents assemblages muraux étudiés. La référence est un mur en pisé homogène de 50 cm d'épaisseur. Les deux matériaux de pisé considérés (H1/H6) ont des propriétés hygriques différentes : le pisé H1 est plus hygroscopique et plus actif par capillarité que le pisé H6. L'influence de cinq différents systèmes d'isolation intérieure conventionnels de 10 cm d'épaisseur appliqués à ce mur est étudiée : un système d'isolation étanche à la vapeur en polystyrène extrudé (XPS), un système étanche à la vapeur en laine

minérale plus pare-vapeur, un système ouvert à la vapeur en laine minérale, un système actif capillaire en fibre de bois, et un système actif capillaire en silicate de calcium.

Tableau 1: Vue d'ensemble des assemblages de murs avec différents systèmes d'isolation intérieure.

<table>
<tr><td>reference</td><td rowspan="7">outside</td><td rowspan="7">rammed earth wall
H1/H6</td><td colspan="3">gypsum plaster</td><td rowspan="7">inside</td></tr>
<tr><td>VT</td><td>GM</td><td>XPS</td><td>gypsum plaster</td></tr>
<tr><td>VT</td><td colspan="2">Mineral wool + VB</td><td>gypsum board</td></tr>
<tr><td>VO</td><td colspan="2">Mineral wool</td><td>gypsum board</td></tr>
<tr><td>(VN-)C</td><td>GM</td><td>Wood fibre</td><td>gypsum plaster</td></tr>
<tr><td>(VO-)C</td><td>GM</td><td>Calcium silicate</td><td>gypsum plaster</td></tr>
</table>

Pour le post-traitement concernant les performances mécaniques, la géométrie du bâtiment est supposée avoir une hauteur de 6,5 mètres et une largeur de 6,5 mètres dans les deux sens. Les propriétés mécaniques sont issues de la littérature et deux variantes de la courbe de résistance à la compression (et de la courbe de déformation de gonflement libre) sont considérées. La première variante correspond au pisé H1, qui conserve sa résistance dans le domaine hygroscopique, et la deuxième variante correspond au pisé H2, qui perd relativement brutalement sa résistance dans le domaine hygroscopique.

5.2.2.2 Conditions climatiques

Le climat de Lyon en 2014 pour un mur orienté Sud est choisi en fonction de la charge de pluie poussée par le vent la plus sévère. Les données brutes sur le climat extérieur sont la température des gaz, l'humidité relative, la vitesse et la direction du vent, l'intensité des précipitations horizontales, la nébulosité et le rayonnement horizontal direct et diffus à ondes courtes. Sur cette base, la température équivalente extérieure, les coefficients de transfert de chaleur et d'humidité de surface par convection et la charge de pluie entraînée par le vent sont calculés. Pour ce dernier, le coefficient de pluie poussée par le vent s'élève à 0.084 s/m sur la base des hypothèses de construction. La quantité totale annuelle de pluie entraînée par le vent qui en résulte est de 154 mm. Les conditions climatiques intérieures de température et d'humidité relative sont déterminées en fonction de la température extérieure moyenne journalière conformément à la norme. Le niveau d'humidité relative intérieure pour une occupation élevée du bâtiment est sélectionné.

5.2.3 Sorties

La **valeur U** stationnaire en pratique, U_{stat} (W/(m² K)), qui peut être comparée à l'exigence, est définie comme la valeur absolue moyenne du flux de chaleur de l'intérieur vers la surface intérieure dans le temps divisée par la moyenne valeur absolue de la différence de température d'un environnement à l'autre dans le temps. La **qualité de l'isolation hygro-thermique** est l'augmentation de la valeur U par l'humidité dans l'isolation, ΔU (%). La **réponse transitoire thermique** (concernant le confort d'été) est évaluée qualitativement au moyen du flux de chaleur entrant et sortant de la surface intérieure. Le risque de **développement de moisissures intérieures** est indiqué par la valeur maximale de l'indice de moisissure (M, -) considérée sur une période de simulation de dix ans. Le risque de **développement de moisissures interstitielles** est évalué des deux côtés des couches d'isolation. Les matériaux sont supposés appartenir à la classe sensible aux moisissures dans le modèle VTT mis à jour utilisé. Le risque d'**humidité dégouttante** est évalué comme le nombre d'heures pendant lesquelles l'humidité relative dépasse 97 % à l'interface entre la laine minérale et le pare-vapeur au cours de l'année. Le risque de **pourriture du bois** est indiqué par la perte totale de masse de bois (ML, %) après dix ans, et est évalué à la profondeur d'extrémité de la poutre et à l'interface. La **réponse transitoire hygrique** est évaluée qualitativement en termes de flux de vapeur entrant et sortant de la surface intérieure. Le risque d'**échec par fracture** est indiqué par la perte maximale de la section portante (S, %) sur l'année. Le risque d'**échec par flambage** est indiqué par la contrainte de flambement relative maximale (B, %) sur l'année. Le risque d'**endommagement par gonflement de l'argile** est indiqué par le nombre maximal de cycles de gonflement de l'argile à la même profondeur dans le mur au cours de l'année. Le risque de **dommages causés par le gel** est indiqué par le nombre maximum de cycles de gel-dégel ($\#F\text{-}TC$, -) (en utilisant la relation de Gibbs-Thomson). Et le risque d'**érosion** est indiqué par le nombre d'heures pendant lesquelles la teneur en humidité de la surface du mur extérieure dépasse 80 % de la teneur en humidité capillaire alors que la charge de pluie entraînée par le vent est supérieure à zéro.

5.3 Résultats et discussion

5.3.1 Mur de référence

Les performances hygrothermiques du mur en pisé non isolé de référence H1 sont évaluées. Au préalable, on observe que les états surhygroscopiques sont adressés 24 % du temps. La valeur U stationnaire en pratique s'élève à 0.82 W/(m² K) et la perte de chaleur totale par transmission s'élève à 72 kW h/m². La réponse transitoire thermique reflète la grande effusivité thermique du matériau en pisé. Les risques de développement de moisissures intérieures et interstitielles sont

nuls. On constate une perte de masse de bois de 1.1 % après dix ans en bout de poutre (au milieu du mur). La réponse transitoire hygrique reflète la grande effusivité de l'humidité du matériau en pisé. Une perte de section portante de 15.2 % est trouvée. Une contrainte relative de flambement de 4.4 % est trouvée. 10 cycles de gonflement de l'argile se trouvent près de la surface extérieure. Le risque d'endommagement par le gel est nul. Et 13 heures de risque d'érosion sont constatées. En conclusion, seule la qualité de l'isolation thermique pose problème pour ce cas de référence.

5.3.2 Influence des systèmes d'isolation

L'impact de cinq systèmes d'isolation intérieure différents de 10 cm d'épaisseur sur la performance hygrothermique du mur est évalué. Au préalable, on observe qu'en appliquant une isolation intérieure, les niveaux d'humidité dans le mur augmentent, reflétant les propriétés hygriques des systèmes d'isolation. Par exemple, les systèmes d'isolation étanches à la vapeur entravent le plus le séchage vers l'intérieur, ce qui entraîne la plus grande accumulation d'humidité dans le mur de pisé de la pluie absorbée chassée par le vent. En revanche, le système d'isolation en silicate de calcium actif capillaire permet un séchage optimal vers l'intérieur tout en tamponnant la condensation interstitielle, ce qui se traduit par des niveaux d'humidité plus proches du mur d'origine.

Avec une épaisseur d'isolation de 10 cm, la valeur U s'élève à 0.16 W/(m² K) pour XPS à 0.32 W/(m² K) pour la fibre de bois. L'augmentation de la valeur U par l'humidité de l'isolant s'élève à 9.8% pour la fibre de bois et à 2.0% pour le silicate de calcium. La réponse transitoire thermique s'aggrave comme prévu. Le risque de développement de moisissures intérieures reste nul. Le risque de développement de moisissures interstitielles est important du côté extérieur des couches d'isolant, sauf pour le système d'isolant au silicate de calcium. 4 % d'heures de risque d'humidité dégouttante sont constatées (condensation estivale contre le pare-vapeur). >100% pour le XPS à 37% pour le silicate de calcium une perte de masse du bois est constatée. 2 cycles gel-dégel sont constatés. Et 14 heures pour le XPS à 13 heures pour le silicate de calcium de risque d'érosion sont retrouvées. Par conséquent, un système d'isolation capillaire actif en silicate de calcium est encouragé car il présente les risques de dommages dus à l'humidité les plus faibles, en particulier la croissance de moisissures interstitielles et la pourriture du bois.

La Fig. 6 résume les résultats des indicateurs de performance pour le mur de référence non isolé et avec les cinq différents systèmes d'isolation intérieure. Dans (Hens et al., 2006), le risque est défini comme la probabilité qu'un événement de défaillance se produise multiplié par la gravité

des conséquences lorsqu'il se produit. La gravité des conséquences s'exprime en coûts (pour réparer les dégâts et compenser toutes les souffrances causées). Dans la présente étude déterministe, pour permettre de tracer graphiquement les valeurs des différents indicateurs sur une échelle commune dans cette synthèse, les indicateurs sont traduits en un coût relatif, comme suit. Tout d'abord, prenez la valeur maximale de l'indicateur sur tous les résultats de configuration étudiés. Ensuite, divisez le résultat de chaque indicateur par cette valeur maximale. Enfin, utilisez un facteur d'échelle par indicateur, voir Tableau 2, pour tenir compte de l'importance relative des différents risques.

Tableau 2: Aperçu des valeurs maximales des indicateurs et des facteurs d'échelle pour les barres de coût relatif des différents indicateurs de performance.

	U-value	ΔU	M interior	M interstitial	DM	ML	S	B	#CSC	#F-TC	ER
maximum	0.84	10.3	0	4.9	4.2	290	100	100	41	3	15
scale factor	1	0.2	0.75	0.75	0.75	2	1.25	1.25	0.6	0.25	0.2
scale factor/maximum	1.19	0.019	NA	0.15	0.18	0.0069	0.013	0.013	0.015	0.083	0.013

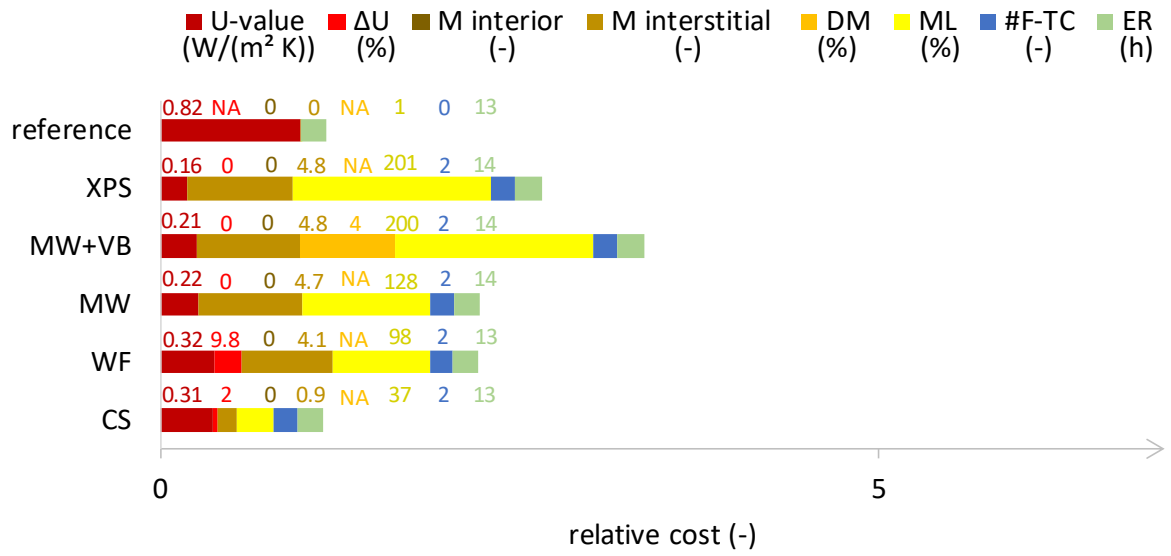

Fig. 6: Aperçu du coût relatif total pour mur en pisé H1 avec différents systèmes d'isolation.

5.3.3 Influence de l'épaisseur de l'isolant

L'influence de quatre épaisseurs d'isolation différentes est prise en compte : 2 cm, 5 cm, 10 cm et 20 cm. Au préalable, on observe que la teneur en humidité dans le mur en pisé augmente avec l'augmentation de l'épaisseur de l'isolant, en raison de la capacité réduite de séchage vers l'intérieur et des températures plus basses. La valeur U diminue avec l'augmentation de l'épaisseur

de l'isolant. L'augmentation de la valeur U par l'humidité de l'isolant augmente avec l'augmentation de l'épaisseur de l'isolant. La réponse transitoire thermique est assez invariable avec l'épaisseur de l'isolant. Le risque de développement de moisissures intérieures reste nul. Le risque de développement de moisissures interstitielles reste important pour les systèmes d'isolation étanches à la vapeur et diminue avec la diminution de l'épaisseur de l'isolant pour les autres systèmes d'isolation. Le nombre d'heures de risque d'humidité dégouttante décroît généralement avec la diminution de l'épaisseur de l'isolant. Le risque de pourriture du bois augmente avec l'augmentation de l'épaisseur de l'isolant. La réponse transitoire hygrique est assez invariable avec l'épaisseur de l'isolant. L'influence de l'épaisseur de l'isolant sur la rupture par fracture, la rupture par flambage et le risque d'endommagement par gonflement de l'argile n'est pas prise en compte. Le risque de dommages par le gel augmente avec l'augmentation de l'épaisseur de l'isolant. Et le risque d'érosion augmente avec l'augmentation de l'épaisseur de l'isolant. Il est conclu que, bien que la qualité de l'isolation thermique s'améliore avec l'augmentation de l'épaisseur de l'isolation, les risques de dommages dus à l'humidité augmentent également. La Fig. 7 montre le coût relatif total avec les cinq systèmes d'isolation pour une épaisseur d'isolation de 2 cm et de 20 cm. On constate par estimation que l'influence du choix du système d'isolation est majoritairement plus importante que l'influence de l'épaisseur de l'isolation. Avec des épaisseurs d'isolation plus petites, d'autres systèmes d'isolation pourraient également être applicables, tels que la fibre de bois ou la laine minérale, mais le silicate de calcium reste le choix le plus performant.

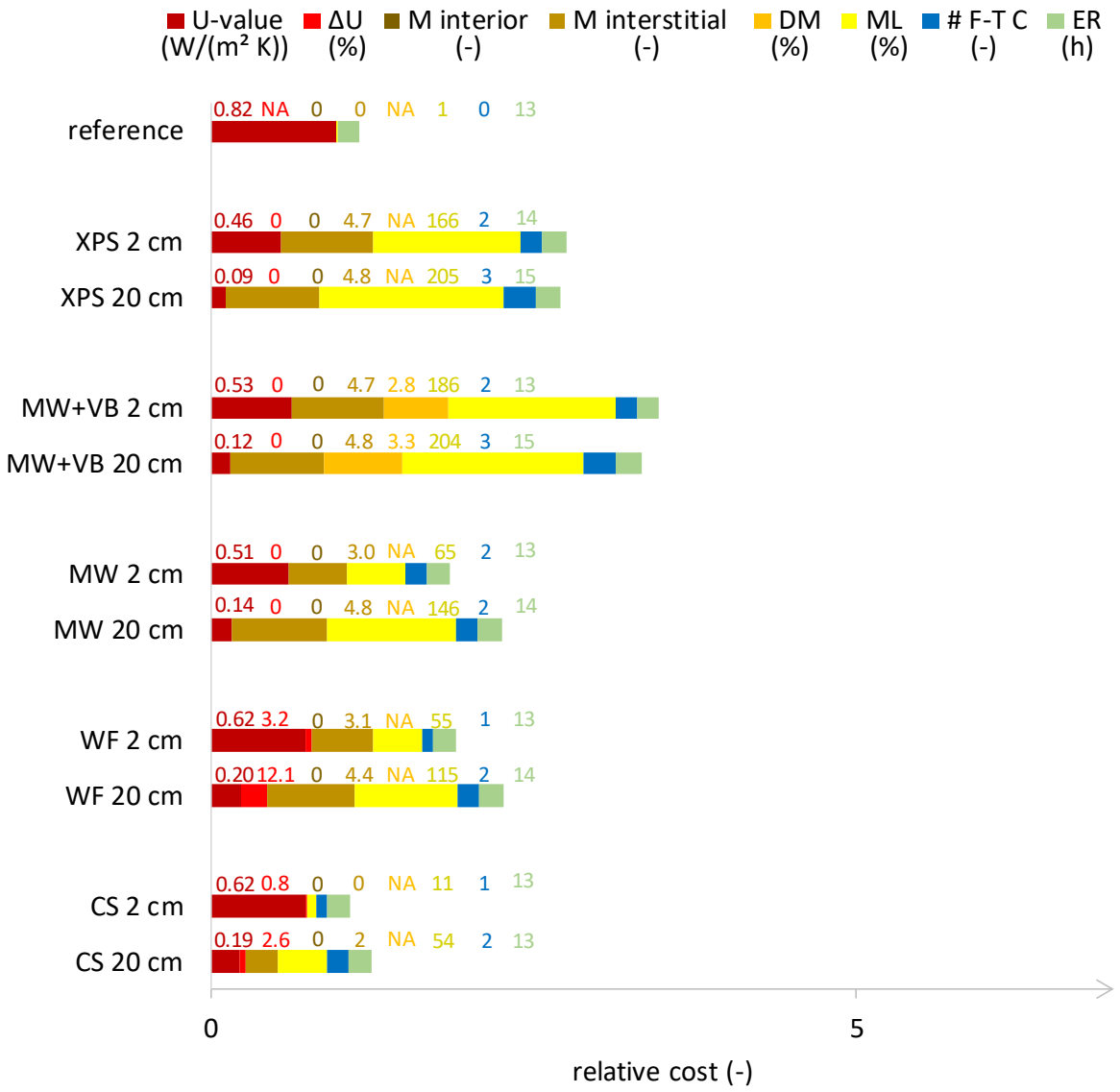

Fig. 7: Schéma de coût relatif total pour mur en pisé H1 avec différentes épaisseurs d'isolant.

5.3.4 Influence du matériau pisé

L'influence des propriétés hygriques du matériau pisé est étudiée via le pisé H6. Au préalable, on observe que le taux d'humidité moyen dans le mur en pisé est en moyenne 28% plus faible pour le pisé H6 que pour le pisé H1, ce qui s'explique par l'évolution hygroscopiquement plus plate de la courbe de rétention d'humidité. L'humidité relative en revanche est plus importante, ce qui s'explique également par l'évolution de la courbe de rétention d'humidité. Cette évolution hygroscopiquement plus plate de la courbe de rétention d'humidité est aussi la raison pour laquelle, à l'exception de la valeur U et du nombre d'heures de risque d'érosion (qui diminuent, comme le taux d'humidité), tous les indicateurs de risque augmentent pour le pisé H6 (l'augmentation de la valeur U par l'humidité de l'isolant, le développement de moisissures

interstitielles, l'humidité qui s'égoutte et, surtout, la pourriture du bois). Le risque de dommages causés par le gel augmente également. Le risque de développement de moisissures intérieures reste nul. La Fig. 8 montre le coût relatif total pour les différentes configurations avec le pisé H6 en plus du pisé H1. On observe que pour ce mur en pisé H6 également, le système d'isolation au silicate de calcium donne beaucoup moins de risque de pourriture du bois et de développement de moisissures interstitielles que les autres systèmes d'isolation. Ainsi, il est généralement recommandé d'utiliser le système de silicate de calcium pour l'isolation. Les systèmes d'isolation étanches à la vapeur sont les moins performants. Par ailleurs, on observe par estimation que le matériau en pisé peut avoir une influence presque aussi importante que le système d'isolation. Par exemple, la différence de coût relatif total entre le mur en pisé H6 avec laine minérale plus pare-vapeur et le mur en pisé H1 avec laine minérale plus pare-vapeur est presque aussi importante que la différence de coût relatif total entre le mur en pisé H6 mur avec laine minérale plus pare-vapeur et le mur en pisé H6 avec isolation XPS. Ou encore, la différence de coût relatif total entre le mur en pisé H6 avec XPS et le mur en pisé H1 avec XPS est tout aussi importante que la différence de coût relatif total entre le mur en pisé H6 avec XPS et le mur en pisé H6 avec isolation en laine minérale.

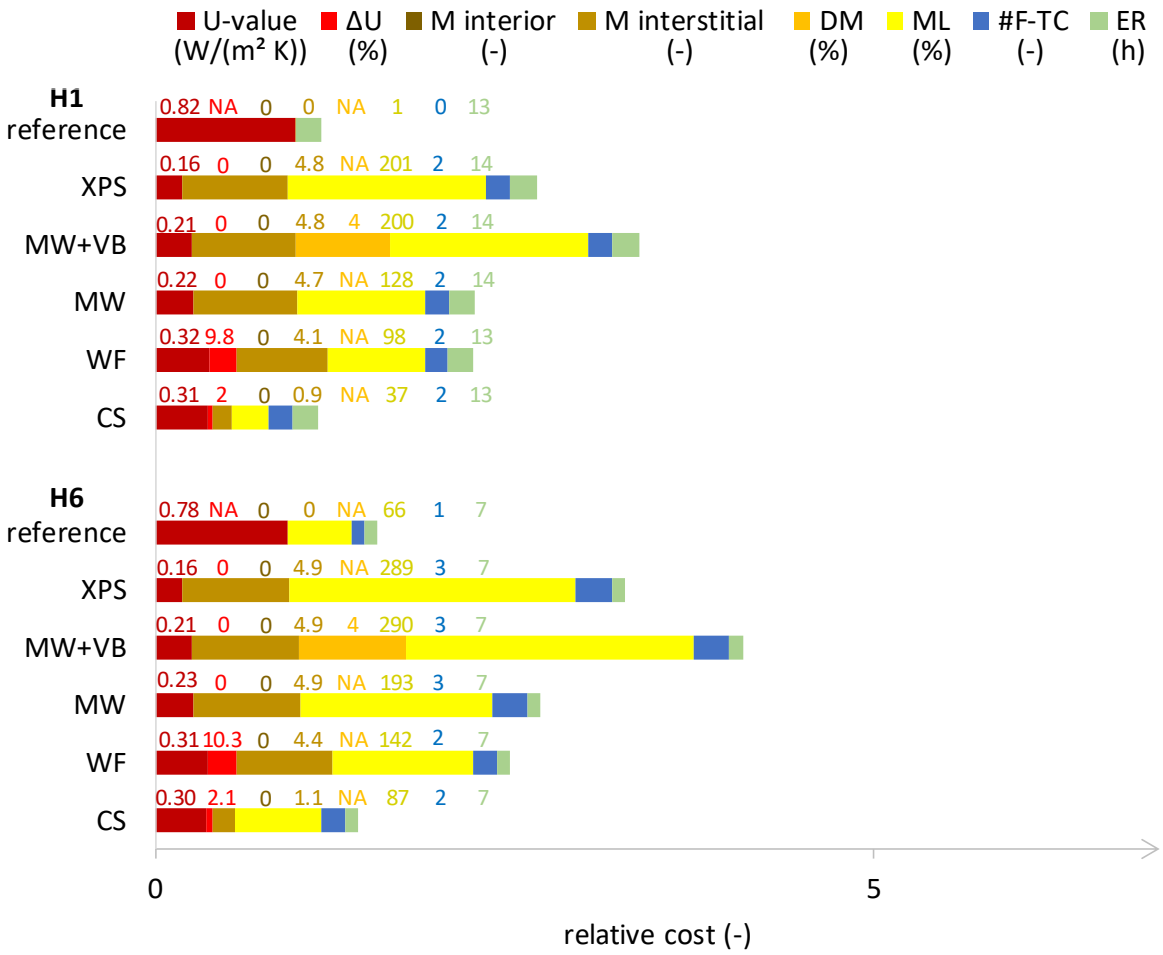

Fig. 8: Aperçu du coût relatif total pour mur en pisé H6 (en plus de H1) avec différents systèmes d'isolation.

5.3.5 Influence de l'épaisseur du mur en pisé

L'influence de trois épaisseurs différentes de murs en pisé est considérée : 30 cm, 50 cm et 80 cm. Au préalable, on observe que plus le mur en pisé est épais, plus l'évolution de l'humidité moyenne dans le temps est plate. De plus, la teneur en humidité à la surface extérieure est la plus élevée pour le mur le plus épais (en raison de la capacité réduite de séchage vers l'intérieur) tandis que la teneur en humidité à la surface intérieure est la plus élevée pour le mur le plus mince (en raison de la pénétration de pluie plus élevée). Cette dernière est la raison pour laquelle, pour le mur plus épais, l'augmentation de la valeur U par l'humidité de l'isolant, le développement de moisissures interstitielles (du côté extérieur) pour le système de laine minérale sans pare-vapeur, l'humidité dégouttante et la pourriture du bois pour le mur non isolé et pour les assemblages de murs à isolation ouverte à la vapeur ou active capillaire, diminuent. Le premier est la raison pour laquelle le risque de dommages par le gel augmente pour le mur plus épais. Le risque d'érosion reste

inchangé. Le risque de développement de moisissures interstitielles pour le système de laine minérale avec pare-vapeur, contre le pare-vapeur, et le risque de pourriture du bois pour les assemblages muraux isolés étanches à la vapeur augmentent, en raison de la capacité réduite de séchage vers l'extérieur. Le risque de développement de moisissures intérieures reste nul. Et la valeur U diminue en raison de l'épaisseur de paroi supplémentaire. La Fig. 9 montre les coûts relatifs totaux pour le mur de 80 cm (en plus de 50 cm) d'épaisseur. On en conclut qu'un mur plus épais favorise globalement l'isolabilité des murs en pisé (sauf avec le système d'isolation XPS). Bien que le silicate de calcium reste la meilleure option, on pourrait également appliquer de la fibre de bois ou de la laine minérale.

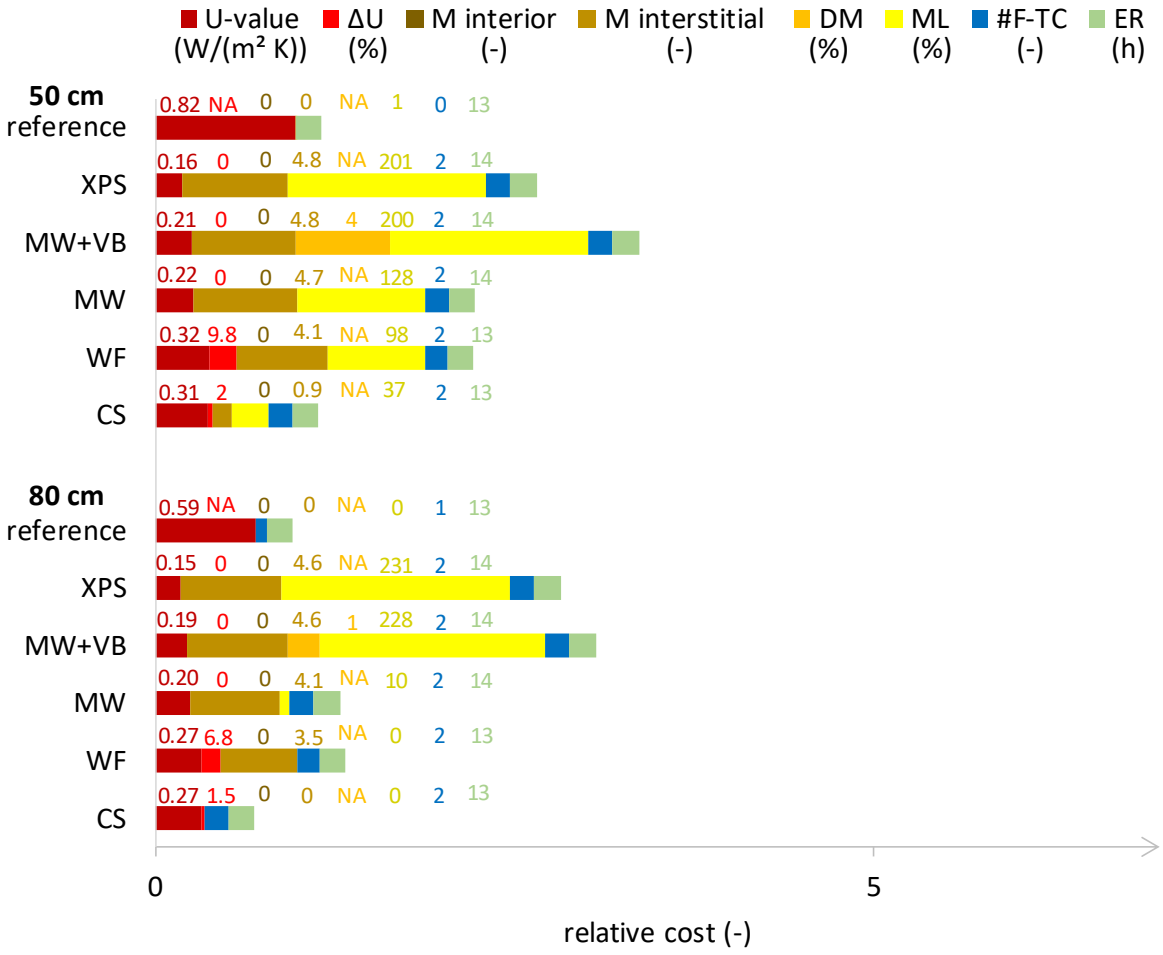

Fig. 9: Schéma de coût relatif total pour mur en pisé H1 de 80 cm (en plus de 50 cm) d'épaisseur avec différents systèmes d'isolation.

5.3.6 Influence de l'orientation du mur

L'influence de quatre orientations différentes des murs est explorée : nord, est, sud et ouest. Plus précisément, il est examiné si l'orientation sud est également la plus critique pour la valeur U et pour les dommages causés par le gel et quel est l'impact de l'orientation du mur sur le choix du système d'isolation. En conséquence, on constate que l'orientation nord est la plus critique pour la valeur U et l'orientation sud la moins, ce qui s'explique par les gains de chaleur solaire. Il est donc recommandé de déterminer l'épaisseur d'isolant requise en fonction de l'orientation nord. Néanmoins, l'orientation sud reste la plus critique pour les dommages causés par le gel en raison de la charge de pluie poussée par le vent plus élevée (en 2014). Enfin, comme le montre la Fig. 10, alors que pour l'orientation sud avec une forte charge de pluie poussée par le vent, le système de silicate de calcium est le seul système d'isolation recommandable, tous les systèmes d'isolation présentent des risques acceptables pour l'orientation est avec une faible charge de pluie poussée par le vent. Les systèmes d'isolation étanches à la vapeur et le système au silicate de calcium sont les plus performants en termes de coût relatif total. Il n'y a aucun risque de pourriture du bois pour cette orientation. Dans l'ensemble, le choix du système d'isolation peut dépendre de l'orientation du mur à travers la charge de pluie poussée par le vent. C'est surtout pour les murs soumis à une forte charge de pluie poussée par le vent que l'utilisation spécifique d'isolants au silicate de calcium devient importante.

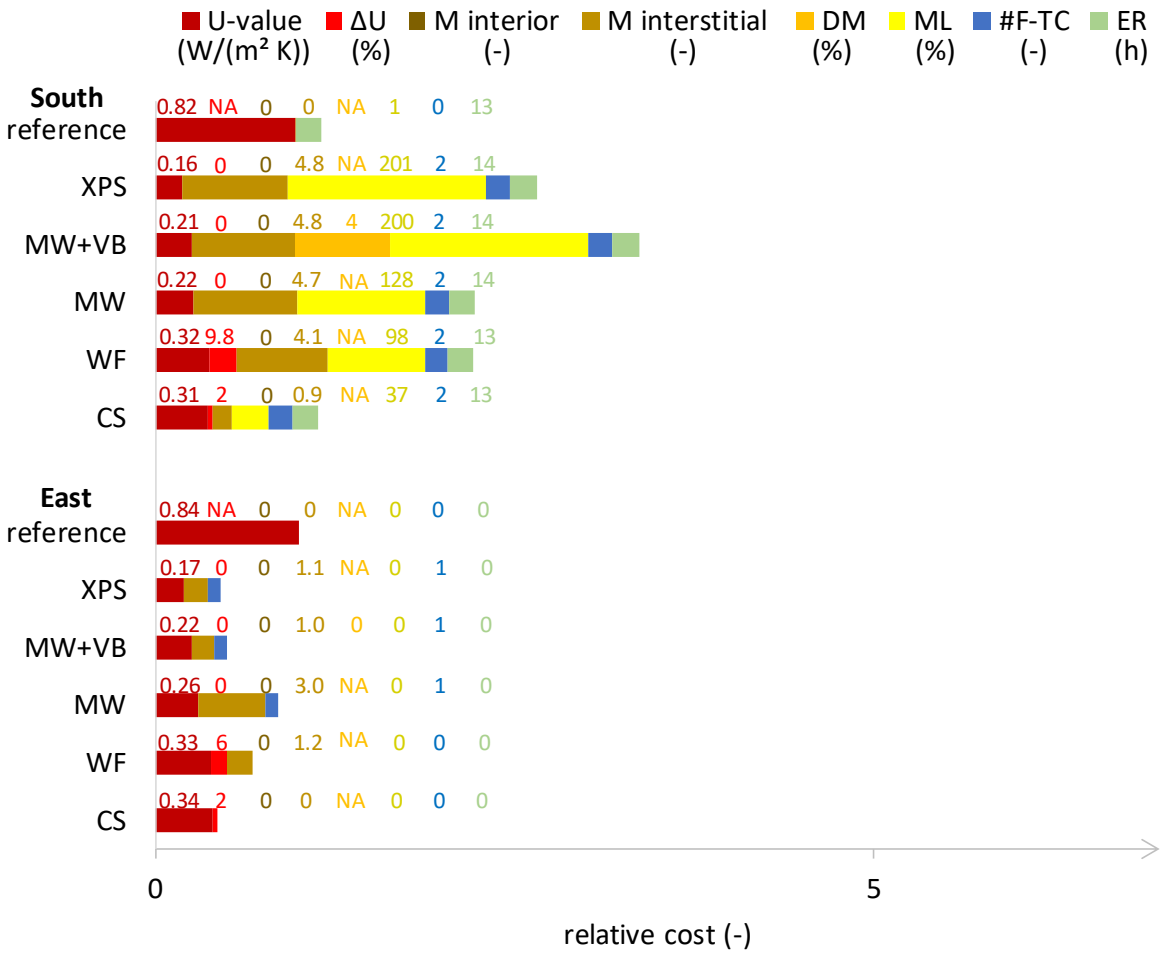

Fig. 10: Schéma de coût relatif total pour mur en pisé H1 orienté est (en plus du sud) avec différents systèmes d'isolation.

5.3.7 Influence de l'échec par fracture, de l'échec par flambement et de l'endommagement par gonflement de l'argile

L'influence de trois indicateurs de performances mécaniques supplémentaires sur l'évaluation du risque hygrothermique est évaluée. Il concerne la perte de section portante, la contrainte de flambement relative et le nombre de cycles de gonflement de l'argile. De plus, l'influence de deux variantes des propriétés mécaniques est déterminée (cf. Section 5.2.2.1). La Fig. 11 montre les résultats. On observe que le risque d'échec par fracture, le risque d'échec par flambement et le risque d'endommagement par gonflement de l'argile changent peu après l'isolation intérieure lorsque la variante 1 des propriétés mécaniques (résistance à la compression) est supposée. Lorsque la variante 2 des propriétés mécaniques est supposée, d'autre part, ces risques augmentent considérablement et l'effondrement structurel se développe par échec de fracture et/ou flambement pour tous les systèmes d'isolation à l'exception du système d'isolation au

silicate de calcium. Il est conclu que les propriétés mécaniques peuvent avoir une influence désastreuse sur le coût relatif et doivent donc être mesurées. Le système d'isolation au silicate de calcium reste le choix le plus sûr.

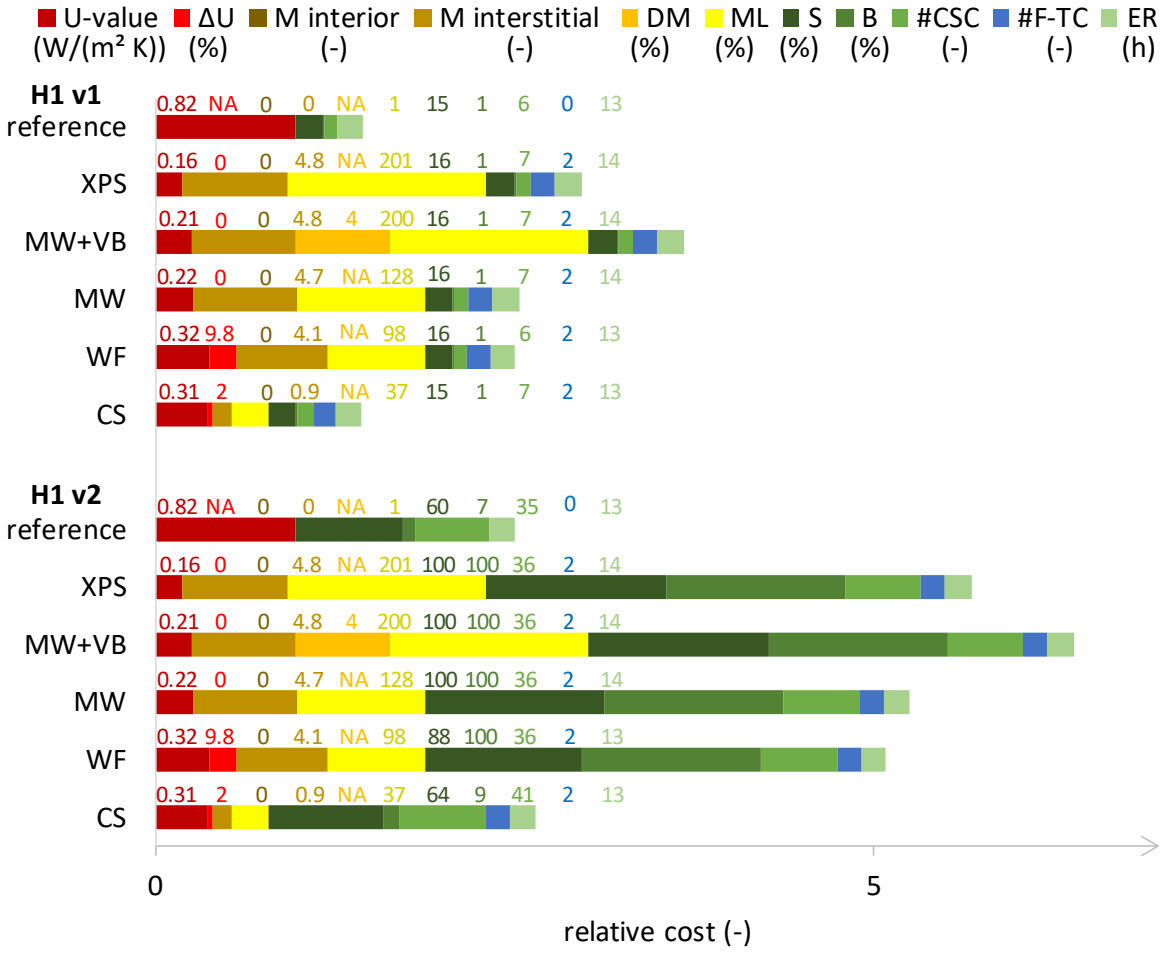

Fig. 11: Schéma de coût relatif total pour mur en pisé H1 avec la variante 2 (en plus de la variante 1) des propriétés méchaniques avec différents systèmes d'isolation.

5.4 Conclusion

L'impact de l'isolation intérieure sur les performances hygrothermiques des murs en pisé dépend entre autres du système d'isolation utilisé. Les systèmes d'isolation étanches à la vapeur et ouverts à la vapeur sont plus performants en qualité d'isolation thermique, mais les systèmes d'isolation actifs capillaires, notamment le silicate de calcium, sont les meilleurs pour minimiser les risques hygrothermiques. Avec tous les systèmes d'isolation étudiés, à l'exception du silicate de calcium, le risque de dégradation des poutres de plancher en bois augmente de manière inquiétante pour les murs soumis à une forte charge de pluie entraînée par le vent. En outre, le risque de

développement de moisissures interstitielles augmente considérablement. En général, le silicate de calcium est donc le seul système d'isolation recommandable. En l'absence de poutres en bois, XPS serait également applicable. Pour un mur en terre battue de 80 cm d'épaisseur et/ou avec une isolation de 2 cm d'épaisseur, la laine minérale et la fibre de bois pourraient également être applicables. Pour les orientations à faible charge de pluie poussée par le vent, tous les systèmes d'isolation étudiés sont éventuellement applicables, toujours avec une préférence pour le silicate de calcium car il présente les risques les plus faibles (sur tous les indicateurs sauf l'augmentation de U- valeur par l'humidité de l'isolant, qui reste cependant acceptable).

Lorsque les propriétés mécaniques du pisé sont prises en compte, elles peuvent avoir un impact désastreux sur les performances hygrothermiques des murs en pisé par échec par fracture et échec par flambement. C'est le cas si la charge de pluie poussée par le vent est élevée et la résistance à la compression diminue fortement dans le domaine hygroscopique avec tous les systèmes d'isolation à l'exception du silicate de calcium.

Il valait donc la peine de développer les indicateurs de performance mécanique dans la Section 4. Et à l'avenir, ils doivent être étudiés et validés plus avant et les propriétés mécaniques mesurées. Par ailleurs, davantage de matériaux en pisé doivent être caractérisés (hygriquement, thermiquement et mécaniquement).

6 Conclusion

6.1 Conclusions

La **technologie de pointe** a montré que deux objectifs préliminaires doivent être abordés pour arriver à l'évaluation de l'isolabilité : la caractérisation hygrique complète du matériau et l'ensemble d'indicateurs de performance complété mécaniquement permettant une évaluation compréhensive.

La **caractérisation** hygrique complète **des matériaux** est réalisée pour deux matériaux en pisé extraits de bâtiments traditionnels en pisé. Ainsi, la courbe de rétention d'humidité est déterminée au moyen de techniques de mesure traditionnelles qui évitent l'évolution de la matière due au mouillage dans la gamme haute (essais au dessiccateur et porosimétrie par intrusion de mercure). La courbe de perméabilité à l'eau liquide est déterminée à partir de la diffusivité de l'humidité "mesurée" (indirectement) lors du test d'absorption capillaire qui est

modifié pour les matériaux en pisé afin d'éliminer l'évolution des matériaux. La courbe de perméabilité à la vapeur est déterminée par des méthodes standard (essais à la coupelle).

Quatre **indicateurs de performance** mécanique sont développés. Ainsi, le risque de rupture par fracture est indiqué par la perte de la section portante. Le risque de rupture par flambage est indiqué par la contrainte de flambement relative. Le risque d'endommagement par gonflement de l'argile est indiqué par le nombre de cycles de gonflement de l'argile. Le risque d'érosion est indiqué par le nombre d'heures de conditions favorables à l'érosion.

L'**analyse** numérique **de l'isolation intérieure** des murs en pisé sans enduit au-dessus du soubassement est effectuée. En conséquence, on constate que l'isolation intérieure des murs en pisé peut provoquer une défaillance mécanique lorsque la résistance à la compression du matériau en pisé diminue fortement dans la plage hygroscopique avec l'augmentation de l'humidité relative, pour tous les systèmes d'isolation à l'exception du système d'isolation en silicate de calcium actif capillaire. La pourriture des poutres de plancher en bois encastrées s'est avérée être le deuxième risque principal à éviter, pour quel but un système d'isolation actif capillaire en silicate de calcium est le mieux adapté. Les autres systèmes d'isolation entraînent en outre le développement de moisissures interstitielles (XPS, … (tous)), l'humidité dégouttante (laine minérale avec pare-vapeur), une qualité d'isolation thermique sous-optimale (fibre de bois) et des dommages causés par le gel (XPS, … (tous)). De plus, il a été démontré que plusieurs paramètres influencent de manière significative les performances hygrothermiques, tels que la charge de pluie entraînée par le vent.

6.2 Recommandations d'améliorations et de recherches supplémentaires

Touchant la **technologie de pointe**, l'impact de l'évolution des matériaux dans la pratique pourrait être étudié. De plus, la charge de pluie poussée par le vent sur les murs des bâtiments en pisé pourrait devenir un sujet de recherche (concernant l'influence du toit).

Dans la **caractérisation du matériau**, la porosité ouverte doit de préférence être mesurée indépendamment. De plus, la courbe de rétention d'humidité doit être déterminée de manière plus fiable pour les matériaux au comportement anormal, comme le pisé H6. De plus, la perméabilité à l'humidité dans la gamme intermédiaire des matériaux en pisé doit être

déterminée. En outre, davantage de matériaux en pisé devraient être caractérisés et les propriétés hygriques, mécaniques et thermiques doivent être déterminées.

Concernant les **indicateurs de performance**, les remontées capillaires restent à étudier, ainsi que les contraintes et déformations hygrothermiques différentielles au niveau du bâtiment. Les indicateurs de performance mécanique (éventuellement élargis) incluant la contrainte hygrique devraient être validés dans des recherches futures.

En ce qui concerne l'**analyse de l'isolation intérieure**, l'isolabilité du soubassement doit encore être étudiée. Le pisé H2 pourrait être intégré jusqu'à la fin de l'étude en plus de H1 et H6. En outre, une charge climatique plus représentative pourrait être utilisée pour l'évaluation des risques, telle que dix années futures successives ou une année climatique hybride. Les poutres en bois pourraient être simulées pour une meilleure fiabilité de l'évaluation du risque de pourriture du bois. D'autres recherches futures sont nécessaires concernant la validation des indicateurs de performance mécanique et la mesure des propriétés mécaniques des matériaux en pisé. En outre, un outil automatisé d'évaluation probabiliste des risques pourrait être utilisé pour faciliter une analyse complète et pour faciliter l'étude d'un plus grand nombre de paramètres d'influence. Enfin, l'isolabilité des murs en pisé plâtrés à l'extérieur doit être étudiée.

Summary and survey

1 Introduction

1.1 Context and problem statement

Patrimonial rammed earth houses are widely present in France. These rammed earth building walls (in which clay particles form the natural binder) typically have 'boots', i.e. the stem wall, and a 'hat', i.e. the roof. These buildings need to be insulated to reduce the heat losses through the envelope and hence save energy. Interior insulation is appropriate for the thermal renovation of these rammed earth building envelopes to preserve the exterior façade looks. Interior insulation can however bring about problems consequent to the modified hygrothermal state of the wall, such as an increased risk on wood decay, mould growth, frost damage, and possibly structural collapse. These risks involved hence need to be analysed beforehand in order to guide the retrofit decisions.

1.2 Objectives and research question

In response to the burning questions in renovation practice, the present work aims at evaluating the interior insulatability of rammed earth walls via numerical simulation. The associated research question is: 'What is the impact of (different) interior insulation (systems) on the hygrothermal performance of rammed earth walls?'. Two subobjectives need to be tackled for this. First, 'How to perform a complete hygric material characterisation for rammed earth?', since the samples become unstable at high moisture contents and still these properties need to be determined as rammed earth walls in practice are also exposed to wind-driven rain. And second, 'How to provide a complete set of performance indicators for rammed earth?', since the current set, that consists of hygric and thermal performance indicators, does not incorporate mechanical performances.

1.3 Methodology and structure

In Section 2, the **state of the art** of the interior insulatability of rammed earth walls is reviewed. This concerns three main topics to be addressed: hygrothermal performance analysis, hygrothermal component simulation modelling, and hygrothermal material characterisation. In Section 3, the full-range hygric **material characterisation** of two different traditional rammed earth building materials is elaborated in the lab. This hygric characterisation comprises the

moisture retention curve and the moisture permeability curve, which are both needed as input in component simulations. The capillary absorption test is redeveloped for the latter. In Section 4, the new mechanical **performance indicators** relevant for the interior insulation of rammed earth walls are developed. The overall strength and stiffness, the differential hygrothermal stresses and strains, and the erosion of rammed earth walls are addressed for this. In Section 5, the **interior insulation analysis** of rammed earth walls is performed by means of hygrothermal numerical component simulation. First, the hygrothermal performance of the non-insulated reference rammed earth wall is evaluated. Next, the impact of different interior insulation systems on the hygrothermal performance is quantified. The influence of the insulation thickness, the rammed earth material, the rammed earth wall thickness, and the wall orientation are studied. Finally, the influence of the mechanical performance indicators of fracture failure, buckling failure and clay swelling damage is evaluated, including the impact of the mechanical properties on the risk assessment.

2 State of the art

2.1 Introduction

About the interior insulatability of rammed earth walls, there are especially a lot of questions in practice and there is a lack of adequate scientific research. The goal of this literature study is to identify specific gaps in the field of knowledge that need to be resolved to assess the interior insulatability of rammed earth walls. In this way, the refined goals and research questions of the present work are determined. First, information on hygrothermal performance analysis is introduced. This includes a review of the hygrothermal performance criteria at the envelope level. Next, the physical equations behind hygrothermal component simulation modelling are given. These comprise transfer equations and surface balances. And finally, hygrothermal material characterisation is reviewed for the hygric and the thermal properties that are needed simulation input.

2.2 Hygrothermal performance analysis

The four main performance criteria of comfort, durability, health, and sustainability according to which the physical quality of a building is assessed are determined by the hygrothermal response of the building (Hens, 2011); (Hens et al., 2006); (Janssen & Roels, 2009); (Tijskens et al., 2017). From these four performance criteria at the building level, several performances required at the

envelope level follow: i.a., thermal insulation quality, thermal transient response, interior mould growth, interstitial mould growth, dripping moisture, wood decay, hygric transient response, overall strength and stiffness, differential hygrothermal stresses and strains, frost damage, erosion, rising damp, air tightness, and thermal bridging. Per performance, a quantifiable indicator is defined. The hygrothermal analysis concerning the insulatability basically consists of a comparison of these indicator values before and after the retrofit for each insulation option. The insulation system resulting in the best balance between the benefits and the risks of the retrofit should be selected (Vereecken et al., 2015). Regarding the insulatability of rammed earth walls, the (HYGROBA, 2013a) project report is available, but the imposed exterior climate conditions (only temperature and relative humidity) (François et al., 2017) and the rammed earth material properties (moisture retention curve only measured in the hygroscopic range, approximation of the liquid permeability by the simulation software) are considered inadequate. Moreover, the outputs only comprise thermal (Hall & Allinson, 2008) and hygric (Allinson & Hall, 2010) performance criteria, while mechanical performances (Kianfar & Toufigh, 2016); (Fabbri et al., 2018) remain unaddressed. Furthermore, only exteriorly plastered wall assemblies are studied. The conclusions of this report are hence insufficient and the opinions on the interior insulatability of rammed earth walls remain divided (Heitz et al., 2015); (Galmiche, 2019); (Atelier Chevillotte, 2020); (Livradois-Forez, 2011); (Buzo et al., 2014).

2.2.1 Thermal insulation quality

The thermal transmittance or U-value of a building envelope wall is required to be about 0.3 W/(m² K) maximum in European countries with a temperate oceanic climate (Hens, 2011), mainly for energy efficiency. Rammed earth walls, that are typically 0.5 m thick with a thermal conductivity of 0.6 W/(m K), hence need to be insulated, with ca. 6 cm to 15 cm insulation thickness depending on the insulation material. Interior insulation is used for this because it is cheap and easy to apply and the exterior looks are preserved. The addition of an interior thermal insulation layer however modifies the hygrothermal performance of the wall which becomes colder and wetter. Phenomena like moisture accumulation by interstitial condensation, reduced drying ability, and increased damage (Livradois-Forez, 2011); (Scarato, 2014); (Avons-Bariot, 2017) can start to play and need to be analysed before the retrofit to find insulation solutions that keep the chances of moisture problems to a minimum (Vereecken et al., 2015); (Zhou et al., 2018). Three classes of interior insulation systems are distinguished. Vapour tight insulation systems avoid interstitial condensation but exclude inward drying of absorbed wind-driven rain (Janssen et al., 2007); (Abuku et al., 2009a). Vapour open insulation systems facilitate inward drying by

vapour diffusion but give free rein to interstitial condensation. Capillary active insulation systems buffer interstitial condensation (Vereecken, 2013) and facilitate inward drying by liquid transport. The thermal insulation quality decreases however as the insulation moistens (Vereecken & Roels, 2015) and a requirement exists that the increase in U-value by moisture should not exceed 10% (Hens, 2011).

2.2.2 Thermal transient response

By the addition of an interior thermal insulation layer to a massive wall, the admittance (Hens, 2011); (Hens, 2010); (Hall & Allinson, 2008) strongly decreases, which is mainly because the thermal mass is eliminated. The thermal comfort (Hens, 2011); (Olesen & Parsons, 2002); (Olesen, 2005) during summer can hence be compromised by overheating. The change in the thermal transient response is not exactly assessable by means of component simulations that use an imposed interior temperature (EN 15026).

2.2.3 Biological deterioration or dripping moisture

2.2.3.1 Interior mould growth

The empirical updated VTT model (Vereecken & Roels, 2012) is commonly used for the evaluation of the mould growth risk in terms of a mould index (M, -), at the interior surface. The critical relative humidity for mould growth is 80% herein.

2.2.3.1 Interstitial mould growth or dripping moisture

Moulds can also grow interstitially where air can come. Besides, moisture dripping from interfaces owing to condensation where two non-capillary materials are involved should be avoided.

2.2.3.1 Structural wood decay

Rammed earth constructions typically have (i.a.) wooden floor beams embedded, for ca. 2/3 of their height (Livradois-Forez, 2011); (TERA, 2018). The empirical VTT wood decay model (Viitanen et al., 2010) is commonly used to evaluate the risk on wood decay development by giant moulds (fungi). The mass loss (ML, %) of the wooden floor beam ends is calculated by the model based on the temperature and the ambient relative humidity. This calculation comprises an activation process and a mass loss process and the critical relative humidity for wood decay is 95%.

2.2.4 Hygric transient response

The risk on interior humidity discomfort (Hens, 2011); (Wolkoff, 2018) can be quantified as the number of hours that the interior relative humidity exceeds 70% (Vereecken et al., 2015) or falls below 30%. In component simulation, however, the interior humidity is commonly imposed in accordance with the standard (EN 15026) and thus independent of the moisture buffering (Wan et al., 2017); (Rode et al., 2005) by the interior elements (Janssen & Roels, 2009); (Abuku et al., 2009a); (Tijskens et al., 2017).

2.2.5 Mechanical response

In case of rammed earth, potential hygrothermal consequences of interior insulation also include mechanical risks concerning the overall strength and stiffness and differential hygrothermal stresses and strains (Fabbri et al., 2019); (Galmiche, 2019); (Scarato, 2014). These have yet never been translated into performance indicators.

2.2.6 Frost damage

The number of frost-thaw cycles can be assessed in various ways (Vereecken et al., 2015); (Feng et al., 2019); (Koči et al., 2017); (Zhou et al., 2017).

2.2.7 Erosion

A destructive natural action most specific to rammed earth walls is wind-driven rain erosion. This has also never been translated into a performance indicator yet.

2.2.8 Rising damp

Rising damp is usually never explored in the analysis of interior insulation because it is presumed to be necessarily excluded a priori (TERA, 2018); (Heitz, 2014); (Livradois-Forez, 2011); (Hens, 2011); (Scarato, 2014).

2.3 Hygrothermal component simulation modelling

2.3.1 Transfer equations

The numerical simulation tool that is used to simulate the hygrothermal behaviour of building components is physically based on two transfer equations: the moisture mass balance, Eq. (1), and the heat balance, Eq. (2) (Carmeliet, 2006); (Hagentoft et al., 2004); (Nicolai & Grunewald, 2006). It is herein assumed that the porous building material remains stable. For the storage term of the moisture mass balance, it is assumed that the gaseous phase does not contribute markedly to the moisture storage, that the water cannot transform into ice, and that no hysteresis occurs. The capillary pressure is defined by the Young-Laplace equation for a circular pore and is assumed to be independent of the temperature (via the surface tension). For the transport terms of the moisture mass balance, Darcy's law is used for the advective liquid water transport (it is i.a. assumed that the material is isotropic) and Fick's law is used for the diffusive water vapour transport (it is i.a. assumed that no moisture transport due to thermal gradients occurs). The vapour pressure is linked to the Kelvin equation for a circular pore. For the heat balance, it is assumed that there is a local thermal equilibrium between the phases and Fourier's law is used for the heat conduction. (The symbols are defined in the Nomenclature.)

$$\frac{\partial w_l}{\partial p_c}\frac{\partial p_c}{\partial t} = -\boldsymbol{\nabla}\cdot(-k_l\boldsymbol{\nabla}p_c - \delta\boldsymbol{\nabla}p_v) \tag{1}$$

$$\frac{\partial}{\partial t}(\rho_d c_d T + w_l c_l T + w_v(c_v T + L_v) + w_a c_a T) = -\boldsymbol{\nabla}\cdot\left(-\lambda\boldsymbol{\nabla}T + \boldsymbol{g}_l c_l T + \boldsymbol{g}_v(c_v T + L_v)\right) \tag{2}$$

2.3.2 Surface balances

Atmospheric boundary conditions in the form of moisture and heat fluxes are imposed at the exterior Eqs. (3),(4) and interior Eqs. (5),(6) surface of a building component (Janssen et al., 2007a); (Nicolai & Grunewald, 2006). (**n** is a unit vector perpendicular to the component's surface.) These form the driving forces for the transfer in the building component.

$$\boldsymbol{g}_{m,se} = \left(-\alpha U_{10} {R_h}^{0.88}\cos(\theta-\varphi)\,(1/3600 s/h) + \beta_e\left(p_{v,se} - p_{v,e}\right)\right)\cdot\boldsymbol{n} \tag{3}$$

$$\boldsymbol{q}_{se} = \left(h_e\left(T_{se} - T_{e,equ}\right) - c_l T_{e,g} g_{l,e} + \left(c_v T_{se/e,g} + L_v\right) g_{v,e}\right)\cdot\boldsymbol{n} \tag{4}$$

$$\boldsymbol{g}_{m,si} = \left(\beta_i\left(p_{v,i} - p_{v,si}\right)\right)\cdot\boldsymbol{n} \tag{5}$$

$$\boldsymbol{q}_{si} = \left(h_i\left(T_{i,g} - T_{si}\right) + \left(c_v T_{i,g/si} + L_v\right) g_{v,i}\right)\cdot\boldsymbol{n} \tag{6}$$

2.4 Hygrothermal material characterisation

The material properties that are needed as an input in the hygrothermal component simulations come forth from the transfer equations: (the derivative of) the moisture retention curve ($w(p_c)$, kg/m³), the vapour permeability curve (δ, s), the liquid permeability curve (k_l, s), the heat capacity (ρc, J/(m³ K)), and the thermal conductivity (λ, W/(m K)).

2.4.1 Hygric properties

2.4.1.1 Moisture storage

The moisture retention curve of stable building materials is typically obtained from a series of experimental tests such as sorption isotherm measurements and pressure plate measurements and/or mercury intrusion analysis (EN 15026); (Feng & Janssen, 2019); (Carmeliet & Roels, 2002); (Carmeliet & Roels, 2001); (Feng & Janssen, 2020); (Feng & Janssen, 2021).

For rammed earth materials, a review of the available moisture retention curves shows that three measurement tactics can be distinguished. The first tactic uses a combination of mercury intrusion porosimetry in the overhygroscopic range and desiccator testing in the hygroscopic range (Arrigoni et al., 2017); (Hall et al., 2013). The second tactic measures the moisture retention curve in desorption starting from the manufacturing moisture content of ca. 0.08 kg/kg to 0.125 kg/kg, using filter papers (Bui et al., 2014); (Gerard et al., 2015); (Jaquin et al., 2009). The third tactic works with samples manufactured at different moisture contents (Abhilash, 2016a); (Soudani, 2017); (Nowamooz & Chazallon, 2011). It is observed that the rammed earth materials are typically hygroscopic.

2.4.1.2 Moisture transport

The vapour permeability curve is usually determined based on the dry cup vapour permeability, the moisture retention curve, and the vacuum saturation moisture content, using a bundle-of-tubes approach (Scheffler & Plagge, 2010).

The liquid permeability curve is commonly determined based on the moisture diffusivity and the moisture retention curve (Carmeliet et al., 2004). The moisture diffusivity in the high range is determined using the capillary absorption test, e.g. with X-ray projection (Ren et al., 2019).

For rammed earth materials, the dry cup vapour resistance factor typically ranges from 9 to 11 (Chabriac, 2014). The capillary absorption coefficient typically ranges from about 0.2 kg/(m² $s^{0.5}$) to 0.4 kg/(m² $s^{0.5}$) and the capillary absorption pattern is ideal (Hall & Djerbib, 2004); (Hall & Allinson, 2009b); (Fabbri et al., 2019). The moisture diffusivity (and hence liquid permeability) has however not been measured yet.

2.4.2 Thermal properties

The specific heat capacity of rammed earth materials typically ranges from 650 J/(kg K) to 1100 J/(kg K) (Chabriac, 2014). The (dry) thermal conductivity ranges from ca. 0.25 W/(m K) to 1.0 W/(m K) (Chabriac, 2014). And the moisture content factor for the thermal conductivity ranges from 0.002 W m²/(kg K) to 0.0056 W m²/(kg K) (Hall & Allinson, 2009a); (Chabriac, 2014).

2.5 Conclusion

Three gaps are identified through the review of the state of the art that will be addressed in the present work. First, in response to the pressing situation of the questions in practice and the lack of research, the interior insulatability of (exteriorly unplastered) rammed earth walls (above the stem wall) that are exposed to driving rain will be evaluated via numerical simulation. Second, for this, mechanical performance indicators will additionally be developed for rammed earth. And third, furthermore, the hygric transport properties in the capillary range will be determined for rammed earth materials, through adapted test methods.

3 Material characterisation

3.1 Introduction

The hygric properties of rammed earth materials are needed to investigate the insulatability of rammed earth walls via simulation. The objective is to perform a complete hygric characterisation of a few rammed earth target materials. The main asset is to redevelop the capillary absorption test, including the Boltzmann transformation method, to enable its proper application to rammed earth materials. Resultantly, the hitherto missing liquid permeability curve of rammed earth materials is determined.

3.2 Material information

3.2.1 Collection

The candidate rammed earth materials for the characterisation are extracted (by means of core drilling) from existing constructions at six different locations in the Auvergne-Rhône-Alpes region, France.

3.2.2 Bulk density

While the reliable determination of the dry mass is the basis for characterising the hygrothermomechanical properties of porous building materials, the bulk density is subsequently useful to convert the intensive properties to volumetric quantities. The bulk density of rammed earth cannot be determined by means of the standard vacuum saturated underwater weighing, and hence it is instead determined by means of immersion in a non-wetting liquid (mercury), as a part of the mercury intrusion porosimetry test procedure. Relative to the caliper volume determination method (that overestimates the volume), the mercury gives more reliable results for the in general relatively rough rammed earth samples. Hence, the mercury intrusion porosimetry bulk density is retained. Resultantly, the bulk density of the rammed earth materials collected ranges from 1540 kg/m³ to 1860 kg/m³ with an average of 1738 kg/m³. Further, the bulk density obtained from two drying methods is compared since the 70 °C oven drying used in this work deviates from the 105 °C used in most of the past rammed earth research. The corresponding dry mass difference is limited.

3.2.3 Pore structure

The pore structure of a building material impacts its hygric properties. The objective is to select the few target materials to be characterised based on their differences in pore structure. For this, the pore volume distribution of the different collected materials is determined by means of mercury intrusion porosimetry.

The mercury intrusion porosimetry is performed on two to nine samples per material, of about 1x1x2 cm³. The porosimetry involves the forced intrusion of mercury into a dry and vacuum porous sample. The stepwise increased intrusion pressure yields an increased intruded mercury volume. The resulting mercury retention curve is recalculated into the main drainage moisture retention curve using the Young-Laplace equation and based on knowledge of the vacuum saturation

moisture content. This vacuum saturation moisture content is in the present work estimated by the sum of the intruded mercury volume at the pressure corresponding to 75% relative humidity and the pore volume filled by moisture during isothermal absorption up to 75% relative humidity (Section 3.3.1), since the finer pores are not covered by the mercury intrusion porosimetry apparatus pressure range. In doing so, it is assumed that hysteresis is negligible at this point of 75% relative humidity. To determine the pore volume distribution, the derivative of the moisture retention curve, the moisture retention curve is fitted with Van Genuchten forms.

Based on the results per sample, it is found that the materials collected can be considered fairly homogeneous, except for the H4 rammed earth. Fig. 1 shows the average obtained moisture retention curve for the different materials. The estimated open porosity of the collected materials ranges from 0.293 m^3/m^3 to 0.406 m^3/m^3, with an average of 0.338 m^3/m^3. Based on the observed differences in pore structure (and discarding the heterogenous H4 rammed earth), the H1, H6, and H2 rammed earths are chosen to be characterised further.

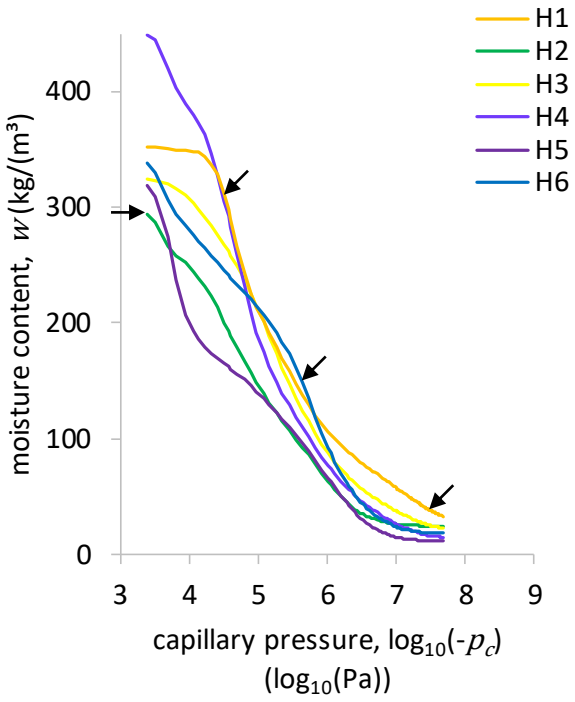

Fig. 1: Average moisture retention curve by mercury intrusion porosimetry per material. Arrows indicate selection criteria for target materials.

3.2.4 Water stability

In preparation of the global test plan, an unconfined small water stability test is performed, i.e. a water uptake test in which a wick is used to counter the liquefaction and in which the swelling of the rammed earth sample is measured. Given that this swelling is significant, it is decided to additionally utilise a confining sealing that keeps the sample mechanically stable in the sequel.

3.3 Moisture storage

3.3.1 Sorption isotherm

The main wetting moisture retention curve in the hygroscopic range is formed by the absorption isotherm. Desiccator testing is used to measure this absorption isotherm, for three samples per target rammed earth and for 11%, 33%, 53%, 75%, 85%, 94%, and 97% relative humidity. The resulting sorption isotherms are first concave and then convex to the relative humidity axis, which is the normal form. Two distinct hygroscopic behaviours are further observed: the H1 rammed earth is strongly hygroscopic in the low range up to 75% relative humidity whereas the H2 and H6 rammed earths are strongly hygroscopic in the high range above 75% relative humidity. For these latter, the deviations between the samples increase significantly above 75% relative humidity.

3.3.2 Moisture retention curve

For the main wetting moisture retention curve in the overhygroscopic range, the mercury intrusion porosimetry results (Section 3.2.3) are compared with main wetting data. Psychrometry in the low overhygroscopic range is used for these main wetting data besides desiccator testing (Section 3.3.1). Moreover, the capillary absorption test (Section 3.4.2) is used to determine the capillary moisture content, which is used to curtail the moisture retention curve in the high overhygroscopic range.

For the H1 rammed earth, a close agreement is found between the mercury intrusion porosimetry and the main wetting data. The mercury intrusion porosimetry curve is hence used to form the main wetting moisture retention curve. For the H2 and H6 rammed earths on the other hand, the mercury intrusion porosimetry and the main wetting data diverge for most of the samples as the moisture content increases, where the mercury intrusion porosimetry is below the main wetting data. This could be explained in several ways: material evolution, (micro)cracks from sample sawing, mercury intrusion porosimetry deformation effects, … An average curve is hence made in the (large) high hygroscopic range and the mercury intrusion porosimetry curve is retained in the overhygroscopic range. The resulting complete moisture retention curves are fitted by Van

Genuchten forms (to provide continuous derivatives). Fig. 2 shows the results. The result of the H1 rammed earth is compared with literature sources.

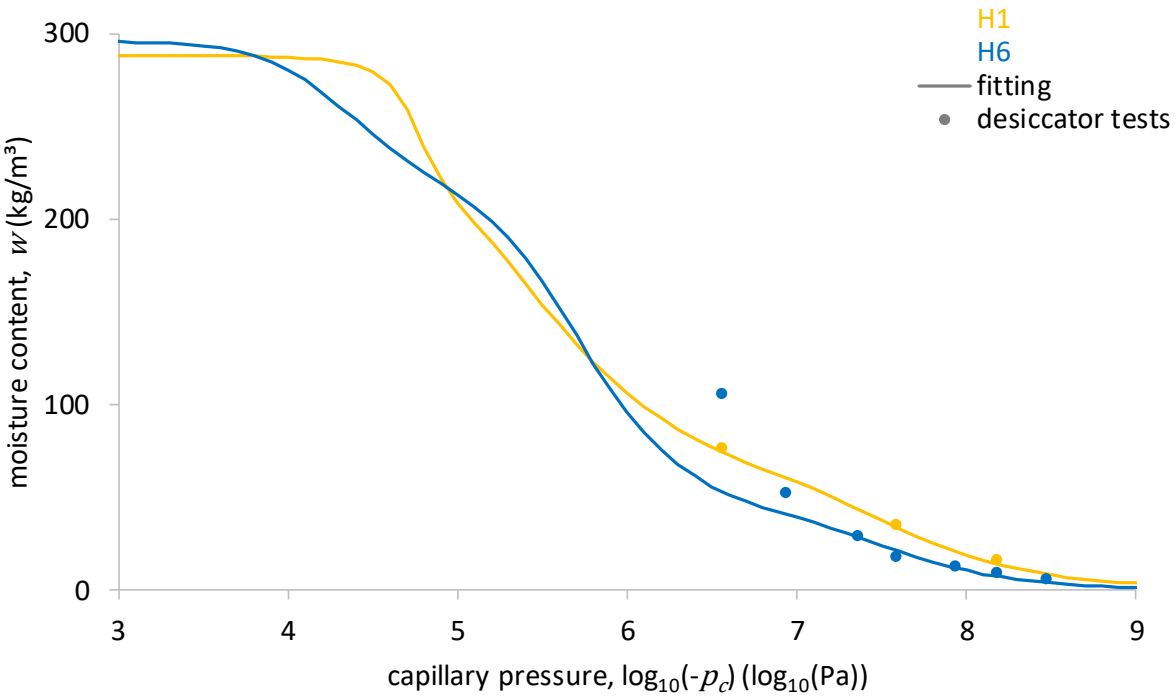

Fig. 2: Moisture retention curve retained for the H1 and H6 rammed earths. The H2 rammed earth is discarded due to heterogeneity (Section 3.4).

3.4 Moisture transport

3.4.1 Vapour permeability

The vapour resistance factor from which the vapour permeability curve is calculated, as well as the moisture permeability in the hygroscopic range, are measured by means of cup tests. A dry cup test (11% - 53% relative humidity (RH)), an intermediate cup test (53% - 84% RH), and a wet cup test (94% - 84% RH) are performed. The resulting dry cup vapour resistance factor amounts to 7.7 for the H1 rammed earth, 8.2 for the H6 rammed earth, and 10.9 for the H2 rammed earth. This reflects the open porosity trend. The increase in the (equivalent) vapour permeability in the wet cup test is the greatest for the H1 rammed earth, which reflects the hygroscopicity trend.

3.4.2 Capillary absorption

The capillary absorption test forms the basis for determining the moisture permeability in the overhygroscopic range. It moreover delivers the capillary moisture content (besides the capillary absorption coefficient). Per target rammed earth, two samples are tested in the lab and two under the X-ray. The H2 rammed earth is considered too heterogenous to be characterised further. Since the rammed earth materials liquefy and expand upon contact with water, the standard test method is modified, as following. A thin permeable brick wick and contact paper are applied as lower sample parts, to counter the liquefaction, and a confining sealing is utilised, against the expansion. In the data processing, Fig. 3, consequently the estimated moisture mass of the lower parts is subtracted to enable determining the capillary moisture content. As the wick and paper are initially dry, absorption in a composite applies. The capillary absorption coefficient is hence obtained from the latest retrieved persistent linear first stage pattern, supported by the coefficient of determination. The intercept of this first stage fitting of the moisture mass in the top part alone against the square root of time, Eq. (7), corresponds to the equivalent height of the lower parts.

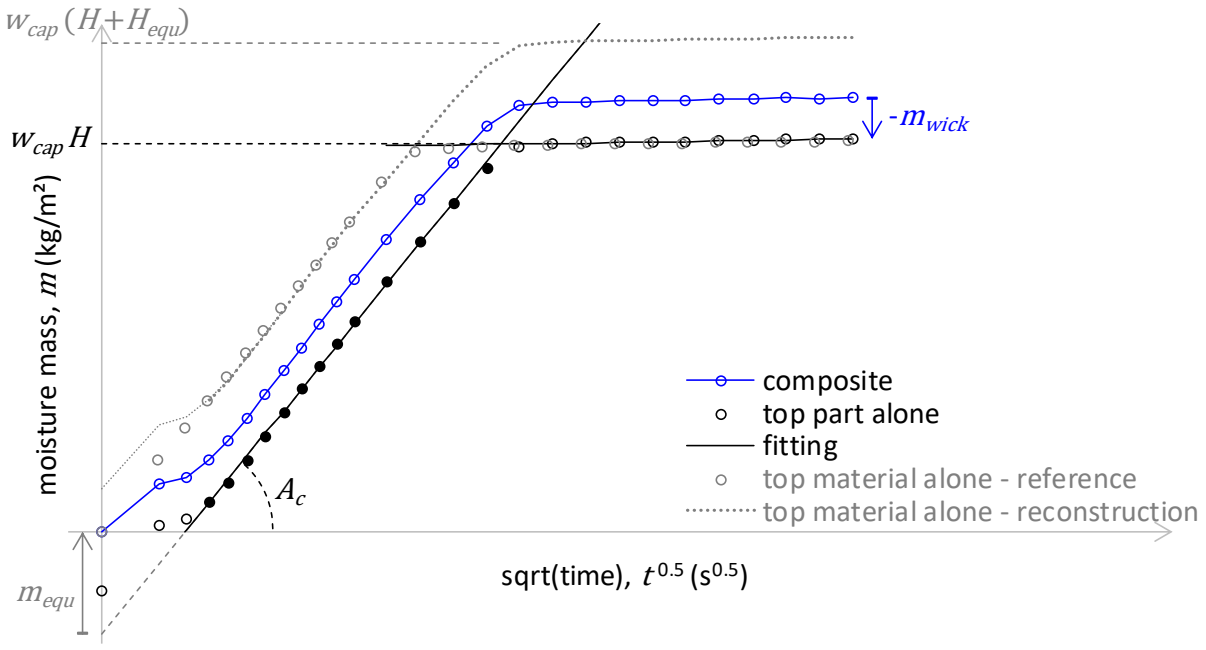

Fig. 3: Data processing method illustration using ceramic brick capillary absorption test results.

$$m_{tpa} = A_c\sqrt{t} - m_{equ} = A_c\sqrt{t} - w_{cap}H_{equ} \tag{7}$$

The resulting capillary moisture content amounts to 288 kg/m³ for the H1 rammed earth and 296 kg/m³ for the H6 rammed earth and the capillary absorption coefficient amounts to 0.262 kg/(m²

$s^{0.5}$) for the H1 rammed earth and 0.188 kg/(m² $s^{0.5}$) for the H6 rammed earth. The equivalent heights are usually similar to or smaller than the wick height of 1 cm.

3.4.3 Moisture diffusivity

The moisture content profiles during the capillary absorption test are measured by means of X-ray radiography. The Boltzmann transformation is applied to these moisture content profiles to obtain the characteristic profile which is used to determine the moisture diffusivity. Since the Boltzmann transformation method standardly requires that the sample is suitably homogeneous and exhibits the ideal square root of time moisture absorption behaviour right from the start, it is necessarily redeveloped for the composite case at hand. The equivalent height of the lower parts is used for this, Eq. (8). Fig. 4 shows the result for a sample of the H1 rammed earth. The moisture diffusivity is obtained by integrating and differentiating this characteristic Boltzmann transformed profile.

$$\lambda^* = \frac{x_{tpa} + H_{equ}}{\sqrt{t}} \tag{8}$$

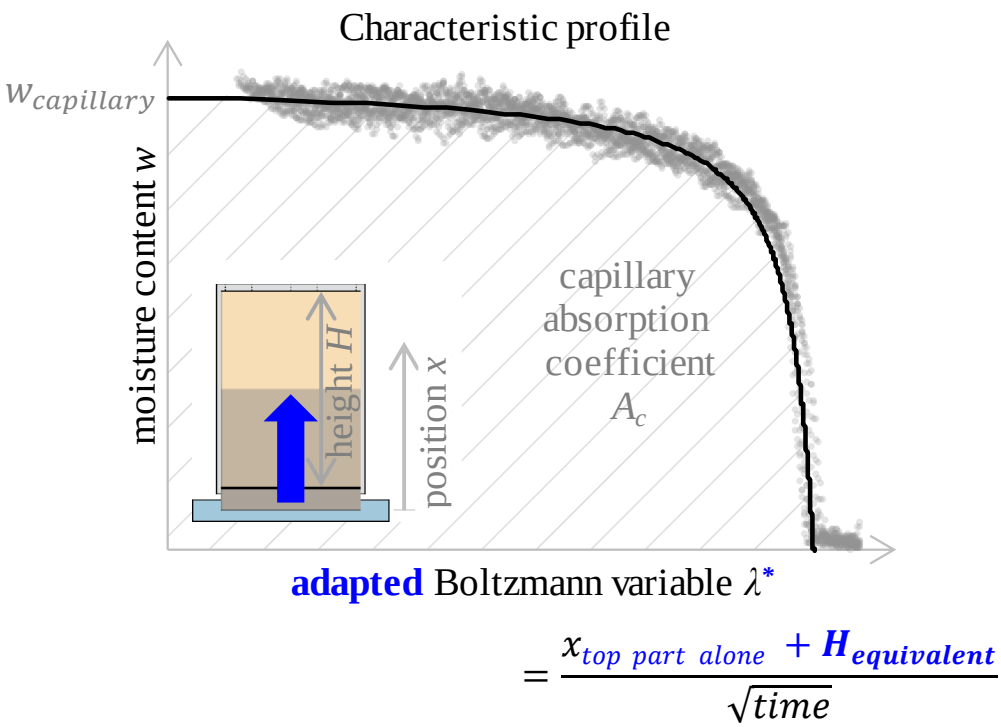

Fig. 4: Characteristic profile fitting and underlying Boltzmann transformed moisture content profiles for H1 rammed earth sample.

3.4.4 Moisture permeability

The moisture permeability in the overhygroscopic range, i.e. the liquid permeability, is obtained by the product of the moisture diffusivity and the moisture capacity, the derivative of the moisture retention curve. It is verified that this permeability reproduces the capillary absorption behaviour via numerical simulation. Fig. 5 shows the results. The target characterisation is hereby complete.

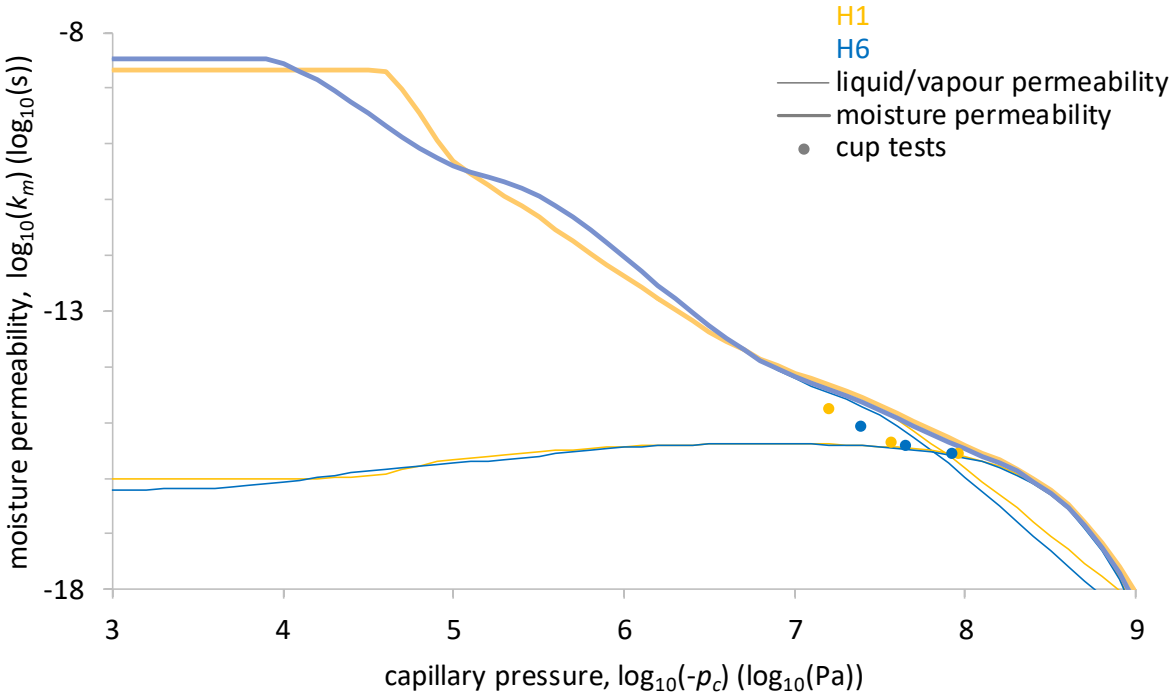

Fig. 5: Moisture permeability of rammed earth target materials H1 and H6.

3.5 Conclusion

The complete hygric characterisation is performed for two different rammed earth materials. Their moisture retention curve is determined by means of a combination of desiccator testing, mercury intrusion porosimetry, and (redeveloped) capillary absorption testing. Their vapour permeability curve is determined using the standard cup test. And their liquid permeability curve is determined through the redeveloped (confined composite) capillary absorption test with X-ray radiography.

4 Performance indicators

4.1 Introduction

To enable evaluating the interior insulatability of rammed earth walls with respect to structural damage risks, mechanical performance indicators are developed.

4.2 Indicator development

4.2.1 Overall strength and stiffness

With increasing moisture content, materials swell, and their strength and stiffness decrease. This is especially pronounced for clay-bound materials, such as rammed earth. To evaluate the overall mechanical performance of rammed earth walls, the relative fracture stress and the relative buckling stress need to be monitored. The normal stresses by compression at the bottom of a rammed earth wall amount to ca. 0.171 MPa, which is estimated on the basis of an exemplary building geometry with prescribed additional mechanical loads. Besides this structural mechanical load, normal stresses of hygric origin add when the associated movement is hindered. In the present work, it is assumed that all expansion relative to the transient stability equilibrium state at the average relative humidity or capillary pressure of the wall is fully suppressed in the height and width direction. The compressive strength, the stiffness modulus, the hygric strain, and the Poisson's ratio curve of the H1 rammed earth are mainly obtained based on literature sources. While the compressive strength can be used directly for fracture, the other three properties are used in combination with the area moment of inertia, the wall fixings and height, and the wall loading form, to determine the buckling strength. The risk on structural failure by compression fracture is indicated by the load-bearing section loss, S (%). Herein, the remaining load-bearing wall section thickness is where the relative fracture stress remains smaller than unity, Eq. (9). The risk on buckling failure is indicated by the relative buckling stress, B (%), Eq. (10).

$$1 > \frac{\sigma_c + \sigma_{hygric,i}}{\sigma_{max,i}} \tag{9}$$

$$B = \frac{\sigma'}{\sigma_{cri}'} \times 100 = \frac{\sigma_c' + \sigma_{hygric,avg}'}{\left(1 + 4.32 \times \frac{N_{hygric,avg}'}{N_c + N_{hygric,avg}'}\right)\left(1 - \nu_{avg}'^2\right)\left(L/\sqrt{2}\right)^2 bh' \times 12} \times 100 \tag{10}$$

4.2.2 Differential hygrothermal stresses and strains and clay swelling damage

The exemplary hygrothermal stresses and strains damage pattern mechanism that is studied in the present work is the hygric clay swelling damage by repeated shear that can be followed by buckling of a surface layer of the rammed earth wall. Such damage should be avoided because the created discontinuity disables moisture redistribution whereby the moisture content in the surface layer increases and consequently also other hygrothermal risks may be invigorated. If moreover buckling occurs of the exterior surface layer, with detachment of the buckled material, the appearance is additionally disturbed and the function even more as well, by the possible water penetration in combination with the reduced drying ability and the reduced wall thickness. The shear cracks can be caused by excessive wetting moisture gradients or by fracture failure. The hygric stress is calculated by means of Hooke's law under equibiaxial plane stress conditions. The shear stress equals the difference in normal stress between each incremental position. The shear strength is approximated as 0.1 times the compressive strength. The risk on clay swelling damage is indicated by the number of clay swelling cycles, i.e. the number of times that the absolute value of the shear stress equals or exceeds the shear strength, Eq. (11), and the shear stress is positive for the exterior surface or negative for the interior surface or fracture failure occurs.

$$1 \leq \frac{|\tau_{imm}|}{\tau_{max,imm}} = \frac{|\sigma_i - \sigma_{i+1}|}{0.1 \times \frac{\sigma_{max,i} + \sigma_{max,i+1}}{2}} \tag{11}$$

4.2.3 Erosion

A quantification of the erosion stresses that result from the raindrop impact pressure and the consequent radial flow and of the erosion resistance of rammed earth materials falls out of the scope of the present work. The risk on erosion damage is indicated in a simplified way by the number of hours that the moisture content of the exterior wall surface exceeds 80% of the capillary moisture content while the wind-driven rain load is positive, Eq. (12).

$$w_{se} > 0.8\, w_{cap}\ and\ R_{wdr} > 0 \tag{12}$$

4.3 Conclusion

Four mechanical performance indicators are developed for the interior insulation of rammed earth walls: fracture failure, buckling failure, clay swelling damage, and erosion. Quantifying these requires additional information such as the mechanical material properties.

5 Interior insulation analysis

5.1 Introduction

To contribute to resolving the uncertainties about the interior insulatability of rammed earth walls, the impact of interior insulation on the hygrothermal performance of (non-plastered) rammed earth walls is analysed (above the stem wall and when rising damp is excluded), by means of numerical simulation. The mechanical properties will be neglected at first. Next, it will be examined what impact these can have.

5.2 Model setup

5.2.1 Software

The hygrothermal component simulation software Delphin is used. One-dimensional heat and moisture transfer are considered (Section 2.3). The grid element size is taken to be 1 mm.

5.2.2 Input parameters

5.2.2.1 Materials

Table 1 shows the composition of the different wall assemblies studied. The reference is a 50 cm thick homogeneous rammed earth wall. The two rammed earth materials considered (H1/H6) have different hygric properties: the H1 rammed earth is more hygroscopic and more capillary active than the H6 rammed earth. Investigated is the influence of five different 10 cm thick conventional interior insulation systems applied to this wall: a vapour tight extruded polystyrene (XPS), a vapour tight mineral wool plus vapour barrier, a vapour open mineral wool, a capillary active wood fibre, and a capillary active calcium silicate insulation system.

Table 1: Overview of wall assemblies with different interior insulation systems.

reference	outside	rammed earth wall H1/H6	gypsum plaster			inside
VT			GM	XPS	gypsum plaster	
VT			Mineral wool + VB		gypsum board	
VO			Mineral wool		gypsum board	
(VN-)C			GM	Wood fibre	gypsum plaster	
(VO-)C			GM	Calcium silicate	gypsum plaster	

For the post-processing concerning the mechanical performance, the building geometry is assumed to be 6.5 metres high and 6.5 metres wide in both directions. The mechanical properties are taken from the literature and two variants of the compressive strength curve (and of the free swelling strain curve) are considered. The first variant corresponds to the H1 rammed earth, which retains its strength over the hygroscopic range, and the second variant corresponds to the H2 rammed earth, which loses its strength relatively sharply in the hygroscopic range.

5.2.2.2 Climate conditions

The climate of Lyon in 2014 for a South-oriented wall is chosen based on the wind-driven rain load that is most severe. The raw exterior climate data are the gas temperature, relative humidity, wind speed and direction, horizontal rainfall intensity, cloudiness, and short-wave direct and diffuse horizontal radiation. Based hereon, the exterior equivalent temperature, convective surface heat and moisture transfer coefficients, and wind-driven rain load are calculated. For the latter, the wind-driven rain coefficient amounts to 0.084 s/m based on building assumptions. The resulting total yearly wind-driven rain amount is 154 mm. The interior temperature and relative humidity climate conditions are determined based on the daily mean exterior temperature in accordance with the standard. The interior relative humidity level for high building occupancy is selected.

5.2.3 Outputs

The stationary **U-value** in practice, U_{stat} (W/(m² K)), that can be compared with the requirement, is defined as the average absolute value of the heat flux from the interior to the interior surface in time divided by the average absolute value of the temperature difference from environment to environment in time. The **hygro-thermal insulation quality** is the increase in U-value by moisture in the insulation, ΔU (%). The **interior mould growth** risk is indicated by the maximum value of the mould index (M, -) over a ten-year simulation period considered. The **interstitial mould growth** risk is evaluated at both sides of the insulation layers. The materials are assumed to belong to the mould sensitive class in the updated VTT model used. The **dripping moisture** risk is evaluated as the number of hours that the relative humidity exceeds 97 % at the interface between the mineral wool and the vapour barrier over the year. The **wood decay** risk is indicated by the total wood mass loss (ML, %) after ten years, and is evaluated at the beam end depth and at the interface. The **fracture failure** risk is indicated by the maximum load-bearing section loss (S, %) over the year. The **buckling failure** risk is indicated by the maximum relative buckling stress (B, %) over the year. The **clay swelling damage** risk is indicated by the maximum number of clay swelling cycles at the same depth in the wall over the year. The **frost damage** risk is indicated by the maximum

number of frost-thaw cycles (using Gibbs-Thomson relation). And the **erosion** risk is indicated by the number of hours that the exterior wall surface moisture content exceeds 80 % of the capillary moisture content while the wind-driven rain load is greater than zero.

5.3 Results and discussion

5.3.1 Reference wall

The hygrothermal performance of the non-insulated reference H1 rammed earth wall is evaluated. Preliminarily, it is observed that overhygroscopic states are addressed 24 % of the time. The stationary U-value in practice amounts to 0.82 W/(m² K) and the total transmission heat loss amounts to 72 kW h/m². The interior and interstitial mould growth risks are zero. 1.1 % wood mass loss after ten years at the beam end (in the middle of the wall) is found. The frost damage risk is zero. And 13 hours erosion risk are found. To conclude, only the thermal insulation quality is problematic for this reference case.

5.3.2 Influence of insulation systems

The impact of five different 10 cm thick interior insulation systems on the hygrothermal performance of the wall is evaluated. Preliminarily, it is observed that by applying interior insulation, the moisture levels in the wall increase, reflecting the hygric properties of the insulation systems. E.g., the vapour tight insulation systems hinder the inward drying the most, leading to the greatest moisture accumulation in the rammed earth wall of the absorbed wind-driven rain. In contrast, the capillary active calcium silicate insulation system enables an optimal inward drying while buffering interstitial condensation, resulting in moisture levels closest to the original wall.

With 10 cm insulation thickness, the U-value amounts to 0.16 W/(m² K) for XPS to 0.32 W/(m² K) for wood fibre. The increase in U-value by insulation moisture amounts to 9.8 % for wood fibre and 2.0 % for calcium silicate. The interior mould growth risk remains zero. The interstitial mould growth risk is significant at the exterior side of the insulation layers, except for the calcium silicate insulation system. 4 % dripping moisture risk hours are found (from summer condensation against the vapour barrier). > 100 % for XPS to 37 % for calcium silicate wood mass loss is found. 2 frost-thaw cycles are found. And 14 hours for XPS to 13 hours for calcium silicate erosion risk are found. Resultantly, a capillary active calcium silicate insulation system is promoted because it yields the lowest moisture damage risks, particularly interstitial mould growth and wood decay.

Fig. 6 summarises the results of the performance indicators for the non-insulated reference wall and with the five different interior insulation systems. In (Hens et al., 2006), risk is defined as the probability a failure event happens multiplied with the severity of the consequences when happening. The severity of the consequences is expressed in costs (to repair the damage and to compensate for all distress caused). In the present, deterministic study, to enable graphically plotting the values of the different indicators on a common scale in this summary, the indicators are translated into a relative cost, as follows. First, take the maximum value of the indicator over all studied configuration results. Next, divide each indicator result by this maximum value. Finally, use a scale factor per indicator, see Table 2, to take into account the relative importance of the different risks.

Table 2: Overview of maximum indicator values and scale factors for the relative cost bars of the different performance indicators.

	U-value	ΔU	M interior	M interstitial	DM	ML	S	B	#CSC	#F-TC	ER
maximum	0.84	10.3	0	4.9	4.2	290	100	100	41	3	15
scale factor	1	0.2	0.75	0.75	0.75	2	1.25	1.25	0.6	0.25	0.2
scale factor/maximum	1.19	0.019	NA	0.15	0.18	0.0069	0.013	0.013	0.015	0.083	0.013

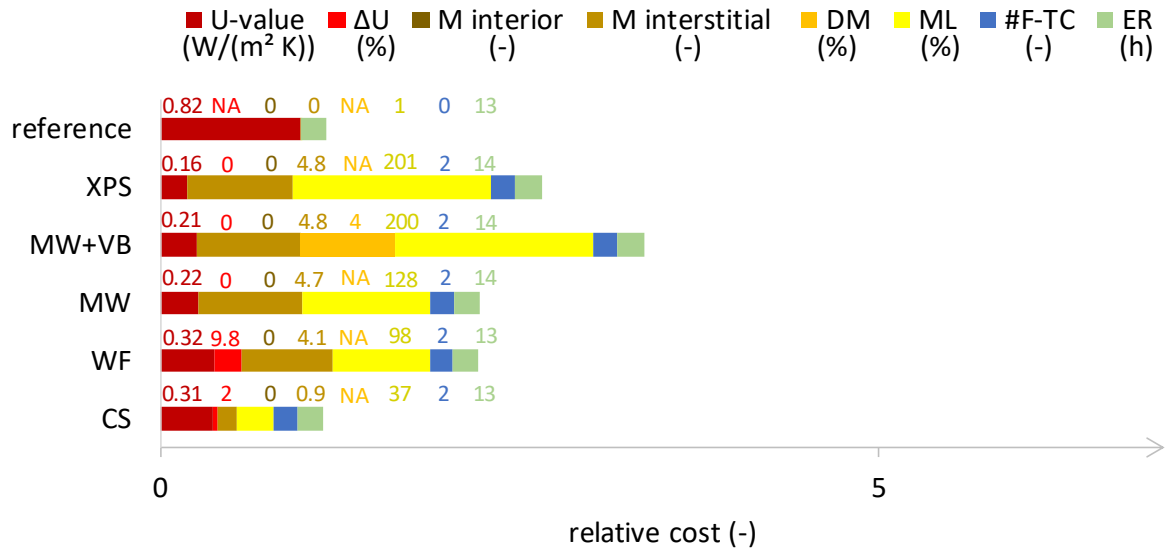

Fig. 6: Total relative cost outline for H1 rammed earth wall with different insulation systems.

5.3.3 Influence of insulation thickness

The influence of four different insulation thicknesses is considered: 2 cm, 5 cm, 10 cm, and 20 cm. Preliminarily, it is observed that the moisture contents in the rammed earth wall increase with

increasing insulation thickness, owing to the reduced inward drying ability and the lower temperatures. The U-value decreases with increasing insulation thickness. The increase in U-value by insulation moisture increases with increasing insulation thickness. The interior mould growth risk remains zero. The interstitial mould growth risk remains significant for the vapour tight insulation systems and decreases with decreasing insulation thickness for the other insulation systems. The number of dripping moisture risk hours generally decreases with decreasing insulation thickness. The wood decay risk increases with increasing insulation thickness. The frost damage risk increases with increasing insulation thickness. And the erosion risk increases with increasing insulation thickness. It is concluded that, while the thermal insulation quality improves with increasing insulation thickness, the moisture damage risks increase as well. Fig. 7 shows the total relative cost with the five insulation systems for 2 cm and for 20 cm insulation thickness. It is observed by estimate that the influence of the insulation system choice is mostly more important than the influence of the insulation thickness. With smaller insulation thicknesses, also other insulation systems might be applicable, such as wood fibre or mineral wool, but the calcium silicate remains the best performing choice.

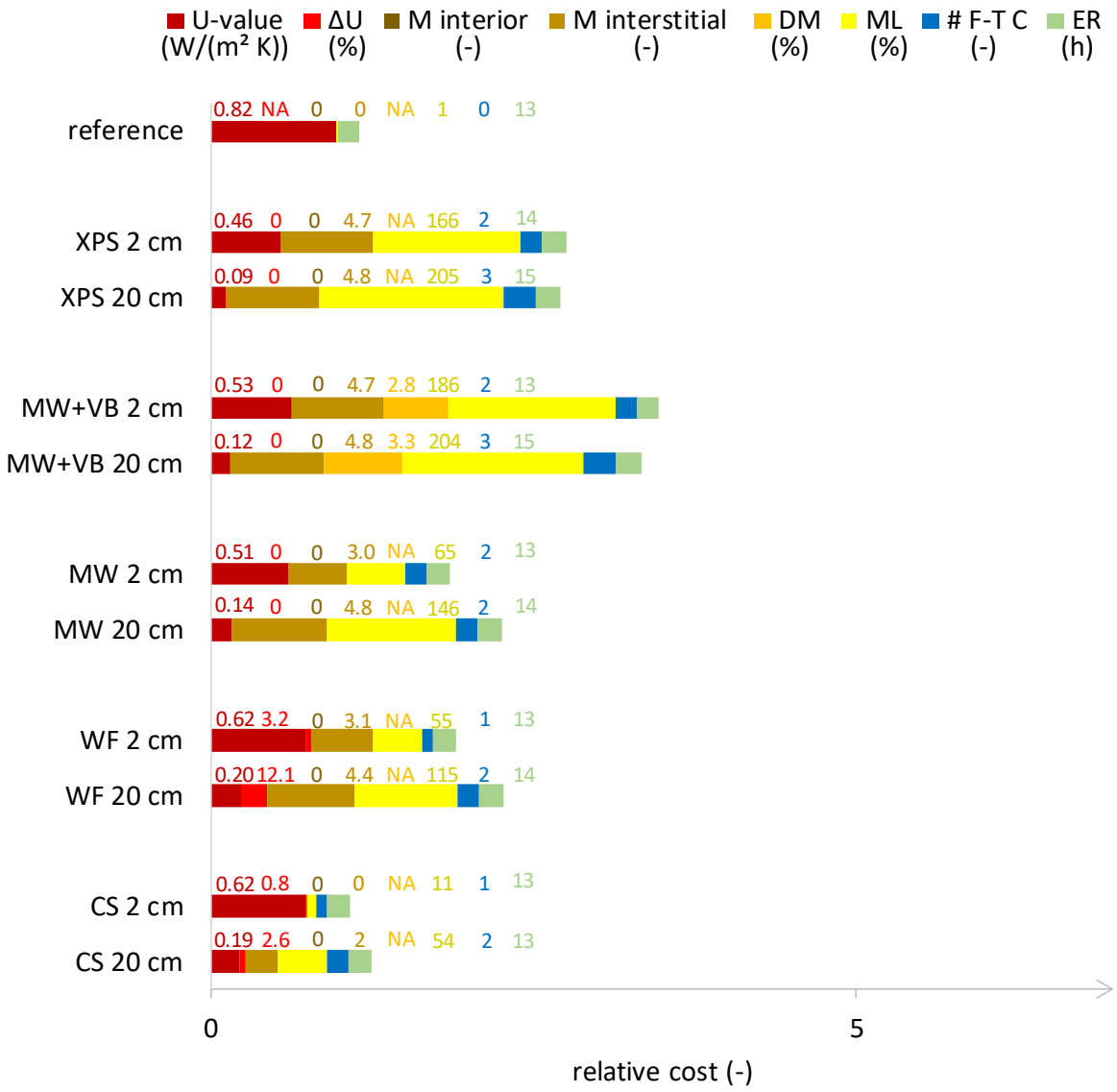

Fig. 7: Total relative cost outline for H1 rammed earth wall with different insulation thicknesses.

5.3.4 Influence of rammed earth material

The influence of the hygric rammed earth material properties is studied via the H6 rammed earth. Preliminarily, it is observed that the average moisture content in the rammed earth wall is on average 28 % smaller for the H6 rammed earth than for the H1 rammed earth, which is explained by the hygroscopically flatter course of the moisture retention curve. The relative humidity on the other hand is greater, which is also explained by the course of the moisture retention curve. This hygroscopically flatter course of the moisture retention curve is also the reason why, except for the U-value and the number of erosion risk hours (that decrease, like the moisture content), all the risk indicators increase for the H6 rammed earth (the increase in U-value by insulation moisture, the interstitial mould growth, the dripping moisture, and, especially, the wood decay).

The frost damage risk increases also. The interior mould growth risk remains zero. Fig. 8 shows the total relative cost for the different configurations with the H6 rammed earth besides the H1 rammed earth. It is observed that also for this H6 rammed earth wall, the calcium silicate insulation system gives much less risk of wood rot and interstitial mould growth than the other insulation systems. So, it is generally recommended to use the calcium silicate system for insulation. The vapour-tight insulation systems perform the worst. Besides, it is observed by estimate that the rammed earth material can have an almost equally important influence as the insulation system. For example, the difference in total relative cost between the H6 rammed earth wall with mineral wool plus vapour barrier and the H1 rammed earth wall with mineral wool plus vapour barrier is almost equally as important as the difference in total relative cost between the H6 rammed earth wall with mineral wool plus vapour barrier and the H6 rammed earth wall with XPS insulation. Or still, the difference in total relative cost between the H6 rammed earth wall with XPS and the H1 rammed earth wall with XPS is equally as important as the difference in total relative cost between the H6 rammed earth wall with XPS and the H6 rammed earth wall with mineral wool insulation.

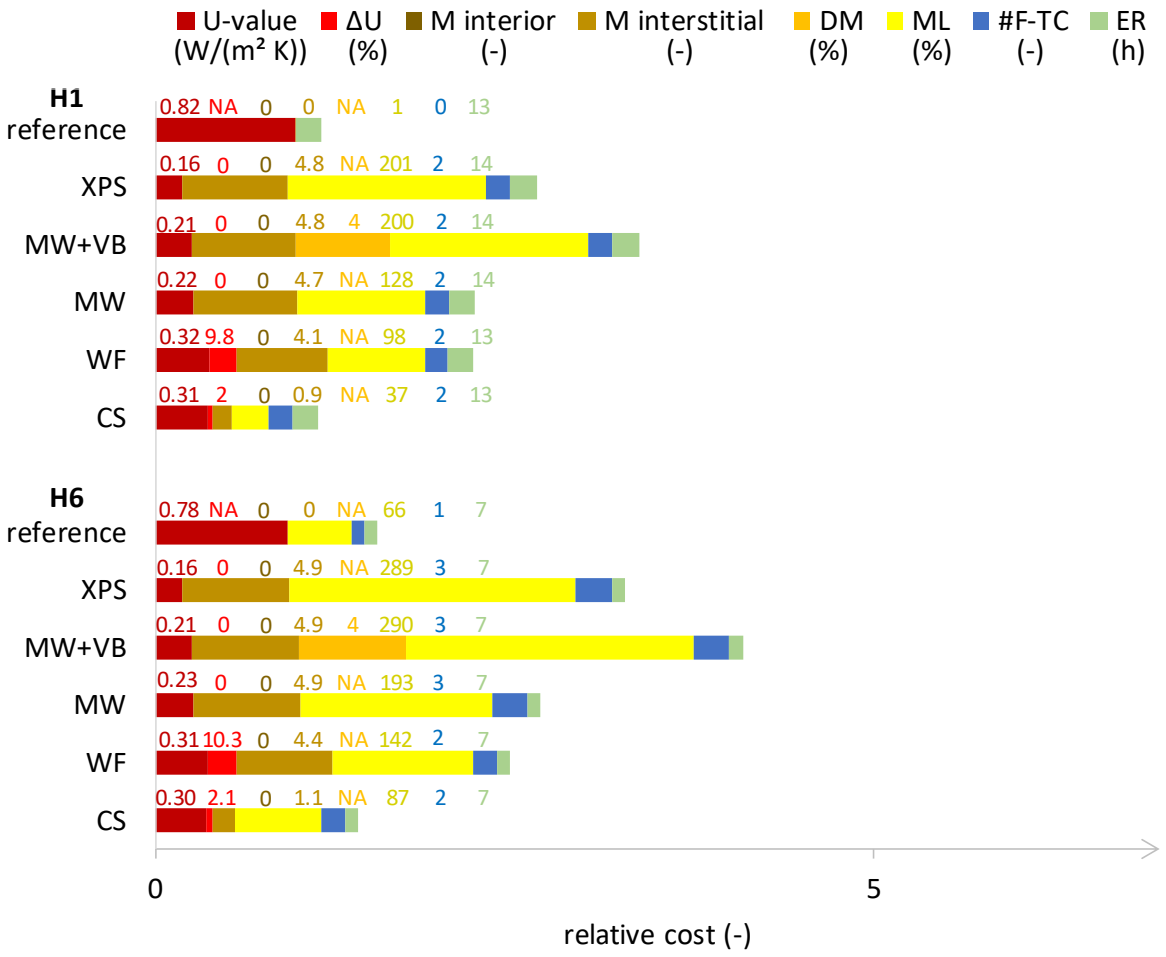

Fig. 8: Total relative cost outline for H6 (besides H1) rammed earth wall with different insulation systems.

5.3.5 Influence of rammed earth wall thickness

The influence of three different rammed earth wall thicknesses is considered: 30 cm, 50 cm and 80 cm. Preliminarily, it is observed that the thicker the rammed earth wall, the flatter the course of the average moisture content over time. Furthermore, the moisture content at the exterior surface is the greatest for the thicker wall (owing to the reduced inward drying ability) while the moisture content at the interior surface is the greatest for the thinner wall (owing to the higher rain penetration). The latter is the reason why for the thicker wall, the increase in U-value by insulation moisture, the interstitial mould growth, the dripping moisture, and the wood decay for the non-insulated wall and for the vapour open or capillary active insulated wall assemblies, decrease. The former is the reason why the frost damage risk increases for the thicker wall. The erosion risk remains unchanged. The wood decay risk for the vapour tight insulated wall assemblies increases, owing to the reduced outward drying ability. The interior mould growth risk

remains zero. And the U-value decreases owing to the extra wall thickness. Fig. 9 shows the total relative costs for the 80 cm (besides 50 cm) thick wall. It is concluded that a thicker wall overall favours the insulatability of rammed earth walls (except with the XPS insulation system). While calcium silicate remains the best option, one might besides also be able to apply wood fibre or mineral wool.

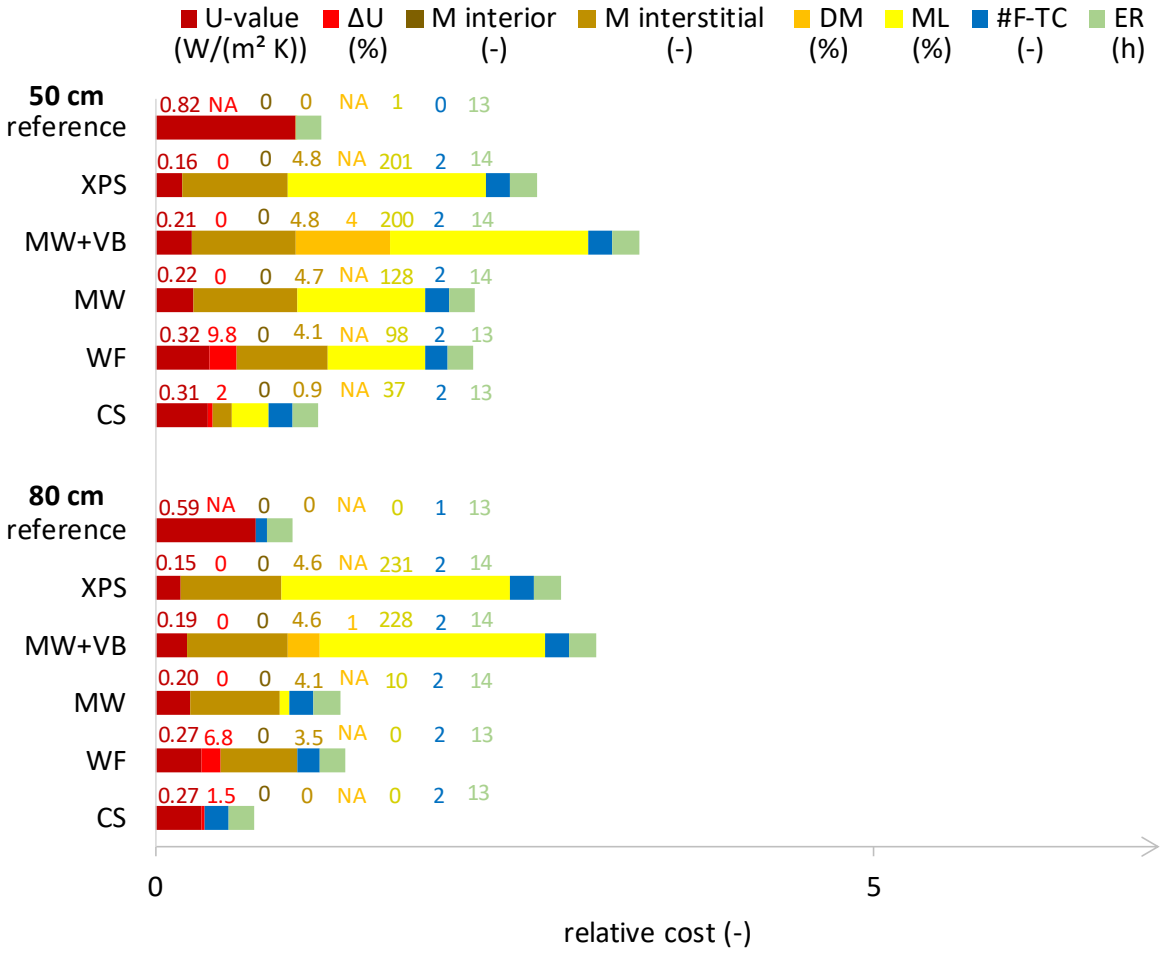

Fig. 9: Total relative cost outline for 80 cm (besides 50 cm) thick H1 rammed earth wall with different insulation systems.

5.3.6 Influence of wall orientation

The influence of four different wall orientations is explored: North, East, South, and West. Specifically, it is examined whether the South orientation is also the most critical for the U-value and for frost damage and what is the impact of the wall orientation on the insulation system choice. Resultantly, it is found that the North orientation is the most critical for the U-value and the South orientation the least, which is explained by the solar heat gains. It is hence

recommended to determine the required insulation thickness based on the North orientation. Nevertheless, the South orientation remains the most critical for the frost damage because of the higher wind-driven rain load (in 2014). Finally, as Fig. 10 shows, whereas for the South orientation with the high wind-driven rain load the calcium silicate system is the only recommendable insulation system, all the insulation systems give acceptable risks for the East orientation with the low wind-driven rain load. The vapour tight insulation systems and the calcium silicate system perform the best in total relative cost. There is no risk on wood decay for this orientation. All together, the choice of the insulation system can depend on the wall orientation through the wind-driven rain load. It is especially for walls with a high wind-driven rain load that the specific use of calcium silicate insulation becomes important.

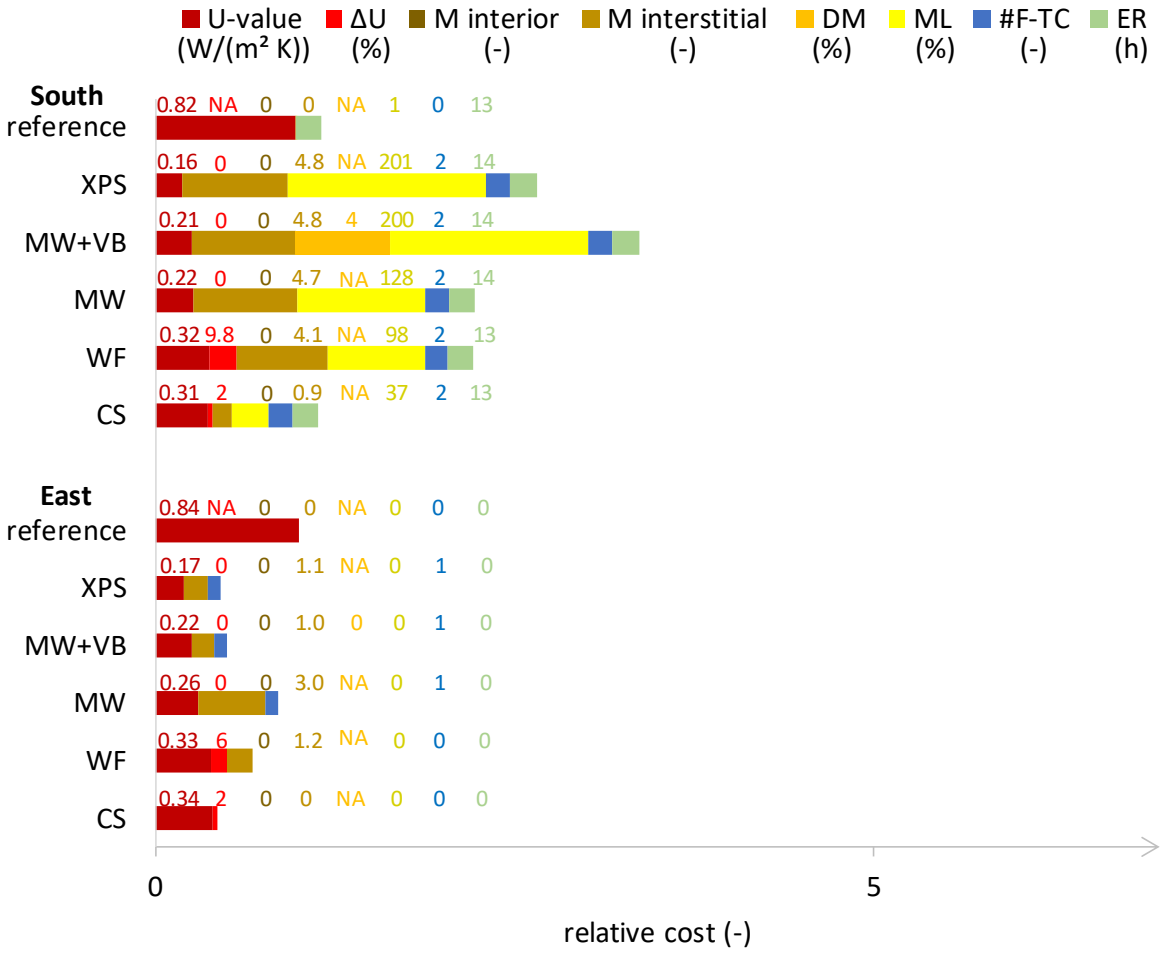

Fig. 10: Total relative cost outline for East (besides South) oriented H1 rammed earth wall with different insulation systems.

5.3.7 Influence of fracture failure, buckling failure and clay swelling damage

The influence of three additional mechanical performance indicators on the hygrothermal risk assessment is evaluated. It concerns the load-bearing section loss, the relative buckling stress, and the number of clay swelling cycles. Moreover, the influence of two variants of the mechanical properties is determined (cf. Section 5.2.2.1). Fig. 11 shows the results. It is observed that the fracture failure risk, the buckling failure risk, and the clay swelling damage risk change barely upon interior insulation when variant 1 of the mechanical properties (compressive strength) is assumed. When variant 2 of the mechanical properties is assumed, on the other hand, these risks increase drastically and structural collapse develops through fracture and/or buckling failure for all insulation systems except for the calcium silicate insulation system. It is concluded that the mechanical properties can have a disastrous influence on the relative cost and thus need to be measured. The calcium silicate insulation system remains the safest choice.

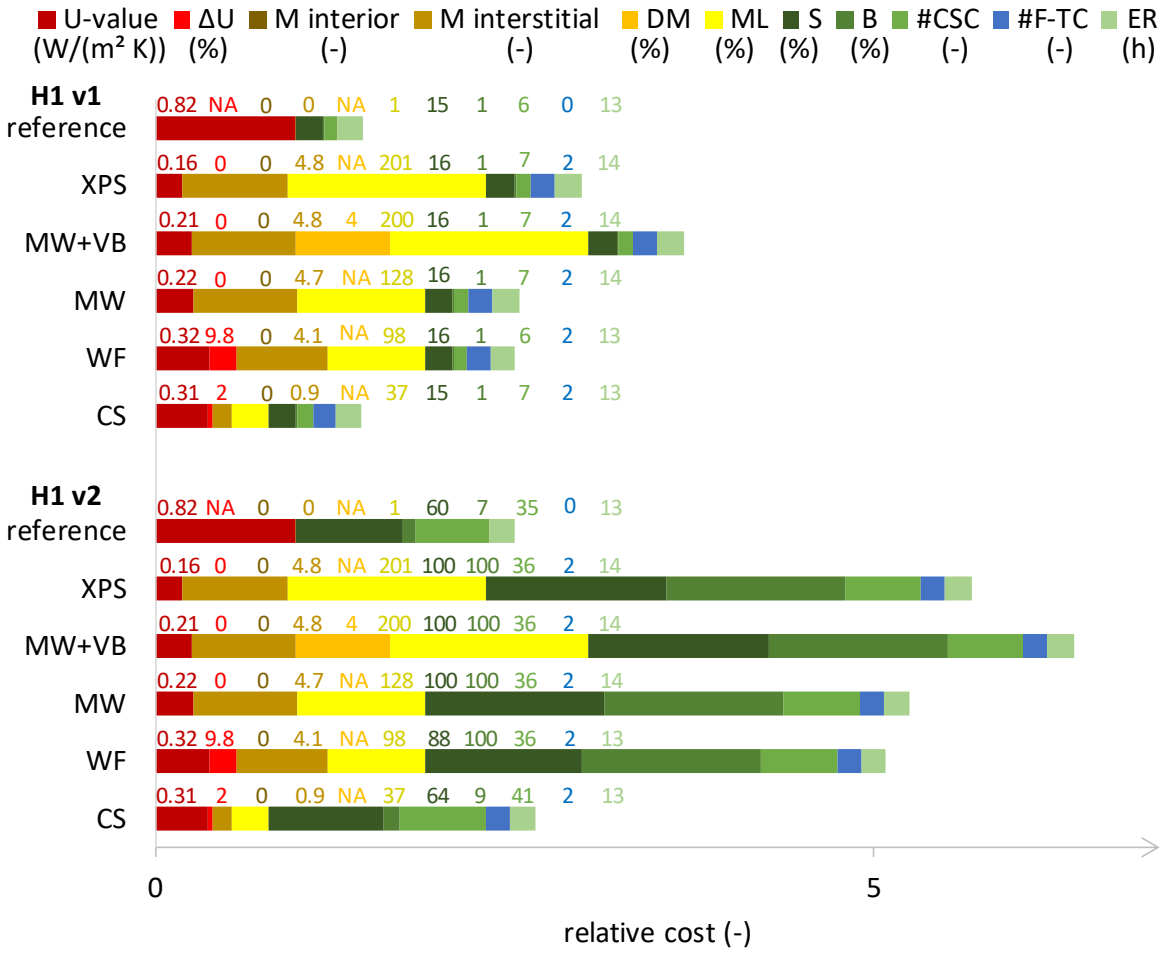

Fig. 11: Total relative cost outline for H1 rammed earth wall with variant 2 (besides variant 1) of the mechanical properties with different insulation systems.

5.4 Conclusion

The impact of interior insulation on the hygrothermal performance of rammed earth walls depends *inter alia* on the insulation system used. The vapour tight and vapour open insulation systems perform better in thermal insulation quality, but the capillary active insulation systems, particularly calcium silicate, are the best to minimise the hygrothermal risks. With all investigated insulation systems except the calcium silicate, the risk of decay of wooden floor beams increases balefully for walls with a high wind-driven rain load. Besides, the risk of interstitial mould growth increases significantly. In general, the calcium silicate is thus the only recommendable insulation system. If no wooden beams were present, XPS would also be applicable. For a 80 cm thick rammed earth wall and/or with 2 cm thick insulation, mineral wool and wood fibre might also be applicable. For orientations with a low wind-driven rain load, all the investigated insulation systems are eventually applicable, still with a preference for the calcium silicate because it yields the lowest risks (on all indicators except the increase in U-value by insulation moisture, which remains acceptable though).

When the mechanical properties of rammed earth are taken into account, they can have a disastrous impact on the hygrothermal performance of rammed earth walls through fracture failure and buckling failure. This is the case if the wind-driven rain load is high and the compressive strength decreases sharply in the hygroscopic range with all insulation systems except the calcium silicate.

So it was worth developing the mechanical performance indicators in Section 4. And in the future they must be further investigated and validated and the mechanical properties measured. Moreover, more rammed earth materials must be characterised (hygrically, thermally, and mechanically).

6 Conclusion

6.1 Conclusions

The **state of the art** study has shown that two preliminary objectives need to be tackled to get to the evaluation of the insulatability: the complete hygric material characterisation and the mechanically completed set of performance indicators enabling a comprehensive evaluation.

The full-range hygric **material characterisation** is performed for two rammed earth materials that are extracted from traditional rammed earth buildings. The moisture retention curve is

determined by means of traditional measurement techniques that avoid material evolution due to wetting in the high range (desiccator testing and mercury intrusion porosimetry). The liquid permeability curve is determined from the moisture diffusivity 'measured' (indirectly) during the capillary absorption test that is modified for rammed earth materials to eliminate material evolution. The vapour permeability curve is determined via standard methods (cup testing).

Four mechanical **performance indicators** are developed. The fracture failure risk is indicated by the load-bearing section loss. The buckling failure risk is indicated by the relative buckling stress. The clay swelling damage risk is indicated by the number of clay swelling cycles. The erosion risk is indicated by the number of hours of erosion-favourable conditions.

The numerical **interior insulation analysis** for unplastered rammed earth walls above the stem wall is performed. As a result, it is found that the interior insulation of rammed earth walls can cause mechanical failure when the compressive strength of the rammed earth material decreases sharply in the hygroscopic range with increasing relative humidity, for all insulation systems except the capillary active calcium silicate insulation system. The decay of embedded wooden floor beams has been found to be the second main risk to avoid, for which purpose a capillary active calcium silicate insulation system is best suited. The other insulation systems moreover yield interstitial mould growth (XPS, … (all)), dripping moisture (mineral wool with vapour barrier), suboptimal thermal insulation quality (wood fibre), and frost damage (XPS, … (all)). In addition, several parameters have been shown to influence significantly the hygrothermal performance, such as the wind-driven rain load.

6.2 Recommendations for improvements and further research

Concerning the **state of the art**, the impact of material evolution in practice could be investigated. Furthermore, the wind-driven rain load on rammed earth building walls could become a research topic (concerning the influence of the roof).

In the **material characterisation**, the open porosity should preferably be measured independently. In addition, the moisture retention curve should be determined more reliably for materials that behave abnormally, such as the H6 rammed earth. Moreover, the moisture permeability in the intermediate range of rammed earth materials should be determined. Further, more rammed earth materials should be characterised and the hygric, mechanical, and thermal properties should be determined.

Regarding the **performance indicators**, rising damp should still be investigated, as well as differential hygrothermal stresses and strains at the building level. The mechanical performance indicators (possibly expanded) including the hygric stress should be validated in future research.

As for the **interior insulation analysis**, the insulatability of the stem wall should still be investigated. The H2 rammed earth could be integrated until the end of the study besides H1 and H6. Furthermore, a more representative climate loading could be used for the risk evaluation, such as ten successive future years or a hybrid climate year. The wooden beams could be simulated for an improved reliability of the wood decay risk assessment. More future research is necessary concerning the validation of the mechanical performance indicators and the measurement of the mechanical properties of rammed earth materials. Furthermore, an automatised probabilistic risk assessment tool could be used to facilitate a comprehensive analysis and to facilitate investigating more influence parameters. Finally, the insulatability of exteriorly plastered rammed earth walls should be investigated.

Nomenclature

Greek symbols

α	absorptivity	-
α	relative measure of the state of the fungi with respect to their state at the initiation of the wood mass loss process	-
α	wind-driven rain coefficient	s/m
α_i	scaling parameter for subcurve i	m^{-1}
β	convective surface moisture transfer coefficient	s/m
δ	declination	°
δ	dimensional correction factor	m
δ	vapour permeability	s
ε	strain	m/m
ϵ	volumetric energy content	J/m^3
F_i	weighing factor for subcurve i	-
θ	temperature	°C
θ	wind direction	°
θ_l	liquid water content	m^3/m^3
ϑ	contact angle	°
λ	Boltzmann variable	$m/s^{0.5}$
λ	thermal conductivity	W/(m K)
λ^*	adapted Boltzmann variable	$m/s^{0.5}$
λ_f	average boundary lambda value	$m/s^{0.5}$
μ	attenuation coefficient	m^{-1}
μ	vapour resistance factor	-
ν	Poisson's ratio	-
ξ_φ	specific moisture ratio	kg/(kg -)
ρ	density	kg/m^3
ρ	reflectivity	-
σ	normal stress	Pa
σ	Stefan-Boltzmann constant	5.67×10^{-8} W/(m² K⁴)
σ	surface tension	N/m
σ_c	compressive structural normal stress	Pa
σ_{cri}	buckling strength	Pa
σ_{max}	compressive strength	Pa

σ_z	normal stress on shear failure plane	Pa
τ	shear stress	Pa
τ_{max}	shear strength	Pa
φ	internal friction angle	°
φ	latitude	°
φ	relative humidity	-
φ	surface normal	°
χ	sun incidence angle	°
Ψ_o	open porosity	m³/m³
ω	time angle	°

Roman symbols

A	surface area	m²
A'	remaining load-bearing wall section surface area	m²
A_c	capillary absorption coefficient	kg/(m² $s^{0.5}$)
a	azimuth of surface	°
a	fitting parameter	kg/m³
a	moisture content factor	W m²/(kg K)
B	relative buckling stress	Pa/Pa, %
b	fitting parameter	$s^{0.5}$/m
b	temperature factor	W/(m K²)
b	wall width	m
C	Biot's poroelastic coupling coefficient scaling factor	-
C_R	roughness coefficient	-
C_T	topography coefficient	-
c	cloud cover	-
c	cohesion or cohesive strength	Pa
c	constant	Pa
c	fitting parameter	-
c	specific heat capacity	J/(kg K)
D	diameter	m
DM	number of dripping moisture risk hours	h
D_m	moisture diffusivity	m²/s
d	thickness	m
d_R	optic factor	-

E	solar constant	W/m²
E	stiffness modulus	Pa
ER	number of erosion risk hours	h
e	emissivity	-
F	normal force	N
F	view factor	-
F_R	radiation factor	-
f_v	pore volume distribution	kg/(m³ $\log_{10}$(Pa))
G	mass flow	kg/s
g	gravitational acceleration	m/s²
g	mass flux	kg/(m² s)
g	solar heat gain coefficient	-
H	height	m
h	surface heat transfer coefficient	W/(m² K)
h	wall thickness	m
h_s	solar height	-
I	area moment of inertia	m^4
I	transmitted intensity	-
I_0	incident intensity	-
K_R	terrain factor	-
K_1	fitting parameter	Pa
K_2	fitting parameter	-
k	growth rate parameter	-
k	modality	-
k	permeability	s
L	wall height	m
L_m	latent heat of melting	333550 J/kg
L_v	latent heat of vapourisation	2.5 x 10^6 J/kg
M	mass	kg
M	mould index	-
ML	mass loss	%
m	air factor	-
m	moisture mass	kg/m²
N_c	compressive structural normal section force	N
N_{cri}	critical buckling normal force	N

n	air change rate	h^{-1}
$\boldsymbol{n}$	unit normal vector	-
n_i	shape parameter for subcurve i	-
O	obstruction factor	-
P	total pressure	Pa
p	pressure	Pa
Q	heat flow	W
q	heat flux	W/m²
R	thermal resistance	m² K/W
RH	relative humidity	%
R_h	unobstructed horizontal rainfall intensity	kg/(m² h)
$R'_{h(orizontal)}$	unobstructed horizontal rainfall intensity, raw data	mm/h
R_v	specific gas constant of water vapour	461.52 J/(kg K)
R_{wdr}	wind-driven rain intensity	kg/(m² h)
r	equivalent pore radius	m
S	degree of moisture saturation	kg/kg
S	load-bearing section loss	m²/m², %
S_l	degree of liquid water saturation	m³/m³
$S'_{h(orizontal)}$	cumulative unobstructed horizontal rainfall intensity, raw data	mm
S_{wdr}	cumulative wind-driven rain load	kg/m²
s	slope	°
T	temperature	K
T_{frost}	freezing point of water in relation to pore radius	K
$T_{ref,h}$	reference temperature for heat	K
T_0	standard freezing point of water	273.15 K
Tu_{Atm}	turbidity of atmosphere on clear day with mean air pollution	-
t	time	s
U	thermal transmittance	W/(m² K)
U_{10}	reference wind speed	m/s
u	moisture content	kg/kg
V	volume	m³
V_{loc}	local wind velocity	m/s
W	wall factor	-
W	width	m

w	(volumetric) moisture content	kg/m³
x	position	m
Z	vapour diffusion resistance	m² s Pa/kg
z	height above the ground	m
z	height above the sea level	m
z_0	aerodynamic roughness length	m
$\#CSC$	number of clay swelling cycles	-
$\#F\text{-}TC$	number of frost-thaw cycles	-

Subscripts

a	air
avg	average
B	boundary
bul	bulk
C	of top material C for tri-layer composite
c	capillary
cal	caliper
cap	capillary
$conv$	convective
cri	critical
d	for dry material
dif	diffuse
dir	direct
e	exterior
equ	equivalent
fin	final
flu	fluid
g	gas
g	glass
h	horizontal
i	depth from exterior surface mm
i	ice
i	interior
i	position no.
i	for subcurve i

int	intruded
L	long-wave
l	liquid (water)
lim	maximum limit
m	moisture
mat	material
mer	mercury
min	minimum
pen	penetrometer
$prod$	production
rad	radiative
req	required
S	short-wave
s	surface
sam	sample
sat	(vacuum) saturation
$stat$	stationary
ste	stem
tpa	top part alone
$trans$	transmission
v	water vapour
vac	vacuum
wat	water
0	initial
75%	at 75% relative humidity
$(*)$	(for one pore)

Abbreviations

C	capillary active
CS	calcium silicate
ext	exterior
GB	gypsum board
GM	glue mortar
GP	gypsum plaster
H	house

ins. thickn.	insulation thickness
int	interior
max	maximum
MIP	mercury intrusion porosimetry
MW	mineral wool
NA	not applicable
NE	not evaluated
P	pressed
R	rammed
ref.	reference
VB	vapour barrier
VN	vapour neutral
VO	vapour open
VT	vapour tight
WF	wood fibre
XPS	extruded polystyrene

Bibliography

Abhilash, H. N. (2016a). *Mechanical Testing Procedure for Local Building Materials: Rammed Earth and Laterite Building Stones*. L'Ecole Nationale des Travaux Publics de l'Etat.

Abhilash, H. N. (2016b). Personal communication.

Abuku, M., Janssen, H., Poesen, J., & Roels, S. (2009). Impact, absorption and evaporation of raindrops on building facades. *Building and Environment*, *44*, 113–124. https://doi.org/10.1016/j.buildenv.2008.02.001.

Abuku, M., Janssen, H., & Roels, S. (2009). Impact of wind-driven rain on historic brick wall buildings in a moderately cold and humid climate: Numerical analyses of mould growth risk, indoor climate and energy consumption. *Energy and Buildings*, *41*, 101–110. https://doi.org/10.1016/j.enbuild.2008.07.011.

Al Haffar, N. (2017). *Hydro-mechanical behavior of cement stabilized compacted earth*. Université Grenoble Alpes.

Allinson, D., & Hall, M. (2010). Hygrothermal analysis of a stabilised rammed earth test building in the UK. *Energy and Buildings*, *42*, 845–852. https://doi.org/10.1016/j.enbuild.2009.12.005.

Arrigoni, A., Grillet, A. C., Pelosato, R., Dotelli, G., Beckett, C. T. S., Woloszyn, M., & Ciancio, D. (2017). Reduction of rammed earth's hygroscopic performance under stabilisation: an experimental investigation. *Building and Environment*, *115*, 358–367. https://doi.org/10.1016/j.buildenv.2017.01.034.

Augarde, C. E. (2012). 8 Soil mechanics and earthen construction: strength and mechanical behaviour. In *Modern earth buildings: Materials, engineering, construction and applications* (pp. 204–221). https://doi.org/10.1533/9780857096166.2.204.

Avons-Bariot, J. (2017). La sinistralité du bâti ancien en pisé : le diagnostic global comme acte préventif. Retrieved from https://docplayer.fr/88393432-Le-diagnostic-global-comme-acte-preventif.html (accessed on 14 January 2021).

Beckett, C., & Ciancio, D. (2014). Effect of compaction water content on the strength of cement-stabilized rammed earth materials. *Canadian Geotechnical Journal*, *51*, 583–590. https://doi.org/10.1139/cgj-2013-0339.

Berger, J., Guernouti, S., Woloszyn, M., & Buhe, C. (2015). Factors governing the development of moisture disorders for integration into building performance simulation. *Journal of Building Engineering*, *3*, 1–15. https://doi.org/10.1016/j.jobe.2015.04.008.

Blocken, B., & Carmeliet, J. (2002). Spatial and Temporal Distribution of Driving Rain on Buildings: Numerical Simulation and Experimental Verification. In *Buildings VIII/Moisture Model Inputs-Principles* (pp. 1–11). Retrieved from https://web.ornl.gov/sci/buildings/conf-archive/2001 B8 papers/038_Blocken.pdf (accessed on 21 June 2018).

Blocken, B., & Carmeliet, J. (2010). Overview of three state-of-the-art wind-driven rain assessment models and comparison based on model theory. *Building and Environment*, *45*, 691–703. https://doi.org/10.1016/j.buildenv.2009.08.007.

Blocken, B., Derome, D., & Carmeliet, J. (2013). Rainwater runoff from building facades: A review. *Building and Environment*, *60*, 339–361. https://doi.org/10.1016/j.buildenv.2012.10.008.

Brinkmann, M., & Wiehle, P. (2023). Correlation between relative humidity and the strength and deformation characteristics of unstabilised earth masonry. *Construction and Building Materials*, *366*, 130048.

Bruno, A. W. (2016). *Hygro-mechanical characterisation of hypercompacted earth for building construction*. Université de Pau et des Pays de l'Adour.

Bruno, A. W., Gallipoli, D., Perlot, C., & Mendes, J. (2017). Mechanical behaviour of hypercompacted earth for building construction. *Materials and Structures*, *50*, [160]. https://doi.org/10.1617/s11527-017-1027-5.

Bui, Q.-B. (2008). *Stabilité des structures en pisé : durabilité, caractéristiques mécaniques*. Institut National Des Sciences Appliquées De Lyon.

Bui, Q. B., Morel, J. C., Hans, S., & Walker, P. (2014). Effect of moisture content on the mechanical characteristics of rammed earth. *Construction and Building Materials*, *54*, 163–169. https://doi.org/10.1016/j.conbuildmat.2013.12.067.

Bui, Q. B., Morel, J. C., Venkatarama Reddy, B. V., & Ghayad, W. (2009). Durability of rammed earth walls exposed for 20 years to natural weathering. *Building and Environment*, *44*, 912–919. https://doi.org/10.1016/j.buildenv.2008.07.001.

Bui, R., Goffart, J., Mcgregor, F., Woloszyn, M., Fabbri, A., & Grillet, A. (2020). Uncertainty and sensitivity analysis applied to a rammed earth wall : evaluation of the discrepancies between experimental and numerical data, *17004*, 1–7.

Bui, T. T., Bui, Q. B., Limam, A., & Maximilien, S. (2014). Failure of rammed earth walls: From observations to quantifications. *Construction and Building Materials*, *51*, 295–302. https://doi.org/10.1016/j.conbuildmat.2013.10.053.

Bulson, P. S. (1970). Introduction to plate buckling. In *Theory of Flat Plates* (pp. 1–12). Chatto and Windus, London.

Buzo, A., Cho, H. J., Génis, L., & Paccoud, G. (2014). Practices and demands in retrofitting of vernacular rammed earth houses. In *Proceedings of International Conference on Vernacular Heritage, Sustainability and Earthen Architecture*. Valencia.

Calabrese, G. (2012). 16 Conservation of historic earth buildings. In *Modern Earth Buildings: Materials, Engineering, Constructions and Applications* (pp. 401–424). https://doi.org/10.1533/9780857096166.3.401.

Carmeliet, J. (2006). Coupled heat and mass transfer. Theory. Moisture transport properties, 1–31.

Carmeliet, J., Hens, H., Roels, S., Adan, O., Brocken, H., Cerny, R., … Pel, L. (2004). Determination of the Liquid Water Diffusivity from Transient Moisture Transfer Experiments. *Journal of Thermal Envelope and Building Science*, *27*(4), 277–305. https://doi.org/10.1177/1097196304042324.

Carmeliet, J., & Roels, S. (2001). Determination of the Isothermal Moisture Transport Properties of Porous Building Materials. *Journal of Thermal Envelope and Building Science*, *24*, 183–210. https://doi.org/10.1106/Y6T2-9LLP-04Y5-AN6T.

Carmeliet, J., & Roels, S. (2002). Determination of the Moisture Capacity of Porous Building Materials. *Journal of Building Physics*, *25*, 209–237. https://doi.org/10.1106/109719602022835.

Carmeliet, J., & Van Den Abeele, K. (2004). Poromechanical approach describing the moisture influence on the non-linear quasi-static and dynamic behaviour of porous building materials. *Materials and Structures*, *37*, 271–280. https://doi.org/10.1617/14166.

Chabriac. (2014). *Mesure du comportement hygrothermique du pise*. l'Ecole Nationale des Travaux Publics de l'Etat.

Chanvillard, G., & Scherer, G. W. (2006). Effect of the pore size distribution on crystallization pressure. In M. S. Konsta-Gdoutos (Ed.), *Measuring, Monitoring and Modeling Concrete Properties* (pp. 669–673). https://doi.org/10.1007/978-1-4020-5104-3.

Chatel, M. (2012). Conservation de l'architecture vernaculaire en pisé d'Isère. Retrieved from https://docplayer.fr/56552326-Conservation-de-l-architecture-vernaculaire-en-pise-d-isere-ue-learning-from-vernacular-marie-chatel.html (accessed on 8 August 2018).

Chevillotte, A. (n.d.). Pourquoi isoler du pisé avec une laine de verre est inapproprié? Retrieved from https://www.atelier-chevillotte.fr/laine-verre-pise-348726.htm (accessed in 2020).

Chitimbo, T., Prime, N., Samad, F. A., & Plé, O. (n.d.). Effect of capillary rise on mechanical behaviour of unstabilized rammed earth. In *NOMAD 2022 - 4e conférence internationale francophone Nouveaux Matériaux et Durabilité, IMT Mines Alès; LMGC; LIFAM* (p. hal-03880924). Montpellier, France.

Ciancio, D., Jaquin, P., & Walker, P. (2013). Advances on the assessment of soil suitability for rammed earth. *Construction and Building Materials*, *42*, 40–47. https://doi.org/10.1016/j.conbuildmat.2012.12.049.

CSTS EN 1991-1-1. (2015). *Eurocode 1 - Actions on structures - Part 1-1: General actions - Densities, self-weight, imposed loads for buildings.* Retrieved from https://www.wtcb.be/homepage/download.cfm?lang=nl&dtype=na_eurocodes&doc=Fiche_EN1991-1-1_nl.pdf (accessed on 14 January 2021).

Cuccurullo, A., Gallipoli, D., Bruno, A. W., Augarde, C., Hughes, P., & La Borderie, C. (2020). Influence of particle grading on the hygromechanical properties of hypercompacted earth. *Journal of Building Pathology and Rehabilitation*, *5*, 1–9. https://doi.org/10.1007/s41024-019-0066-4.

Cuisinier, O., Auriol, J., Borgne, T. Le, & Deneele, D. (2011). Microstructure and hydraulic conductivity of a compacted lime-treated soil. *Engineering Geology*, *123*, 187–193. https://doi.org/10.1016/j.enggeo.2011.07.010.

Decagon Devices. (2015). *WP4C Dew Point PotentiaMeter. Operator's Manual*.

Deconinck, A.-H. (2017). *Reliable thermal resistance estimation of building components from on-site measurements*. KU Leuven.

Delage, P., Audiguier, M., Cui, Y.-J., & Howat, M. D. (1996). Microstructure of a compacted silt. *Canadian Geotechnical Journal*, *33*, 150–158. https://doi.org/10.1139/t96-030.

DELPHIN. (n.d.). Retrieved from http://bauklimatik-dresden.de/ (accessed in 2021).

Dorothée, A. (2018). Recognition of a heritage in danger: rammed-earth architecture in Lyon

city, France. In *IOP Conference Series: Earth and Environmental Science*. https://doi.org/10.1088/1755-1315/143/1/012054.

Durner, W. (1994). Hydraulic conductivity estimations for soils with heterogeneous pore structure. *Water Resources Research*, *30*, 211–223.

El Nabouch, R. (2017). *Mechanical behavior of rammed earth walls under Pushover tests*. Université Grenoble Alpes, Université Savoie Mont Blanc.

EN 15026. (2007). *Hygrothermal performance of building components and building elements - Assessment of moisture transfer by numerical simulation*.

Engel, O. G. (1958). Erosion Damage to Solids Caused by High-Speed Collision With Rain. *Journal of Research of the National Bureau of Standards*, *61*(1), 47–52.

ENTPE. (n.d.). Retrieved from http://idmp.entpe.fr/mesfr.htm (accessed in 2020).

Erkal, A., D'Ayala, D., & Sequeira, L. (2012). Assessment of wind-driven rain impact, related surface erosion and surface strength reduction of historic building materials. *Building and Environment*, *57*, 336–348. https://doi.org/10.1016/j.buildenv.2012.05.004.

Evangelides, C., Arampatzis, G., Tsambali, A. A., Tzanetaki, E., & Tzimopoulos, C. (2018). Moisture estimation in building materials with a simple procedure. *Construction and Building Materials*, *164*, 830–836. https://doi.org/10.1016/j.conbuildmat.2017.12.138.

Fabbri, A., Morel, J.-C., & Gallipoli, D. (2018). *Assessing the performance of earth building materials : a review of recent developments*. https://doi.org/10.21809/rilemtechlett.2018.71.

Fabbri, A., Morel, J. C., Aubert, J. E., Bui, Q. B., Gallipoli, D., Reddy, V. B. V, … Narayanaswamy, H. (2021). An overview of the remaining challenges of the RILEM TC 274 - TCE , testing and characterisation of earth - based building materials and elements, 150–157.

Fabbri, A., Soudani, L., McGregor, F., & Morel, J. C. (2019). Analysis of the water absorption test to assess the intrinsic permeability of earthen materials. *Construction and Building Materials*, *199*, 154–162. https://doi.org/10.1016/j.conbuildmat.2018.12.014.

Fazio, A. T., Cavicchioli, A., Penna, D. S. A., Chambergo, F. S., & de Faria, D. L. A. (2015). Towards a better comprehension of biodeterioration in earthen architecture: Study of fungi colonisation on historic wall surfaces in Brazil. *Journal of Cultural Heritage*, *16*(6), 934–938. https://doi.org/10.1016/j.culher.2015.04.001.

Feng, C., & Janssen, H. (2018). Hygric properties of porous building materials (III): Impact factors and data processing methods of the capillary absorption test. *Building and Environment*, *134*, 21–34. https://doi.org/10.1016/j.buildenv.2018.02.038.

Feng, C., & Janssen, H. (2019). Hygric properties of porous building materials (IV): Semi-permeable membrane and psychrometer methods for measuring moisture storage curves. *Building and Environment*. https://doi.org/10.1016/j.buildenv.2019.01.054.

Feng, C., & Janssen, H. (2020). Modified pressure plate method for measuring adsorption moisture retention curves. In *E3S Web of Conferences* (Vol. 172, pp. 1–5). 12th Nordic Symposium on Building Physics. https://doi.org/10.1051/e3sconf/202017214004.

Feng, C., & Janssen, H. (2021). Hygric properties of porous building materials (VII): Full-range benchmark characterizations of three materials. *Building and Environment*, *195*, 107727. https://doi.org/10.1016/j.buildenv.2021.107727.

Feng, C., Janssen, H., Feng, Y., & Meng, Q. (2015). Hygric properties of porous building materials: Analysis of measurement repeatability and reproducibility. *Building and Environment*, *85*, 160–172. https://doi.org/10.1016/j.buildenv.2014.11.036.

Feng, C., Janssen, H., Wu, C., Feng, Y., & Meng, Q. (2013). Validating various measures to accelerate the static gravimetric sorption isotherm determination. *Building and Environment*, *69*, 64–71. https://doi.org/10.1016/j.buildenv.2013.08.005.

Feng, C., Roels, S., & Janssen, H. (2019). Towards a more representative assessment of frost damage to porous building materials. *Building and Environment*, *164*, 106343. https://doi.org/10.1016/j.buildenv.2019.106343.

François, B., Palazon, L., & Gerard, P. (2017). Structural behaviour of unstabilized rammed earth constructions submitted to hygroscopic conditions. *Construction and Building Materials*, *155*, 164–175. https://doi.org/10.1016/j.conbuildmat.2017.08.012.

Gallipoli, D., Bruno, A. W., Bui, Q., Fabbri, A., Faria, P., Oliveira, D. V, … Silva, R. A. (2022). *Durability of Earth Materials : Weathering Agents , Testing Procedures and Stabilisation Methods*. Springer International Publishing. https://doi.org/10.1007/978-3-030-83297-1.

Galmiche, V. (2019). *CONSTRUCTION ET RÉHABILITATION EN TERRE CRUE : points de vigilance*. Retrieved from https://docplayer.fr/4667143-La-pathologie-humide-du-pise-prescription-architecture-en-terre.html.

Genis, L. (2018). *Réhabiliter le bâti ancien et les cultures constructives : engagements, épreuves et attachements autour de la réhabilitation du bâti ancien en pisé en Isère*. Université Grenoble Alpes.

Gerard, P., Mahdad, M., Robert McCormack, A., & François, B. (2015). A unified failure criterion for unstabilized rammed earth materials upon varying relative humidity conditions. *Construction and Building Materials*, *95*, 437–447. https://doi.org/10.1016/j.conbuildmat.2015.07.100.

Girgin, Z. C., & Girgin, K. (2011). Stability and Vibration Analysis of Non-Uniform Columns Under Concentrated and Distributed Axial Loads. In *World Congress on Advances in Structural Engineering and Mechanics*. Seoul.

Gonzalez, I. J., Rodriguez-Navarro, C., & Scherer, G. W. (2008). Role of clay minerals in the physicomechanical deterioration of sandstone. *Journal of Geophysical Research*, *113*, 1–17. https://doi.org/10.1029/2007JF000845.

Gonzalez, I. J., & Scherer, G. W. (2004). Effect of swelling inhibitors on the swelling and stress relaxation of clay bearing stones. *Environmental Geology*, *46*, 364–377. https://doi.org/10.1007/s00254-004-1038-8.

Gutiérrez, F. (2016). *Valorisation du patrimoine en pisé de la Région Auvergne-Rhône-Alpes*. Ecole Nationale Supérieure d'Architecture de Grenoble. Retrieved from https://issuu.com/gearquitectura/docs/valorisation_du_patrimoine_en_pise_.

Hagentoft, C. E., Kalagasidis, A. S., Adl-Zarrabi, B., Roels, S., Carmeliet, J., Hens, H., … Djebbar, R. (2004). Assessment Method of Numerical Prediction Models for Combined Heat, Air and Moisture Transfer in Building Components: Benchmarks for One-dimensional Cases. *Journal of Building Physics*, *27*(4), 327–352. https://doi.org/10.1177/1097196304042436.

Hall, M., & Allinson, D. (2008). Assessing the moisture-content-dependent parameters of stabilised earth materials using the cyclic-response admittance method. *Energy and Buildings*, *40*, 2044–2051. https://doi.org/10.1016/j.enbuild.2008.05.009.

Hall, M., & Allinson, D. (2009a). Analysis of the hygrothermal functional properties of stabilised rammed earth materials. *Building and Environment*, *44*, 1935–1942. https://doi.org/10.1016/j.buildenv.2009.01.007.

Hall, M., & Allinson, D. (2009b). Influence of cementitious binder content on moisture transport in stabilised earth materials analysed using 1-dimensional sharp wet front theory. *Building and Environment*, *44*, 688–693. https://doi.org/10.1016/j.buildenv.2008.05.013.

Hall, M., & Djerbib, Y. (2004). Moisture ingress in rammed earth: Part 1 - The effect of soil particle-size distribution on the rate of capillary suction. *Construction and Building Materials*, *18*, 269–280. https://doi.org/10.1016/j.conbuildmat.2003.11.002.

Hall, M. R., Mooney, S. J., Sturrock, C., Matelloni, P., & Rigby, S. P. (2013). An approach to characterisation of multi-scale pore geometry and correlation with moisture storage and transport coefficients in cement-stabilised soils. *Acta Geotechnica*, *8*, 67–79. https://doi.org/10.1007/s11440-012-0178-3.

Heitz, P. (2014). *Architecture en terre. La pathologie humide du pisé*. *In Qualité construction* (Vol. 143). Retrieved from https://docplayer.fr/4667143-La-pathologie-humide-du-pise-prescription-architecture-en-terre.html.

Heitz, P., Morel, J.-C., Fabbri, A., Soudani, L., Champiré, F., & Meunier, N. (2015). Construction terre. L'isolation du pisé : pertinence et principes. https://doi.org/10.13140/RG.2.1.1238.1688.

Hens, H. (2010). *Bouwfysica: warmte- en massatransport*. ACCO, Leuven.

Hens, H. (2011). *Applied Building Physics: Boundary Conditions, Building Performance and Material Properties*. Ernst & Sohn, Berlin. https://doi.org/10.1002/9783433600917.

Hens, H., Carmeliet, J., Roels, S., & Janssen, H. (2006). Whole building approach and hygrothermal risk analysis. In *Proceedings of the 3rd International Building Physics Conference - Research in Building Physics and Building Engineering* (pp. 519–526). Montreal. Retrieved from http://www.scopus.com/inward/record.url?eid=2-s2.0-56249108716&partnerID=tZOtx3y1.

Hockey, B. J., Wiederhorn, S. M., & Johnson, H. (1978). Erosion of Brittle Materials By Solid Particle Impact. In *Proc. 2nd Int. Symp. Fract. Mech.* (pp. 379–402). Retrieved from https://nvlpubs.nist.gov/nistpubs/Legacy/IR/nbsir77-1396.pdf.

HYGROBA. (2013a). *Etude de la réhabilitation hygrothermique des parois anciennes Cahier n°0 : Généralités*. Retrieved from https://www.rehabilitation-bati-ancien.fr/espace-documentaire/hygroba-etude-la-rehabilitation-hygrothermique-des-parois-anciennes.

HYGROBA. (2013b). Etude de la réhabilitation hygrothermique des parois anciennes Cahier n°1 : Murs en terre crue. Retrieved from https://www.rehabilitation-bati-ancien.fr/espace-documentaire/hygroba-etude-la-rehabilitation-hygrothermique-des-parois-anciennes.

Janssen, H. (2002). *The influence of soil moisture transfer on building heat loss via the ground*. KU Leuven.

Janssen, H., Blocken, B., & Carmeliet, J. (2007). Conservative modelling of the moisture and heat transfer in building components under atmospheric excitation. *International Journal of Heat and Mass Transfer*, *50*, 1128–1140. https://doi.org/10.1016/j.ijheatmasstransfer.2006.06.048.

Janssen, H., Blocken, B., Roels, S., & Carmeliet, J. (2007). Wind-driven rain as a boundary condition for HAM simulations: Analysis of simplified modelling approaches. *Building and Environment*, *42*, 1555–1567. https://doi.org/10.1016/j.buildenv.2006.10.001.

Janssen, H., Carmeliet, J., & Hens, H. (2004). The influence of soil moisture transfer on building heat loss via the ground. *Building and Environment*, *39*, 825–836. https://doi.org/10.1016/j.buildenv.2004.01.004.

Janssen, H., & Roels, S. (2009). Qualitative and quantitative assessment of interior moisture buffering by enclosures. *Energy and Buildings*, *41*(4), 382–394. https://doi.org/10.1016/j.enbuild.2008.11.007.

Jaquin, P. A., Augarde, C. E., Gallipoli, D., & Toll, D. G. (2009). The strength of unstabilised rammed earth materials. *Géotechnique*, *59*(5), 487–490. https://doi.org/10.1680/geot.2007.00129.

Kianfar, E., & Toufigh, V. (2016). Reliability analysis of rammed earth structures. *Construction and Building Materials*, *127*, 884–895. https://doi.org/10.1016/j.conbuildmat.2016.10.052.

Kinnell, P. I. A. (2005). Raindrop-impact-induced erosion processes and prediction: a review. *Hydrological Processes*, *19*, 2815–2844. https://doi.org/10.1002/hyp.5788.

Koči, J., Madera, J., Keppert, M., & Robert, Č. (2017). Damage functions for the cold regions and their applications in hygrothermal simulations of different types of building structures. *Cold Regions Science and Technology*, *135*, 1–7. https://doi.org/10.1016/j.coldregions.2016.12.004.

Leylavergne, E. (2012). *La filière terre crue en France. Enjeux, freins et perspectives.* Ecole Nationale Supérieure d'Architecture de Grenoble.

Liuzzi, S., Hall, M. R., Stefanizzi, P., & Casey, S. P. (2013). Hygrothermal behaviour and relative humidity buffering of unfired and hydrated lime-stabilised clay composites in a Mediterranean climate. *Building and Environment*, *61*, 82–92. https://doi.org/10.1016/j.buildenv.2012.12.006.

Livermore, C. (2007). Elasticity. Course materials for Design and Fabrication of Microelectromechanical Devices. Retrieved from https://ocw.mit.edu/courses/electrical-engineering-and-computer-science/6-777j-design-and-fabrication-of-microelectromechanical-devices-spring-2007/lecture-notes/07lecture06split.pdf (accessed on 30 June 2020).

Livradois-Forez, P. (2011). Rénover & Construire en Pisé dans le Parc naturel régional Livradois-Forez. Retrieved from https://craterre.hypotheses.org/files/2017/05/8421_Construire_et_renover_en_Pise_PNR_LF.pdf.

Madsen, F. T., & Müller-Vonmoos, M. (1989). The Swelling Behaviour of Clays. *Applied Clay Science*, *4*, 143–156. https://doi.org/10.1016/0169-1317(89)90005-7.

Maniatidis, V., & Walker, P. (2003). A review of rammed earth construction, 1–109. Retrieved

from http://staff.bath.ac.uk/abspw/rammedearth/review.pdf.

Météo France. (n.d.). Retrieved from https://donneespubliques.meteofrance.fr/?fond=produit&id_produit=110&id_rubrique=37 (accessed in 2020).

Micromeritics. (2001). *Porosimetry*. Retrieved from http://www.micromeritics.com/Repository/Files/Porosimetry_brochure.pdf (accessed on 8 August 2018).

Minke, G. (2006). *Building with Earth. Design and Technology of a Sustainable Architecture*. Birkhäuser. https://doi.org/10.1007/3-7643-7873-5.

Mohaddes Foroushani, S. S., Ge, H., & Naylor, D. (2014). Effects of roof overhangs on wind-driven rain wetting of a low-rise cubic building: A numerical study. *Journal of Wind Engineering and Industrial Aerodynamics*, *125*, 38–51. https://doi.org/10.1016/j.jweia.2013.10.007.

Montazeri, H., Blocken, B., Derome, D., Carmeliet, J., & Hensen, J. L. M. (2015). CFD analysis of forced convective heat transfer coefficients at windward building facades: Influence of building geometry. *Journal of Wind Engineering*, *146*, 102–116. https://doi.org/10.1016/j.jweia.2015.07.007.

Moonen, P., & Wangler, T. (2015). An analytical approach to the characterization of swelling in clay-bearing stone. *Philosophical Magazine*, *95*(28–30), 3103–3121. https://doi.org/10.1080/14786435.2015.1063788.

Morel, J. (2012). Weathering and durability of earthen material and structures. In *Modern earth buildings* (pp. 282–303). Woodhead. https://doi.org/10.1533/9780857096166.2.282.

Morris, H. W. (2012). 19 Natural disasters and earth buildings: resistant design and construction. In *Modern earth buildings: Materials, engineering, construction and applications*. https://doi.org/10.1533/9780857096166.4.481.

Nicolai, A., & Grunewald, J. (2006). *Delphin 5 User Manual and Program Reference*.

Nowamooz, H., & Chazallon, C. (2011). Finite element modelling of a rammed earth wall. *Construction and Building Materials*, *25*(4), 2112–2121. https://doi.org/10.1016/j.conbuildmat.2010.11.021.

NZS 4297. (1998). *New Zealand Standard. Engineering Design of Earth Buildings.*

Olesen, B. W. (2005). INTERNATIONAL STANDARDS FOR THE INDOOR ENVIRONMENT . WHERE ARE WE AND DO THEY APPLY WORLDWIDE?

Olesen, B. W., & Parsons, K. C. (2002). Introduction to thermal comfort standards and to the proposed new version of EN ISO 7730. *Energy and Buildings*, *34*, 537–548.

Pease, B. J., Scheffler, G. A., & Janssen, H. (2012). Monitoring moisture movements in building materials using X-ray attenuation: Influence of beam-hardening of polychromatic X-ray photon beams. *Construction and Building Materials*, *36*, 419–429. https://doi.org/10.1016/j.conbuildmat.2012.04.126.

Protopapadaki, C. (2018). *A probabilistic framework towards metamodeling the impact of residential heat pumps and PV on low-voltage grids*. KU Leuven.

Rauch, M. (2015). *Refined earth construction & design with rammed earth*. DETAIL. Retrieved

from https://issuu.com/detail-magazine/docs/978-3-95553-273-4-bk-en-rauch-refin.

Rees, D. W. A. (2009). Appendix B. Plate Buckling Under Uniaxial Compression. In *Mechanics of Optimal Structural Design: Minimum Weight Structures* (pp. 525–535). John Wiley & Sons.

Ren, P., Feng, C., & Janssen, H. (2019). Hygric properties of porous building materials (V): Comparison of different methods to determine moisture diffusivity. *Building and Environment*, *164*, 106344. https://doi.org/10.1016/j.buildenv.2019.106344.

Reppel bv. (2020). *LEWIS Zwaluwstaartplaten Geluidsisolerende vloeren*. Retrieved from https://reppel.nl/storage/assets/lewis-geluidsisolerende-vloeren.pdf (accessed on 14 January 2021).

Rode, C., Peuhkuri, R., Mortensen, L. H., Hansen, K. K., Time, B., Gustavsen, A., … Arfvidsson, J. (2005). *Moisture Buffering of Building Materials*.

Roels, S. (2000). *Modelling unsaturated moisture transport in heterogeneous limestone*. KU Leuven.

Roels, S., & Carmeliet, J. (2006). Analysis of moisture flow in porous materials using microfocus X-ray radiography. *International Journal of Heat and Mass Transfer*, *49*(25–26), 4762–4772. https://doi.org/10.1016/j.ijheatmasstransfer.2006.06.035.

Roels, S., Carmeliet, J., Hens, H., Adan, O., Brocken, H., Cerny, R., … Plagge, R. (2004). Interlaboratory Comparison of Hygric Properties of Porous Building Materials. *Journal of Thermal Envelope and Building Science*, *27*(4), 307–325. https://doi.org/10.1177/1097196304042119.

Roels, S., Elsene, J., Carmeliet, J., & Hens, H. (2001). Characterisation of pore structure by combining mercury porosimetry and micrography. *Materials and Structures/Matériaux et Constructions*, *34*(March), 76–82. https://doi.org/10.1007/BF02481555.

Roels, S., Moonen, P., Proft, K. De, & Carmeliet, J. (2006). A coupled discrete-continuum approach to simulate moisture effects on damage processes in porous materials. *Computer Methods in Applied Mechanics and Engineering*, *195*, 7139–7153. https://doi.org/10.1016/j.cma.2005.05.051.

Sanders, C. (2008). Climate Change and its Implications for Hygrothermal Modelling. In *IEA Annex 41 whole building heat, air, moisture response: Closing seminar, Nordic Building Physics Conference* (pp. 105–116).

Scarato, P. (2014). *Pour finir avec les sinistres - maisons en terre*. Retrieved from http://www.canalc2.tv/video/12981.

Scheffler, G. A., & Plagge, R. (2010). A whole range hygric material model: Modelling liquid and vapour transport properties in porous media. *International Journal of Heat and Mass Transfer*, *53*(1–3), 286–296. https://doi.org/10.1016/j.ijheatmasstransfer.2009.09.030.

Scherer, G. W. (2006). Internal stress and cracking in stone and masonry. In M. S. Konsta-Gdoutos (Ed.), *Measuring, Monitoring and Modeling Concrete Properties* (pp. 633–641).

Scherer, G. W., & Gonzalez, I. J. (2005). Characterization of swelling in clay-bearing stone. *Geological Society of America Special Paper*, *390*, 51–61. https://doi.org/10.1130/2005.2390(06).

Schroeder, H. (2012). 4 Modern earth building codes, standards and normative development.

In *Modern earth buildings: Materials, engineering, construction and applications*. https://doi.org/10.1533/9780857096166.1.72.

Sharples, S. (1984). Full-scale measurements of convective energy losses from exterior building surfaces. *Building and Environment*, *19*(1), 31–39. https://doi.org/10.1016/0360-1323(84)90011-8.

Sing, K. S. W., Everett, D. H., Haul, R. A. W., Moscou, L., Pierotti, R. A., Rouquérol, J., & Siemieniewska, T. (1985). REPORTING PHYSISORPTION DATA FOR GAS / SOLID SYSTEMS with Special Reference to the Determination of Surface Area and Porosity. *Pure & Applied Chemistry*, *57*(4), 603–619.

Soebarto, V. (2009). Analysis of indoor performance of houses using rammed earth walls. In *IBPSA 2009 - Eleventh International Building Performance Simulation Association Conference* (pp. 1530–1537). Glasgow, Scotland. Retrieved from http://www.scopus.com/inward/record.url?eid=2-s2.0-84870167731&partnerID=tZOtx3y1.

Sontag, L., Nicolai, A., & Vogelsang, S. (2013). *Validierung der Solverimplementierung des hygrothermischen Simulationsprogramms Delphin*. Retrieved from http://www.qucosa.de/fileadmin/data/qucosa/documents/12896/DelphinValidierung.pdf.

Soudani, L. (2017). *Modelling and experimental validation of the hygrothermal performances of earth as a building material*. Ecole Nationale des Travaux Publics de l'Etat.

Teifouet, M., Robinson, A., & Adali, S. (2017). Buckling of nonuniform carbon nanotubes under concentrated and distributed axial loads. *Mechanical Sciences*, *8*, 299–305. https://doi.org/10.5194/ms-8-299-2017.

Teifouet, M., Robinson, A., & Adali, S. (2019). Buckling of elastically restrained nonlocal carbon nanotubes under concentrated and uniformly distributed axial loads. *Mechanical Sciences*, *10*, 145–152. https://doi.org/10.5194/ms-10-145-2019.

TERA. (2018). CONSTRUIRE TERRE CRUE. Guide des bonnes pratiques de la construction en terre crue. Retrieved from https://arpenormandie.org/wp-content/uploads/2019/07/GBP_CTC_2018_web.pdf.

Tijskens, A., Janssen, H., & Roels, S. (2017). A simplified dynamic zone model for a probabilistic assessment of hygrothermal risks in building components. In *Energy Procedia* (Vol. 132, pp. 717–722). https://doi.org/10.1016/j.egypro.2017.10.012.

Troppová, E., Švehlík, M., Tippner, J., & Wimmer, R. (2015). Influence of temperature and moisture content on the thermal conductivity of wood-based fibreboards. *Materials and Structures/Materiaux et Constructions*, *48*(12), 4077–4083. https://doi.org/10.1617/s11527-014-0467-4.

van Genuchten, M. T. (1980). A Closed-form Equation for Predicting the Hydraulic Conductivity of Unsaturated Soils.

Vereecken, E. (2013a). *Draft Hygrothermal Analysis of Interior Insulation. Ph.D Thesis*.

Vereecken, E. (2013b). *Hygrothermal Analysis of Interior Insulation for Renovation Projects*. KU Leuven.

Vereecken, E., & Roels, S. (2012). Review of mould prediction models and their influence on

mould risk evaluation. *Building and Environment*, *51*, 296–310. https://doi.org/10.1016/j.buildenv.2011.11.003.

Vereecken, E., & Roels, S. (2013). Hygric performance of a massive masonry wall: How do the mortar joints influence the moisture flux? *Construction and Building Materials*, *41*, 697–707. https://doi.org/10.1016/j.conbuildmat.2012.12.024.

Vereecken, E., & Roels, S. (2015). Capillary active interior insulation: do the advantages really offset potential disadvantages? *Materials and Structures/Materiaux et Constructions*, *48*(9), 3009–3021. https://doi.org/10.1617/s11527-014-0373-9.

Vereecken, E., & Roels, S. (2016). Capillary Active Interior Insulation Systems for Wall Retrofitting: A More Nuanced Story. *International Journal of Architectural Heritage*, *10*(5), 558–569. https://doi.org/10.1080/15583058.2015.1009575.

Vereecken, E., Van Gelder, L., Janssen, H., & Roels, S. (2015). Interior insulation for wall retrofitting - A probabilistic analysis of energy savings and hygrothermal risks. *Energy and Buildings*, *89*, 231–244. https://doi.org/10.1016/j.enbuild.2014.12.031.

Viitanen, H., Toratti, T., Makkonen, L., Peuhkuri, R., Ojanen, T., Ruokolainen, L., & Räisänen, J. (2010). Towards modelling of decay risk of wooden materials. *European Journal of Wood and Wood Products*, *68*(3), 303–313. https://doi.org/10.1007/s00107-010-0450-x.

Wan, H., Xu, X., & Li, A. (2017). Application analysis of theoretical moisture penetration depths of conventional building material. *Advances in Mechanical Engineering*, *9*(5), 1–10. https://doi.org/10.1177/1687814017699803.

Wangler, T., Ngo, E., & Scherer, G. W. (2012). SWELLING PRESSURE AND STRESS DEVELOPMENT IN CLAY-BEARING SANDSTONES. In *12th International Congress on the Deterioration and Conservation of Stone* (pp. 1–9). New York.

Wangler, T., & Scherer, G. W. (2009). Clay swelling inhibition mechanism of a,w-diaminoalkanes in Portland Brownstone. *Journal of Materials Research*, *24*(5), 1646–1652. https://doi.org/10.1557/jmr.2009.0190.

Wilson, M. A., Hoff, W. D., & Hall, C. (1995). Water Movement in Porous Building Materials - XIII. Absorption into a Two-Layer Composite. *Building and Environment*, *30*(2), 209–219. https://doi.org/10.1016/0360-1323(94)00035-Q.

Wolkoff, P. (2018). Indoor air humidity, air quality, and health – An overview. *International Journal of Hygiene and Environmental Health*, *221*, 376–390. https://doi.org/10.1016/j.ijheh.2018.01.015.

WTCB. (2001). *DIMENSIONEREN VAN HOUTCONSTRUCTIES. Deel 2: Houten dakconstructies*. Retrieved from http://www.confederatiebouw.be/portals/38/CDSchrijnwerk/data_tech_doc_schrijnwerk/docs/Houtconstructies/Dimensionering van houtconstructies. Deel 2.pdf.

Zhao, J., & Plagge, R. (2015). Characterization of hygrothermal properties of sandstones - Impact of anisotropy on their thermal and moisture behaviors. *Energy and Buildings*, *107*, 479–494. https://doi.org/10.1016/j.enbuild.2015.08.033.

Zhou, X., Carmeliet, J., & Derome, D. (2018). Influence of envelope properties on interior insulation solutions for masonry walls. *Building and Environment*, *135*, 246–256. https://doi.org/10.1016/j.buildenv.2018.02.047.

Zhou, X., Derome, D., & Carmeliet, J. (2016). Robust moisture reference year methodology for hygrothermal simulations. *Building and Environment*, *110*, 23–35. https://doi.org/10.1016/j.buildenv.2016.09.021.

Zhou, X., Derome, D., & Carmeliet, J. (2017). Hygrothermal modeling and evaluation of freeze-thaw damage risk of masonry walls retrofitted with internal insulation. *Building and Environment*, *125*, 285–298. https://doi.org/10.1016/j.buildenv.2017.08.001.